

University of Warwick institutional repository: <http://go.warwick.ac.uk/wrap>

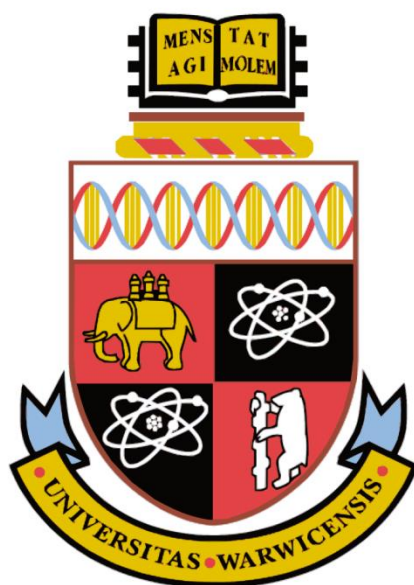
A Thesis Submitted for the Degree of PhD at the University of Warwick

<http://go.warwick.ac.uk/wrap/67483>

This thesis is made available online and is protected by original copyright.

Please scroll down to view the document itself.

Please refer to the repository record for this item for information to help you to cite it. Our policy information is available from the repository home page.



The Fabrication and application of diamond sensors for electrochemical analysis in single and multiple phase systems

Jonathan Christopher Newland

A thesis submitted for the degree of Doctor of Philosophy

University of Warwick, Department of Chemistry

September 2014

To my Dad

Table of Contents

List of Figures -----	iv
List of Tables -----	xiv
Acknowledgements -----	xv
Declaration -----	xvi
Abstract -----	xvii
Abbreviations -----	xviii
Glossary of symbols -----	xxii
1 Introduction -----	1
1.1 Electrochemistry as a method for analysis in stationary and under flow regimes-----	1
1.1.1 Introduction to electrochemistry: Electrochemical cells-----	2
1.1.2 Dynamic electrochemistry -----	3
1.2 Synthetic diamond as an electrode material -----	28
1.2.1 Introduction to synthetic diamond -----	28
1.2.2 Growth of synthetic diamond-----	29
1.2.3 Properties of diamond -----	30
1.2.4 Electrochemistry on boron-doped diamond electrodes -----	35
1.2.5 Applications of boron-doped diamond-----	38
1.3 Multiphase flow -----	38
1.3.1 Introduction to multiphase flow-----	38
1.3.2 Applications in industry-----	40
1.4 Microfluidics: Lab on a chip -----	41
1.4.1 Introduction to microfluidics -----	41
1.5 Aims and Objectives-----	46
1.6 References -----	47
2 Experimental-----	52
3 : Materials, instrumentation and techniques -----	52
2.1 Materials -----	52
2.1.1 CVD diamond -----	52
2.1 Chemicals -----	52
2.2 Electrochemical instrumentation: -----	53
2.3 Electrochemical techniques-----	55

2.3.1	Chronoamperometry-----	55
2.3.2	Double potential step chronoamperometry-----	55
2.3.3	Differential pulse voltammetry-----	56
2.4	Fabrication techniques-----	57
2.4.1	Laser micromachining-----	57
2.4.2	Metallisation of surfaces-----	60
2.4.3	Reactive Ion Etching: RIE-----	60
2.5	Boron-doped diamond electrode fabrication-----	63
2.5.1	Laser machining of pBDD-----	63
2.5.2	Acid cleaning-----	63
2.5.3	Metallisation and formation of an Ohmic contact-----	64
2.5.4	Glass-sealed macroelectrodes-----	64
2.6	Characterisation techniques-----	65
2.6.3	White Light Interferometry (WLI)-----	68
2.6.4	Atomic force microscopy-----	68
2.7	References-----	70
3	Detection of hydrazine using metal-nanoparticle functionalised pBDD electrodes-----	71
3.1	Introduction-----	71
3.2	Experimental-----	73
3.2.1	Reagents & materials-----	73
3.2.2	Apparatus-----	73
3.2.3	Preparation and characterisation of electrodes-----	73
3.3	Results and Discussion-----	74
3.3.1	Hydrazine Voltammetry-----	74
3.3.2	Acetaminophen voltammetry-----	77
3.3.3	Promazine voltammetry-----	78
3.3.4	Detection of hydrazine with AuNP-p-BDD macroelectrodes in non-aqueous solvents	81
3.3.5	Detection of hydrazine derivatives in acetonitrile with an AuNP-p-BDD macroelectrode-----	84
3.3.6	Detection of hydrazine in polymer degradation-----	86
3.4	Conclusions-----	88
3.5	References-----	89
4	An electrochemical technique for probing the partition of electro-active bromine between aqueous and non-aqueous phases-----	92
4.1	Introduction-----	92
4.2	Experimental-----	94

4.2.1	Chemicals -----	94
4.2.2	Instrumentation and protocols -----	94
4.2.3	Simulations -----	96
4.2.4	DPSC Experiments -----	101
4.3	Results and Discussion -----	102
4.3.1	Effect of droplet size -----	102
4.3.2	Effect of τ -----	107
4.3.3	Effect of electrode size -----	108
4.3.4	Non-spherical droplets -----	109
4.3.5	Droplet arrays -----	110
4.4	Conclusions -----	111
4.5	References -----	112
5	Chapter 5: Electrochemical detection of phase changes in microfluidic systems -----	114
5.1	Introduction -----	114
5.2	Results and Discussion -----	118
5.2.1	Fabrication of PDMS microfluidic devices -----	119
5.2.2	Droplet generation geometries -----	125
5.2.3	Integration of thin-film metal electrodes in microfluidic devices -----	131
5.2.4	Electrochemical detection of water droplets containing an electroactive mediator ---	136
5.3	Conclusions -----	145
5.4	References -----	147
6	Chapter 6: All-Diamond Microfluidic Devices for Solution Analysis -----	150
6.1	Introduction -----	150
6.1.1	Micro-scale devices fabricated from synthetic diamond -----	151
6.1.2	Laser machining of diamond -----	151
6.2	Results and Discussion -----	153
6.2.1	The fabrication of microfluidic channels in synthetic, intrinsic diamond using laser micromachining. -----	153
6.2.2	Boron-doped diamond electrodes -----	159
6.2.3	Fabrication of diamond microfluidic device with integrated diamond electrodes ----	167
6.2.4	Microdroplet generation in a diamond microfluidic device -----	172
6.3	Conclusions -----	175
6.4	References -----	178
	Chapter 7: Conclusions and Further Work -----	181

List of Figures

<i>Figure 1.1: An electrochemical cell consisting of two electrodes immersed in an aqueous solution containing a redox active species “O” and electrolyte. The cell is capable of (1) measuring potential via a voltmeter or (2) applying current/potential and measuring potential/current via a potentiostat.</i>	2
<i>Figure 1.2: schematic representing factors that govern electrode dynamics in a heterogeneous reaction</i> -----	4
<i>Figure 1.3: A schematic of a typical self-contained Ag AgCl reference electrode.</i> -----	7
<i>Figure 1.4: schematic of a 3-electrode set-up consisting of a working electrode, AgAgCl reference electrode and a Platinum gauze counter electrode</i> -----	8
<i>Figure 1.5: Free energy plot for a transition state model of a one electron reduction of a species O(aq) to species R(aq) via a transition state \ddagger.</i> -----	10
<i>Figure 1.6: schematic of the electrical double layer as proposed by Helmholtz where x represents the distance extending from the electrode surface into the bulk solution</i> -----	14
<i>Figure 1.7: schematic of the Bockris-Devanathan-Müller model for the electronic double layer at an electrode/electrolyte interface.</i> -----	15
<i>Figure 1.8: Schematic of (a) an outer-sphere electrode reaction and (b) an inner-sphere electrode reaction.</i> -----	17
<i>Figure 1.9: The evolution of concentration profiles with time, t for a diffusion controlled process involving the reduction of O; where x is the distance into bulk solution from the electrode surface(x = 0).</i> -----	19
<i>Figure 1.10: i-t transient for a diffusion limited process</i> -----	20
<i>Figure 1.11: Diffusion profiles of (a) uniform diffusion to a planar electrode, (b) diffusion to a hemispherical electrode and (c) non-uniform diffusion to a microelectrode.</i> -----	21
<i>Figure 1.12: Schematic of convective flow regimes often adopted in electrochemical experiments: (a) a rotating disc (RDE), (b) flow in a channel and (c) an impinging jet.</i> -----	23
<i>Figure 1.13: Schematic of a laminar flow regime in a channel with width, L. The arrow size in the parabolic flow represent the velocities of the fluid layers.</i> -----	24
<i>Figure 1.14: Schematic showing the relationship between the diffusion layer and hydrodynamic layer for a hydrodynamic electrode where x extends out from the electrode surface into solution.</i> -----	24
<i>Figure 1.15: (a) E-t plot for a cyclic voltammogram, scanning the potential from E_1 to E_2 and then in reverse; (b) A typical voltammogram for a simple redox mediator undergoing reduction and then oxidation where i_p^C and E_p^C are the cathodic peak current and potential, respectively and i_p^A and E_p^A are the anodic peak current and potential, respectively.</i> -----	26

Figure 1.16: A typical voltammogram for the reduction of a simple redox mediator on a microelectrode where i_{lim} is the steady state current resulting from the reduction of the mediator ----28

Figure 1.17: The tetrahedral lattice structure of diamond. Red atoms highlight a tetrahedral unit within the lattice structure -----31

Figure 1.18: Schematic of differential grain growth in polycrystalline diamond films grown via CVD -----32

Figure 1.19: Schematic of electronic density of states and band structures for (a) insulating, intrinsic diamond, (b) boron-doped diamond and (c) highly boron-doped diamond; where μ_f is the Fermi level, E_a and E_d are the energy associated with acceptor and donor levels respectively. -----34

Figure 1.20: Electrical resistivity (at room temperature) as a function of boron doping density in single-crystal boron-doped diamond samples grown by Lagrange et al⁶³. -----35

Figure 1.21: Comparison of oxygen and hydrogen terminated polycrystalline intrinsic diamond with (a) the contact angle of a water droplet on a hydrogen terminated surface in air, (b) the contact angle of a water droplet on an oxygen-terminated surface in air, (c) a schematic of a hydrogen-terminated surface; (d) schematic of an oxygen terminated surface. -----37

Figure 1.22: Schematic of multiphase flow patterns for a system consisting of two immiscible phases 1 and 2 in (a) horizontal flow: (i) plug flow, (ii) stratified flow, (iii) wavy-stratified flow, (iv) bubbly flow; (b) vertical flow: (i) bubbly flow, (ii) plug flow, (iii) churn flow, (iv) annular flow; where the density of phase 1 > phase 2. -----39

Figure 1.23: (a) Schematic of diffusional mixing of two miscible fluid streams in a rectangular microfluidic channel; (b) an illustration of the uniaxial Poiseuille-like velocity field seen in a rectangular channel with flow in the z direction; (c) schematic showing the non-uniform interfacial region generated under uniaxial Poiseuille-like flow; (d) Schematic of the action of Taylor dispersion on a plug of material flowing through a channel under a laminar regime, with time. -----44

Figure 1.24: Schematic of a microfluidic geometry designed to induce convective mixing between two miscible fluids via the Coanda effect. -----45

Figure 2.1: Schematic of a simple potentiostat consisting of an operational amplifier (OA) and a 3-electrode electrochemical cell with working electrode (WE), reference electrode (RE) and counter electrode (CE).¹ -----54

Figure 2.2: (a) E - t plot for a typical CA experiment and (b) the resulting i - t plot -----55

Figure 2.3: (a) E - t plot for a typical DPSC experiment and (b) the resulting i - t plot -----56

Figure 2.4: (a) Schematic showing the time dependence of non-faradaic, double layer charging current (dotted line), faradaic current (solid line) and the total observed current as a result of the previous two components (dashed line); (b) the waveform for a DPV experiment; (c) i - t plot for a typical DPV (solid line) compared with the equivalent LSV (dotted line). -----57

Figure 2.5: The layout of the beam (blue line) delivery optics contained in the optics cabinet of the Oxford Lasers system: (A) laser cavity, (B) safety shutter, (C) alignment iris, (D) 1st telescopic lens, (E) 50 μm spatial filter, (F) 2nd telescopic lens, (G) turning mirror, (H) attenuator, (I) polariser, (J) beam dump, (K) turning mirror, (L) alignment iris, (M) $\frac{1}{4}$ λ plate and (N) laser trepan optics module.

-----58

Figure 2.6: Schematic of a laser trepan optics set up consisting of two wedge optics: Trepan A and Trepan B, focusing lens and the resulting beam path on the machined substrate. -----59

Figure 2.7: Schematic of a benching cut along the x-axis with a laser beam to create a “V”-shaped cut. -----60

Figure 2.8: Schematic of a simple RIE system -----62

Figure 2.9: Photographs of a 1 mm diameter glass-sealed pBDD macroelectrode: (a) top view; (b) side view. -----64

Figure 2.10: Schematic of the different photon scattering modes and their associated transitions. ---66

Figure 2.11: Schematic of an AFM system: (1) the probe is scan while (2) a laser beam is directed onto the cantilever (3), reflecting onto the (4) photodiode detector. -----69

Figure 3.1: Tapping mode AFM images of (a) bare pBDD; (b) electrodeposited Au NP-pBDD and (c) electrodeposited Pt NP-pBDD electrodes with cross sectional height analysis of the three different surfaces in the zones indicated by the white lines -----74

Figure 3.2: LSVs of 1 mM HZ oxidation on (---) Pt NP-pBDD, (---) Au NP-pBDD and (—) bare pBDD, recorded at a potential scan rate of 0.1 V s⁻¹. -----75

Figure 3.3: HZ oxidation on an Au NP-pBDD electrode using (a) LSV and (b) DPV, with the corresponding graphs of peak current (LSV, c) or peak area (DPV, d) versus concentration. HZ concentrations 0, 10, 100, 250, 500, 750 and 1000 μM HZ ($n = 5$). -----76

Figure 3.4: ACM oxidation on an Au NP-pBDD electrode in a solution containing 1 mM ACM in 0.1 M PBS, using (a) LSV and (b) DPV. -----77

Figure 3.5: (a) DPV of varying concentrations of HZ in the presence of 1 mM ACM at an AuNP-pBDD electrode with 0, 10, 100, 250, 500, 750 and 1000 μM HZ. (b) Plot of HZ DPV peak areas versus concentration ($n = 5$). -----78

Figure 3.6: PZ oxidation in a solution containing 1 mM PZ in 0.1 M PBS, at a bare pBDD (—) and an Au NP-pBDD electrode (---) using (a) LSV and (b) DPV -----79

Figure 3.7: DPV of varying concentrations of HZ in the presence of 1 mM PZ, at an AuNP-pBDD electrode with 0, 10, 100, 250, 500, 750 and 1000 μM HZ. -----79

Figure 3.8: (a) DPV of varying concentrations of HZ in the presence of 1 mM PZ, at a PtNP-pBDD electrode with 0, 10, 100, 250, 500, 750 and 1000 μM HZ. (b) Plot of HZ DPV peak areas versus HZ concentration ($n = 5$). -----80

Figure 3.9: (a) CV response for (red) 1 mM HZ in MeCN with 0.1 M TBAHFP and (black) 0.1 M TBAHFP in MeCN; (b) plot of i_p vs. HZ concentration for a concentration range of 0.5 – 10 μ M HZ ($n = 5$). -----82

Figure 3.10: (a) CV response for (black) 10 mM HZ in DMSO with 0.1 M TBAHFP and (pink) a solution of just 0.1 M TBAHFP; (b) plot of i_p vs. HZ concentration for solutions of concentrations ranging from 0.01 – 20 mM HZ ($n = 5$).-----83

Figure 3.11: Molecular structures of (a) 2-hydroxyethylhydrazine, (b) phenylhydrazine, (c) 4-(trifluoromethyl)-phenylhydrazine.-----84

Figure 3.12: (a) CVs of acetonitrile solutions containing 1 mM: 2-hydroxyethylhydrazine (black), phenylhydrazine (blue) and 4-(trifluoromethyl)-phenylhydrazine (red dotted), all with TBAHFP as supporting electrolyte; (b) CV of acetonitrile solutions containing all three HZ derivatives at 1 mM concentrations of each. -----85

Figure 3.13: Molecular structures of (a) Methacryloyl Hydrazide monomer and (b) poly(methacryloyl hydrazide); (c) schematic of the hydrolysis of poly(methacryloyl hydrazide, producing HZ.-----86

Figure 3.14: (a) CV responses for solutions of 0.015 % (w/w) MH polymer with 1 mM MH monomer and 0.3 mM HZ (black); 1 mM MH monomer (red); 0.015 % (w/w) MH polymer with 0.85 mM HZ; back ground response of 0.015 % (w/w) MH polymer, all solutions in 0.1 M PBS. (b) CVs for PtNP=pBDD electrode in solution of 0.015 % (w/w) MH polymer with 24 hrs (black), 168 hrs (red), 336 hrs (blue) and 408 hrs (pink). (c) plot of i_p vs. time for HZ detection in polymer solution with time ($n = 5$). -----87

Figure 4.1: Simulation geometry for (a) single oil droplets on the electrode surface and (b) oil droplet arrays. -----97

Figure 4.2: (a) CVs of 10 mM KBr in 0.5 M H_2SO_4 , scan rate 100 mV s^{-1} at a bare 1 mm diameter disc pBDD electrode (black line), 2 mm diameter disc Pt macroelectrode (red dashed line) and a Pt NP-pBDD electrode (blue line). The currents have been normalized with respect to electrode area. (b) Tapping mode AFM image of electrodeposited Pt NPs on the pBDD electrode surface. ----- 102

Figure 4.3: (a) Q - t plots generated from integrating the DPSC i - t response for 1 mM $FcTMA^+$ generation-collection at a bare Pt NP-pBDD electrode (-) and one containing a single dodecane droplet of diameter 100 μ m (■), 200 μ m (▲) and 400 μ m (▼). (b) Plot of normalized charge (Q/Q_{max}) vs. t for the last 0.5 s of the collection step. (c) FEM-simulated diffusion profiles of $FcTMA^{+2+}$ generation/collection in the presence of dodecane droplets of diameter (i) 100 μ m and (ii) 400 μ m diameter at times $t = 2\text{ s}$ and $t = 4\text{ s}$. (d) Optical images of dodecane droplets (of diameter 100-400 μ m) on a Pt NP-pBDD electrode. ----- 103

Figure 4.4: (a) Q - t plots for 1 mM Br^-/Br_2 generation-collection at a bare PtNP-pBDD electrode (-) and one containing a single dodecane droplet of diameter 100 μ m (■), 200 μ m (▲), 400 μ m (▼), 1000 μ m (◀) and 1450 μ m (◆). (b) Optical images of dodecane droplets (of diameter 1000 and 1450 μ m) on the PtNP-pBDD electrode. (c) Plot of normalized charge (Q/Q_{max}) vs. t for the collection step. ----- 105

Figure 4.5: Diffusion profiles generated from FEM simulation of Br^-/Br_2 generation/collection in the presence of dodecane droplets (a) 100 μm and (b) 400 μm diameter at times $t = 2$ s and $t = 4$ s. Note the different scale bars for Br_2 concentration inside the oil droplet for both (a) and (b). ----- 106

Figure 4.6: Plot of normalized charge (Q/Q_{max}) vs. t for the collection step i.e. collection of electrogenerated Br_2 at a bare electrode (—) and one containing a single dodecane droplet of diameter 100 μm (■), 200 μm (▲), 400 μm (▼): (a) simulated data and (b) experimental data. --- 107

Figure 4.7: Normalized experimental Q - t plots for the DPSC Br_2 collection step with bare Pt NP-pBDD (—) and 100 μm (●) and 200 μm (▲) oil droplets present on the electrode for $\tau =$ (a) 200 ms, (b) 1 s, (c) 10 s and (d) 20 s. ----- 108

Figure 4.8: Plot of normalized charge (Q/Q_{max}) vs. t for the simulated collection step i.e. Br_2 collection for a PtNP - pBDD electrode of diameter 500 μm (■), 300 μm (▼), 200 μm (▲) and 100 μm (●) containing a single oil droplet of diameter 100 μm (red) and 200 μm (blue). ----- 109

Figure 4.9: (a) Optical images of droplets of effective diameter (i) 1000 μm , (ii) 1700 μm , (iii) 2500 μm and (iv) 3000 μm taken side on (left hand side) and top down (right hand side). The dashed circles show the contact area of the droplet with the electrode. (b) Normalized Q - t plots for droplets of effective diameter 1000 μm (■), 1700 μm (●), 2500 μm (▲) and 3000 μm (▼). ----- 110

Figure 4.10: (a) Optical image of the oil microdroplet array on the Pt NP-pBDD electrode surface from above. (b) Normalized Q - t plots comparing the DPSC response of a single ~ 100 μm diameter droplet with a ~ 100 μm diameter microdroplet array (21 droplets in total). — Bare electrode, ▲ ~ 100 μm droplet array, ■ ~ 100 μm droplet. (c) Diffusion profile along vector “s” generated by an array simulation at $t = 2$ s, multiple repeats of modelled diffusion domain stitched together. ----- 111

Figure 5.1: Schematic of the convective flow profile induced in (a) droplets and (b) in a continuous flow between droplets.----- 116

Figure 5.2: Schematics of common microfluidic droplet generating geometries: (a) Co-flow; (b) Restricted T-junction; and (c) Flow-focussing. ----- 117

Figure 5.3: Photo of a 4” silicon wafer after spincoating with SU-8 photoresist. Edge-bead and air bubbles are present in photoresist. ----- 120

Figure 5.4: Photo of a 4” silicon wafer spincoated with SU-8, sprayed with EC solvent and left 24 hrs on a levelled hotplate at 25° C. ----- 121

Figure 5.5: Photo of SU-8 patterned features on a 4” silicon wafer, broken after PDMS moulding. 121

Figure 5.6: Schematic of silicon mould fabrication using RIE-ICP: (a) Silicon substrate is cleaned; (b) PMGIF6 deep UV resist and S1818 photoresists are spincoated onto the Si wafer; (c) Resists are exposed to UV through a patterned UV mask, and developed in MF-319 developer; (d) a thin film of metal e.g. aluminium is sputter deposited onto the patterned wafer; (e) metal “lift-off” is performed in acetone, dissolving the underlying photoresist; (f) silicon not protected by the metal film is etched by the RIE plasma to produce microfeatures in the silicon wafer. ----- 123

<i>Figure 5.7: Silicon microfeatures created by RIE-ICP etching: (a) 3-armed T-junction device; (b) focus flow device</i> -----	124
<i>Figure 5.8: Microscope images of (a) 3-armed T-junction device; (b) a simple T-junction device; and (c) a focus flow device, all created from SU-8 moulds, with no flow.</i> -----	125
<i>Figure 5.9: (a) Microscope images of a PDMS device under a flow of dodecane and aqueous solution containing blue dye. Images show the extent of PDMS swelling due to dodecane over the space of an hour; (b) T-junction geometry after an hour of flow with dodecane</i> -----	126
<i>Figure 5.10: (a) 3-armed T-junction device under a flow of aqueous solution containing blue dye; (b) device after introduction of hexane.</i> -----	126
<i>Figure 5.11: Microscope images of a 3-armed T-junction generating droplets of octanol (DP) in a 200 μm wide, 150 μm high channel with a continuous aqueous phase containing a blue dye (CP). $V_f = 0.1$ and 1 $\mu\text{L}/\text{min}$ for DP and CP respectively.</i> -----	127
<i>Figure 5.12: Microscope images of a simple T-junction generating droplets of octanol (DP) in a 200 μm wide, 150 μm high channel with a continuous aqueous phase containing a blue dye (CP). $V_f = 0.1$ and 1 $\mu\text{L}/\text{min}$ for DP and CP respectively.</i> -----	127
<i>Figure 5.13: A three-dimensional schematic of a focus-flow geometry with a 40 μm restriction at the intersection point between a 150 μm wide channel and a 200 μm wide channel. The height of the channels is 150 μm.</i> -----	128
<i>Figure 5.14: Droplet geometry orientations for producing: (a) “bubble”-like droplets; (b) “plug”-like droplets.</i> -----	128
<i>Figure 5.15: Microscope images of focus flow geometry producing (a) “bubble”-like droplets, V_f (DP:CP) = 0.02 $\mu\text{L}/\text{min}$: 1.3 $\mu\text{L}/\text{min}$ and (b) “plug”-like droplets, V_f (DP:CP) = 1 $\mu\text{L}/\text{min}$: 2 $\mu\text{L}/\text{min}$</i> -----	129
<i>Figure 5.16: “bubble”-like water droplet generation, in mineral oil CP, within a focus flow geometry under different relative V_f (DP:CP): (a) 0.05 $\mu\text{L}/\text{min}$: 2 $\mu\text{L}/\text{min}$, (b) 0.2 $\mu\text{L}/\text{min}$: 1.3 $\mu\text{L}/\text{min}$, (c) 0.05 $\mu\text{L}/\text{min}$: 1 $\mu\text{L}/\text{min}$, (d) 1 $\mu\text{L}/\text{min}$: 1 $\mu\text{L}/\text{min}$; (e)Plot of droplet diameter as measured via microscopy($N = 15$) as a function of $V_{f(DP)}/V_{f(CP)}$.</i> -----	130
<i>Figure 5.17: “plug”-like water droplet generation in mineral oil CP, within a focus flow geometry V_f (DP): $V_{f(CP)} = 1$ $\mu\text{L}/\text{min}$: 2 $\mu\text{L}/\text{min}$</i> -----	130
<i>Figure 5.18: (a)Schematic of channel electrodes consisting of reference electrode (RE: 80 μm width), working electrode (WE: 40 μm width) and counter electrode (CE: 400 μm width); (b) optical image of Pt channel electrodes integrated into a PDMS microfluidic channel (200 \times 100 μm, $w \times h$)</i> -----	132
<i>Figure 5.19: A schematic of a single channel microfluidic device (200 μm width, 150 μm height, 50 mm long) shown in red with integrated electrodes shown in yellow supported on a glass slide. PDMS has been omitted for clarity.</i> -----	133

Figure 5.20: (a) LSV responses of microfluidic channel electrodes for 1 mM FcTMA⁺ with 0.1 M KNO₃ under various flow rates; (b) Plot of I_{lim} vs. $V_f^{1/3}$ for LSV responses at various flow rates: comparing experimental (red triangle) to Levich fitted to experimental (black square) with $h = 75 \mu\text{m}$ and $d/w = 290 \mu\text{m}$. ----- 134

Figure 5.21: Schematic of focus-flow device for generating “plug”-like droplets of electrolyte solution (green) in a continuous flow of mineral oil (red) with integrated electrodes shown in yellow. ----- 136

Figure 5.22: Schematic of aqueous droplet (green) interaction with channel electrodes as flowing through a channel with velocity V_f : (a) “plug”-like droplet bridging all three channel electrodes creating an electrical contact; (b) “plug”-like droplet smaller than the bridging distance to contact all three electrodes resulting in no electrical contact; (c) “bubble”-like droplet does not contact electrodes at all. ----- 137

Figure 5.23: CV response for 0.1 M KNO₃ solution on Au channel electrodes (scan rate = 100 mV/s) showing the capacitance region between 0 – 0.5 V. ----- 138

Figure 5.24: (a) Current-time response of electrolyte (0.1 M KNO₃) containing water droplets flowing in a mineral oil continuous phase (DP = 8 $\mu\text{L}/\text{min}$, CP = 10 $\mu\text{L}/\text{min}$) on microfluidic channel electrodes held at 0.5 V versus Au quasi-reference electrode; (b) a single electrolyte droplet event on the channel electrodes where (i) dictates the onset of a droplet event and (ii) signifies the end of a droplet event. ----- 138

Figure 5.25: Histogram of 54 droplet charging/discharging events over a period of 30 s. ----- 139

Figure 5.26: (a) i-t plot of an electrolyte droplet event on Au band electrodes under flow with labels corresponding to subsections in (b): Schematics of droplets of water moving through a microfluidic channel containing Au band electrodes with a separation of S_e between the first and final electrodes: (i) droplet makes contact with all three electrodes; (ii) droplet moves over electrodes following the direction of flow, maintaining contact with all three electrodes; (iii) droplet breaks contact with first electrode. ----- 140

Figure 5.27: Current-time responses for two-phase flows of DP = 1 $\mu\text{L}/\text{min}$ with (a) CP = 1 $\mu\text{L}/\text{min}$; (b) CP = 2 $\mu\text{L}/\text{min}$; and (c) CP = 4 $\mu\text{L}/\text{min}$.----- 142

Figure 5.28: (a) Comparison of single droplet events for current-time responses of droplets described in Table 5.1 with droplet event times indicated by the coloured arrows corresponding to the relevant volume flow rate; Histograms of droplets events for two-phase flows of DP = 1 $\mu\text{L}/\text{min}$ with (b) CP = 1 $\mu\text{L}/\text{min}$; (c) CP = 2 $\mu\text{L}/\text{min}$; and (d) CP = 4 $\mu\text{L}/\text{min}$.----- 144

Figure 5.29: Schematic of (a) microfluidic channel electrodes configured for a generation/collection regime where an (i) electroactive species is generated at the first electrode in flow and subsequently collected at an electrode further down-stream; (ii) introduction of a droplet/particle flowing over the electrode distorts the diffusion field at the generation electrode reducing the observed current at both electrodes; (iii) the droplet/particle moves off the first electrode and onto the second, restoring the diffusion field profile and increasing the generation current while reducing the collection current due to the presence of the droplet; (iv) droplet/particle moves off collection electrode restoring the diffusion field generated and subsequently increasing the current. (b) 3D schematics of

generation/collection regime with droplet/particles under flow through a cylindrical channel with ring electrodes (arrow indicates direction of flow) (i) droplet/particle before passing over generation electrode; (ii) droplet/particle after passing over collection electrode.----- 147

Figure 6.1: Photographs of (a) 4×4 mm square and (b) microfluidic channels with inlets/outlets, laser micromachined into polycrystalline intrinsic wafers. ----- 154

Figure 6.2: schematic of the “hatch” pattern used for laser machining of features ----- 155

Figure 6.3: Machining of a $100\ \mu\text{m}$ square with (a) one pass and (b) two passes of the laser beam set to a laser pulse frequency of 100 Hz and stage traversing speed of 0.3 mm/s: (i) a schematic of the beam path and separation between laser pulses (red) achieved; (ii) machined surface roughness measured via WLI for $100\ \mu\text{m}$ squares machined at attenuator power ranging from 30-70 %; (iii) depth profiles measured by WLI for $100\ \mu\text{m}$ squares machined with attenuator powers of 30-70 %. ----- 155

Figure 6.4: Machining of a $100\ \mu\text{m}$ square with one pass of the laser beam set to a laser pulse frequency and stage traversing speed of (a) 200 Hz, 0.6 mm/s and (b) 300 Hz, 0.9 mm/s: (i) machined surface roughness measured via WLI for $100\ \mu\text{m}$ squares machined at attenuator power ranging from 30-70 %; (ii) depth profiles measured by WLI for $100\ \mu\text{m}$ squares machined with attenuator powers of 30-70 %.----- 157

Figure 6.5: Plot of laser output power as a function of laser pulse frequency and corresponding power per pulse for the 355 nm Nd:YAG laser system used.----- 158

Figure 6.6: Schematic of a hexagonal $15\ \mu\text{m}$ diameter pBDD microelectrode array fabricated in intrinsic diamond as reported by Compton et al³⁷ ----- 159

Figure 6.7: Schematics of BNCD electrode containing microfluidic described by Forsberg et al:³⁸ (a) Overview, + and – indicate contacts for applying a voltage yielding an external electric field in the channel. (b) Cross section view showing the device layers and dimensions (not to scale). (c) Top view of the channel and electrodes. ----- 160

Figure 6.8: (a) A typical solvent window generated by CV on a CVD grown, polished microcrystalline, $40\ \mu\text{m}$ wide pBDD band electrode in a solution of 0.1 M KNO_3 . (b) A solvent window of BNCD electrodes in 0.5 M KNO_3 presented by Forsberg et al³⁸ ----- 161

Figure 6.9: A 3D depth profile generated using interferometry of a laser machined trench structure in an intrinsic wafer. Such structures are used for pBDD electrode fabrication via an overgrowth process. ----- 162

Figure 6.10: Schematic of overgrown pBDD electrode designs with: reference electrode (blue), width $120\ \mu\text{m}$; working electrode (pink), width $80\ \mu\text{m}$; counter electrode (red) width $400\ \mu\text{m}$; with a separation (green) of $80\ \mu\text{m}$. ----- 163

Figure 6.11: Schematic of the overgrowth procedure used to fabricate diamond electrode structures: (a) An intrinsic diamond wafer is polished to a roughness of approx. 3 nm; (b) laser micromachining is used to create a trench structure in the diamond wafer as per the electrode design; (c) a layer of

pBDD is overgrown on the machined wafer via MWCVD; (d) the resulting pBDD layer is polished back until the electrode design is revealed. ----- 164

Figure 6.12: Field-emission scanning electron microscopy of pBDD band electrodes overgrown in intrinsic diamond via CVD: (a) cross-section view of pBDD bands (outlined in red); (b) top view of pBDD bands (outlined in red). ----- 164

Figure 6.13: (a) A photograph of a diamond electrode device set up with copper contact pins and a PDMS microfluidic channel; (b) top-contact pads of deposited Ti/Au film on a laser roughened section of pBDD with silver paint added to protect the Ti/Au films. ----- 165

Figure 6.14: (a) interferometry data for a laser machined back-contact hole made in a diamond wafer containing an electrode structure; (b) a photograph of back-contact holes contacting a set of 100 μm wide pBDD electrodes in an intrinsic wafer. ----- 166

Figure 6.15: Photograph of a diamond electrode structure with laser machined back-contact holes coated with a Ti/Au metal film, deposited via sputtering, providing an Ohmic contact with the pBDD bands on the reverse of the structure. ----- 166

Figure 6.16: (a) Raman spectroscopy of (i) intrinsic diamond (blue) and (ii) pBDD regions (green) of the electrode structure shown in (b). The characteristic peak corresponding to sp^3 carbon at 1332 cm^{-1} is indicated with arrows. ----- 167

Figure 6.17: (a) photograph of a 200 μm tapered to 110 μm wide, 135 μm deep microfluidic channel laser machined into a polycrystalline intrinsic diamond wafer; (b) depth profile of laser machined microfluidic channel recorded by WLI. ----- 168

Figure 6.18: An exploded view of an all-diamond microfluidic device with components indicated.- 169

Figure 6.19: Photograph of a diamond electrode structure with a spin-coated, 3 μm thick PDMS gasket present over the electrodes. ----- 170

Figure 6.20: (a) CVs for 1 mM FcTMA^+ oxidation on pBDD channel electrodes with 0.1 M KNO_3 electrolyte at a range of volume flow rates: 10-100 $\mu\text{L}/\text{min}$; (b) Plot of I_{lim} vs. $V_f^{1/3}$ for CV responses at various flow rates: comparing experimental (Black square) to Levich (red line). ----- 171

Figure 6.21: Schematics of the channel and electrode geometry as (a) measured and (b) channel geometry approximated for calculation of corresponding Levich current. ----- 171

Figure 6.22: Photographs of (a) a microfluidic T-junction geometry laser machined in a polycrystalline intrinsic diamond wafer; (b) pBDD electrodes incorporated into a T-junction device for electrochemical droplet analysis. ----- 173

Figure 6.23: Microscope images of a T-junction device ($200 \times 100\text{ }\mu\text{m}$, $w \times h$) fabricated from diamond without a PDMS gasket generating “plug”-like droplets of mineral oil (coloured with Sudan blue II dye and outlined in pink for clarity) in an aqueous continuous phase. ----- 174

Figure 6.24: Schematic of (a) a diamond microfluidic channel with no gasket present between the diamond wafers; (b) An oil droplet occupying a microfluidic channel without interacting with the channel walls. ----- 175

Figure 6.25: Schematic of the fabrication of a diamond microfluidic channel using a sacrificial mould: (a) a silicon wafer mould is fabricated; (b) CVD diamond is grown onto the silicon mould; (c) the silicon is etched off stopping just after the silicon dioxide layer is removed and CVD diamond is grown over the resulting surface; (d) silicon encapsulated by the diamond is etched out leaving behind a hollow channel. ----- 177

List of tables

<i>Table 1.1: Properties of diamond</i> -----	31
<i>Table 2.1: Chemicals and materials used in this thesis including purity and supplier</i> -----	53
<i>Table 4.1: Boundary conditions for the finite element model where n is the inward-pointing unit normal vector; N is the normal flux of species; species A_w is A in the aqueous phase, species B_w is B in the aqueous phase and B_o is B in the oil phase (Br^-/Br_2 system only), with the subscript denoting the phase occupied by the species; k_l and k_{-l} are the mass transfer coefficients equal to 0.5 cm s^{-1} and 0.05 cm^{-1} respectively, D_j is the diffusion coefficient of a given species j where $j = A$ or B. When considering the Br^-/Br_2 system, for species A_w, $D = 1.85 \times 10^{-5}\text{ cm}^2\text{ s}^{-1}$; species B_w and B_o, $D = 9.4 \times 10^{-6}\text{ cm}^2\text{ s}^{-1}$. For the $FcTMA^{+/2+}$ system, for both species A_w and B_w, $D = 7.6 \times 10^{-6}\text{ cm}^2\text{ s}^{-1}$.</i> -----	99
<i>Table 4.2: Boundary conditions for droplet array finite element model where n is the inward-pointing unit normal vector; N is the normal flux of species; species A_w is A in the aqueous phase, species B_w is B in the aqueous phase and B_o, B in the oil phase (Br^-/Br_2 system only), with the subscript denoting the phase occupied by the species; k_l and k_{-l} are the mass transfer coefficients equal to 0.5 cm s^{-1} and 0.05 cm s^{-1} respectively, D_j is the diffusion coefficient of a given species (A or B). When considering the Br^-/Br_2 system, for species A_w, $D = 1.85 \times 10^{-5}\text{ cm}^2\text{ s}^{-1}$; species B_w and B_o, $D = 9.4 \times 10^{-6}\text{ cm}^2\text{ s}^{-1}$.</i> -----	101
<i>Table 5.1: $E_{1/2}$ of LSV waves recorded on channel electrodes in a single channel (200 μm width, 100 μm height) microfluidic device as a function of V_f.</i> -----	135
<i>Table 5.2: Comparison of current signals from aqueous droplets and calibrated Levich currents for flow under various flow rates.</i> -----	143
<i>Table 6.1: Laser parameters used for electrode structure fabrication in intrinsic diamond</i> -----	161

Acknowledgements

I would like to thank my supervisor, Prof. Julie Macpherson, for her unwavering support and guidance over the last four years. I would also thank Prof. Patrick Unwin and Prof. Mark Newton for their support.

I would also like to especially thank Tim Mollart, Nicola Palmer and co-workers from Element Six for providing the materials for this work and for many helpful discussions. Also BP for project funding.

I have to thank members of the Warwick Electrochemistry Group for their help and friendship, during both the good times and the bad. I am especially grateful to Dr. Aleix Güell, Dr. Maxim Joseph and Dr. Laura Hutton for imparting their knowledge and providing invaluable advice and support throughout my time in the group.

I am indebted to Rod Wesson: without his extraordinary efforts and technical expertise, much of this work would not have been possible. Also, I have to acknowledge the fantastic work of the chemistry department's mechanical technicians Lee Butcher and Marcus Grant whose advice and expertise helped the realisation of many devices described in this work.

Finally, to my friends and family whom I owe the most thanks, for always being there, providing encouragement and for helping me to realise my goals.

Declaration

I declare that the work contained in this thesis is entirely original and my own work, except where acknowledged. I confirm that this thesis has not been submitted for a degree at any other university.

The experiments in Chapter 3 were carried out in conjunction with Robert Channon, Electrochemistry Group, Department of Chemistry, University of Warwick. Diamond material described in this thesis was grown and polished by Nicola Palmer and co-workers at Element Six Ltd. Hydrazide monomer and polymer solutions analysed in chapter 3 were synthesised by Yunhua Chen, from the Polymer Group, Department of Chemistry, University of Warwick.

Parts of this thesis have been published as detailed below:

R. B. Channon, J. C. Newland, A. W. T. Bristow, A. D. Ray, and J. V. Macpherson, *Selective detection of hydrazine in the presence of excess electrochemically active pharmaceutical ingredients, using Boron Doped Diamond Metal Nanoparticle Functionalised Electrodes*, *Electroanalysis*, **2013**, 25 (12), 2613–2619.

J. C. Newland, P. R. Unwin and J. V. Macpherson, *Investigation of molecular partitioning between non polar oil droplets and aqueous solution using double potential step chronoamperometry* *Phys. Chem. Chem. Phys.*, **2014**, 16, 10456-10463.

Abstract

Polycrystalline boron-doped diamond (pBDD) has acquired great interest as a electrode material exhibiting low background currents, wide potential windows and a host of extreme physical properties such as mechanical hardness, chemical inertness and a high resistance to harsh environments. pBDD's exceptional electrochemical characteristics have made its application as a material for high performance electrochemical sensors the basis of a huge amount of research over the last decade.

Work in this thesis describes the fabrication and application of pBDD sensors in both stationary and fluid flow environments where conventional electrode materials would be unsuitable or problematic. pBDD electrodes functionalised with catalytic metal nano-particles are demonstrated as a means of detecting hydrazine, a genotoxic impurity of interest in pharmaceutical analysis, even in the presence of potentially interfering pharmaceutical matrix. This same sensor is then employed as a means of detecting the presence of non-polar oils on an electrode surface in dual-phase, aqueous/oil systems.

An investigation of electrochemical techniques for detecting and characterising phase changes in the form of microdroplets moving under flow in microfluidic systems is detailed. Limitations to the use of conventional materials used to fabricate such microfluidic devices are discussed. In an effort to address these issues as well as those expected in extreme environments, with aggressive media, a fabrication route for realising all-diamond microfluidic devices with integrated, high-quality pBDD electrodes is outlined.

Abbreviations

ACM	acetaminophen
AFM	atomic force microscopy
API	active pharmaceutical ingredient
ATR	attenuated total reflection
BDD	boron-doped diamond
BNCD	boron-doped nanocrystalline diamond
CA	chronoamperometry
CCD	charge-coupled device
CE	counter electrode
CMOS	complementary metal-oxide-semiconductor
CNC	computerised numerical control
CP	continuous phase
CV	cyclic voltammetry or cyclic voltammograms
CVD	chemical vapour deposition
DCP	direct coupled pump

DNA	deoxyribonucleic acid
DP	droplet phase
DPSC	double potential step chronoamperometry
DPV	differential pulse voltammetry
ECT	electrical capacitance tomography
ERT	electrical resistivity tomography
ET	electron transfer
FEM	finite element method
FE-SEM	field emission scanning electron microscopy
FIA	flow injection analysis
FTIR	fourier-transform infrared detection
fcc	face centred cubic
GI	genotoxic impurities
HET	heterogeneous electron transfer
HFCVD	hot filament chemical vapour deposition
HPHT	high-pressure high-temperature
HPLC	high-performance liquid chromatography
HZ	hydrazine
ICP	inductively coupled plasma

IHP	inner Helmholtz plane
IT	ion transfer
LOD	limit of detection
LSV	linear sweep voltammetry or linear sweep voltammograms
MEMED	microelectrochemical measurements at expanding droplets
MEMS	micro electromechanical systems
MFM	multiphase flow metering
MH	methacryloyl hydrazide
MWCVD	microwave plasma chemical vapour deposition
Nd:YAG	neodymium-doped yttrium aluminium garnet
NLO	non-linear optic
NPs	nanoparticles
OA	operational amplifier
OHP	outer Helmholtz plane
PS	potential step
PDMS	polydimethylsiloxane
PZ	promazine
pBDD	polycrystalline boron-doped diamond
Ra	arithmetic average roughness

RDE	rotating disk electrode
RE	reference electrode
RF	radio frequency
RIE	reactive ion etching
RMS	root-mean squared
SAVR	surface area to volume ratio
SCE	saturated calomel electrode
SECM	scanning electrochemical microscopy
SIMS	secondary ion mass spectrometry
TAS	total chemical analysis systems
UMEs	ultramicroelectrodes
UV	ultra-violet light
WE	working electrode
WLI	white light interferometry
XPS	x-ray photoelectron spectroscopy
μTAS	micro total chemical analysis systems

Glossary of symbols

A	electrode area
A'	pre-exponential factor
A_g	open-loop gain
a	electrode radius
C	capacitance
C_d	differential capacitance
Ca	capillary number
D	diffusion coefficient of species
D_L	droplet length
d_c	channel width
d_i	interpolate spacing
E	potential
\mathbf{E}	electric field
E^o	standard electrode potential
$E^{0'}$	formal potential
E_{cell}	total cell potential
E_e	equilibrium potential

E_e^A	potential of anode
E_e^C	potential of cathode
E_p^A	anodic peak potential
E_p^C	cathodic peak potential
e_o	output voltage
e_s	difference in voltage between inputs
e_+	non-inverting voltage input
e_-	inverting voltage input
F	Faraday's constant
h	channel height
i	current
i_0	exchange current
i_{lim}	limiting current
i_{ox}	anodic current
i_{red}	cathodic current
i_p	peak current
i_p^C	cathodic peak current
i_p^A	anodic peak current
iR	potential drop

j	flux
K	partition coefficient
k	first order heterogeneous rate constant
k_0	standard rate constant
k_{ox}	first-order heterogeneous rate constant for oxidative reaction
k_{red}	first-order heterogeneous rate constant for reductive reaction
k_t	mass transfer coefficient
L	characteristic length
m	number of moles used in a reaction
N	normal flux of species
n	apparent number of electrons transferred
\mathbf{n}	inward-pointing unit normal to vector
$[O]$	concentration of species “O”
\mathbf{p}	electrical dipole moment
Q	charge
S_e	separation between reference and counter band electrodes
R	gas constant
R_a	radius of curvature
R_m	series resistor

R_s	system resistance
Re	Reynolds number
r	radial coordinate
T	temperature
t	time
t_{res}	residence time of the droplet on the electrodes
t_i	moment in electric field
U	mean fluid velocity
u	mobility of species
V_f	volume flow rate
v_x	velocity in x-direction
w	band electrode width
x_e	band electrode length
z	charge of species
α_g	geometry dependent constant
α_p	polarisability
α_{ox}	transfer coefficient for oxidative reaction
α_{red}	transfer coefficient for reductive reaction
γ	activity of species

γ_i	interfacial tension
ΔE_p	difference in peak potential
ΔG_{in}	Gibbs free energy input for a system
ΔG_{red}^\ddagger	difference in free energy between transition state and reactant state
ΔG_{ox}^\ddagger	difference in free energy between product state and transition state
δ	diffusion layer thickness
δ_H	hydrodynamic layer thickness
ε	dielectric constant
ε_0	permittivity of free space
η	overpotential
η_A	overpotential of anodic reaction
η_C	overpotential of cathodic reaction
μ	dynamic viscosity
μ_b	mean of background response
ν	scan rate
ρ	fluid density
σ	surface charge
σ_m	charge density on electrode

σ_s	charge density in solution
σ_b	standard deviation of background response
τ	time width/ pulse width
ν_0	vibrational frequency
ν_m	frequency of scattered light
ν_v	vibrational frequency of the normal coordinate of a molecule
ϕ	rotational coordinate
Ψ	electric surface potential
ω	Raman wavenumber
∇	del-operator

Chapter 1: Introduction

The application of an electrochemical sensor for the purpose of multiphase flow profiling has yet to be realized and could represent a cost-effective alternative. Specifically, the main advantages of utilizing an electrochemical sensor are the ability to perform measurements quickly, and relatively cheaply, and the inherent low costs of maintenance. For these reasons electrochemical sensors have found a range of applications in medical,¹ environmental,^{2,3} and food analyses.⁴

In the case of long term use in harsh environments, conventional electrode materials such as platinum, gold and glassy carbon are impractical due to degradation over time. The application of conducting diamond addresses this issue. Diamond is one of the four allotropes of carbon. Its structure comprises sp^3 bonded carbon where each carbon atom is bound to another four carbon atoms. Intrinsic diamond is highly electrically insulating⁵, however, when doped with nitrogen or boron, n-type or p-type semiconductors are produced respectively. In the case of boron doping, it is possible to achieve doping at such a high level that the material shows semi-metallic behaviour.

1.1 Electrochemistry as a method for analysis in stationary and under flow regimes

At its simplest, electrochemistry can be described as charge transfer across an interface for example, the oxidation or reduction of a redox species in solution at a metal surface, due to electron transfer. Other examples include adsorption and desorption processes as well as corrosion or the electrodeposition of material onto an electrode surface.

The study of electrochemical processes has given rise to applications in sensor technology which range from chemical sensors in solutions,^{6,7} gas phase sensors⁸ through to biosensors.^{9,10} The advantages of electrochemical sensors include low cost, high performance with the possibility of *in-situ* measurements and the ability to miniaturise into micro-scale systems.^{11,12}

1.1.1 Introduction to electrochemistry: Electrochemical cells

Electrochemistry can be defined as either thermodynamic or dynamic. In an electrochemical cell system, as shown in *Figure 0.1* it is possible to either (1) measure the resulting cell potential (thermodynamic) or (2) apply a potential or current to drive a redox reaction at the working electrode (dynamic), with respect to a reference electrode. All experiments described in this thesis are carried out under dynamic conditions.

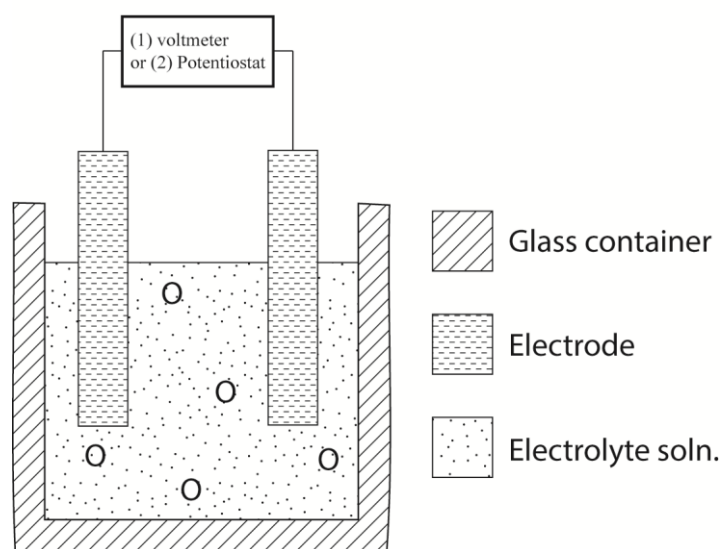
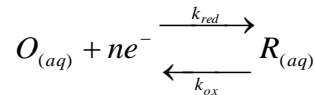


Figure 0.1: An electrochemical cell consisting of two electrodes immersed in an aqueous solution containing a redox active species "O" and electrolyte. The cell is capable of (1) measuring potential via a voltmeter or (2) applying current/potential and measuring potential/current via a potentiostat.

1.1.2 Dynamic electrochemistry

Dynamic electrochemistry can be defined as the study of reactions involving the transfer of electrons between an electrode and a reactant species under non-equilibrium conditions.¹³ This can be in a solution phase or even a plasma.¹⁴

A simple redox reaction is as follows:



0.1

Where n is the number of electrons involved in the reaction; k_{red} and k_{ox} are the first-order heterogeneous rate constants for the reductive and oxidative reactions, respectively.

Electrochemical cells can be used to drive otherwise non-spontaneous reactions at an electrode via the application of a potential or current. This is known as electrolysis and can only occur at an electrode surface if a second, opposing process occurs at a second electrode in order to balance the overall charge of the cell. In an electrochemical cell the first electrode is typically referred to as the working electrode with the second electrode termed the reference (see section 1.1.2.1). For example, an oxidation at one electrode (the anode) must be accompanied by a reduction at the opposing electrode (the cathode). For a spontaneous reaction to occur the free energy change for the net cell reaction of interest must be negative. Hence an input of energy, ΔG_{in} is required, via the application of a potential difference, E between the two electrodes, to drive non-spontaneous reactions. E must therefore be greater than the difference in reversible potentials of the cathode, E_e^C and anode, E_e^A so that

$$E > (E_e^C - E_e^A)$$

0.2

This applied potential difference, E provides the thermodynamic driving force to initiate electrolysis but the rate will be dictated by the kinetics of the electrode reaction.

The total cell potential, E_{cell} represents the energy per unit charge needed by the electrochemical cell to induce a chemical change via electrolysis, which includes not only the required reaction driving

potential E , but also the excess energy required i.e. an overpotential, η in order to overcome any kinetic limitations, to drive the movement of ions in solution and overcome any resistance in the cell:

$$E_{cell} = (E_e^C - E_e^A) - |\eta_A| - |\eta_C| - iR$$

0.3

Where η_A and η_C are the overpotentials for the anodic and cathodic reactions, respectively; iR is the potential drop term which accounts for resistance in the electrochemical cell. It is common practice to design the cell in order to minimise iR , for example adding a supporting electrolyte to solution to reduce the solution resistance and keeping the electrodes close together¹⁵.

Factors that govern electrode dynamics are summarised by the schematic in *Figure 0.2*, and can be divided into two regimes (1) *electron transfer kinetics* i.e. the rate at which electrons are transferred between the species of interest and the electrode surface; and (2) *mass transport* of species to and from the electrode surface.

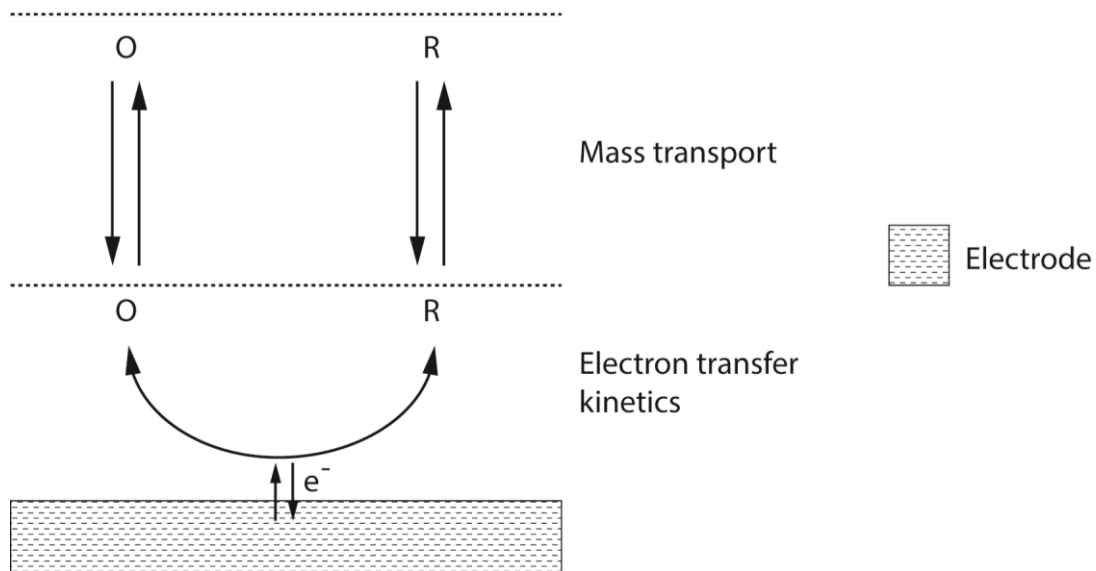


Figure 0.2: schematic representing factors that govern electrode dynamics in a heterogeneous reaction

1.1.2.1 Reference electrodes

The integration of an electrode with a well-defined and constant potential is of critical importance if the overall potential of a cell is to be measured or potential control of a system is to be achieved. Such an electrode is referred to as the reference electrode. As the name suggests, it provides a reference potential by which the rest of the system is compared.

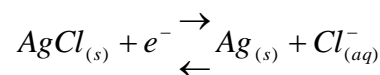
A typical reference electrode is the silver/silver chloride electrode (Ag|AgCl) described by the following cell notation:



0.4

where | represents a phase boundary. In this case, a silver wire is coated with a layer of the insoluble solid silver halide salt, silver chloride (so that no silver wire is exposed to solution) and immersed in a solution containing a constant concentration of chloride ions (3 M). This solution is contained within a glass vial and connected to the rest of the electrochemical cell via a porous ceramic frit that allows the slow passage of ions while maintaining an electrical contact through a liquid junction; see *Figure 0.3*.

The potential determining equilibrium established at the Ag|AgCl electrode can be described by



0.5

The containment and separation of the chloride ion solution from the bulk solution of the electrochemical cell ensures that the concentration of chloride ions remains constant and the reference electrode maintains a stable potential, as described by the Nernst equation¹⁶:

$$E_e = E^o + \frac{RT}{nF} \ln \frac{1}{a_{Cl^-}}$$

0.6

where E_e is the equilibrium potential and E^o is the standard electrode potential, F is Faraday's constant ($C\ mol^{-1}$) and a_{Cl^-} is the activity of chloride ions in solution.

Since the activity of a species is defined by as follows:

$$a = \gamma[O]$$

0.7

where γ , is the activity coefficient of a species and $[O]$ is the concentration of a dilute species, equation 0.6 can be rewritten as

$$E = E^{o'} + \frac{RT}{nF} \ln \frac{1}{\gamma_{Cl^-}[Cl^-]}$$

0.8

where $E^{o'}$ is the formal potential.

If a solution contains an excess of supporting electrolyte i.e. an inert salt, which takes no part in any reaction in solution or at the electrode/solution interface, it can be assumed that γ is equal to 1 and so

$$a \approx [O]$$

0.9

and

$$E^{o'} = E^0$$

0.10

For non-aqueous systems frit-based reference electrodes are not suitable, as typically the, silver halide salts are soluble¹⁷ in non-aqueous solvents, changing the composition of the electrode/solution interface and so destabilising the reference electrode. Moreover, leaking of aqueous solvent into the non-aqueous solution restricts use to short measurements only and the liquid-liquid junction formed at the frit can lead to precipitation of salts inside the frit.¹⁸

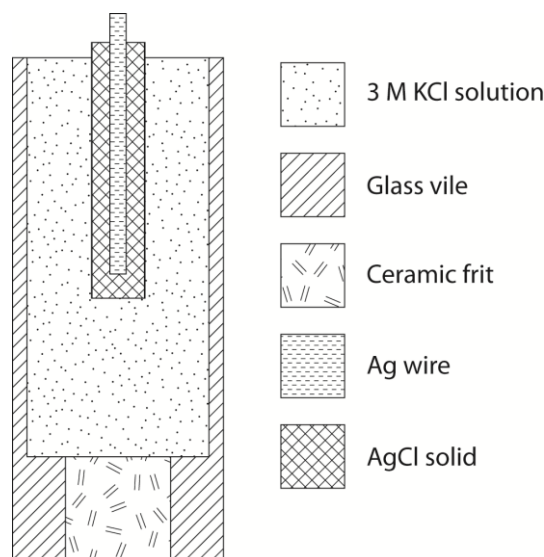


Figure 0.3: A schematic of a typical self-contained Ag|AgCl reference electrode.

For systems that require the use of a reference electrode in a non-aqueous media, it is typical to use a bare silver wire as a “quasi-reference” electrode, the potential of which is dependent on the solution environment it is placed into. Quasi references are still very usable in electrochemical systems as long their potential can be defined for that system using a reference redox mediator i.e. a mediator whose redox potential is known verses a standard hydrogen electrode (SHE).¹⁸

1.1.2.2 Three-electrode measurements

In order to study electrode dynamics, it is often necessary to adopt a three-electrode set-up whereby an auxiliary electrode, commonly referred to as a counter electrode is added to the system. This is shown schematically in *Figure 0.4*. Under potential control, the counter electrode enables the passage of current between itself and the working electrode while the cell potential is applied between just the working and the reference electrode. This prevents any significant currents from being passed through the reference electrode that would otherwise change the interfacial composition of the electrode and so affect the potential of the electrode/solution interface. Thus, any changes in potential can be attributed to the working electrode. The counter electrode also acts to reduce Ohmic drop that results from attempts to pass large currents through the reference electrode. As a rule of thumb for currents < 1 μ A two-electrodes can be used instead of three.¹⁶ The counter electrode is often made of an inert metal with a high density of states e.g. platinum, shaped to have a large surface area relative to the

working electrode. These features ensure that any electrical resistance in the electrochemical cell resulting from the counter electrode are minimised, restricting any current limiting processes to the working electrode.

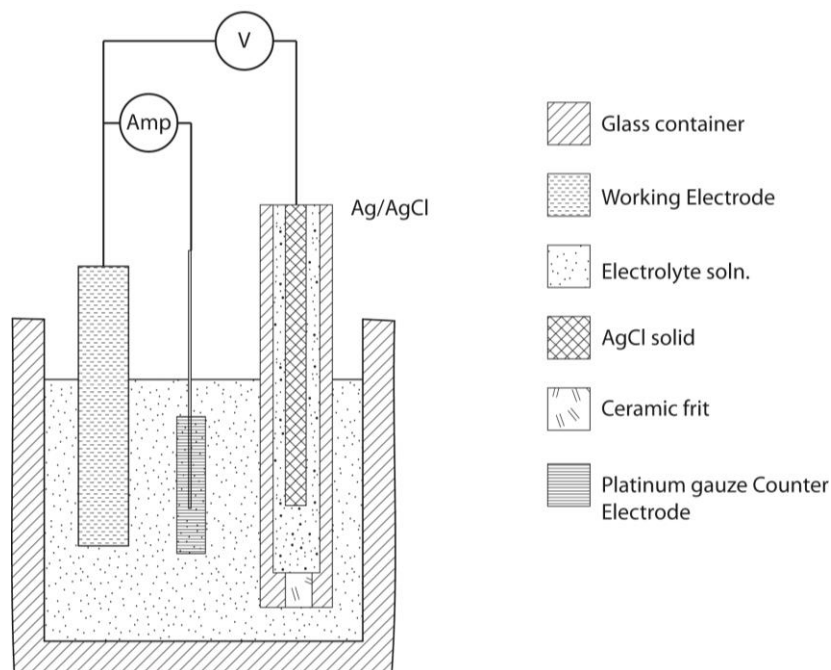


Figure 0.4: schematic of a 3-electrode set-up consisting of a working electrode, AgAgCl reference electrode and a Platinum gauze counter electrode

1.1.2.3 Electron transfer kinetics

The rate of the electrochemical reaction is referred to as the flux, j ($\text{mol cm}^{-2} \text{s}^{-1}$). This can either be mass transport or kinetically controlled. The current, i passed at an electrode of area, A (cm^2) is related to j via:

$$i = nAFj$$

0.11

The extent of a reaction, i.e. the amount of species turned over at the electrode can be deduced from the amount of charge, Q passed by the electrochemical cell during the experiment as per

$$Q = \int_0^t i dt = mnF$$

0.12

where t is time (s) and m is the number of moles used in the reaction.

The flux is a measure of the rate limiting process in *Figure 1.2*. Under kinetic limitations i.e. where the rate of mass transport is significantly higher than the rate of electron transfer:

$$j = k[O]_0$$

0.13

where k (cm s^{-1}) is the rate constant for a first order heterogeneous reaction and $[O]_0$ is the concentration of reactant O at the electrode surface (mol cm^{-3}).

For reaction 0.1, the rate law for the overall net process can be written as

$$j = k_{ox}[R]_0 - k_{red}[O]_0$$

0.14

Substituting equation 0.11 with equation 0.13 for reaction 0.1 provides

$$i_{red} = -nFAk_{red}[O]_0$$

0.15

$$i_{ox} = nFAk_{ox}[R]_0$$

0.16

And so

$$i = nFA(k_{ox}[R]_0 - k_{red}[O]_0)$$

0.17

The kinetics of a reaction can be expressed by the standard rate constant k_0 which is the rate constant when the system is at equilibrium and the Nernst equation, equation 0.6, can be applied i.e.

$$E = E^o = E_e$$

0.18

The net current flow is given by

$$i = i_{red} + i_{ox}$$

0.19

where i_{red} and i_{ox} are the cathodic and anodic contributions to the current, respectively. Under equilibrium conditions, the overall net current flow at the electrode surface is zero.

It follows then that flux, $k_{red}[O]_0$ and $k_{ox}[R]_0$ are in balance so that

$$k_{red}[O]_0 = k_{ox}[R]_0$$

0.20

From transition state theory, the free energy plot for the simple one electron reaction in 0.1 can be described as in *Figure 0.5*. The free energy of activation for passing between reactant and the transition state, ΔG_{red}^\ddagger is the difference in free energy between the transition state and the reactant state whilst the free energy associated for passing between product and transition state, ΔG_{ox}^\ddagger is equal to the difference in free energy between the product and transition state.

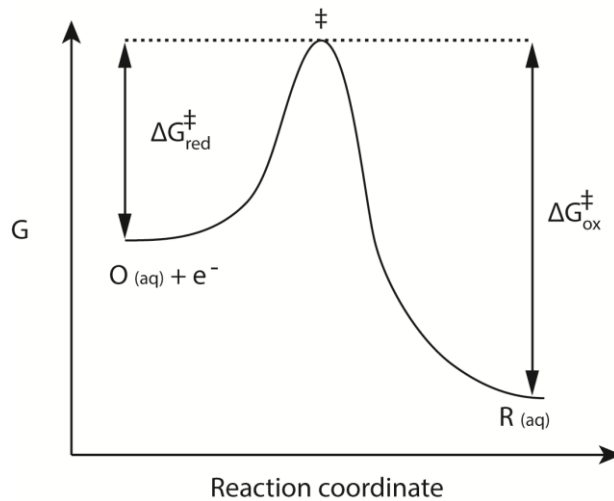


Figure 0.5: Free energy plot for a transition state model of a one electron reduction of a species $O(aq)$ to species $R(aq)$ via a transition state \ddagger .

From this transition state model, k_{red} can be described by the following Arrhenius equation:

$$k_{red} = A' \exp\left(\frac{-\Delta G_{red}^{\ddagger}}{RT}\right) \quad 0.21$$

where A' is a pre-factor relating to the frequency of molecular collisions between species O and the electrode surface. Here in 0.21, the dependency of k_{red} on the activation energy and temperature can be seen. From 0.21 and the relationship between free energy and potential:

$$\Delta G = -nFE \quad 0.22$$

the rate constants k_{ox} and k_{red} will change with variations in the applied electrode potential as per the following Arrhenius-type equations:

$$k_{ox} = k_0 \exp\left(\frac{\alpha_{ox} nF}{RT} E\right) \quad 0.23$$

$$k_{red} = k_0 \exp\left(-\frac{\alpha_{red} nF}{RT} E\right) \quad 0.24$$

where, the constants α_{ox} and α_{red} are the transfer coefficients for the oxidative and reductive reactions respectively. α_{ox} and α_{red} can take values between 0 and 1 but commonly hold a value of 0.5. For simple electron transfer reactions,

$$\alpha_{ox} + \alpha_{red} = 1 \quad 0.25$$

The transfer coefficient can be thought as the symmetry of the energy barrier for the reaction.

The application of a potential, E , different to E_e may make electrolysis thermodynamically favourable; however, it is the kinetics of the electrode reaction that dictate whether current will flow. The difference in potential between E and E_e is referred to as η , where:

$$\eta = E - E_e$$

0.26

Substituting equations 0.23 and 0.24 into 0.17 produces the Butler-Volmer equation¹⁶

$$i = i_0 \left[\exp\left(\frac{\alpha_{ox} nF}{RT} \eta\right) - \exp\left(-\frac{\alpha_{red} nF}{RT} \eta\right) \right]$$

0.27

where i_0 is the exchange current, a scaling factor dependent on the standard rate constant and concentration of reactants. The value of i_0 provides a good indication of whether an electrode reaction is reversible or irreversible. Large values of i_0 mean a very low overpotential is needed in order to drive a reaction whereas small values of i_0 will require a high overpotential in order to overcome the activation barrier.

1.1.2.3.1 Interfacial electron transfer and the electrode/solution interface

1.1.2.3.1.1 The electrical double layer region

Since heterogeneous electron transfer (HET) occurs at the electrode/electrolyte interface, it is also important to consider the region close to the electrode surface i.e. the double layer region. Under an applied potential where no HET occurs, the charge density that builds up on an electrode surface, σ_m as a result of the applied potential is counteracted by an equal charge density in solution, σ_s so that

$$\sigma_m = -\sigma_s$$

0.28

and charge neutrality is maintained in the system. The charge density in the solution is attributed to the electrolyte ions and reorientation of dipoles in the solvent molecules as they adsorb to the electrode surface. The electrostatic attraction induced by the electric field drives the build-up of charged species at the interfacial region until any excess charge on the electrode surface is neutralised.

In an aqueous solution containing charged species, the electrode surface can be considered as shown in *Figure 0.6*. The schematic describes the simplest model of the double layer as proposed by Helmholtz¹⁹ where the potential drop occurs linearly in the region between the electrode surface and

the “outer Helmholtz plane” OHP; the distance of closest approach for a solvated ion. This model is analogous with a parallel plate capacitor where the stored charge density or surface charge, σ (C m^{-2}) is expressed as

$$\sigma = \frac{\varepsilon_0}{d_i} \Psi \quad 0.29$$

where ε is the dielectric constant of the medium, ε_0 is the permittivity of free space, d_i is the interpolate spacing (m) and Ψ is the electric surface potential or potential drop between the plates¹⁶. The ability of a surface to store charge with changing potential is described by the differential capacitance, C_d so that

$$\frac{\partial \sigma}{\partial \Psi} = C_d = \frac{\varepsilon_0}{d_i} \quad 0.30$$

Since C_d would be a constant if equation 0.30 were to hold, a new model needs to be considered where C_d varies with both potential and concentration of electrolyte as observed in real systems.¹⁶

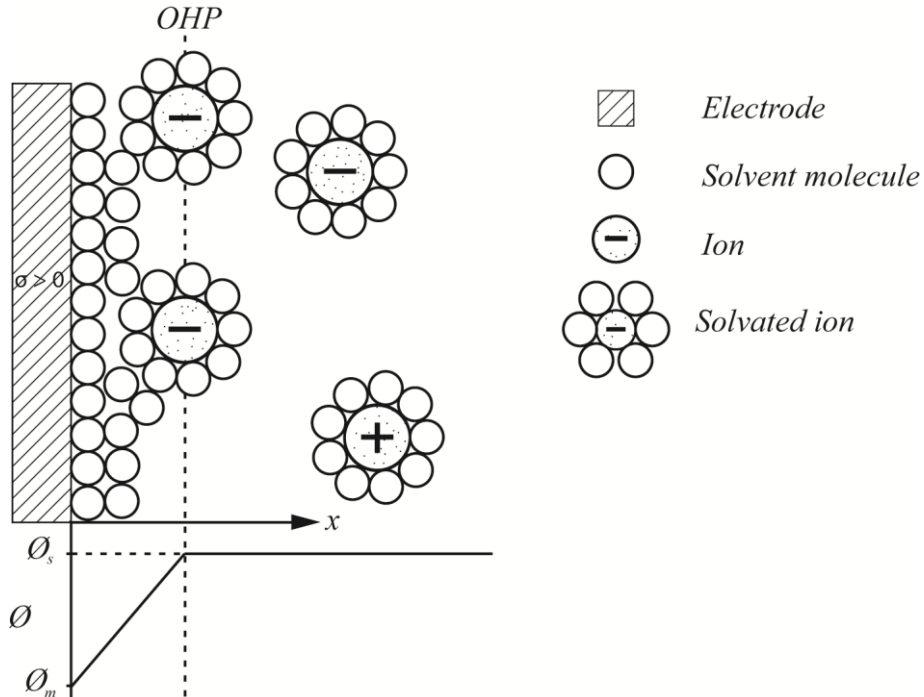


Figure 0.6: schematic of the electrical double layer as proposed by Helmholtz where x represents the distance extending from the electrode surface into the bulk solution

The Helmholtz model was expanded on by Gouy and Chapman²⁰ who found that σ_s was distributed over an area extending further than the OHP. They proposed that the electrostatic forces concentrating the ions in solution would be counteracted by Brownian motion which would disperse the ions. Their new model describes ions as point charges that occupy a “diffuse layer” that extends from the electrode surface out a short distance past the OHP into the bulk solution where the potential gradient is distributed so that it is high close to the electrode surface and decreases with increasing distance.

The thickness of the diffuse layer replaces d_i in equation 0.30, which now allows the dependency of C_d with potential and electrolyte concentration to be understood as follows: (1) a rise in the surface potential increases the charge density which in turn increases electrostatic forces, compressing the diffuse layer thus leading to a higher value of C_d ; (2) higher concentrations of electrolyte result in the compression of the diffuse layer, again leading to a higher value of C_d .

Unfortunately, the treatment of ions as point charges without restriction on location is impractical as it ignores the restrictions placed on the minimum distance of approach for an ion of finite size to a solvated electrode surface when the ion itself possesses a solvation shell. In order to address this, the double layer model was further expanded on by Stern²¹ who proposed a combination of the Helmholtz and Gouy-Chapman descriptions so that the potential gradient is split into two regions: a sharp potential drop between the electrode surface and the OHP followed by a gradual decay to the potential of the bulk solution over a “diffuse layer” extending from the OHP out into the solution.²²

This improved model was then improved by Grahame^{23, 24} so that unsolvated species (charged or non-charged) could adsorb at the electrode surface “specifically adsorbed”. The consequence of specific adsorption is a reduction in the charge density required to neutralise the charge density on the electrode. With species adsorbing onto the electrode surface, a new distance of minimum approach is described by the “inner Helmholtz plane” (IHP), defined as the mean position of an adsorbed species on the electrode surface. Bockris, Devanathan and Müller²⁵ made further developments to account for

the solvent interactions with the electric field at the electrode, assigning orientations to dipoles of the solvent molecules which are dependent on the relative charge, as shown in *Figure 0.7*.

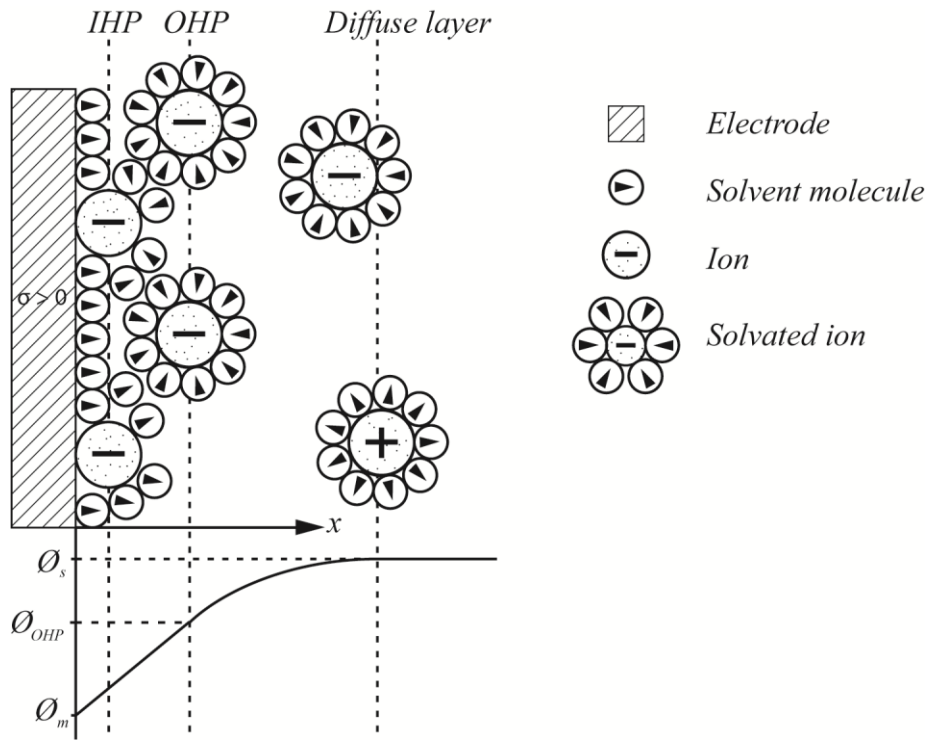


Figure 0.7: schematic of the Bockris-Devanathan-Müller model for the electronic double layer at an electrode/electrolyte interface.

The current observed at an electrode can thus be divided into contributions from both faradaic and non-faradaic processes. The current flowing as a result of double layer charging can be referred to as non-faradaic. The capacitance of the electrode surface, C is calculated using equation 0.31.

$$\frac{Q}{E} = C$$

0.31

With an applied potential E , Q accumulates at the electrode/solution interface until equation 0.31 is satisfied during which time a current will flow as a result of charging. If a system is considered where no HET takes place at the electrode, only the development of the double layer contributes to any measured current, the magnitude of the current will be:

$$i = \frac{E}{R_s} \exp\left(-\frac{t}{R_s C_d}\right)$$

0.32

where R_s is the resistance in the system.¹⁶

For trace level electroanalysis experiments significant non-faradaic processes are undesirable. A number of electrochemical techniques exist to minimise the contributions of non-faradaic current which will be described later in chapter 2.

1.1.2.3.1.2 Inner sphere versus outer sphere reactions at electrodes

Until now, there has been no consideration of how HET kinetics are affected by the molecular structure and environment of a redox species and the chemical nature of the electrode surface. The Marcus microscopic model for charge transfer²⁶ allows the prediction of structural and environmental effects on HET kinetics and introduces the terms “outer-sphere” and “inner-sphere”. These terms are analogous with HET reactions in coordination compound chemistry¹⁶.

Outer-sphere electrode reactions (*Figure 0.8a*) involve no interaction between reactant, intermediates or products and the electrode surface, with a species coming no closer to the electrode surface than the OHP i.e. electron tunnelling distance. By contrast, inner-sphere reactions (*Figure 0.8b*) involve strong interaction between reactant species, or reaction intermediates and the electrode surface. For example, a species may need to specifically adsorb to the electrode surface forming e.g. a ligand bridge in order for the HET process to proceed in a facile manner¹⁶.

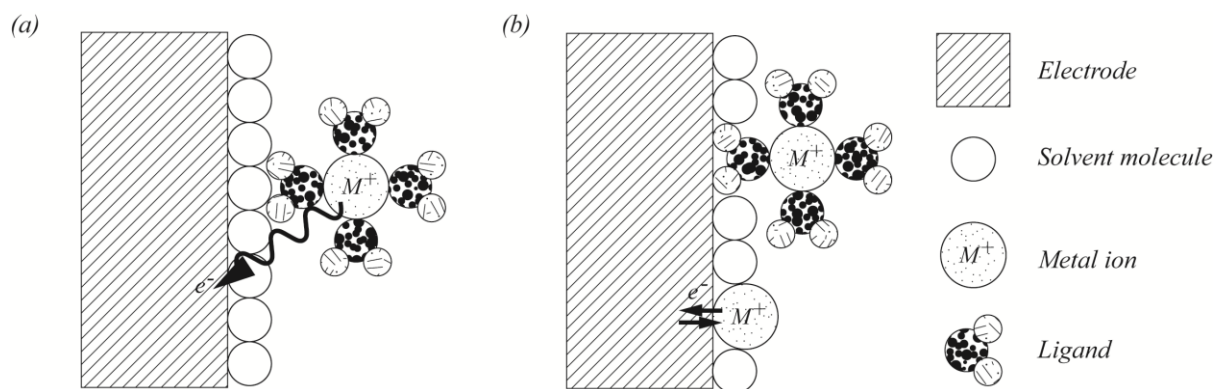


Figure 0.8: Schematic of (a) an outer-sphere electrode reaction and (b) an inner-sphere electrode reaction.

1.1.2.4 Mass transport

Movement of species towards and from the electrode surface is referred to by the term “mass transport” which can be attributed to one or more of three modes: diffusion, migration and convection. Quantification and control of mass transport in any system is important for several reasons e.g. (1) quantifying HET for a redox couple of interest; (2) being able to deliver solution to an electrode surface in a controlled and reproducible fashion.

1.1.2.4.1 Diffusion

Diffusion can be defined as the movement of species along a concentration gradient, driven by entropy. The rate of diffusion is defined by Fick’s first law for a 1D system:

$$j_o = -D_o \frac{\partial[O]}{\partial x}$$

0.33

where j_o is the flux of species O , D_o is the diffusion coefficient of species O ($\text{cm}^2 \text{s}^{-1}$), and $\partial[O]/\partial x$ is the concentration gradient in the x -direction.

The change in concentration with t as a result of diffusion can be described by Fick’s second law in 1D:

$$\frac{\partial c}{\partial t} = D \frac{\partial^2 c}{\partial x^2}$$

0.34

Diffusion in a three-dimensional system can be defined according to electrode geometry so that for any coordinate system

$$j = -D\nabla c$$

0.35

and

$$\frac{\partial c}{\partial t} = D\nabla^2 c$$

0.36

where ∇ is the del-operator corresponding to the geometry so that for a Cartesian coordinate system

$$\nabla = \frac{\partial}{\partial x} + \frac{\partial}{\partial y} + \frac{\partial}{\partial z}$$

0.37

and, for example

$$\nabla = \frac{\partial}{\partial r} + \frac{1}{r} \frac{\partial}{\partial \phi} + \frac{\partial}{\partial x}$$

0.38

for a cylindrical coordinate system, where r is the radial coordinate and ϕ is the rotational coordinate.

If we take a simple electrode reaction where O is reduced to R at a large, planar electrode upon application of a sufficient potential, with diffusion as the only mass transport term, the transport can be simplified to 1D with the corresponding current given by

$$i = -nFAD_o \left(\frac{\partial [O]}{\partial x} \right)_{x=0}$$

0.39

The concentration profile generated during this reaction (i.e. during a potential step experiment) with the evolution of time can be seen in *Figure 0.9*. At short times (t_1), the concentration gradient between the electrode and bulk is steep as the perturbation in concentration is close to the electrode surface.

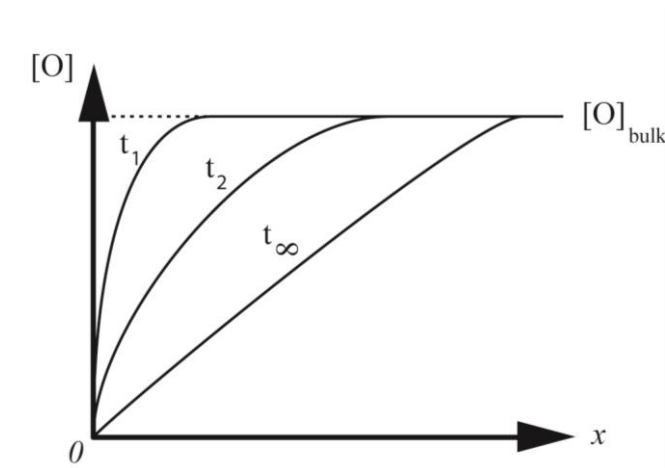


Figure 0.9: The evolution of concentration profiles with time, t for a diffusion controlled process involving the reduction of O ; where x is the distance into bulk solution from the electrode surface($x = 0$).

With increasing time, the concentration gradient, also referred to as the diffusion layer, extends further out from the electrode surface into the bulk so that the gradient becomes less and less steep as shown in *Figure 0.10* and described by the Cottrell equation¹⁶

$$i = -\frac{nAFD_O^{1/2} [O]_{bulk}}{(\pi t)^{1/2}}$$

0.40

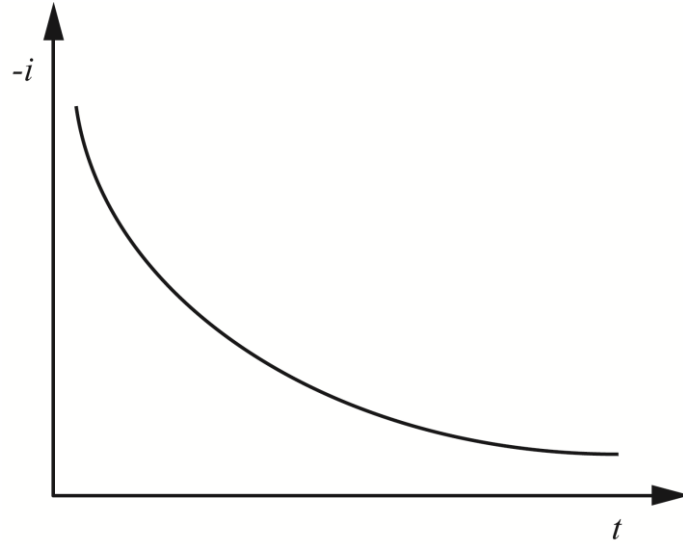


Figure 0.10: i - t transient for a diffusion limited process

The region over which the concentration gradient evolves i.e. the region between the electrode surface and bulk solution is known as the diffusion layer and can be defined by

$$D_o \left(\frac{\partial [O]}{\partial x} \right)_{x=0} = D_o \frac{([O]_{bulk} - [O]_0)}{\delta}$$

0.41

where δ is the diffusion layer thickness, a measure of how far the evolving diffusion field extends out into the bulk solution. From equation 0.40, an expression for the diffusion layer thickness can be derived:

$$\delta = (\pi D t)^{\frac{1}{2}}$$

0.42

The diffusion profile of species to and from an electrode e.g. planar versus radial depends on electrode geometry, as shown in *Figure 0.11*. For a hemispherical or disc shaped microelectrode, i.e. at least one dimension in the micrometre range, access to the surface is no longer equivalent across the surface, radial diffusion is prevalent and diffusion to the electrode is therefore non-uniform.

For a microelectrode, the presence of both radial and linear diffusion means that for a potential step experiment, equation 0.40 becomes¹⁶

$$i = \frac{nFAD_O^{1/2} [O]_{bulk}}{(\pi)^{1/2}} + \frac{nFAD_O^{1/2} [O]_{bulk}}{a}$$

0.43

where a is the electrode radius.

At short times, the first part of this expression dominates, however, as δ grows with time so that $\delta > a$, the second part of the expression dominates, enabling the system to achieve a steady-state. The deployment of microelectrodes allows the study of electrode reaction kinetics, decoupled from mass transport in the system.¹⁶

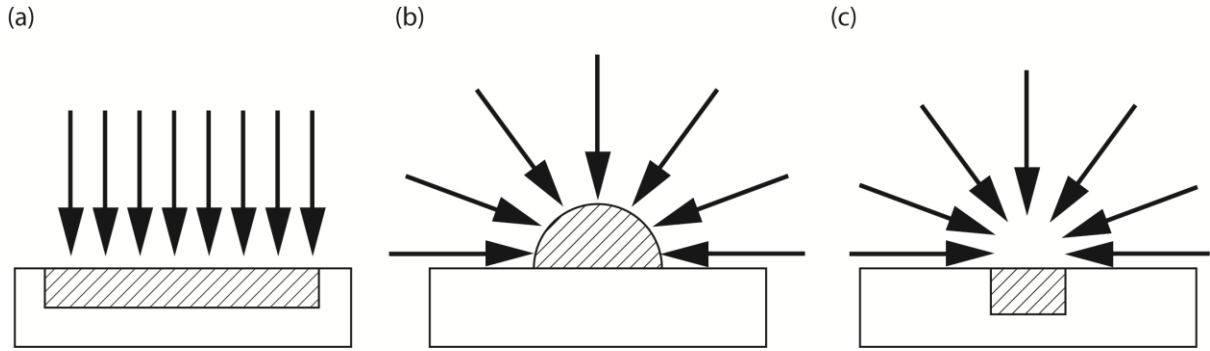


Figure 0.11: Diffusion profiles of (a) uniform diffusion to a planar electrode, (b) diffusion to a hemispherical electrode and (c) non-uniform diffusion to a microelectrode.

The mass transfer coefficient k_t (cm s^{-1}) describes the rate of transport in a heterogeneous electrode/electrolyte reaction and can be related to the current by:

$$i = nAFk_t [O]_{bulk}$$

0.44

therefore,

$$k_t = \frac{i}{nAF[O]_{bulk}}$$

0.45

The observed rate of an electrode reaction is governed by both mass transport and electron transfer kinetics, the rates of both expressed by k_t and k_0 respectively. Whether a reaction is limited by either k_t or k_0 dictates whether the reaction is reversible or non-reversible. In a reversible reaction, $k_0 > k_t$ so that the overall rate of reaction is limited by the mass transport. For a non-reversible reaction, $k_0 < k_t$ and so the kinetics of HET are limiting.

1.1.2.4.2 Convection

Convection is the transport of species via the action of a mechanical force. Such forces can include stirring of a solution, pressure induced flow and thermal gradients. Natural convection acts on a solution via a mixture of thermal and density gradients. Usually, these effects are seen in stationary electrochemical systems after a time period of around 20 seconds or greater¹⁶.

The expression for convection in one dimension is comparable to that for diffusion

$$\frac{\partial[O]}{\partial t} = -v_x \frac{\partial[O]}{\partial x}$$

0.46

where v_x is the velocity in the x -direction.

In practice, enhanced mass transport via induced convection is achieved using either mechanical rotation of the solution i.e. stirring or rotation disc electrodes (RDE),²⁷ or alternatively pressure driven flow within a channel²⁸ or a jet.²⁹⁻³¹ Schematics of convective flow profiles are shown in *Figure 0.12*

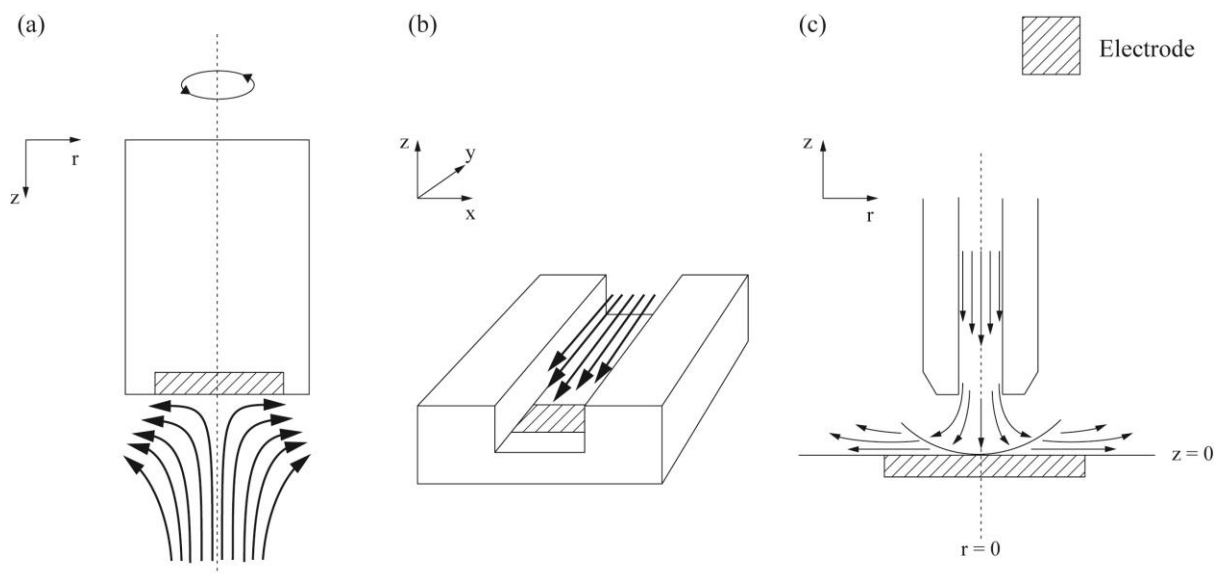


Figure 0.12: Schematic of convective flow regimes often adopted in electrochemical experiments: (a) a rotating disc (RDE), (b) flow in a channel and (c) an impinging jet.

A common theme with these electrodes is the establishment of laminar flow profiles. Laminar flow can be defined as flow where layers of fluid move in parallel, maintaining their relationship throughout the flow profile, characterised by a low Reynolds number (Re).

Re is a ratio between the inertial and viscous forces acting in a system, defined as

$$\text{Re} = \frac{\rho UL}{\mu}$$

0.47

where ρ is the fluid density (kg m^{-3}), U is the mean velocity of a fluid (m s^{-1}), L is the characteristic length (m) and μ is the dynamic viscosity (kg m.s^{-1}). For high values of Re, inertial forces dominate and the system becomes turbulent. For low Re, viscous forces dominate and the system is laminar, as shown in Figure 0.13 for a channel flow system

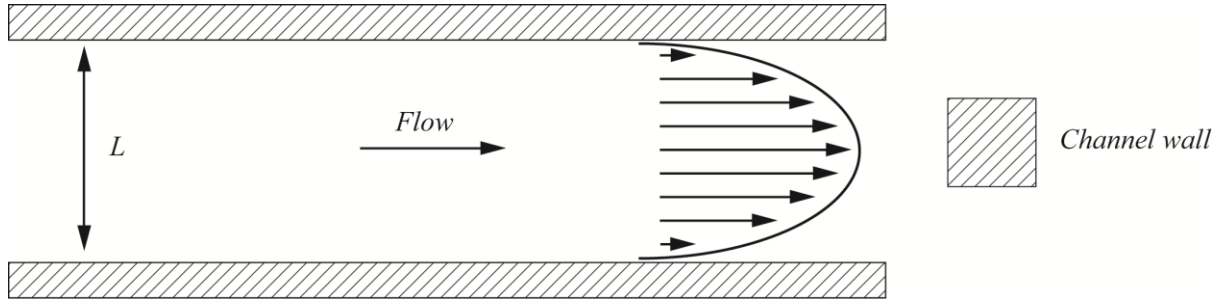


Figure 0.13: Schematic of a laminar flow regime in a channel with width, L . The arrow size in the parabolic flow represent the velocities of the fluid layers.

1.1.2.4.3 Convection-diffusion systems

Systems employing electrodes under convective-diffusive transport control are referred to as hydrodynamic electrodes. Such systems require a description of mass transport that includes both convection and diffusion so that

$$\frac{\partial[O]}{\partial t} = D_o \frac{\partial^2[O]}{\partial z^2} - v_z \frac{\partial[O]}{\partial z}$$

0.48

It is assumed that the region close to the electrode surface, within a distance δ is subject to diffusion only and is void of convection. Convection acts outside of this diffusion-only region within a second region known as the hydrodynamic layer, with a thickness of δ_H . The relationship between these two regions is described in the schematic in Figure 0.14.

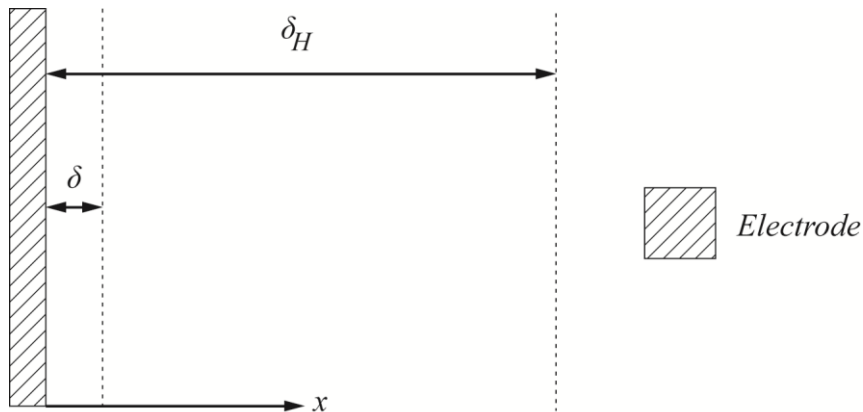


Figure 0.14: Schematic showing the relationship between the diffusion layer and hydrodynamic layer for a hydrodynamic electrode where x extends out from the electrode surface into solution.

1.1.2.4.4 Migration

Migration is the transport of charged species driven via the application of an electric field. The electrostatic force generated by the potential drop at an electrode/solution interface can drive the movement of charged species in the interfacial region close to the electrode. The migration contribution to flux of a species O can be described as

$$j_o = \frac{|z_o|}{z_o} u_o [O] \frac{\partial \phi}{\partial x} \quad 0.49$$

where j_o is the flux of species O , z_o is the charge of species O , u_o is the mobility of species O so that

$$u_o = \frac{|z_o| F D_o}{RT} \quad 0.50$$

and $\partial \phi / \partial x$ describes a linear electric field where

$$\frac{\partial \phi}{\partial x} = \frac{\Delta E}{l} \quad 0.51$$

where l is the length over which a potential difference, ΔE is applied.

From equations 0.11 and 0.49, the current resulting from the flux of an electroactive species O can be expressed as

$$i_o = |z_o| F A u_o [O] \frac{\partial \phi}{\partial x} \quad 0.52$$

In order to simplify the description of mass transport within a system, migration can be eliminated via the addition of excess electrolyte to the solution. The presence of inert ions in solution maintains electroneutrality through the solution, preventing the build-up of electric fields except in the region close to the electrode i.e. the double layer where there is an electric field created as a result of the potential drop at the electrode/solution interface. The double layer region is compressed by the

presence of high levels of electrolyte ions, confining the area over which the interfacial potential drop occurs to within $10\text{-}20 \text{ \AA}^{16}$ i.e. within electron tunnelling distance.

1.1.2.5 Cyclic Voltammetry

By far the most widely used electrochemical techniques belong to a class known as voltammetry. In conventional voltammetry, the potential applied to an electrochemical cell is swept linearly (1) from an initial value, E_1 to a second, E_2 : referred to as linear sweep voltammetry (LSV); or (2) from E_1 to E_2 followed by a reverse sweep to a final value E_3 (E_3 may be equal to E_1 but can also hold a different value): referred to as cyclic voltammetry (CV). The speed at which the potential is swept is indicated by the scan rate, ν (V s^{-1}) with typical experiments ranging from $0.01 - 1 \text{ V s}^{-1}$. The waveform of a typical CV experiment is presented in *Figure 0.15a* along with the resulting i - E plot or voltammogram: *Figure 0.15b*.

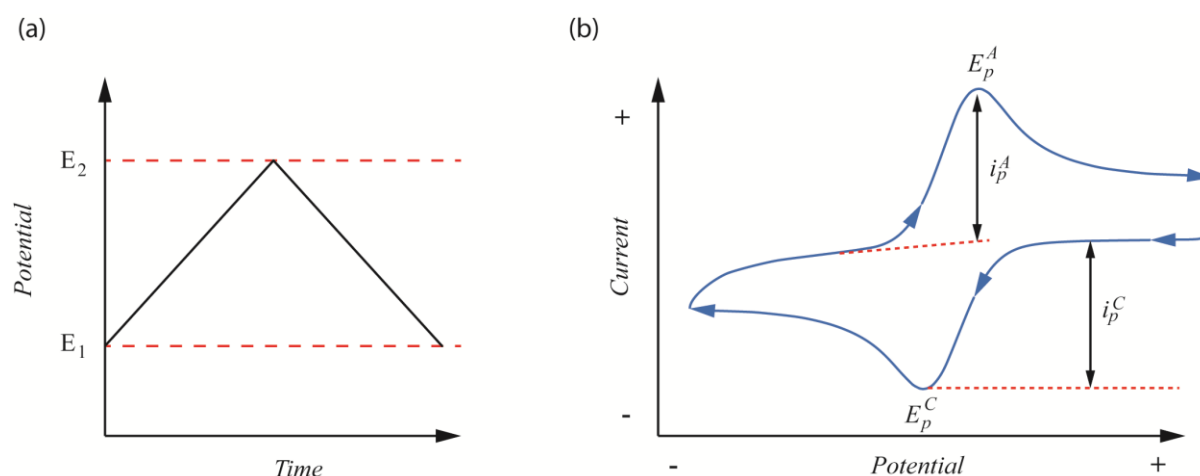


Figure 0.15: (a) E - t plot for a cyclic voltammogram, scanning the potential from E_1 to E_2 and then in reverse; (b) A typical voltammogram for a simple redox mediator undergoing reduction and then oxidation where i_p^C and E_p^C are the cathodic peak current and potential, respectively and i_p^A and E_p^A are the anodic peak current and potential, respectively.

When applying a CV approach to investigate an electrochemical reaction such as that described in reaction **Error! Reference source not found.** on a macroelectrode, the value of E_1 is chosen to be in a region where no appreciable reaction occurs and the applied potential is scanned to E_2 . At some point between E_1 and E_2 , reduction of O to R will occur resulting in a faradaic current (cathodic). As

the potential is scanned towards E_2 the current observed reaches a maximum (peak), i_p^C at a peak potential, E_p^C before falling off, as described by equation 0.56, under diffusion limited conditions with continued scanning towards E_2 . Upon reaching E_2 the potential is scanned in the reverse direction towards E_3 resulting in a current flow (anodic) and a current peak, i_p^A at E_p^A . The difference in peak potential, ΔE_p where

$$\Delta E_p = |E_p^C - E_p^A| \quad 0.53$$

should be equal to $59/n$ mV for a reversible (diffusion-limited) reaction (at 298 K) as dictated by the Nernst equation. The value of i_p on the first sweep of a voltammogram can also be described by the Randles-Sevcik equation:^{16, 32}

$$i_p = (2.69 \times 10^5) n^{3/2} A D_O^{1/2} [O]_{bulk} \nu^{1/2} \quad 0.54$$

for a reversible HET process at room temperature (298K).

From equation 0.54, the dependence of i_p on ν is described as

$$i_p \propto \nu^{1/2} \quad 0.55$$

This is indicative of a diffusion controlled system. For reversible systems E_p is independent of ν .

During the first sweep of a reversible CV, at potentials beyond E_p , the drop-off in current observed should follow

$$i \propto t^{-1/2} \quad 0.56$$

as is observed for a system under planar diffusional control described in 1.1.2.4.1.

In the case where the CV is under kinetic control, ΔE_p increases above $59/n$ mV. For systems which display much higher diffusional fluxes e.g. a UME or convective-diffusive transport systems, the CV response is very different, as the current can now attain a steady-state.

A typical UME CV is shown in *Figure 0.16*. The steady state or limiting current, i_{lim} observed at a coplanar disc shaped microelectrode can be described by:¹⁶

$$i_{lim} = 4nFaD[O]_{bulk}$$

0.57

The condition of reversibility here is $E_{3/4} - E_{1/4} = 59/n$ mV ($E_{3/4}$ and $E_{1/4}$ correspond to the potentials at current values equal to $3/4$ and $1/4$ of i_{lim} respectively).

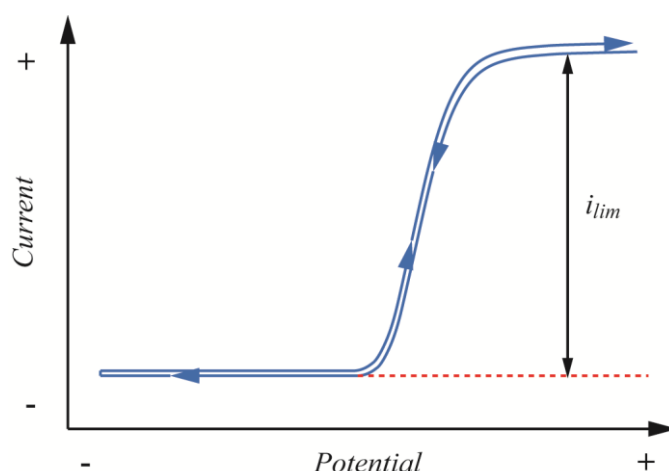


Figure 0.16: A typical voltammogram for the reduction of a simple redox mediator on a microelectrode where i_{lim} is the steady state current resulting from the reduction of the mediator

1.2 Synthetic diamond as an electrode material

1.2.1 Introduction to synthetic diamond

Diamond is conventionally thought of as a rare gemstone of considerable value but is also recognised for a multitude of extraordinary properties including a broad wavelength transparency, high thermal conductivity ($2200 \text{ Wm}^{-1}\text{K}^{-1}$)³³ as well as being the hardest known material (85-100 GPa).³³ The artificial synthesis of diamond has allowed the development of diamond as an extreme material for fabricating a range of devices such as heavy-ion³⁴ and radiation detectors,³⁵ high performance windows,³⁶ and high power lasers.³⁷ Advances in diamond synthesis methods such as chemical vapour deposition (CVD) enable the growth of large wafers of high quality material, the composition of which can be carefully controlled.³⁸

An important aspect of diamond growth is the incorporation of impurities such as boron, nitrogen or lattice defects. Often these impurities are undesirable; however, in the case of producing conducting diamond, boron is deliberately incorporated into the diamond lattice. The adoption of conducting polycrystalline boron-doped diamond (pBDD) as an electrode material has been rapidly expanding in the last 20 years³⁹⁻⁴¹ in light of properties such as wide solvent windows,⁴⁰ low background capacitance⁴² and reduced fouling compared to other electrode surfaces.³⁹

1.2.2 Growth of synthetic diamond

The extreme conditions necessary for diamond growth are naturally found deep within the planet⁴³ but diamonds were successfully synthesised in 1955 by Tracey Hall's team at General Electric.⁴⁴ This process produced the thermodynamically stable conditions of high pressure, high temperature (HPHT) in which graphitic carbon is compressed (5 GPa) at temperatures between 1800-2300 K with a metallic solvent, to thermodynamically drive the formation of diamond⁴⁵. Growth under these conditions yields single-crystal diamonds of dimensions ranging from microns to a millimetre and have been used to grow industrial grade diamonds since the 1960s, with HPHT diamonds predominately used as abrasives for tools.

Since CVD was first reported as a viable method for low pressure diamond growth,⁴⁶⁻⁴⁸ it has formed the basis for over 30 years of research⁴⁹ with the development of a wide variety of CVD techniques to produce high-quality polycrystalline diamond films with properties matching those of natural diamonds. The process of CVD involves the reaction of chemicals in a gas-phase adjacent to a solid surface resulting in the deposition of material. Such a reaction is induced via the activation of gas-phase reactants (generating a plasma) by either thermal energy e.g. hot filament (HFCVD), or microwaves (MWCVD) to create reactive radical species which then react with the adjacent solid substrate surface. The temperature of the reaction is usually maintained in excess of 1000 K and the gas-phase consists of a carbon-containing precursor e.g. methane (0.5-5%) with a large excess of hydrogen. To grow BDD, a boron-containing gas e.g. B_2H_6 is added to the gas-phase feedstock.

The excess hydrogen present in the gas-phase is critical for diamond growth in CVD systems serving to stabilise the diamond lattice, preventing rearrangement to the more thermodynamically stable graphitic sp^2 carbon form. Hydrogen atoms generated during gas-phase activation react with both carbon containing molecules in the gas-phase and C-H bonds on the substrate, producing reactive carbon-containing radicals in both the gas-phase (CH_3^\bullet) and on the substrate surface. Surface radical sites are then able to react with carbon-containing radicals, adding to the diamond lattice. The massive excess of hydrogen atoms means these sites are more likely to recombine with hydrogen stabilising the diamond lattice. In this way CVD diamond growth is kinetically rather than thermodynamically driven, in contrast to HPHT. The reactive atomic hydrogen also serves to convert any non-carbon sp or sp^2 bonded carbon to diamond sp^3 bonded carbon. The constant “turn-over” at the diamond surface means that growth is fairly slow i.e. $0.1 - 10 \mu m \text{ hr}^{-1}$ but the resulting diamond film is of a high quality with very little incorporation of non-diamond-carbon (NDC: sp^2 carbon). More in-depth reviews of CVD diamond growth can be found in the literature.⁴⁹⁻⁵²

1.2.3 Properties of diamond

1.2.3.1 Structure of diamond

Diamond is formed from tetrahedral, sp^3 bonded carbon atoms creating a face centred cubic (fcc) lattice; as shown in *Figure 0.17*. All bonds between atoms are single σ bonds with no π bonding as seen in other allotropes of carbon such as graphite. This covalent, sp^3 structure gives diamond its rigidity along with many other fundamental properties, which are listed in *Table 0.1*.

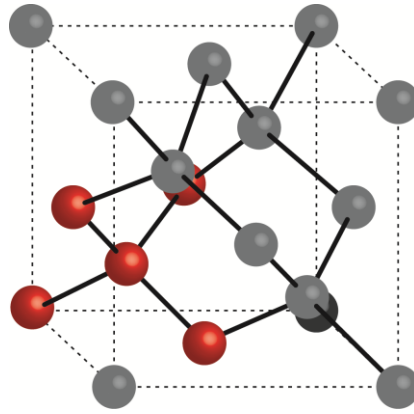


Figure 0.17: The tetrahedral lattice structure of diamond. Red atoms highlight a tetrahedral unit within the lattice structure.

Diamond can be grown in two forms: (1) single crystal where the diamond lattice is homogeneous as one crystallite and (2) polycrystalline where the diamond is formed from multiple crystallites with different crystal orientations. CVD growth of single crystal diamonds is achieved using single-crystal diamond as the growth substrate.⁵³⁻⁵⁵ Carbon atoms deposited onto the single crystal substrate adopt the orientation of the parent substrate and simply add to the lattice. Polycrystalline diamond is commonly formed in CVD growth when the substrate used is not diamond i.e. tungsten, titanium, silicon,³³ or where a substrate is seeded with diamond particles before growth.⁵¹

<i>Property</i>	<i>Value</i>
Extreme Hardness	85-102 GPa ³³
Spectral Transparency	226 nm – 500 μm ³³
Thermal Conductivity	2200 $\text{Wm}^{-1}\text{K}^{-1}$ (300 K) ³³
Resistance to Thermal Shock	1000 MWm^{-1} ⁵⁶
Thermal Expansion Coefficient	0.9 ppmK^{-1} ³³
Electrical Insulator	10^{15} - 10^{16} $\Omega \text{ cm}$ ⁵
Low Dielectric Constant	5.68 ± 0.15 (35 GHz) ⁵⁶
Low Dielectric loss	$8\text{-}20 \times 10^{-6}$ (145 GHz) ⁵⁶
Wide Electronic Band-gap	5.47 eV ³³
High Electronic Mobility	4500 $\text{cm}^2\text{V}^{-1}\text{s}^{-1}$ (electron), 3800 $\text{cm}^2\text{V}^{-1}\text{s}^{-1}$ (hole) ³³

Table 0.1: Properties of diamond

Under these conditions, crystallites of diamond nucleate or continue to grow from seed particles, and grow in all directions to form a thin film across the substrate with crystallites forming “grains” within the film.⁵⁷ The growth rates of the different grains are dependent on the preferential facets and crystal orientations, with some orientations growing at faster rates than others.⁵⁷ Once a film is formed, the grains continue to grow, increasing in size as the film grows thicker. A cross-section of a polycrystalline film is shown in *Figure 0.18* where the grain size is seen to increase between the nucleation face and the growth face.

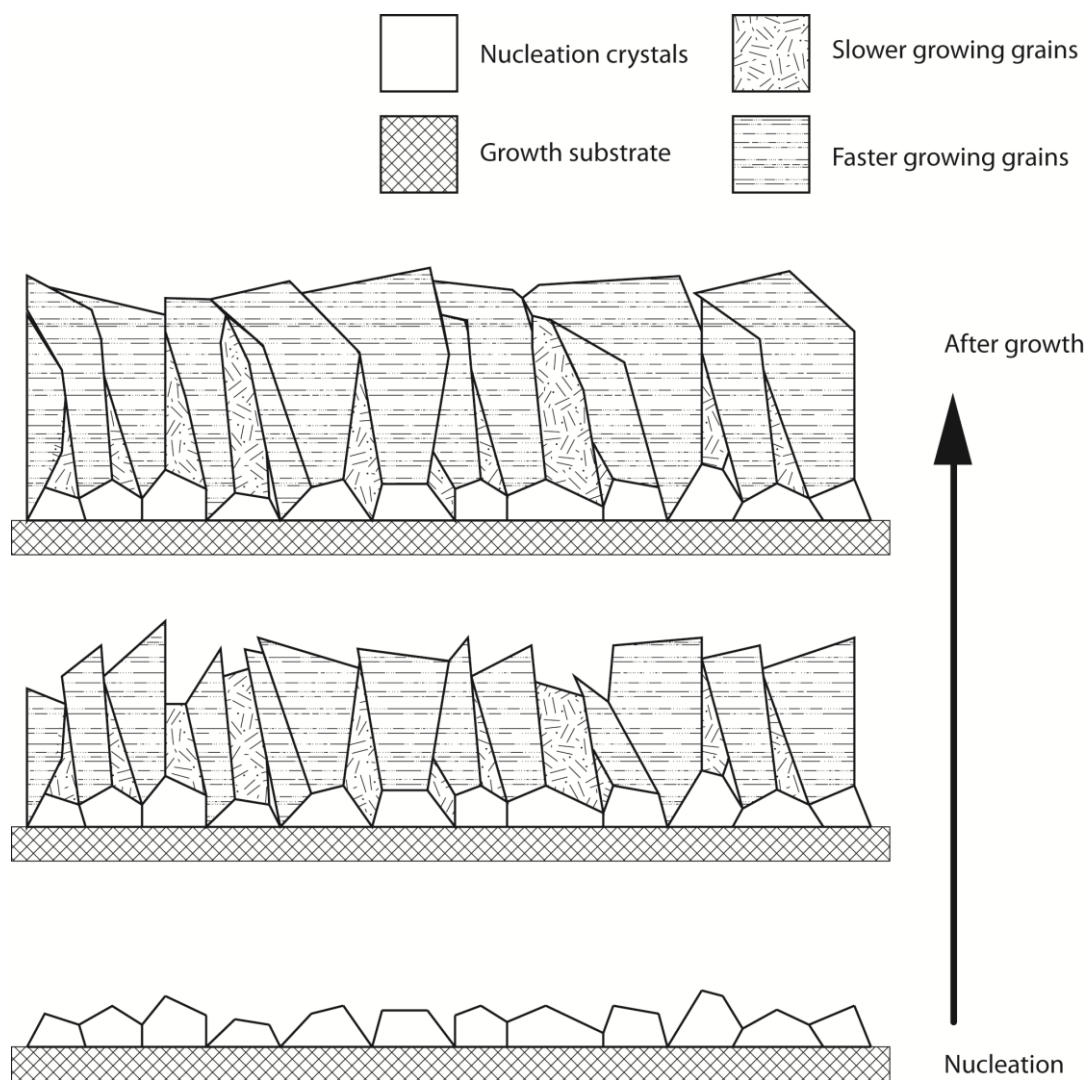


Figure 0.18: Schematic of differential grain growth in polycrystalline diamond films grown via CVD

1.2.3.2 Doping of diamond

Un-doped or intrinsic diamond is by virtue of its sp^3 structure, where all available electrons are used in bonding, a wide band gap semiconductor with a 5.47 eV³³ energy difference separating the valence band from the conduction band; see *Figure 0.19a*. This leads to two properties of intrinsic diamond: firstly, it has a wide spectral transmission range (226 nm – 500 μm)³³ making it visually colourless; secondly, it has extremely high electrical resistivity ($10^{16} \Omega \text{ cm}$).⁵

Doping diamond replaces a small number of carbon atoms in the lattice with the dopant. For example, there are around $3 \times 10^{23} \text{ C atoms cm}^{-3}$ in a diamond lattice with doping typically replacing anywhere (but controlled) between 10^{16} - $10^{21} \text{ C atoms cm}^{-3}$ with dopant. The doping density of a material is typically measured using secondary ion mass spectrometry (SIMS).⁵⁸

When doped with boron, an electron hole is introduced into the lattice resulting in an acceptor level, E_a at 0.37 eV above the valence band; see *Figure 0.19a*. In the case of a very lowly doped lattice i.e. $< 10^{17} \text{ B atoms cm}^{-3}$, the activation energy for excitation of electrons from the valence band to the acceptor level is still quite high and so large resistances are seen in this material. At medium doping concentrations in the range $\sim 10^{18} - 10^{19} \text{ B atoms cm}^{-3}$, the boron atom-atom spacing becomes small enough that wavefunction overlap between boron atoms induces the formation of an impurity band and thus a lowering of the activation energy;^{59, 60} see *Figure 0.19b*. Materials of this doping range exhibit resistivities of $\sim 2 \times 10^3 \Omega \text{ cm}$ and are considered semiconducting. As boron concentrations approach $1.5 \times 10^{19} \text{ B atoms cm}^{-3}$, hopping conduction is thought to occur and the resistivity of the material falls sharply. Once boron concentrations reach $\geq 10^{20} \text{ B atoms cm}^{-3}$ (1 in 1000 carbon atoms replaced with boron), the activation energy for electron excitation from the valence band to the acceptor band reaches zero and the transition to metallic conductivity occurs.⁶¹ The resulting material is considered semi-metallic i.e. the number of charge carriers (holes) is high enough to see metal-like electrical conduction behaviour i.e. resistivities of $\leq 0.1 \Omega \text{ cm}$. Such high doping densities cause an overlap of wavefunctions in acceptor atoms creating a continuum of states between the acceptor level at 0.37 eV and the valence band⁶² as shown in *Figure 0.19c*.

The relationship between electrical resistivity and boron concentration in synthetic single-crystal diamonds is shown in *Figure 0.20*.⁶³ Here the transition between conduction modes with varying boron doping density can be clearly seen.

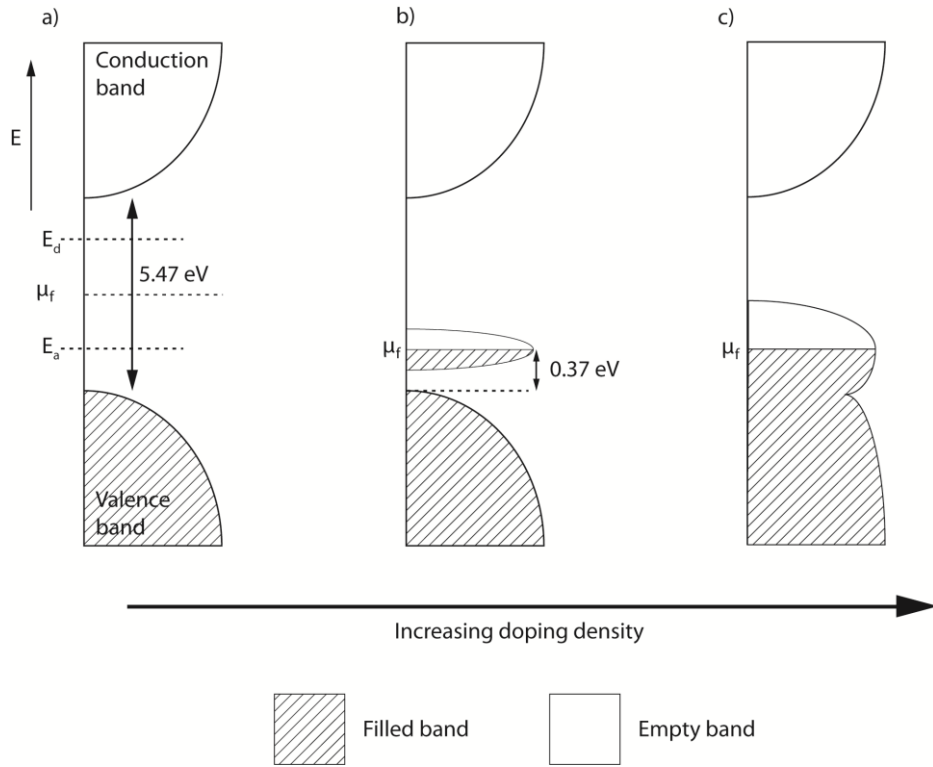


Figure 0.19: Schematic of electronic density of states and band structures for (a) insulating, intrinsic diamond, (b) boron-doped diamond and (c) highly boron-doped diamond; where μ_f is the Fermi level, E_a and E_d are the energy associated with acceptor and donor levels respectively.

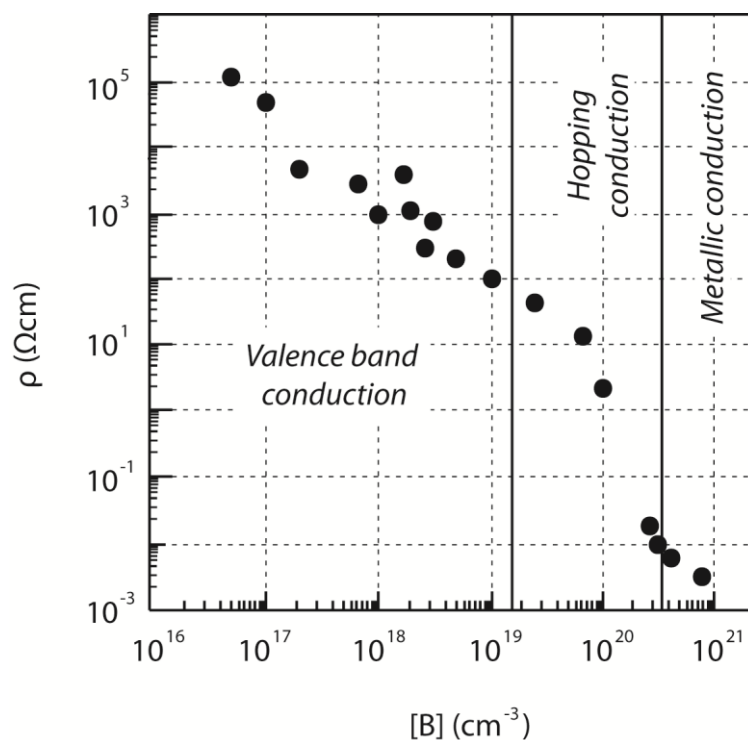


Figure 0.20: Electrical resistivity (at room temperature) as a function of boron doping density in single-crystal boron-doped diamond samples grown by Lagrange *et al.*⁶³

The concentration of boron taken up into the diamond lattice has a near linear dependency on the boron concentration of the gas mixture of the reactor^{58, 64} and is very much dependent on the crystal face undergoing growth. For example, boron up-take into the crystal face (111) is 10 times higher than for a (100) crystal surface.^{46, 65} pBDD can thus be considered a heterogeneously doped electrode. Electrochemical studies have shown for pBDD electrodes doped above the metallic threshold, k_o for two different outer sphere redox couples scales with boron content in the electrode.⁶⁶ As an electrode material, pBDD will exhibit an average behaviour with contributions from all the differently doped grains.

1.2.4 Electrochemistry on boron-doped diamond electrodes

The first reported use of a diamond based material as an electrode was made in 1983 where natural intrinsic diamond was implanted with zinc ions.⁶⁷ This report first highlighted the wide potential windows and low background currents commonly associated with diamond electrochemistry. In the 1990s, Swain and co-workers documented the characteristic low capacitance and wide, featureless solvent windows of high quality thin-film pBDD which they applied to electroanalysis.^{68, 69}

1.2.4.1 Electrochemical characteristics of boron-doped diamond

Although highly doped, pBDD is referred to as metal-like, it still does not possess the same high density of states (DOS) attributed to metal electrodes. In lowly doped material i.e. $\leq 10^{19}$ B atoms cm^{-3} the limitations of such low DOS are apparent when applying potentials negative of the flat band potential resulting in a depletion of charge carriers. The resulting electrochemistry is resistive which can make any interpretation of electrode kinetics ambiguous. To avoid resistive effects, highly doped pBDD i.e. $> 10^{20}$ B atoms cm^{-3} must be used. A good electrochemical test of electrode doping levels is electrochemical characterisation with a redox mediator possessing a redox potential lower than the flat band potential of semi-conducting diamond (e.g. ruthenium hexamine).⁷⁰ For metallic BDD the CV will appear reversible, whilst for semi-conducting BDD, the CV will appear drawn out i.e. resistive.

BDD also represents a catalytically inert electrode surface, with a low DOS, which does not encourage inner sphere processes; this means that large overpotentials are required to drive the electrolysis of water. As a result, BDD shows the widest solvent window of any carbon material, or indeed classical electrode, and displaying low background currents and resistance to electrochemical fouling.

The incorporation of sp^2 carbon into the diamond lattice reduces the quality of the resulting electrode material. sp^2 addition increases the DOS and provides surface sites for adsorption thus reducing the overpotential required for the onset of water electrolysis.⁴² In aqueous solutions this results in a narrowing of the solvent window and an increase in the background capacitance.

1.2.4.2 The effect of surface termination

The two most common diamond surface terminations are hydrogen and oxygen. The surface properties of diamond are highly dependent on the surface termination, particularly the wetting of the material with solvents such as water; see *Figure 0.21a & b*, *Figure 0.21c* and *Figure 0.21d* show schematics of hydrogen and oxygen surface terminations respectively, on polycrystalline intrinsic diamond. Hydrogen termination is usually present directly after CVD growth as it is this termination that stabilises the diamond lattice as it grows. Contact angles of hydrogen terminated diamond with

water in air are typically around 90° .⁷¹ Although stable in air, hydrogen terminated surfaces are believed to oxidise with time to a more stable oxygen terminated surface⁷² particularly when subjected to electrochemically oxidising conditions.⁷³⁻⁷⁵

Due to the greater stability oxygen-terminated surfaces are preferred for electrochemical applications. Oxygen-terminated diamond surfaces are easily achieved via treatment in oxygen plasmas,^{76, 77} oxidative acid⁷⁶ and anodic polarisation.⁷⁵ The oxygen containing groups present on oxygen termination surfaces have been determined via x-ray photoelectron spectroscopy (XPS); groups such as hydroxyl C-OH, ether C-O-C as well as carbonyl groups such as ketones $>C=O$ and carboxylic groups.^{78, 79}

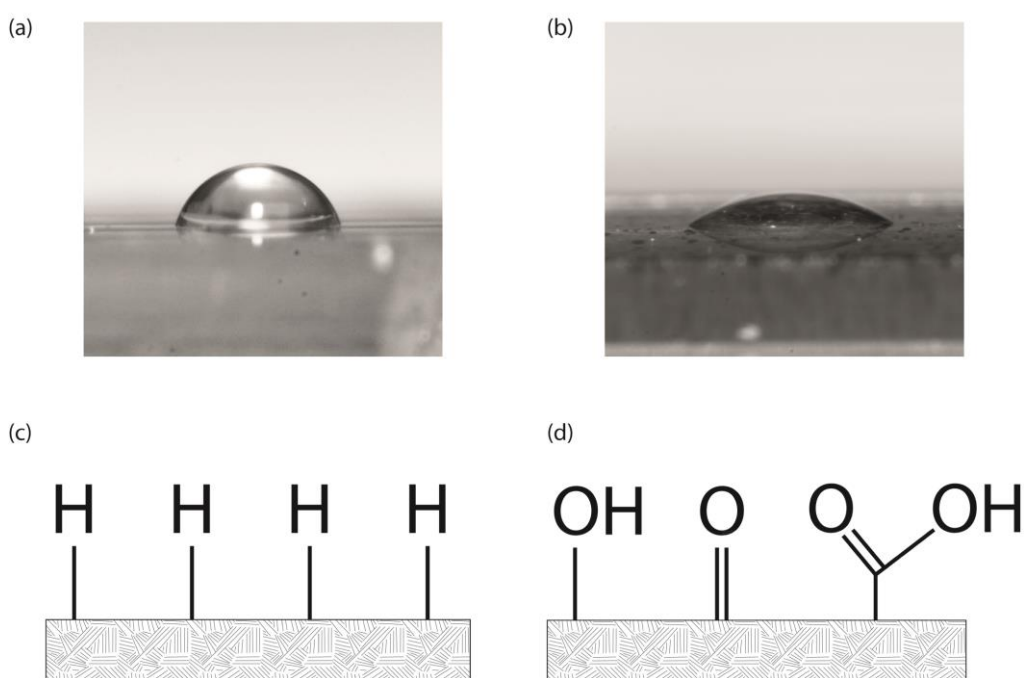


Figure 0.21: Comparison of hydrogen and oxygen terminated polycrystalline intrinsic diamond with (a) the contact angle of a water droplet on a hydrogen terminated surface in air, (b) the contact angle of a water droplet on an oxygen-terminated surface in air, (c) a schematic of a hydrogen-terminated surface; (d) schematic of an oxygen terminated surface.

As well as doping, the surface termination of diamond can have a dramatic effect on the electrochemistry observed. In the presence of a thin water film on an intrinsic diamond surface,

hydrogen termination impacts the electronic structure of diamond by generating an accumulation of electron holes at the diamond surface⁸⁰ coupled with a migration of electrons to the water. This electron exchange creates a charge separation between the diamond and water resulting in a surface conductivity of around $10^{-5} \Omega^{-1}$ at room temperature.⁸¹

1.2.5 Applications of boron-doped diamond

The applications of BDD electrodes are extensive^{82, 83} and have been the subject of a considerable body of research with particular focus in areas such as waste water treatment,^{84, 85} electroanalysis of neurotransmitters,⁸⁶ metal ions^{87, 88} and organic species.⁸⁹⁻⁹¹ BDD's resistance to chemical and mechanical wear make it highly suitable to applications requiring operation in aggressive environments.

1.3 Multiphase flow

1.3.1 Introduction to multiphase flow

Multiphase flow can be defined as the simultaneous flow of two or more immiscible substances. This can describe mixtures of aggregate states: solid, liquid and gas, or immiscible mixtures of one aggregate state e.g. oil/water mixtures. Due to the dynamic nature of the phase interfaces, the distribution of phases within a flow can take on many different shapes. These different distributions can be described using flow patterns such as those shown in *Figure 0.22*. Here a number of common flow patterns are presented for a two phase, gas-liquid system in both horizontal and vertical flow directions.

1. Slug flow (plug flow): *Figure 0.22(a)i, Figure 0.22(b)ii* the Continuous phase 1 is interspersed with “slugs” of phase 2 which vary in length and cross-section.
2. Stratified flow: *Figure 0.22(a)ii* the flow is split into a two regions consisting of just one phase with a single interface between the two phases, resulting from the action of gravitational separation.
3. Wavy-stratified flow: *Figure 0.22(a)iii* as with stratified flow but with a wavy interface between the two phases as a result of increased flow velocity of phase 2.

4. Bubbly flow: *Figure 0.22(a)iv, Figure 0.22(b)i*, a continuous phase 1 with dispersed bubbles of phase 2. Due to buoyancy differences in the two phases, bubbles of phase 2 tend to migrate to the top of the pipe.
5. Churn flow: *Figure 0.22(b)iii*, at higher velocities, slug/plug flow begins to break down into an unstable “churn” flow regime where liquid phases exhibit an induced oscillatory motion.
6. Annular flow: *Figure 0.22(b)iv*, The gaseous phase 2 flows rapidly through the centre of the pipe, surrounded by a thin film of liquid phase 1 which flows between the gas and the pipe wall. An amount of phase 1 may also be carried in the centre of the pipe by the gas phase.

The parameters governing the flow patterns include the flow rates of the different phases, fluid properties of each phase, operating pressure and temperature, the direction of flow and the geometry of the pipe in which flow takes place.

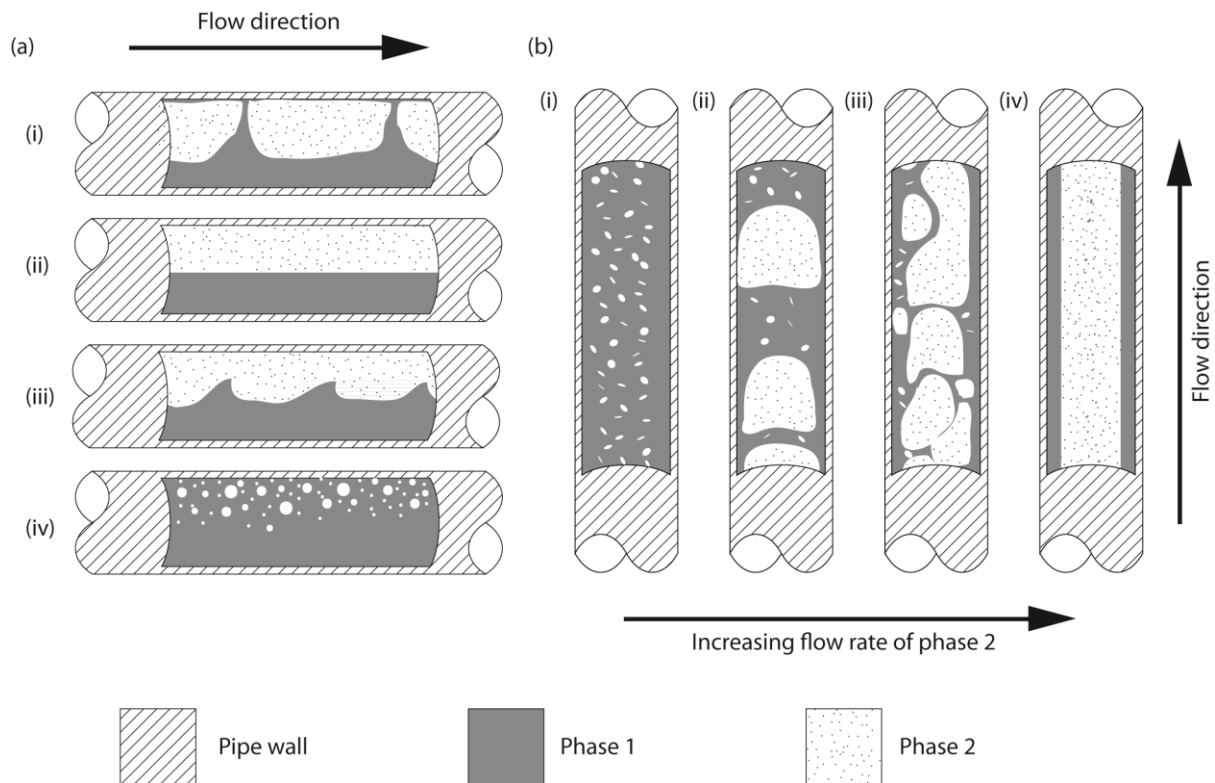


Figure 0.22: Schematic of multiphase flow patterns for a system consisting of two immiscible phases 1 and 2 in (a) horizontal flow: (i) plug flow, (ii) stratified flow, (iii) wavy-stratified flow, (iv) bubbly flow; (b) vertical flow: (i) bubbly flow, (ii) plug flow, (iii) churn flow, (iv) annular flow; where the density of phase 1 > phase 2.

In the case of immiscible liquid-liquid systems, flow patterns are similar to those described for gas-liquid systems; however, liquid-liquid patterns can be more complex and are strongly influenced by the relative densities of the different phases.

The transition between flow patterns is often indicated by a flow pattern map which plots the flow rate of one phase as a function of the other. Visual observations of flow patterns then allow the assignment of boundary lines, marking the transition points between flow pattern regions.

Techniques for quantitative measurement of multiphase flow are of great interest both in research and in industry.

1.3.2 Applications in industry

Multiphase flow metering (MFM) is the measurement of the flow rates of individual phases within a mixed component flow without the need for separation of individual phases. From these measurements, a multiphase flow profile can be derived along with the phase fraction of the flow. MFM has been identified by the oil and gas industries as an important tool for monitoring and testing multiphase fluids removed from oil wells.⁹² Conventional oil well-testing requires the separation of the individual phases that constitute a multiphase flow. Separators and additional test lines for individual phases increase the cost and space required to perform measurements. These issues are particularly significant for off-shore operations where space is limited and maintenance costs are much higher. The adoption of MFM eliminates the need for expensive separators and unlike conventional oil well-testing techniques, MFM devices do not require stabilized flow conditions and are capable of continuous real-time flow monitoring, which is principle for optimizing an oil fields performance.⁹²

Current approaches for probing multiphase flow include Venturi meters,⁹³ ECT/ERT,⁹⁴ Gamma⁹⁵ and X-ray densitometers.⁹⁶ Each approach is based on a different measurement principle to extract information from multiphase flow such as velocity (Venturi meter) and phase composition (ECT/ERT, X-ray densitometers). Typically, a MFM device will employ two or more of these approaches making it more versatile.⁹⁷

1.4 Microfluidics: Lab on a chip

1.4.1 Introduction to microfluidics

Microfluidics deals with the manipulation of volumes of fluid ranging from nanolitres to attolitres within channels where the characteristic length is between 10-1000 μm . It is through this that microfluidics offer the capacity to work with very small reagent volumes, induce rapid mixing, yielding shorter reaction times and allow the detection of analytes with high sensitivity, with reduced analysis time, high reproducibility and is highly suited to running multiple, parallel processes on one device. All of these advantages make microfluidics a compelling medium for areas such as chemical synthesis and analysis, particularly for the massive reduction in material requirements, enabling high throughput at reduced cost.⁹⁸

Microfluidics as a field is considered young and in the early stages of development.⁹⁸ Interest in microfluidic systems for chemical analysis grew dramatically in the 1990's with the introduction of miniaturised total chemical analysis systems (TAS) or micro-TAS (μTAS).⁹⁹ Around this time, the field saw the application of photolithographic techniques, used in the fabrication of micro electromechanical systems (MEMS), to the fabrication of microfluidic devices.¹⁰⁰ Until the year 2000, the majority of microfluidic devices were fabricated from silicon or glass using lithography and micromachining techniques,¹⁰¹ however, with the introduction of "soft-lithography", polymeric elastomers such as PDMS gained popularity on account of massively reduced production times and costs compared with glass or silicon.^{102, 103} The adoption of PDMS also allowed the fabrication of actuators far smaller than that possible with traditional, stiff micromachining materials¹⁰⁴ which cannot produce the required forces to function on the microscale. This soft-lithography "revolution" resulted in a rapid growth of work in microfluidic technologies with biological and chemical applications.^{105, 106}

1.4.1.1 Physical factors in microfluidics

When considering systems on the micro-scale, forces that would otherwise be comparatively minor on a macroscopic scale suddenly become dominant. These forces can result in enhancements in heat

transfer, transport of species as well as providing a well-defined, reproducible system. As a result, microfluidic devices are designed to take advantage of these enhancements.

1.4.1.1.1 Laminar flow

In microfluidic systems, the channel dimensions are small enough that flow is almost always laminar. This is advantageous in terms of modelling a microfluidic system as the equations describing the flow are much simpler compared with non-laminar, turbulent flow. As described in 1.1.2.4.2, a flow regime can be characterised by Re .

As a result of laminar flow, two streams of miscible fluid can flow in contact with each other without convective mixing occurring. Under a laminar regime, transport of species between the two streams is limited to diffusion and migration only.

1.4.1.1.2 Mass transport

Being constructed from layers of fluid flowing in parallel, laminar flow does not support convective-type mixing as found in turbulent flow. As such, any species contained within different layers of flow can only move to adjacent layers via diffusional transport. A schematic of diffusional mixing between two parallel streams of miscible fluid in a microfluidic channel, under laminar flow is shown in *Figure 0.23a*. The velocity profile along the cross-section, in the rectangular channel can be described as uniaxial Poiseuille-like (*Figure 0.23b*) with the highest velocities seen at the centre of the channel. With the action of diffusion, the interfacial region between the two streams is seen to change with time. However, with the application of a uniaxial Poiseuille-like velocity field, inequalities in the interfacial region thickness are observed along the cross-section of the channel (x,y); see *Figure 0.23c*. At points close to the channel walls, the velocity of flow varies linearly as a function of distance from the channel wall i.e. flow is slower close to the wall and faster moving out into the channel. By contrast, points around the centre of the channel experience a more uniform velocity profile. This means diffusion will have a greater effect in the regions around the channel walls where the velocity is much slower. This diffusional mixing profile has been studied by researchers using confocal microscopy.¹⁰⁷

When a plug of material is introduced to a channel under pressure driven flow, the formation of a Poiseuille velocity field in the direction of flow induces convective radial diffusion or dispersion of the plug material with time/movement along the channel; see *Figure 0.23d*. This dispersion is referred to as Taylor dispersion.¹⁰⁸ In analytical applications, it is often desirable to reduce the amount of dispersion in a channel as to maximise the concentration of an analyte under investigation and perform detection processes before dilution via dispersion can occur.¹⁰⁹ A strategy for reducing dispersion in microfluidic channels is to encapsulate an analyte within an immiscible droplet.¹¹⁰ This will be discussed further in Chapter 5.

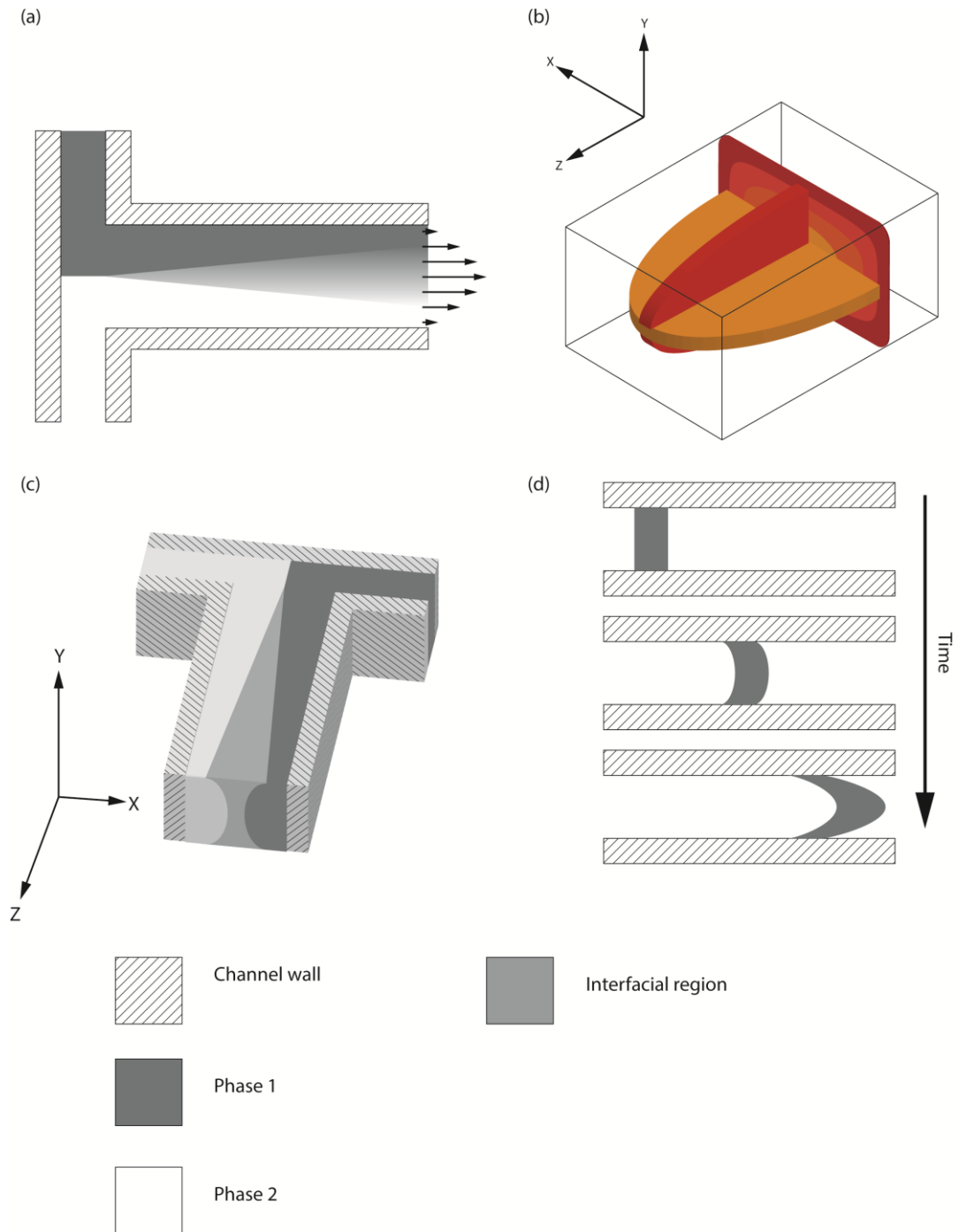


Figure 0.23: (a) Schematic of diffusional mixing of two miscible fluid streams in a rectangular microfluidic channel; (b) an illustration of the uniaxial Poiseuille-like velocity field seen in a rectangular channel with flow in the z direction; (c) schematic showing the non-uniform interfacial region generated under uniaxial Poiseuille-like flow; (d) Schematic of the action of Taylor dispersion on a plug of material flowing through a channel under a laminar regime, with time.

Although considered slow on a macroscopic scale, diffusional transport on the micron-scale becomes more significant as diffusional times will be much shorter. However, fast mixing in microchannels via diffusion alone requires large interfaces between components.

Convective mixing can be induced in microfluidic channels using novel geometries. *Figure 0.24* describes a geometry where the flow of two miscible fluids is split and then recombined creating eddies at the point of recombination. This principle is known as the Coanda effect¹¹¹ and is an example of a passive mixer, using the channel geometry to induce mixing rather than an external force i.e. as with an active mixer.

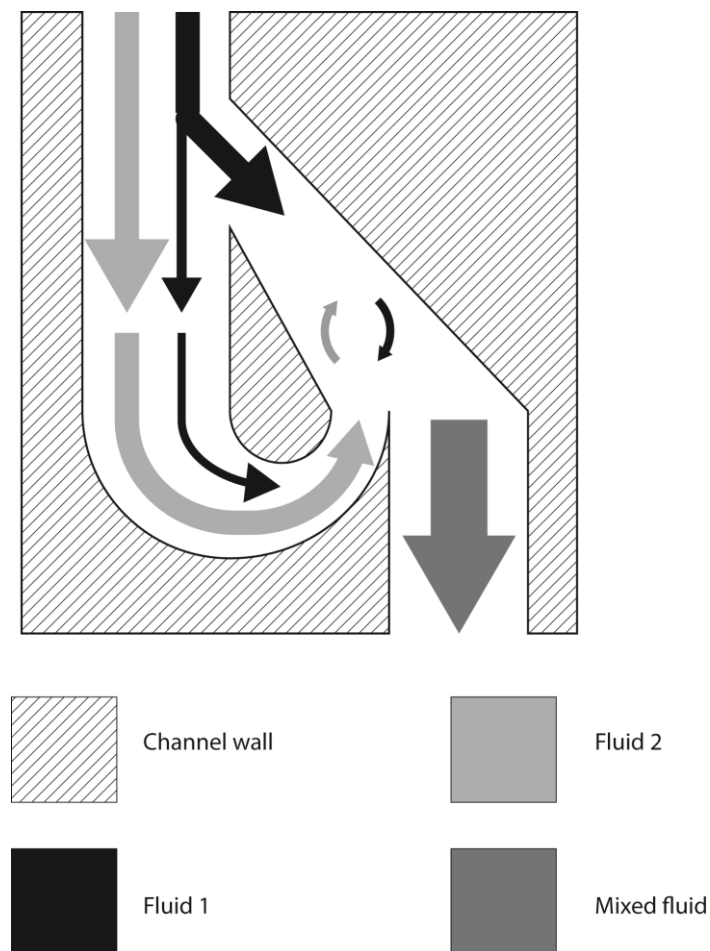


Figure 0.24: Schematic of a microfluidic geometry designed to induce convective mixing between two miscible fluids via the Coanda effect.

1.4.1.1.3 Surface area to volume ratio

When going from macro-scale to micro-scale devices, the surface area to volume ratio (SAVR) becomes an important factor with major enhancements in SAVR seen in micro-scale devices compared with their macro-scale counterparts, often by a few orders of magnitude.¹⁰¹ This has an impact on the thermal properties of micro-scale devices which through large interfaces, allows the rapid transfer of heat. This property is particularly advantageous in electrophoresis where excess heat can be removed quickly.¹¹²

1.4.1.2 Fabrication methods

Common methods for fabricating microfluidic devices include micromachining,¹¹³ soft lithography,¹⁰² injection molding,¹¹⁴⁻¹¹⁶ embossing,¹¹⁷⁻¹¹⁹ and laser ablation.¹²⁰ More detailed information on microfluidic fabrication techniques can be found in Chapter 5.

1.5 Aims and Objectives

Work in this thesis is based around the application of pBDD as a sensor material in both stationary and fluid flow environments, ultimately for investigation of challenging environments where traditional electrodes would be unsuitable. Emphasis is on both single phase and multiphase (liquid-liquid) systems under both stationary and flow regimes. Proposed applications are presented which could show eventual use in both pharmaceutical analysis and MFM.

Work in Chapter 3, initially focuses on developing an understanding of pBDD as an electrochemical sensing material in both aqueous and non-aqueous solutions, by investigating the use of pBDD as an electrode material for the electrochemical detection of the genotoxic impurity, hydrazine (and associated derivatives) in pharmaceutical products. The aim is to resolve electrochemical signals for the toxic reagent hydrazine from those of electroactive ingredients present in excess.

The system is then developed by considering, in Chapter 4, electrochemical sensing at the electrode/non polar oil/water interface using an electroactive species as a probe, which is not soluble in the oil phase, whereas its electrolysis product is. Double potential step chronoamperometry in

combination with finite element simulations are used to explore the relationship between droplet size and generation/collection responses for the electroactive probe species.

Chapter 5 then moves onto describing immiscible oil-water droplet generation in a microfluidic device incorporating electrochemical sensors. Initial work focuses on the use of PDMS in combination with platinum microband electrochemical sensors for the detection of droplets of water, containing a redox active species, in a channel flow of oil. The electrochemical response as a function of droplet size and velocity is discussed. The limitations of PDMS microfluidic devices for the investigation of non-aqueous, volatile solvents are examined.

In Chapter 6, the fabrication of an all-diamond microfluidic device with integrated pBDD sensing electrodes is outlined and characterised in both aqueous and non-aqueous solvents. Design considerations are examined and the application of such a device to the investigation of harsh and challenging environments is considered.

Finally, Chapter 7 discusses the conclusions of the thesis and further work relating to the potential applications of the all-diamond fabricated devices described in Chapter 6.

1.6 References

1. S. Andreescu and O. A. Sadik, *Methods*, 2005, **37**, 84-93.
2. G. Hanrahan, D. G. Patil and J. Wang, *Journal of Environmental Monitoring*, 2004, **6**, 657-664.
3. L. J. J. Janssen and L. Koene, *Chemical Engineering Journal*, 2002, **85**, 137-146.
4. S. Viswanathan, H. Radecka and J. Radecki, *Monatsh Chem*, 2009, **140**, 891-899.
5. J. W. Vandersande and L. D. Zoltan, *Diamond and Related Materials*, 1995, **4**, 641-644.
6. U. Guth, W. Vonau and J. Zosel, *Measurement Science and Technology*, 2009, **20**, 042002.
7. B. J. Privett, J. H. Shin and M. H. Schoenfisch, *Analytical Chemistry*, 2008, **80**, 4499-4517.
8. J. R. Stetter and J. Li, *Chemical Reviews*, 2008, **108**, 352-366.
9. D. W. Kimmel, G. LeBlanc, M. E. Meschievitz and D. E. Cliffel, *Analytical Chemistry*, 2011, **84**, 685-707.
10. J. Wang, *Biosensors and Bioelectronics*, 2006, **21**, 1887-1892.
11. J. Wang, *Talanta*, 2002, **56**, 223-231.
12. F. J. del Campo, *Electrochemistry Communications*, 2014, **45**, 91-94.
13. J. L. Anderson, L. A. Coury and J. Leddy, *Analytical Chemistry*, 2000, **72**, 4497-4520.
14. A. Elahi and D. J. Caruana, *Physical Chemistry Chemical Physics*, 2013, **15**, 1108-1114.
15. J. C. Myland and K. B. Oldham, *Analytical Chemistry*, 2000, **72**, 3972-3980.
16. A. J. Bard and L. R. Faulkner, *Electrochemical Methods: Fundamentals and Applications*, 2 edn., John Wiley & Sons, 2001.
17. D. C. Luehrs, R. T. Iwamoto and J. Kleinberg, *Inorganic Chemistry*, 1966, **5**, 201-204.
18. A. Bott, *Current Separations*, 1995, **14**, 64-68.

19. H. Helmholtz, *Annalen der Physik*, 1879, **243**, 337-382.
20. D. L. Chapman, *Philosophical Magazine Series 6*, 1913, **25**, 475-481.
21. O. Stern, *Zeit. Elektrochem*, 1924, **30**, 508-516.
22. K. B. Oldham, *Journal of Electroanalytical Chemistry*, 2008, **613**, 131-138.
23. D. C. Grahame, *Chemical Reviews*, 1947, **41**, 441-501.
24. D. C. Grahame, *Zeitschrift für Elektrochemie, Berichte der Bunsengesellschaft für physikalische Chemie*, 1958, **62**, 264-274.
25. J. O. M. Bockris, M. A. V. Devanathan and K. Müller, *Proceedings of the Royal Society of London. Series A, Mathematical and Physical Sciences*, 1963, **274**, 55-79.
26. R. A. Marcus, *Electrochimica Acta*, 1968, **13**, 995-1004.
27. F. Opekar and P. Beran, *Journal of Electroanalytical Chemistry and Interfacial Electrochemistry*, 1976, **69**, 1-105.
28. N. V. Rees, R. A. W. Dryfe, J. A. Cooper, B. A. Coles, R. G. Compton, S. G. Davies and T. D. McCarthy, *The Journal of Physical Chemistry*, 1995, **99**, 7096-7101.
29. J. Yamada and H. Matsuda, *Journal of Electroanalytical Chemistry and Interfacial Electrochemistry*, 1973, **44**, 189-198.
30. D. T. Chin and C. H. Tsang, *Journal of The Electrochemical Society*, 1978, **125**, 1461-1470.
31. M. B. Glauert, *Journal of Fluid Mechanics*, 1956, **1**, 625-643.
32. J. E. B. Randles, *Transactions of the Faraday Society*, 1948, **44**, 327-338.
33. R. S. Balmer, J. R. Brandon, S. L. Clewes, H. K. Dhillon, J. M. Dodson, I. Friel, P. N. Inglis, T. D. Madgwick, M. L. Markham, T. P. Mollart, N. Perkins, G. A. Scarsbrook, D. J. Twitchen, A. J. Whitehead, J. J. Wilman and S. M. Woollard, *Journal of Physics: Condensed Matter*, 2009, **21**, 364221.
34. E. Berdermann, K. Blasche, P. Moritz, H. Stelzer and B. Voss, *Diamond and Related Materials*, 2001, **10**, 1770-1777.
35. B. Planskoy, *Physics in Medicine and Biology*, 1980, **25**, 519.
36. K. Sakamoto, A. Kasugai, M. Tsuneoka, K. Takahashi, T. Imai, T. Kariya and Y. Mitsunaka, *Review of Scientific Instruments*, 1999, **70**, 208-212.
37. H. P. Godfried, S. E. Coe, C. E. Hall, C. S. J. Pickles, R. S. Sussmann, X. Tang and W. K. van der Voorden, 2000.
38. P. W. May, *Endeavour*, 1995, **19**, 101-106.
39. J. Xu, M. C. Granger, Q. Chen, J. W. Strojek, T. E. Lister and G. M. Swain, *Analytical Chemistry*, 1997, **69**, 591A-597A.
40. M. Panizza and G. Cerisola, *Electrochimica Acta*, 2005, **51**, 191-199.
41. R. G. Compton, J. S. Foord and F. Marken, *Electroanalysis*, 2003, **15**, 1349-1363.
42. H. B. Martin, A. Argoitia, U. Landau, A. B. Anderson and J. C. Angus, *Journal of The Electrochemical Society*, 1996, **143**, L133-L136.
43. S. E. Haggerty, *Earth and Planetary Science Letters*, 1994, **122**, 57-69.
44. F. P. Bundy, H. T. Hall, H. M. Strong and R. H. Wentorf, *Nature*, 1955, **176**, 51-55.
45. F. P. Bundy, *The Journal of Chemical Physics*, 1963, **38**, 631-643.
46. M. Kamo, Y. Sato, S. Matsumoto and N. Setaka, *Journal of Crystal Growth*, 1983, **62**, 642-644.
47. B. V. Spitsyn, L. L. Bouilov and B. V. Derjaguin, *Journal of Crystal Growth*, 1981, **52**, Part 1, 219-226.
48. S. Matsumoto, Y. Sato, M. Kamo and N. Setaka, *Japanese Journal of Applied Physics*, 1982, **21**, L183.
49. P. K. Bachmann, D. Leers and H. Lydtin, *Diamond and Related Materials*, 1991, **1**, 1-12.
50. J. E. Butler, Y. A. Mankelevich, A. Cheesman, J. Ma and M. N. R. Ashfold, *Journal of Physics: Condensed Matter*, 2009, **21**, 364201.
51. J. C. Angus, A. Argoitia, R. Gat, Z. Li, M. Sunkara, L. Wang and Y. Wang, *Philosophical Transactions: Physical Sciences and Engineering*, 1993, **342**, 195-208.
52. J. E. Butler, R. L. Woodin, L. M. Brown and P. Fallon, *Philosophical Transactions: Physical Sciences and Engineering*, 1993, **342**, 209-224.
53. G. Janssen, W. J. P. van Enckevort, W. Vollenberg and L. J. Giling, *Diamond and Related Materials*, 1992, **1**, 789-800.

54. A. Tallaire, J. Achard, F. Silva, R. S. Sussmann and A. Gicquel, *Diamond and Related Materials*, 2005, **14**, 249-254.
55. P. Djemia, A. Tallaire, J. Achard, F. Silva and A. Gicquel, *Diamond and Related Materials*, 2007, **16**, 962-965.
56. www.e6.com, 2014.
57. F. G. Celii and J. E. Butler, *Annual Review of Physical Chemistry*, 1991, **42**, 643-684.
58. H. Spicka, M. Griesser, H. Hutter, M. Grasserbauer, S. Bohr, R. Haubner and B. Lux, *Diamond and Related Materials*, 1996, **5**, 383-387.
59. E. Gheeraert, A. Deneuve and J. Mambou, *Diamond and Related Materials*, 1998, **7**, 1509-1512.
60. T. Inushima, T. Matsushita, S. Ohya and H. Shiomi, *Diamond and Related Materials*, 2000, **9**, 1066-1070.
61. A. W. S. Williams, E. C. Lightowers and A. T. Collins, *Journal of Physics C: Solid State Physics*, 1970, **3**, 1727.
62. X. Blase, E. Bustarret, C. Chapelier, T. Klein and C. Marcenat, *Nat Mater*, 2009, **8**, 375-382.
63. J. P. Lagrange, A. Deneuve and E. Gheeraert, *Diamond and Related Materials*, 1998, **7**, 1390-1393.
64. B.-J. Lee, B.-T. Ahn and Y.-J. Baik, *Diamond and Related Materials*, 1999, **8**, 251-256.
65. K. Ushizawa, K. Watanabe, T. Ando, I. Sakaguchi, M. Nishitani-Gamo, Y. Sato and H. Kanda, *Diamond and Related Materials*, 1998, **7**, 1719-1722.
66. H. V. Patten, K. E. Meadows, L. A. Hutton, J. G. Iacobini, D. Battistel, K. McKelvey, A. W. Colburn, M. E. Newton, J. V. Macpherson and P. R. Unwin, *Angewandte Chemie International Edition*, 2012, **51**, 7002-7006.
67. M. Iwaki, S. Sato, K. Takahashi and H. Sakairi, *Nuclear Instruments and Methods in Physics Research*, **209–210, Part 2**, 1129-1133.
68. S. Alehashem, F. Chambers, J. W. Strojek, G. M. Swain and R. Ramesham, *Analytical Chemistry*, 1995, **67**, 2812-2821.
69. G. M. Swain and R. Ramesham, *Analytical Chemistry*, 1993, **65**, 345-351.
70. L. A. Hutton, J. G. Iacobini, E. Bitziou, R. B. Channon, M. E. Newton and J. V. Macpherson, *Analytical Chemistry*, 2013, **85**, 7230-7240.
71. L. Ostrovskaya, V. Perevertailo, V. Ralchenko, A. Dementjev and O. Loginova, *Diamond and Related Materials*, 2002, **11**, 845-850.
72. G. R. Salazar-Banda, L. S. Andrade, P. A. P. Nascente, P. S. Pizani, R. C. Rocha-Filho and L. A. Avaca, *Electrochimica Acta*, 2006, **51**, 4612-4619.
73. H. B. Martin, A. Argoitia, J. C. Angus and U. Landau, *Journal of The Electrochemical Society*, 1999, **146**, 2959-2964.
74. H. A. Girard, E. de La Rochefoucauld, D. Ballutaud, A. Etcheberry and N. Simon, *Electrochemical and Solid-State Letters*, 2007, **10**, F34-F37.
75. H. A. Girard, N. Simon, D. Ballutaud, E. de La Rochefoucauld and A. Etcheberry, *Diamond and Related Materials*, 2007, **16**, 888-891.
76. P. E. Pehrsson, J. P. Long, M. J. Marchywka and J. E. Butler, *Applied Physics Letters*, 1995, **67**, 3414-3416.
77. S. Wang, V. M. Swope, J. E. Butler, T. Feygelson and G. M. Swain, *Diamond and Related Materials*, 2009, **18**, 669-677.
78. T. N. Rao, D. A. Tryk, K. Hashimoto and A. Fujishima, *Journal of The Electrochemical Society*, 1999, **146**, 680-684.
79. J. Shirafuji, Y. Sakamoto, A. Furukawa, H. Shigeta and T. Sugino, *Diamond and Related Materials*, 1995, **4**, 984-988.
80. F. Maier, M. Riedel, B. Mantel, J. Ristein and L. Ley, *Physical Review Letters*, 2000, **85**, 3472-3475.
81. J. Ristein, M. Riedel and L. Ley *Journal of The Electrochemical Society*, 2004, **151**, E315-E321.
82. J. H. T. Luong, K. B. Male and J. D. Glennon, *Analyst*, 2009, **134**, 1965-1979.
83. O. Chailapakul, W. Siangproh and D. A. Tryk, *Sensor Letters*, 2006, **4**, 99-119.

84. D. Gandini, E. Mahé, P. A. Michaud, W. Haenni, A. Perret and C. Comninellis, *Journal of Applied Electrochemistry*, 2000, **30**, 1345-1350.
85. P. Cañizares, J. García-Gómez, J. Lobato and M. A. Rodrigo, *Industrial & Engineering Chemistry Research*, 2003, **42**, 956-962.
86. B. V. Sarada, T. N. Rao, D. A. Tryk and A. Fujishima, *Analytical Chemistry*, 2000, **72**, 1632-1638.
87. A. Manivannan, D. A. Tryk and A. Fujishima, *Electrochemical and Solid-State Letters*, 1999, **2**, 455-456.
88. T. L. Read, E. Bitziou, M. B. Joseph and J. V. Macpherson, *Analytical Chemistry*, 2013, **86**, 367-371.
89. K. L. Soh, W. P. Kang, J. L. Davidson, Y. M. Wong, D. E. Cliffel and G. M. Swain, *Diamond and Related Materials*, 2008, **17**, 900-905.
90. T. N. Rao, B. V. Sarada, D. A. Tryk and A. Fujishima, *Journal of Electroanalytical Chemistry*, 2000, **491**, 175-181.
91. T. N. Rao, I. Yagi, T. Miwa, D. A. Tryk and A. Fujishima, *Analytical Chemistry*, 1999, **71**, 2506-2511.
92. G. Falcone, G. Hewitt and C. Alimonti, *Multiphase Flow Metering: Principles and Applications*, 2009.
93. F. Lide, Z. Tao and J. Ningde, *Journal of Petroleum Science and Engineering*, 2007, **57**, 247-256.
94. I. Ismail, J. C. Gamio, S. F. A. Bukhari and W. Q. Yang, *Flow Measurement and Instrumentation*, 2005, **16**, 145-155.
95. S. A. Tjugum, B. T. Hjertaker and G. A. Johansen, *Measurement Science and Technology*, 2002, **13**, 1319.
96. H. M. Prasser, M. Misawa and I. Tiseanu, *Flow Measurement and Instrumentation*, 2005, **16**, 73-83.
97. S. Teniou and M. Meribout, *Can. J. Sci. Ind. Res*, 2011, **2**, 290-293.
98. G. M. Whitesides, *Nature*, 2006, **442**, 368-373.
99. A. Manz, N. Graber and H. M. Widmer, *Sensors and Actuators B: Chemical*, 1990, **1**, 244-248.
100. P. Gravesen, J. Branebjerg and O. S. Jensen, *Journal of Micromechanics and Microengineering*, 1993, **3**, 168.
101. D. J. Beebe, G. A. Mensing and G. M. Walker, *Annual Review of Biomedical Engineering*, 2002, **4**, 261-286.
102. D. C. Duffy, J. C. McDonald, O. J. A. Schueller and G. M. Whitesides, *Analytical Chemistry*, 1998, **70**, 4974-4984.
103. J. C. McDonald and G. M. Whitesides, *Accounts of Chemical Research*, 2002, **35**, 491-499.
104. M. A. Unger, H.-P. Chou, T. Thorsen, A. Scherer and S. R. Quake, *Science*, 2000, **288**, 113-116.
105. D. B. Weibel and G. M. Whitesides, *Current Opinion in Chemical Biology*, 2006, **10**, 584-591.
106. K.-i. Ohno, K. Tachikawa and A. Manz, *ELECTROPHORESIS*, 2008, **29**, 4443-4453.
107. R. F. Ismagilov, A. D. Stroock, P. J. A. Kenis, G. Whitesides and H. A. Stone, *Applied Physics Letters*, 2000, **76**, 2376-2378.
108. G. Taylor, *Proceedings of the Royal Society of London. Series A, Mathematical and Physical Sciences*, 1953, **219**, 186-203.
109. H. A. Stone and S. Kim, *AIChE Journal*, 2001, **47**, 1250-1254.
110. A. Gunther and K. F. Jensen, *Lab on a Chip*, 2006, **6**, 1487-1503.
111. C.-C. Hong, J.-W. Choi and C. H. Ahn, *Lab on a Chip*, 2004, **4**, 109-113.
112. J. W. Jorgenson and K. D. Lukacs, *Clinical Chemistry*, 1981, **27**, 1551-1553.
113. A. M. Hynes, H. Ashraf, J. K. Bhardwaj, J. Hopkins, I. Johnston and J. N. Shepherd, *Sensors and Actuators A: Physical*, 1999, **74**, 13-17.
114. U. Attia, S. Marson and J. Alcock, *Microfluid Nanofluid*, 2009, **7**, 1-28.
115. J. Giboz, T. Copponnex and P. Mélé, *Journal of Micromechanics and Microengineering*, 2007, **17**, R96.

- 116. M. Hecke and W. K. Schomburg, *Journal of Micromechanics and Microengineering*, 2004, **14**, R1.
- 117. H. Becker and U. Heim, *Sensors and Actuators A: Physical*, 2000, **83**, 130-135.
- 118. H. Becker, W. Dietz and P. Dannberg, in *Micro Total Analysis Systems '98*, eds. D. J. Harrison and A. van den Berg, Springer Netherlands, 1998, pp. 253-256.
- 119. L. Martynova, L. E. Locascio, M. Gaitan, G. W. Kramer, R. G. Christensen and W. A. MacCrehan, *Analytical Chemistry*, 1997, **69**, 4783-4789.
- 120. H. Klank, J. P. Kutter and O. Geschke, *Lab on a Chip*, 2002, **2**, 242-246.

Chapter 2: Experimental, materials, instrumentation and techniques

2.1 Materials

2.1.1 CVD diamond

All polycrystalline diamond samples used throughout this work were grown and prepared by Element Six Ltd., Ascot, UK, via a commercial MWCVD process described in 1.2.2 which has been developed in-house.

Code	Type	[B] (atom cm ⁻³)	Wafer	Surface
			thickness (μm)	roughness (nm)
MR14	pBDD (EA)	5×10^{20}	630 ± 2	1-3
MR8	pBDD	5×10^{20}	500 ± 2	1-3
DR3	Optical polycrystalline intrinsic	n/a	1000 ± 2	1-3
TG1	Thermal grade intrinsic	n/a	500 ± 2	1-3

2.1 Chemicals

All aqueous solutions were prepared from triply distilled, Milli-Q water (Millipore Corp.) with a resistivity of 18.2 MΩ upon dispensing at 25°C. All chemicals were weighed using a four figure analytical balance (Sartorius A2008). Chemicals and materials used in this work are listed in *Table 0.1*.

Chemicals	Formula	Details	Supplier
<i>Solvents</i>			
Acetone	$(\text{CH}_3)_2\text{CO}$	99%	Fisher Scientific UK Ltd.,UK
Acetonitrile	$\text{C}_2\text{H}_3\text{N}$	99.9%	Fisher Scientific UK Ltd.,UK
Dodecane	$\text{CH}_3(\text{CH}_2)_{10}\text{CH}_3$	99%	Merck, Germany
Ethanol	$\text{C}_2\text{H}_6\text{O}$	99.8%	VWR, France
Hexane	C_6H_{14}	98%	VWR, France
Propan-2-ol		99.99%	Fisher Scientific UK Ltd.,UK
<i>Chemicals for electroanalysis</i>			
Ferrocene	Fc	98%	Fluka, Sigma Aldrich, USA
Ferrocenyltrimethylammonium	$\text{FcN}(\text{CH}_3)_3.\text{PF}_6$		Made in house
Hexafluorophosphate, (FcTMA. PF_6)			
Hydrochloric acid	HCl	38%	Fisher Scientific UK Ltd.,UK
Potassium Bromide	KBr	99.5%	Fison Scientific, UK
Potassium Chloride	KCl	99-100%	Sigma Aldrich, USA
Potassium Nitrate	KNO_3	99%	Sigma Aldrich, USA
Sulphuric Acid	H_2SO_4	$\geq 95\%$	Fluka, Sigma Aldrich, USA
Tetrabutylammonium	$\text{C}_{16}\text{H}_{36}\text{F}_6\text{NP}$	99%	Fluka, Sigma Aldrich, USA
Hexafluorophosphate			
<i>Substrate materials</i>			
Silicon wafer	Si	<100> n-type	IDB Technologies Ltd., UK
<i>Photoresists and developers</i>			
S1818 positive photoresist			MicroChem Corp., USA
Microposit MF-319			DOW, USA
SU-8 (2100)			MicroChem Corp., USA
Microposit EC solvent			Rohm and Hass, Denmark

Table 0.1: Chemicals and materials used in this thesis including purity and supplier

2.2 Electrochemical instrumentation:

In order to maintain control over the applied potential of an electrochemical experiment, an electrical instrument known as a potentiostat is used. A schematic of the basic principle of a 3-electrode potentiostat is shown in *Figure 0.1*. At the heart of the potentiostat is an Operational Amplifier (OA) which maintains an output voltage, e_o based on the difference in voltage, e_s between an input, e_+ and a second input, e_- .¹ During operation of the OA, e_o will be such that

$$e_o = -A_g e_s = -A_g e_- + A_g e_+$$

where A_g is the open-loop gain (amplification factor).

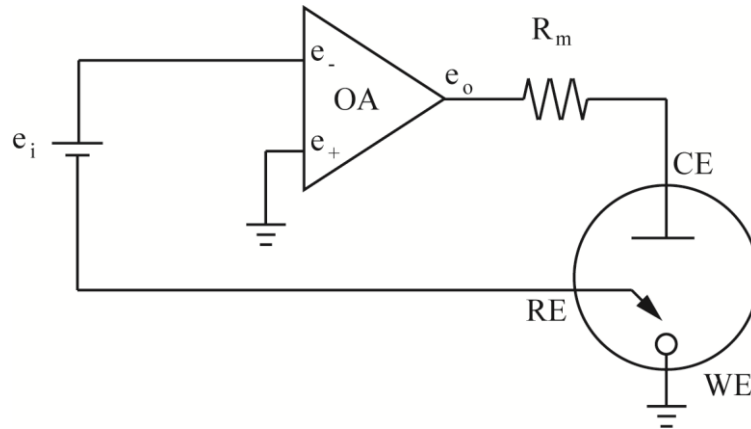


Figure 0.1: Schematic of a simple potentiostat consisting of an operational amplifier (OA) and a 3-electrode electrochemical cell with working electrode (WE), reference electrode (RE) and counter electrode (CE).¹

In order to maintain a potential difference between the working electrode (WE) and reference electrode (RE) of value e_i , the OA applies a current through the Counter electrode (CE) which is measured over a series resistor R_m , and controlled by the amplifier so that the potential of the RE is maintained at $-e_i$ versus ground and therefore the potential of the WE, e_{wk} versus RE must be

$$e_{wk} (vs. RE) = e_i$$

0.2

Instrumentation for electrochemical analysis will typically consist of a potentiostat for potential control, a function generator to create the desired changes in potential with time (often described by a waveform $E-t$) and a recording system to measure the results¹.

Electrochemical measurements made in this work were carried out using a model 1040A Multi-potentiostat (CH Instruments Inc., USA).

2.3 Electrochemical techniques

2.3.1 Chronoamperometry

Chronoamperometry (CA)^{2,3} is an electrochemical technique whereby a potential, E_1 is applied to the working electrode for a defined time width, τ and the resulting current, i , recorded as a function of time, t . The E - t plot and resulting current transient are shown in *Figure 0.2a* and *Figure 0.2b* respectively.

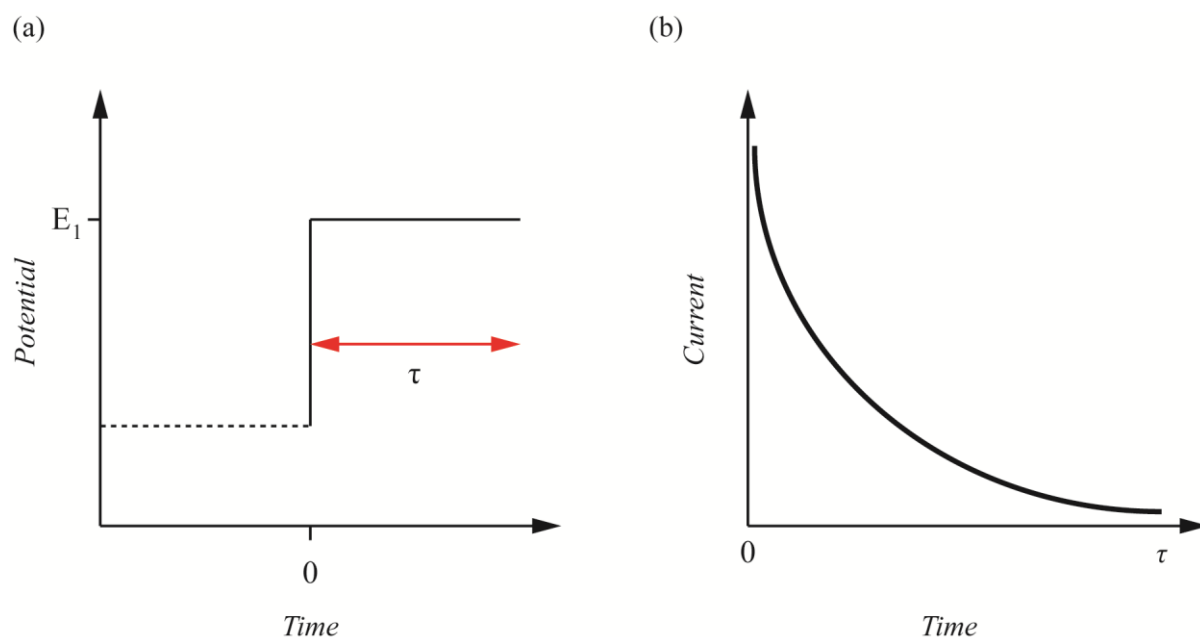


Figure 0.2: (a) E - t plot for a typical CA experiment and (b) the resulting i - t plot

2.3.2 Double potential step chronoamperometry

Double potential step chronoamperometry (DPSC), as with CA, applies a potential, E_1 to the working electrode for a time width, τ after which, a second potential, E_2 is applied, typically, for an equal time. Each applied potential is referred to as a potential step (PS). In DPSC, the first PS is applied in order to generate a species while the second PS collects back what was generated with the resulting current transient being recorded for a time period equal to 2τ . *Figure 0.3* shows plots of (a) E - t and (b) i - t for a typical DPSC experiment. Examples of such experiments are common place in the literature.^{4,5}

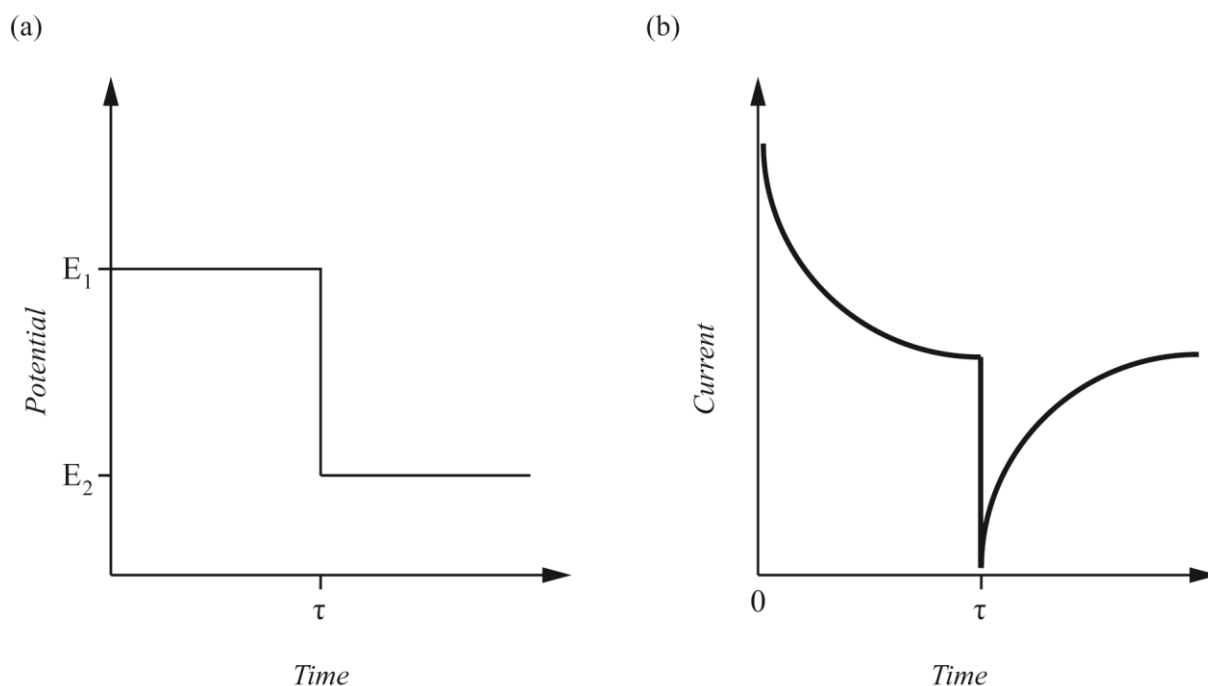


Figure 0.3: (a) E - t plot for a typical DPSC experiment and (b) the resulting i - t plot

2.3.3 Differential pulse voltammetry

Differential pulse voltammetry (DPV) is a voltammetric technique designed to reduce contributions of non-faradaic processes i.e. background capacitance, to the observed current response via a pulsing method¹. The charging current as a result of an applied potential, decays exponentially towards zero with time. This occurs at a much faster rate than the decay of the faradaic current which instead is proportional to $t^{-1/2}$ (Section 1.1.2.4.1); as shown in *Figure 0.4a*. DPV uses a series of pulses whereby the potential applied is stepped initially by an amplitude ζ and held for τ (ms) before dropping to a base potential for a width τ_b which itself is stepped by ζ_b relative to the previous base potential. The current is measured at the point before the potential pulse is applied i.e. τ' and again at the end of the pulse i.e. τ . The current recorded is the difference between $i(\tau')$ and $i(\tau)$ ¹. The wave form (*Figure 0.4b*) and i - t plot for a typical DPV experiment is shown in *Figure 0.4*: (a) Schematic showing the time dependence of non-faradaic, double layer charging current (dotted line), faradaic current (solid line) and the total observed current as a result of the previous two components (dashed line); (b) the

waveform for a DPV experiment; (c) i - t plot for a typical DPV (solid line) compared with the equivalent LSV (dotted line). Figure 0.4c.

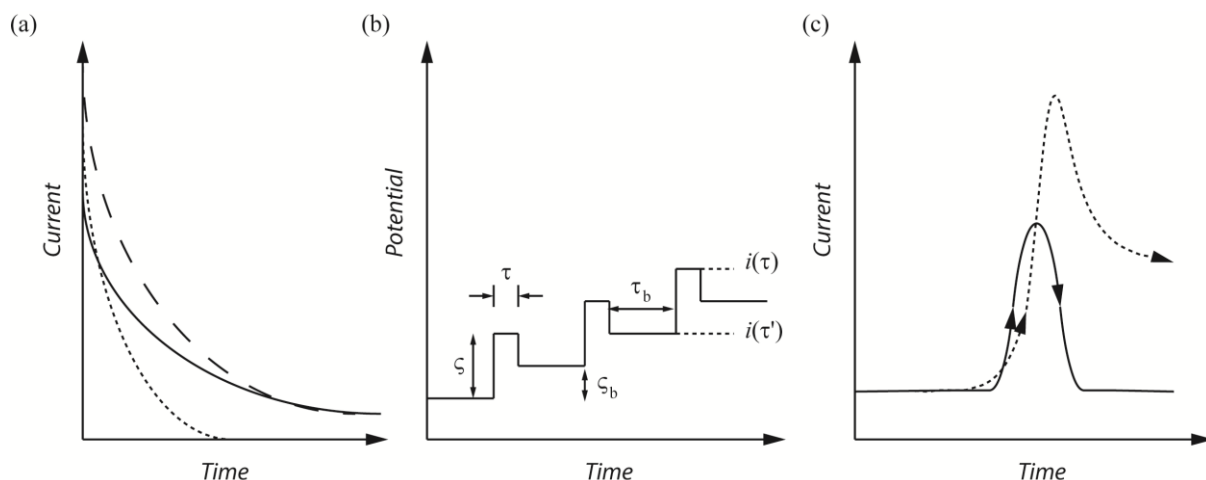


Figure 0.4: (a) Schematic showing the time dependence of non-faradaic, double layer charging current (dotted line), faradaic current (solid line) and the total observed current as a result of the previous two components (dashed line); (b) the waveform for a DPV experiment; (c) i - t plot for a typical DPV (solid line) compared with the equivalent LSV (dotted line).

2.4 Fabrication techniques

2.4.1 Laser micromachining

Laser micromachining was performed using an Oxford Lasers Ltd. E-355H-3-ATHI-O system equipped with a Q-switched fully diode-pumped solid state Nd:YAG laser medium with a primary output wavelength of 355 nm. The average output power of the system is 6 W (at 10 kHz) with a pulse frequency range between 1 Hz – 250 kHz and pulse duration of 34 ns (nominal at 10 kHz). The laser optics cabinet is shown in Figure 0.5

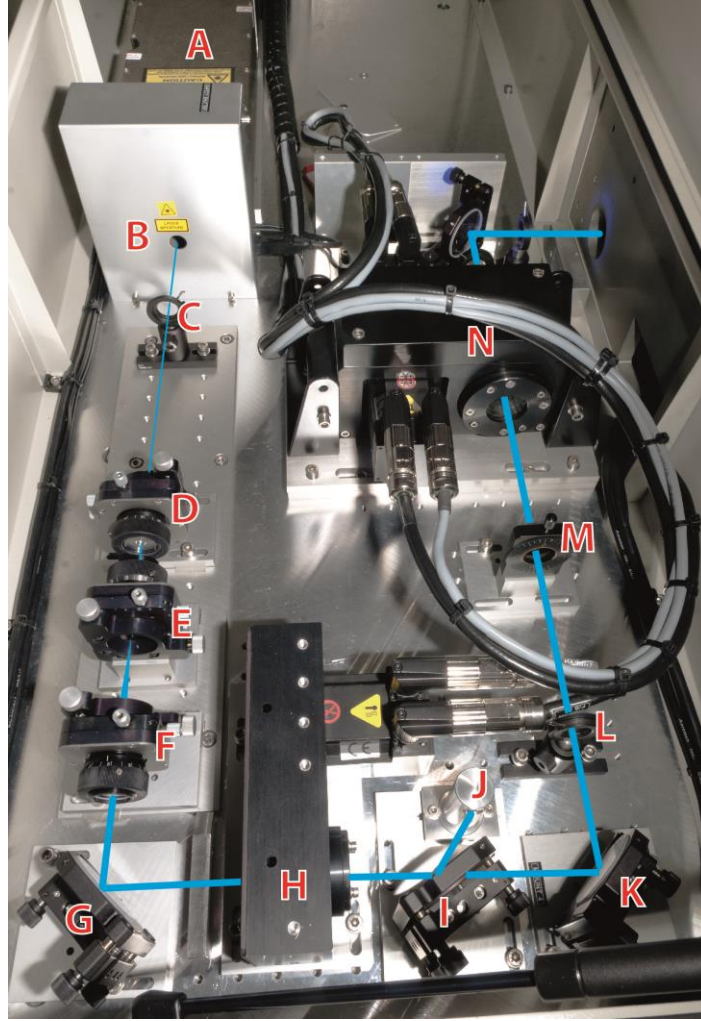


Figure 0.5: The layout of the beam (blue line) delivery optics contained in the optics cabinet of the Oxford Lasers system: (A) laser cavity, (B) safety shutter, (C) alignment iris, (D) 1st telescopic lens, (E) 50 μm spatial filter, (F) 2nd telescopic lens, (G) turning mirror, (H) attenuator, (I) polariser, (J) beam dump, (K) turning mirror, (L) alignment iris, (M) $\frac{1}{4} \lambda$ plate and (N) laser trepan optics module.

The laser uses a Nd:YAG gain medium pumped by diodes based on direct coupled pump (DCP) technology ⁶. Pump diode emission is between 800-815 nm. The output infra-red light (1064 nm) is converted to the harmonic frequency via frequency doubling and then tripling to 355 nm light using a set of non-linear optic (NLO) crystals⁶. The loss from the laser cavity is regulated by an acoustic-optic Q-switch driven by a low-voltage radio-frequency (RF) operating at 40.68 MHz.

Residual light of frequencies 1064 nm, 532 nm and 800 nm are present in the output, however, these wavelengths typically constitute 1% of the output beam and are further reduced by a factor 10^4 travelling through the beam delivery system. For example, 355 nm output is horizontally polarised

while 1064 nm output is vertically polarised and so passage through beam delivery mirrors that are reflective of horizontally polarised light but transmit vertically polarised light, filters out the unwanted residual 1064 nm light from the beam. The laser micromachining system is equipped with a laser trepanning module which utilises a set of rotating, wedge optics: trepan A and trepan B to offset the beam relative to its central axis as shown in *Figure 0.6*.

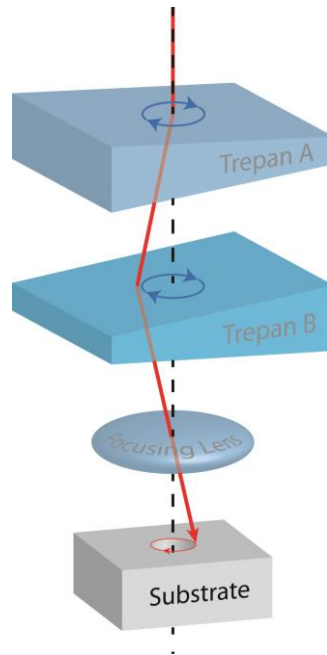


Figure 0.6: Schematic of a laser trepan optics set up consisting of two wedge optics: Trepan A and Trepan B, focusing lens and the resulting beam path on the machined substrate.

In order to create laser machined cuts in thick materials, a technique referred to in this work as “Benching” was used. This technique requires that the laser makes multiple passes along the axis of the desired cut with an offset with each pass. The laser focus is then stepped down in the z -axis and a second set of passes performed as described in *Figure 0.7* for a benched cut along the x -axis. Benching results in a “V”-shaped cut due to the excess material removed either side of the central axis of the cut. Adoption of a benched cut is advantageous for cutting through thick materials as it overcomes the limitations of a narrow single-beam-diameter cut whereby the effectiveness of laser cutting is reduced with increasing depth. Widening of the cut geometry with a bench cut promotes effective laser cutting by comparison to single beam cuts.

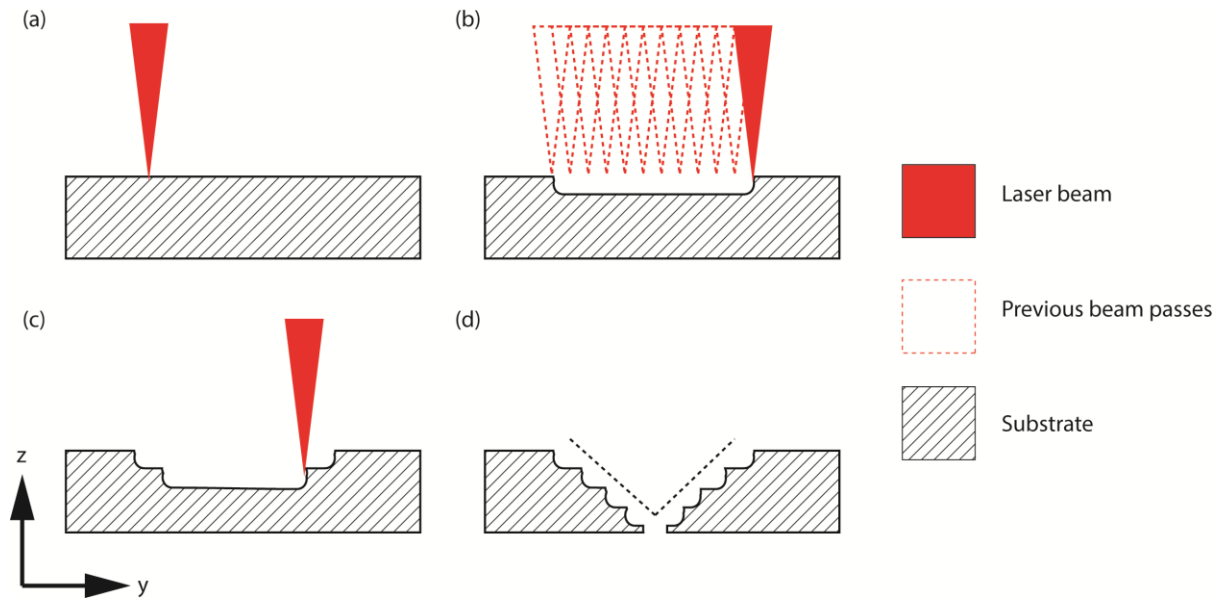


Figure 0.7: Schematic of a benching cut along the x -axis with a laser beam to create a “V”-shaped cut.

2.4.2 Metallisation of surfaces

Metal films were deposited using a Moorfields MiniLab 060 platform sputter/evaporator system comprising of two flexi-hood magnetron sources for 2” and 3” targets with quartz crystal microbalance controllers for process control. Samples were mounted onto a plate and positioned inside the deposition chamber which was then placed under a vacuum ($\sim 1 \times 10^{-6}$ Torr). Once under vacuum, argon gas was introduced into the chamber so that a process pressure of around 5 mbar was achieved. A plasma was struck using a DC electric field with a power of between 30-40 W over the target material resulting in the deposition of material onto samples suspended directly about the plasma. Once a film of adequate thickness was deposited, as indicated by an internal, calibrated quartz crystal microbalance, the chamber was vented under nitrogen gas before removing the samples.

2.4.3 Reactive Ion Etching: RIE

Reactive Ion Etching (RIE) is a common micromachining technique particularly for the processing of silicon for the fabrication of MEMs devices.^{7, 8} It is a useful technique for fabricating silicon moulds for elastomer based microfluidic devices. In conventional RIE, a reactive species is generated in a plasma above a substrate of interest via the excitation of a source gas (CF_4) by an applied

radiofrequency (rf) power supply.⁹ The substrate to be etched is placed on a high-frequency driven and dc-biased, capacitatively coupled electrode. Alternatively, the plasma can be generated via an inductively coupled plasma (ICP) where a time-varying electric current is applied to a metal coil creating a magnetic field which is then powered by RF. ICP systems generate very high plasma densities and are often coupled with a parallel plate bias (as shown in *Figure 0.8*) to achieve fast etching with high anisotropy.¹⁰

Upon ignition of the plasma, the electrode acquires a negative charge, causing the substrate surface to be bombarded by positive ions generated in the adjacent plasma.¹¹ Neutral chemical species generated in the plasma diffuse⁸ from the bulk plasma to the substrate surface whereas positive ions are subject to forced convection towards the negatively charged electrode/substrate.¹¹ Chemical reactions between plasma generated species and the substrate material occur at the substrate surface resulting in etching of the surface material. Positive species are accelerated towards the substrate surface and collide removing material via sputtering¹² resulting in higher material removal rates in the vertical as opposed to the lateral direction,¹³ leading to etching with high aspect ratios.⁸ Features are defined on a substrate using a patterned mask of a material such as SiO_2 or Al_2O_3 ¹³ which etches at a significantly slower rate than the substrate material under the conditions of the etch. This is referred to as a selective mask.

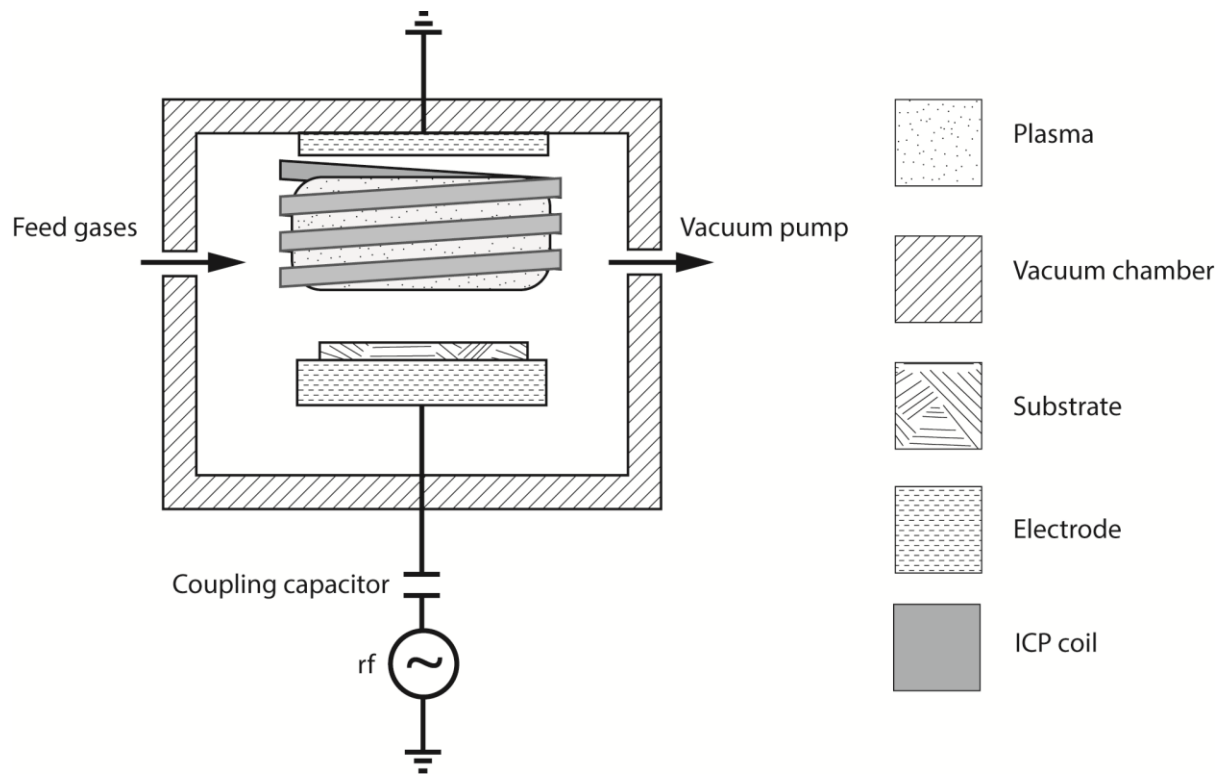


Figure 0.8: Schematic of a simple RIE system

In this work silicon moulds for PDMS microfluidic channel creation were fabricated using a Corial 200 IL RIE-ICP system (Corial, France) system with SiF_6 -based chemistry. Aluminium and Nickel/Vanadium masks were deposited via sputtering and patterned using an underlying S1818 positive photomask as follows:

- (1) A 4" silicon wafer was first cleaned with deionised water, then propan-2-ol and then again with water. The wafer was then dried under a stream of nitrogen. A 1 μm thick film of S1818 positive photoresist was spincoated (G3-8 spin coater, Specialty Coating Systems Inc., USA) 3000 rpm for 45 s and then baked at 115 $^\circ\text{C}$ for 1 min. Coated wafers were exposed to ultra-violet (UV) radiation (MJB4, Süß MicroTec lithography, Germany) through a mask and developed in MF-319 developer solution, removing regions of photoresist exposed to UV radiation.
- (2) Thin films of Al or Ni (400 nm) were sputter deposited onto the patterned silicon wafers as described in 2.4.2. Lift-off of unwanted metal film was performed in acetone, dissolving the

underlying S1818 photoresist resulting in a pattern of microfluidic channels on the silicon wafer. The patterned wafer was washed with deionised water and dried under a stream of nitrogen.

- (3) The patterned silicon wafers were placed into the RIE chamber and evacuated to 1×10^{-3} Torr. A mixture of gases: C_2H_4 , SF_6 , He (1:2:1) and O_2 (5%) were then pumped into the chamber and a plasma ignited via an applied RF. Etch conditions were typically maintained for 2-3 hours to achieve feature depths of between 35-50 μm .
- (4) After removal from the RIE chamber, the etched wafers were cleaned in deionised water and dried under nitrogen. Micro-features were characterised using a stylo-profiler (Ambios Technology Inc., USA) and interferometry (ContourGT, Bruker Nano Inc., USA).

2.5 Boron-doped diamond electrode fabrication

2.5.1 Laser machining of pBDD

1 mm diameter pBDD cylinders were laser machined from a MR14 wafer using a benching technique with the following laser machining parameters: 100% power, 20 kHz, machining traverse speed of 1 $mm\ s^{-1}$.

2.5.2 Acid cleaning

During laser machining, graphitic carbon is formed on regions of diamond subjected to irradiation. The amount of this amorphous carbon is greatly reduced with a treatment of concentrated H_2SO_4 ($\geq 95\%$ Sigma-Aldrich) supersaturated with KNO_3 and heated to $\sim 300\ ^\circ C$ on a hotplate stirrer. The acid mixture is contained in a Pyrex beaker and capped with a watch glass to prevent evaporation. During heating, brown/orange fumes of NO_2 are given off until all KNO_3 is exhausted. Diamond samples are then treated to a further treatment of just concentrated H_2SO_4 ($\geq 95\%$ Sigma-Aldrich) to remove any remaining salt crystals. This oxidative acid cleaning procedure serves to both remove amorphous carbon deposits and generate a highly reproducible oxygen-terminated diamond surface.¹⁴

2.5.3 Metallisation and formation of an Ohmic contact

A 10 nm layer of Ti followed by a 300 nm layer of Au or Pt was sputter-deposited on the pBDD using a Moorfields MiniLab 060 platform sputter/evaporator system. Annealing of the deposited metal film was performed in a tube furnace (MTF 12/25/400, Carbolite, UK) at 500°C for 4 hours. The annealing procedure leads to the formation of a titanium-carbide layer at the Ti-diamond interface which acts as a robust ohmic contact.¹⁵

2.5.4 Glass-sealed macroelectrodes

pBDD macroelectrodes were fabricated in house from 1 mm diameter pBDD columns prepared as described in sections 2.5.1, 2.5.2 and 2.5.3. These pBDD columns were mounted and sealed into a borosilicate glass capillary (i.d. 1.16 mm, o.d. 2 mm, Harvard Apparatus Ltd, UK) by heating the capillary using the heating coil of a capillary puller under vacuum. Silver-loaded epoxy (RS Components Ltd, Northants, UK) was packed into the capillary and set with a copper wire (1 mm diameter) for 24 hrs. The pBDD column containing end of the capillary was polished back using carbimet grit paper of gradually decreasing grades in order to expose the pBDD column surface. *Figure 0.9* shows (a) top and (b) side views of a typical 1 mm diameter pBDD macroelectrode prepared in this way.

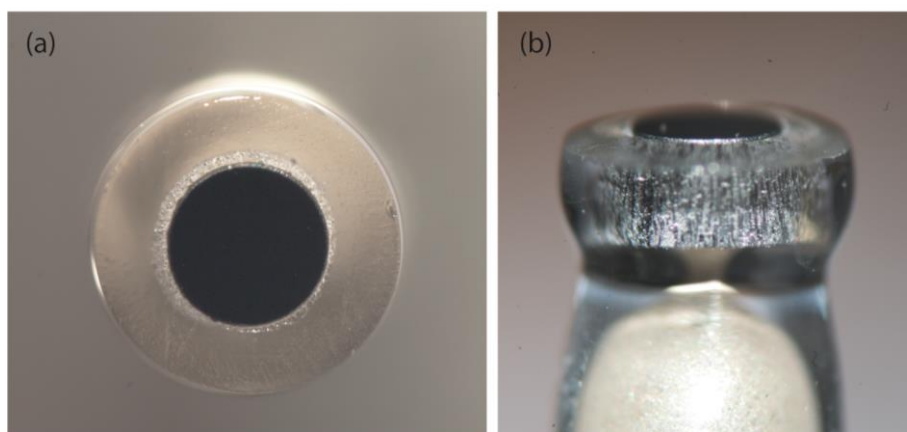


Figure 0.9: Photographs of a 1 mm diameter glass-sealed pBDD macroelectrode: (a) top view; (b) side view.

2.6 Characterisation techniques

2.6.1 Optical Microscopy

Optical microscopy and measurements were made through an Olympus BH2 light microscope (Olympus Corporation, Japan) with magnification capabilities in the range $\times 50$ - $\times 1000$. Digital images were captured using a 2 MP CMOS camera (Olympus Corporation, Japan) interfaced with a computer.

2.6.2 Raman spectroscopy

A molecule positioned in an electric field \mathbf{E} will generate an electrical dipole moment \mathbf{p} (C m).¹⁶ The induced dipole moment can be considered directly proportional to the applied electric field so that

$$\mathbf{p} = \alpha_p \cdot \mathbf{E}$$

0.3

where α_p is the polarisability ($\text{C} \cdot \text{V}^{-1} \cdot \text{m}^2$), a tensor dependent on the shape and dimensions of chemical bonds. Since chemical bonds change during vibrations, α is dependent on the molecular vibrations. \mathbf{E} is supplied by the electromagnetic radiation, often a monochromatic light source such as a laser, providing an oscillating electrical field:

$$\mathbf{E} = \mathbf{E}_0 \cdot \cos(2\pi \cdot \nu_0 \cdot t_t)$$

0.4

where ν_0 is the vibrational frequency of the electromagnetic radiation and t_t is the moment.

With the application of \mathbf{E} , α_p undergoes a harmonic oscillation equal to the vibrational frequency of the normal coordinate of the molecule, ν_v .¹⁶ The resulting dipole moment can be considered as a function of ν_v and ν_0 , and be described as a combination of three different frequency-dependent components¹⁶:

$$\mathbf{p} = \mathbf{p}(\nu_0) + \mathbf{p}(\nu_0 + \nu_v) + \mathbf{p}(\nu_0 - \nu_v)$$

0.5

The first of these components (modes) corresponds to elastic scattering (Rayleigh scattering) of photons where the induced dipole moment is of the same frequency, thus energy as the incident radiation. The second term corresponds to Anti-Stokes scattering where the scattered radiation is of a higher energy than that of the incident radiation. The final term corresponds to Stokes scattering where the scattered radiation is of a lower energy than that of the incident radiation. The different modes of photon scattering are shown schematically in *Figure 0.10*. During Raman spectroscopy, a sample material is irradiated with a laser and the intensity of scattered, re-emitted radiation is measured as a function of its wavelength.

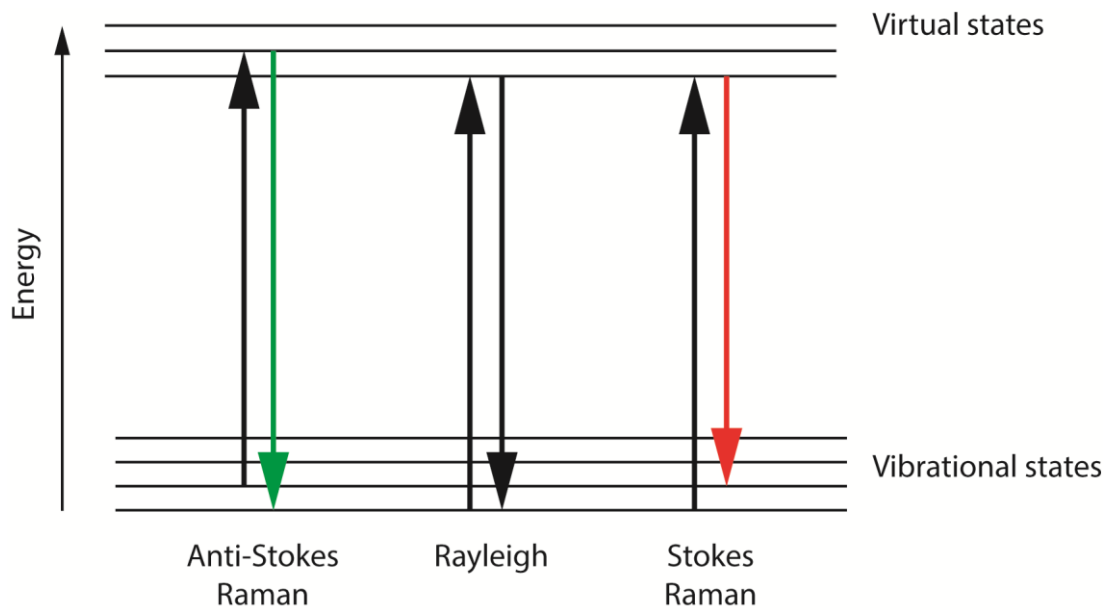


Figure 0.10: Schematic of the different photon scattering modes and their associated transitions.

The Raman spectrum is a plot of the measured intensity of re-emitted light as a function of the Raman wavenumber ω (cm^{-1}) related to the difference in frequency between scattered light ν_m and ν_0 , so that

$$\omega = \frac{U_m}{c} - \frac{U_o}{c}$$

0.6

where c is the speed of light. Whether values of ω are positive or negative is indicative of the different Raman scattering modes with positive wave numbers corresponding to Stokes scattering and negative wavenumbers corresponding to anti-Stokes scattering. Elastic, Rayleigh scattering appears on a Raman spectrum at $\omega = 0$ but the intensity of this line is suppressed by a holographic filter in the spectrometer¹⁶.

Raman spectroscopy provides a powerful tool for the characterisation of diamond and other carbon materials.¹⁷ In diamond, the face-centered cubic lattice of sp^3 hybridised carbon yields a characteristic sharp Raman line at 1332 cm^{-1} indicative of a first order phonon mode.¹⁷ Disordered, amorphous sp^2 carbon is also Raman active with characteristic broad peaks appearing at 1357, 1580, 2700 and 2735 cm^{-1} .¹⁷ The sensitivity of Raman for graphitic sp^2 carbon is significantly greater than that for sp^3 hybridised carbon with scattering efficiencies of 500×10^{-7} and $9 \times 10^{-7} \text{ cm}^{-1}/\text{sr}$ for sp^2 and sp^3 structures respectively.¹⁷ This leads to Raman lines of 50 times greater intensity for sp^2 materials compared with that of sp^3 materials.¹⁷ This makes Raman an effective tool for characterising the quality of diamond materials with a high sensitivity for trace levels of sp^2 impurities within the diamond structure.

Raman spectroscopy can also be used as an indication of the boron doping concentration in pBDD with a characteristic asymmetry in the 1332 cm^{-1} line or Fano line appearing at boron concentrations above $1 \times 10^{20} \text{ B atoms cm}^{-3}$.¹⁸ This Fano interference is thought to be induced by an interaction between valence band states and the continuum formed from mixtures of excited acceptor levels at high boron concentrations in the diamond lattice.¹⁸ At lower boron concentrations, this asymmetry in the 1332 cm^{-1} line is less apparent.

Micro-Raman was performed at room temperature using a Renishaw inVia Raman microscope with an excitation wavelength of 514.5 nm generated from an Ar⁺ laser (10 mW). The average spot size used was around 3 µm with detection performed via a CCD detector for vis-nrIR.

2.6.3 White Light Interferometry (WLI)

White Light Interferometry, WLI is an optical technique for measuring topography through the application of optical interference. The interferometry is equipped with a broad spectrum light source which is collimated and split into two beams: one is reflected off the target surface while the second is reflected off a reference mirror.¹⁹ The two reflected beams are recombined resulting in an interference pattern. Differences in the path length between the reference mirror and the target surface directly impact the interference pattern created which is measured by a CCD camera as the optics are scanned in the z-axis. This allows information on the topography of the surface with sub-nanometric resolution to be collected and analysed.¹⁹ In this work WLI was carried out using a Bruker ContourGT (Bruker Nano Inc., USA).

2.6.4 Atomic force microscopy

Atomic force microscopy (AFM) is an imaging technique capable of providing topographical information with nanometer resolution.²⁰ The principle is based on a very sharp tip or probe being scanned across a surface with the feedback from interaction forces between the tip and the surface being recorded in order to provide the topography of the surface. This is achieved by mounting the tip on a force sensitive cantilever which is deflected by attractive and repulsive forces generated between the tip and surface. Movement in the cantilever is detected with a laser focused onto the cantilever which then reflects the beam onto a photodiode detector. Movement in the cantilever is detected by the photodiode and used to provide a feedback mechanism whereby the sample is repositioned during scanning as to maintain a constant force between tip and sample. A schematic of an AFM system is shown in *Figure 0.11*.

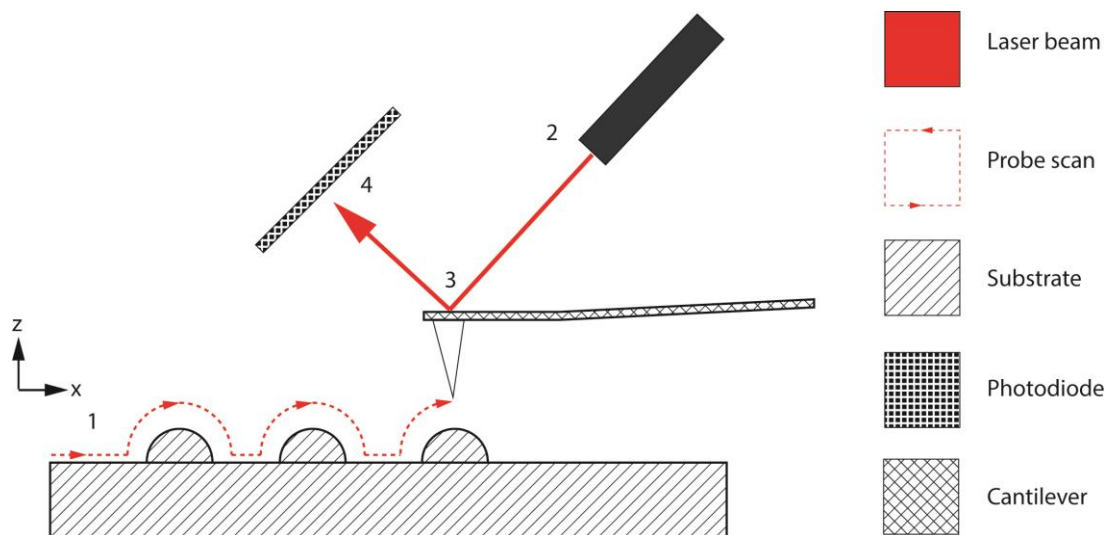


Figure 0.11: Schematic of an AFM system: (1) the probe is scan while (2) a laser beam is directed onto the cantilever (3), reflecting onto the (4) photodiode detector.

An AFM is commonly operated in one of two modes: (1) contact or (2) TappingMode™ (Veeco Instruments). The first mode simply maintains contact (at constant cantilever deflection) between tip and surface, dragging the probe over the sample as the surface is raster-scanned.²⁰ The movement of the probe is controlled by a piezoelectric scanner. In order to maintain contact with the sample surface, a feedback mechanism is used whereby the height of the tip relative to the sample surface is adjusted so that the force between the scanning tip and the sample is maintained constant. Under contact mode, the tip-sample distance is small enough that the net force seen between tip and sample is repulsive i.e. the sample pushing the tip away. The short-range decay of such repulsive forces gives contact mode a high level of sensitivity and so resolution, however, forces in lateral directions can be large which can distort soft samples and even damage the probe tips.

In the second mode, the tip is oscillated at the resonant frequency of the cantilever while being scanned across the surface. The oscillation amplitude of the cantilever is high enough that the tip makes an intermittent contact with the surface to sample short-range repulsive forces, allowing high resolution imaging of surface topography. Contact with the surface generates a dampening in the oscillation amplitude. This damping amplitude is used as a feedback mechanism whereby the

damping amplitude is kept constant in order to track the surface. Since the tip is in intermittent contact with the surface, there is little lateral tip-sample force which reduces deformation in soft samples.

The lateral resolution of an AFM is limited to the radius of curvature (R_a) of the tip apex and scan sizes are limited to the range of the lateral piezos positioning the sample, usually around $100\ \mu\text{m}^2$. Despite this, AFM offers highly accurate vertical measurements ($< \text{nm}$). AFM performed in this work was done on a Veeco EnviroScope AFM with a NanoScope IV controller using RFESP (Veeco) tapping mode tips ($R_a = 8\ \text{nm}$). AFM performed was limited to tapping mode only due to the sensitive nature of samples imaged i.e. nanoparticles.

2.7 References

1. A. J. Bard and L. R. Faulkner, *Electrochemical Methods: Fundamentals and Applications*, 2 edn., John Wiley & Sons, 2001.
2. T. M. Day, P. R. Unwin, N. R. Wilson and J. V. Macpherson, *Journal of the American Chemical Society*, 2005, **127**, 10639-10647.
3. C. G. J. Koopal, B. Eijssma and R. J. M. Nolte, *Synthetic Metals*, 1993, **57**, 3689-3695.
4. J. V. Macpherson and P. R. Unwin, *Analytical Chemistry*, 1997, **69**, 2063-2069.
5. C. J. Slevin, J. V. Macpherson and P. R. Unwin, *The Journal of Physical Chemistry B*, 1997, **101**, 10851-10859.
6. W. T. Silfvast, *Laser Fundamentals*, 2 edn., Cambridge University Press, 2004.
7. F. Marty, L. Rousseau, B. Saadany, B. Mercier, O. Français, Y. Mita and T. Bourouina, *Microelectronics Journal*, 2005, **36**, 673-677.
8. G. S. Oehrlein, *Materials Science and Engineering: B*, 1989, **4**, 441-450.
9. S. W. Pang, *Applications of Dry Etching to Microsensors, Field Emitters, and Optical Devices*, SPIE Optical Engineering Press, 1997.
10. F. A. Khan and I. Adesida, *Applied Physics Letters*, 1999, **75**, 2268-2270.
11. H. Jansen, H. Gardeniers, M. d. Boer, M. Elwenspoek and J. Fluitman, *Journal of Micromechanics and Microengineering*, 1996, **6**, 14.
12. G. S. Oehrlein, *Physics Today*, 1986, **39**, 26.
13. G. C. Schwartz and P. M. Schaible, *Journal of Vacuum Science & Technology*, 1979, **16**, 410-413.
14. I. Yagi, H. Notsu, T. Kondo, D. A. Tryk and A. Fujishima, *Journal of Electroanalytical Chemistry*, 1999, **473**, 173-178.
15. T. Tachibana, B. E. Williams and J. T. Glass, *Physical Review B*, 1992, **45**, 11975-11981.
16. P. Vandenabeele, *Practical Raman Spectroscopy - An Introduction*, John Wiley & Sons, Ltd, 2013.
17. D. S. Knight and W. B. White, *Journal of Materials Research*, 1989, **4**, 385-393.
18. J. W. Ager, W. Walukiewicz, M. McCluskey, M. A. Plano and M. I. Landstrass, *Applied Physics Letters*, 1995, **66**, 616-618.
19. C. O'Mahony, M. Hill, M. Brunet, R. Duane and A. Mathewson, *Measurement Science and Technology*, 2003, **14**, 1807.
20. G. Binnig, C. F. Quate and C. Gerber, *Physical Review Letters*, 1986, **56**, 930-933.

Chapter 3: Detection of hydrazine using metal-nanoparticle functionalised pBDD electrodes

Electrochemical detection of the genotoxic impurity hydrazine (HZ) is demonstrated, in the presence of two important electrochemically active pharmaceutical ingredients (APIs), acetaminophen and promazine, present in excess. Importantly, it is shown that by using metal nanoparticle (NP) functionalised polycrystalline boron-doped diamond (BDD) electrodes it is possible to selectively screen out different API electrochemical interferants simply by changing the chemical identity of the metal NPs on the BDD electrode. HZ detection limits of 11.1 μM and 3.3 μM HZ in the presence of excess acetaminophen and promazine, respectively, were determined in quiescent solutions.

3.1 Introduction

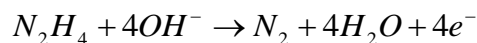
Genotoxic impurities (GI) are compounds which modify DNA and are therefore harmful to human health¹. A variety of chemicals exhibit genotoxic activity and are classified according to key functional groups, resulting in a list of structural alerts². In a pharmaceutical process GIs can be starting materials, intermediates, reaction bi-products or degradation products from the active pharmaceutical ingredient (API). The threshold of toxicological concern³ represents the safe exposure level to GIs, stipulating an intake limit of 1.5 $\mu\text{g/day}$, equating to low parts per million relative to the API.

An important GI in the pharmaceutical industry is the carcinogenic and mutagenic⁴ compound HZ.⁵ HZ is also of great interest due to its use in fuel cells,⁶ and as a chemical reducing agent⁷. Industrially, a variety of techniques are employed to detect HZ in the presence of the API.^{8, 9} For example, gas chromatography-mass spectrometry,¹⁰ ion chromatography¹¹ and high pressure liquid chromatography.¹² Derivatization is also often used to enhance the detection sensitivity of HZ.¹³ Unfortunately, most of these techniques are time consuming and labour intensive, resulting in significant drug development costs in terms of staff resource and instrument utilization.³ Hence new approaches are required that are simple and robust and do not require high levels of expertise.

Electrochemical techniques fall into this category and simply require the GI of interest to possess an electrochemical signature. However, the situation is complicated if the API is also electrochemically active in the same potential region as the GI. HZ has previously been detected in the presence of pharmaceutical substances via capillary electrophoresis.¹⁴ HZ can be electrochemically oxidised in solution and shows an electrochemical signature strongly dependant on the chemical identity and crystallographic orientation of the metal electrode, given its inner sphere nature.^{15, 16} Typically gold (Au) or platinum (Pt) electrodes have been used to detect HZ in aqueous solutions. HZ has also been detected electrochemically in non-aqueous solvents, although this is much less common.¹⁷⁻¹⁹ The rate determining step for oxidation of HZ on Au and Pt electrodes is thought to differ due to the different HZ-metal bond overlap and d-orbital filling between the two metals.^{20, 21}

As a way to increase detection limits and reduce material costs, metal nanoparticle (NP) functionalised electrodes are often employed.²²⁻²⁴ The ideal support electrode is one that serves only to provide electrical contact to the metal NP and is itself electrochemically inactive towards the species of interest. Boron doped diamond (BDD) is ideal for this purpose given its electrocatalytically inactive sp^3 terminated surface, wide potential window, low background currents and high resistance to fouling.²⁵ HZ detection has been previously demonstrated on both bare BDD^{26, 27} and NP functionalised BDD,^{28, 29} although electron transfer is kinetically hindered on the bare electrode. Work here describes the use of highly-doped “metal-like” polycrystalline BDD macrodisk electrodes (pBDD), functionalised with different metal electrodeposited NPs for the detection of HZ in aqueous solution (pH 7.2) in the presence of two important APIs (in excess); acetaminophen (ACM, paracetamol) and promazine (PZ, sparine), which both show interfering electrochemical signatures. ACM is a common analgesic drug electrochemically oxidised in aqueous solution (pH ~7) via a two-electron transfer mechanism.³⁰ Electrochemical detection of ACM has also been demonstrated in pharmaceutical mixtures via differential pulse voltammetry (DPV)³¹ and square-wave voltammetry on a pBDD electrode.³² PZ is an antipsychotic drug used to treat schizophrenia or to induce spinal anaesthesia.³³ Whilst PZ has been studied by cyclic voltammetry,³⁴ potentiometric titration³⁵ and differential-pulse polarography,³⁶ its electrochemical oxidation mechanism is still not fully understood.

The electrooxidation of HZ in aqueous solution is described in equation 0.1.³⁷ It is a 4-electron transfer process which can be further split into a two-step 2-electron mechanism where the first step is rate determining. This is followed by dimerisation of N_2H_2 and decomposition of dimer at the electrode surface.³⁸



0.1

3.2 Experimental

3.2.1 Reagents & materials

Chemical vapour deposited, high quality, free-standing pBDD³⁹, polished to ~ nm surface roughness was supplied by Element Six (DIAFILM EA grade, E6 Ltd., Oxford, UK), with an average boron density of 3×10^{20} atoms cm^{-3} . Potassium hexachloroplatinate(IV), potassium gold (III) chloride, sodium perchlorate monohydrate, phosphate buffer solution (PBS), hydrazine sulphate, promazine hydrochloride and acetaminophen were purchased from Sigma-Aldrich (USA). All analytical solutions were prepared in pH 7.2 PBS, unless otherwise stated, using distilled water (Milli-Q, Millipore, 18.2 M Ω resistivity).

3.2.2 Apparatus

All voltammetric measurements were conducted in a three electrode setup, with a Pt counter electrode and a saturated calomel reference electrode (SCE). All peak potentials are reported versus SCE. A potentiostat (CHI730A, CH Instruments Inc., TX.) connected to a desktop PC was used to run all experiments.

3.2.3 Preparation and characterisation of electrodes

1 mm diameter macro disk pBDD electrodes were fabricated using a procedure described by Hutton *et al.*²⁵ Pt NPs were electrodeposited on pBDD by holding the electrode at – 1 V for 5 s, in a solution containing 1 mM potassium hexachloroplatinate(IV) in 0.1 M HCl, as previously described²⁵. Au NPs were electrodeposited from a solution of 1 mM potassium gold (III) chloride and 0.2 M sodium

perchlorate monohydrate by holding the pBDD electrode at -0.9 V for 2 s. Deposition conditions were chosen to ensure a high density of small NPs. NP electrodeposition was characterised via tapping-mode atomic force microscopy (AFM), as shown in *Figure 0.1*. The heights of the NPs are in the range 10 - 40 nm for Au and 10 - 30 nm for Pt. The diffusion coefficients of all species were determined from the steady-state current recorded at a 25 μm diameter Pt disk ultramicroelectrode.

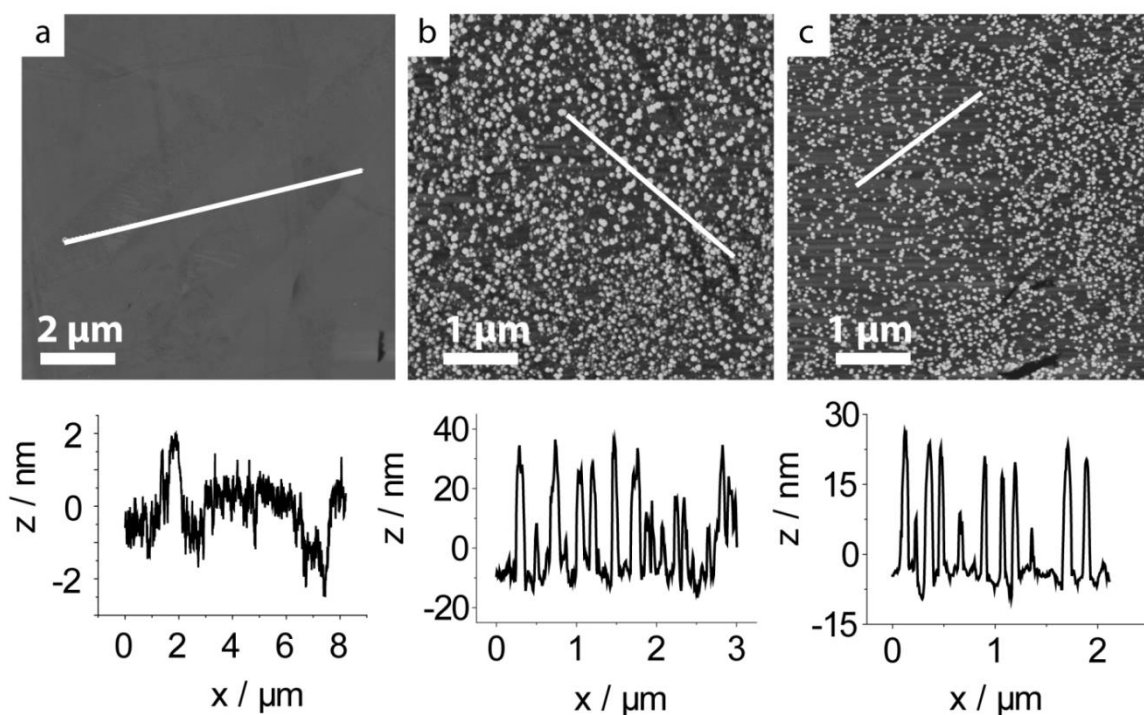


Figure 0.1: Tapping mode AFM images of (a) bare pBDD; (b) electrodeposited Au NP-pBDD and (c) electrodeposited Pt NP-pBDD electrodes with cross sectional height analysis of the three different surfaces in the zones indicated by the white lines

Linear sweep voltammetry (LSV) was typically conducted at a scan rate of 0.1 Vs^{-1} . DPV was executed with the following settings; 5 mV incremental potential, 50 mV amplitude, 0.2 s pulse width and 0.4 s pulse period.

3.3 Results and Discussion

3.3.1 Hydrazine Voltammetry

Initial studies focused on investigating HZ oxidation on different electrodes. *Figure 0.2* shows the LSV characteristics of HZ on bare pBDD (—), Pt NP-pBDD (---) and Au NP-pBDD (....) macrodisk

electrodes in 0.1 M PBS. The HZ oxidation peak occurs at significantly lower overpotentials on the metal NP functionalised pBDD (Pt -0.36 V, Au +0.29 V) electrodes than on bare pBDD (+1.5 V) due to the metal NPs catalysing HZ electro-oxidation.⁴⁰

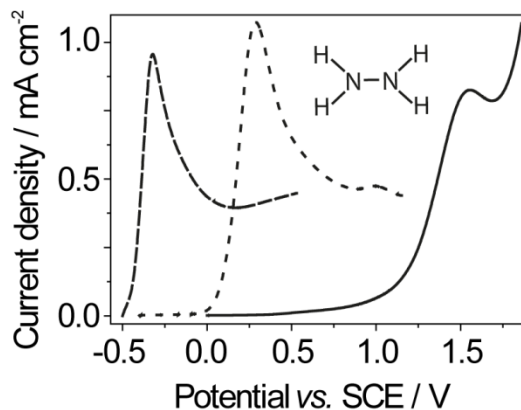


Figure 0.2: LSVs of 1 mM HZ oxidation on (---) Pt NP-pBDD, (···) Au NP-pBDD and (—) bare pBDD, in 0.1 M PBS, recorded at a potential scan rate of 0.1 V s⁻¹.

The difference in HZ peak position for Au and Pt can be attributed to the different oxidation mechanisms on the two metals.^{40, 41} HZ detection was further investigated using both LSV and DPV over the concentration range 10 – 1000 μ M at an Au NP-pBDD electrode, as shown in *Figure 0.3a* and *Figure 0.3b* respectively. The peak current in (LSV) and peak area (DPV) both scale with HZ concentration in a linear fashion, as shown in *Figure 0.3c* and *d* respectively. In LSV over the concentration range 10 - 1000 μ M, the gradient was $8.3 \times 10^{-3} (\pm 0.13 \times 10^{-3}) \mu\text{A } \mu\text{M}^{-1}$ with an R^2 of 0.999 ($n = 5$). For DPV, over the same concentration range, the gradient was $2.63 \times 10^{-2} (\pm 0.086 \times 10^{-2}) \mu\text{C } \mu\text{M}^{-1}$ with an R^2 of 0.997 ($n = 5$).

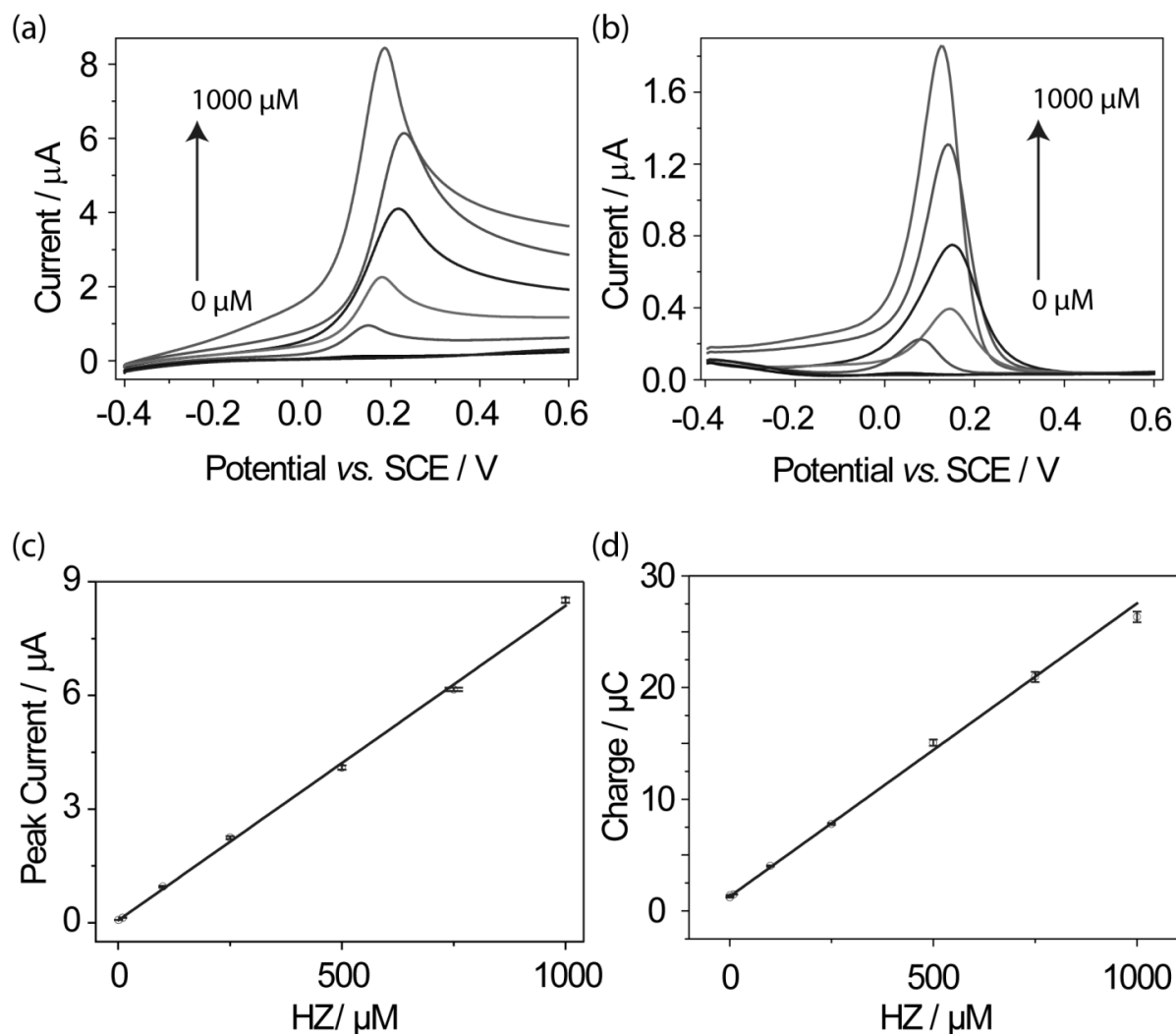


Figure 0.3: HZ oxidation on an Au NP-pBDD electrode using (a) LSV and (b) DPV, with the corresponding graphs of peak current (LSV, c) or peak area (DPV, d) versus concentration. HZ concentrations 0, 10, 100, 250, 500, 750 and 1000 μM HZ ($n = 5$).

The limit of detection (LOD) is the concentration at which a signal is significantly different from the background response, it is often expressed as:⁴²

$$LOD = \mu_b + 3\sigma_b$$

0.2

where μ_b and σ_b are the mean and standard deviation of the background response. The mean background response and the standard deviation are taken from the current at the peak potential over several LSVs in the absence of HZ ($n = 5$). This results in an LOD value for LSV detection of HZ at an Au NP-pBDD electrode of $1.32 \pm 0.02 \mu\text{M}$. In the case of DPV, the mean background response is taken as the y-intercept of the LOD plot (Figure 0.3d) and the standard deviation is calculated from

the variation in the area of several DPVs in the absence of HZ. This results in an LOD for DPV detection of HZ at an Au NP-pBDD electrode of $0.67 \pm 0.03 \mu\text{M}$. The lower LOD for DPV is attributed to the subtraction of background capacitive current contributions present in LSV, during the differential pulse. Thus we focus further quantitative detection studies on DPV because it also provides the best method to both distinguish between two or more mediators and aid quantitative analysis of mixtures.⁴³

3.3.2 Acetaminophen voltammetry

Figure 0.4 shows the (a) LSV and (b) DPV response of the API, ACM, in PBS solution at an Au NP-pBDD electrode. The LSV and DPV peak positions for ACM oxidation are +0.51 V and +0.42 V, respectively. This data indicates that resolution of both ACM (API) and HZ (GI) (Figure 0.3b) DPV peaks should be possible using an AuNP-pBDD electrode, when both are present in solution. Note the area under the DPV peak for 1 mM ACM (18.8 μC) is lower than that for HZ (28.4 μC), by a factor of ~ 1.5 . This is due to ACM oxidation being a two electron process³⁰ compared to a four electron process for HZ³⁷. The diffusion coefficients, D , for HZ and ACM were measured to be $1.19 \times 10^{-5} \text{ cm}^2 \text{ s}^{-1}$ and $4.12 \times 10^{-6} \text{ cm}^2 \text{ s}^{-1}$ respectively, comparing favourably to literature values.^{41, 44}

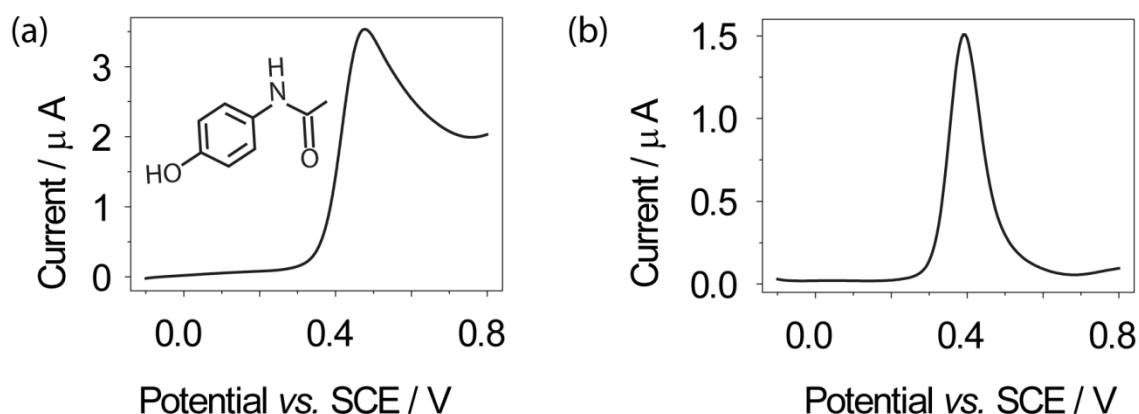


Figure 0.4: ACM oxidation on an Au NP-pBDD electrode in a solution containing 1 mM ACM in 0.1 M PBS, using (a) LSV and (b) DPV.

Figure 0.5a shows the resulting DPV response, recorded at an Au NP-pBDD electrode in a pH 7.2 PBS solution, containing 1 mM ACM and varying concentrations of HZ (10 - 1000 μM). DPV is able

to clearly resolve both the ACM peak and the concentration-varying HZ peaks. Although the DPV peak for the fixed concentration of ACM shifts slightly in peak potential (+0.38 to +0.41 V) with HZ concentration, the area of the peak remains approximately constant ($20.2 \pm 0.6 \mu\text{C}$). Importantly, for a fixed excess concentration of ACM, the area under the HZ DPV peaks varies in a linear fashion with concentration, making electrochemical quantification possible. Over the concentration range 10 - 1000 μM , the slope of the graph is $3.40 \times 10^{-2} \mu\text{C mM}^{-1}$, with an R^2 value of 0.998 ($n = 5$). In the presence of 1 mM ACM, the LOD for HZ is determined as $11.10 \pm 0.02 \mu\text{M}$. This value is larger than that obtained for HZ in the absence of ACM, possibly due to the increased background signal as a result of having the electroactive API present in solution.

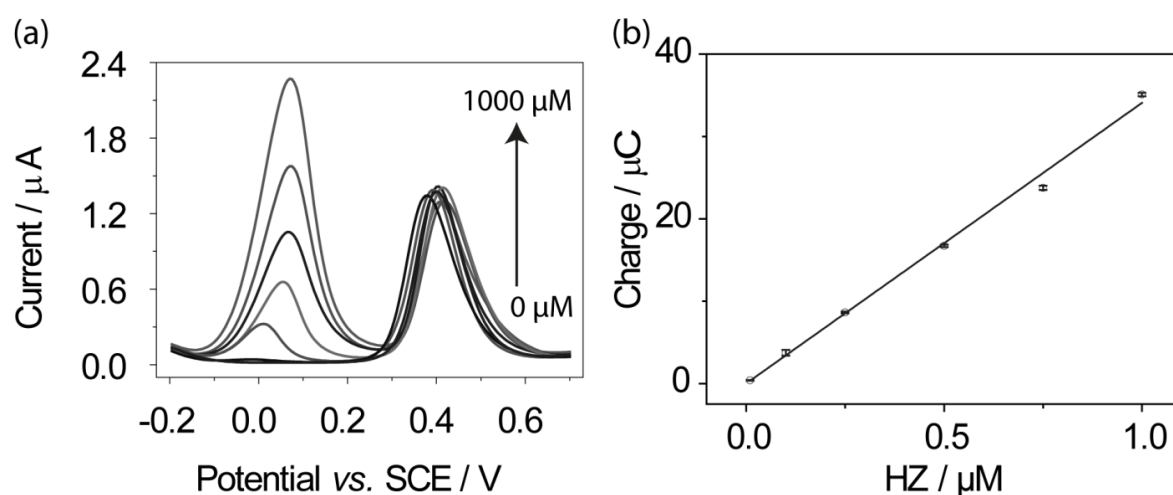


Figure 0.5: (a) DPV of varying concentrations of HZ in the presence of 1 mM ACM at an AuNP-pBDD electrode with 0, 10, 100, 250, 500, 750 and 1000 μM HZ. (b) Plot of HZ DPV peak areas versus concentration ($n = 5$).

3.3.3 Promazine voltammetry

PZ is another important electrochemically active API. Figure 0.6 shows the (a) LSV and (b) DPV signatures for the oxidation of 1 mM PZ at both a bare pBDD (—) and an Au NP-pBDD electrode (- - -). A slightly higher peak current is observed via LSV on Au NP-pBDD than bare pBDD, likely due to the greater background capacitive currents resulting from the presence of the Au NPs. Reduction of the background contributions via DPV results in the DPV response for both the bare pBDD and Au

NP functionalised pBDD being similar, peaking in current at 0.5 V. As this value is more positive than that of ACM it suggests both species should be resolvable using an AuNP-pBDD electrode.

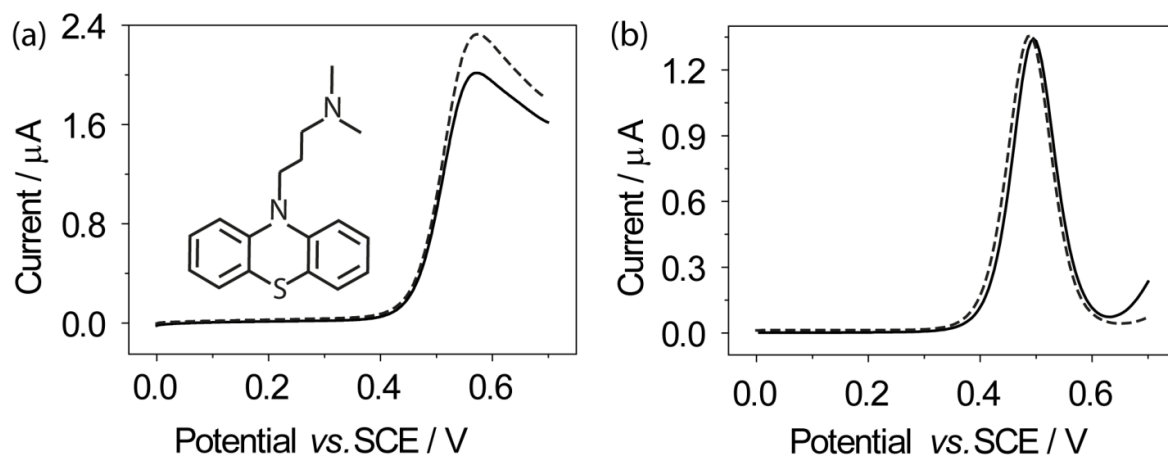


Figure 0.6: PZ oxidation in a solution containing 1 mM PZ in 0.1 M PBS, at a bare pBDD (—) and an Au NP-pBDD electrode (- - -) using (a) LSV and (b) DPV

Moreover, the fact that the PZ DPV peak position does not change with the chemical identity of the electrode, in stark contrast to that observed for HZ (Figure 0.2) on pBDD and Au, suggests that PZ oxidation occurs through an outer sphere ET process, which is surface insensitive.

The DPV response for 1 mM PZ in the presence of varying concentrations of HZ (10 – 1000 μM) is shown in Figure 0.7.

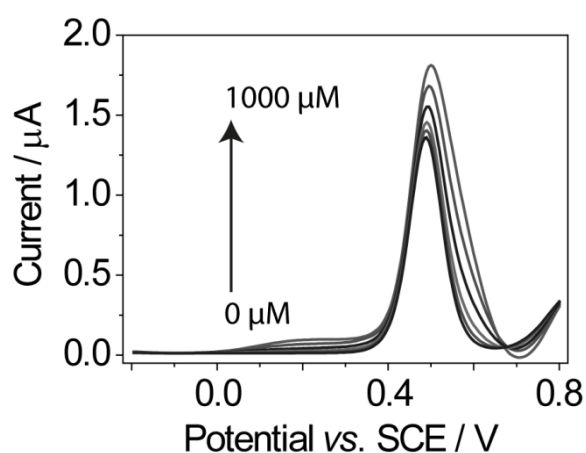


Figure 0.7: DPV of varying concentrations of HZ in the presence of 1 mM PZ, at an AuNP-pBDD electrode with 0, 10, 100, 250, 500, 750 and 1000 μM HZ.

In contrast to HZ detection in the presence of ACM (*Figure 0.5*), it is no longer possible to resolve two distinct DPV peaks associated with the API and HZ. Instead there is one dominant peak (+0.5 V), occurring in the same position as expected for PZ, with a small shoulder at a less positive potential (+0.2 V). With increasing HZ concentration, both the dominant peak and small shoulder only increase slightly in magnitude. This suggests that in the presence of PZ, at an Au NP-pBDD electrode, HZ oxidation is either being retarded, or becoming less kinetically facile, and shifting to more positive potentials, such that the HZ oxidation peak overlaps with that for PZ. However, even if the latter were true, the increase in current would be expected to be much greater than observed. A full explanation of this phenomenon is beyond the scope of this study and work is currently on-going to investigate the mechanistic interaction of PZ with HZ, in the presence of Au. Clearly, HZ and PZ cannot be independently resolved via this approach and quantification of HZ concentrations is thus not possible. As shown in *Figure 0.2*, HZ oxidation occurs at a significantly more negative potential on Pt than on Au. Thus switching metal NP identity may offer a route to separating out the electrochemical signatures of HZ and PZ oxidation. *Figure 0.8a* shows the DPV response for the detection of HZ in the concentration range 10 – 1000 μM , in the presence of 1 mM PZ at a PtNP-pBDD electrode. Two peaks are now clearly identifiable. The PZ DPV peak position is at ~ 0.5 V in accordance with the observation that PZ electron transfer is occurring independently of the chemical identity of the surface.

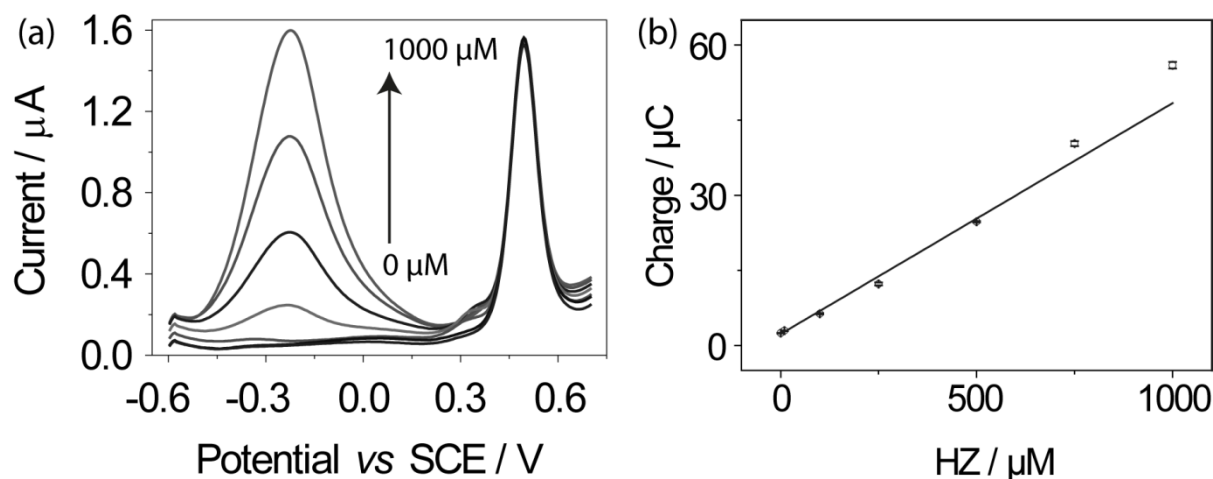


Figure 0.8: (a) DPV of varying concentrations of HZ in the presence of 1 mM PZ, at a PtNP-pBDD electrode with 0, 10, 100, 250, 500, 750 and 1000 μM HZ. (b) Plot of HZ DPV peak areas versus HZ concentration ($n = 5$).

The DPV peak corresponding to HZ oxidation is now seen at -0.25 V, which represents a positive shift of ca. +0.25 V, compared to a HZ only solution, again indicating possible interactions between the PZ and HZ. The area of the 1 mM PZ peak ($\sim 21.7 \mu\text{C}$) is smaller than that of the HZ peak ($56.4 \mu\text{C}$) by a factor of 2.6, which is reasonable given literature assumes a two electron transfer process.⁴⁵

⁴⁶ A D for PZ was determined to be $2.65 \times 10^{-6} \text{ cm}^2 \text{ s}^{-1}$ assuming a two electron process, which is similar to reported values.⁴⁷ However, as with HZ detection, importantly in the presence of ACM the area of the HZ DPV peak (ca - 0.25 V) scales linearly with concentration in the presence of PZ, as shown in Figure 0.8b, with a sensitivity of $4.61 \times 10^{-2} \mu\text{C mM}^{-1}$ and R^2 of 0.991 ($n = 5$). In the presence of 1 mM PZ, the LOD for HZ is calculated as $3.27 \pm 0.04 \mu\text{M}$. Work is currently on-going to significantly lower these reported LODs, in the presence of the API, by moving from quiescent solutions to convective diffusion hydrodynamic flow systems.⁴⁸

3.3.4 Detection of hydrazine with AuNP-p-BDD macroelectrodes in non-aqueous solvents

The aim of the study is to establish a proof-of-concept with the intention of future application of the sensor technology to real-life situations e.g. PGI analysis in pharmaceutical products. Since many

pharmaceutical products are sparingly if at all soluble in aqueous solvents, it is important to also demonstrate the detection of HZ in non-aqueous medium.

Two organic solvents routinely used in industry for the preparation and analysis of pharmaceutical products were chosen for investigation. These include acetonitrile (MeCN) and dimethyl sulfoxide (DMSO). Tetrabutylammonium hexafluorophosphate (TBAHFP), an inert salt was chosen as electrolyte for both of these solvents.

3.3.4.1 Detection of hydrazine in acetonitrile

The CV of HZ oxidation at an AuNP-p-BDD macroelectrode in MeCN is shown in *Figure 0.9a*. The oxidation peak appears at a similar potential in MeCN as it does in aqueous solution i.e. $\sim +0.1$ V to $+0.4$ V vs. SCE. Detection limits for HZ in MeCN with AuNP-p-BDD were calculated using the method outlined in section 3.3.1 from the plot in *Figure 0.9b*. For HZ detection in MeCN $\text{LOD} = 2 \pm 0.02 \mu\text{M}$ ($R^2 = 0.993$) was determined.

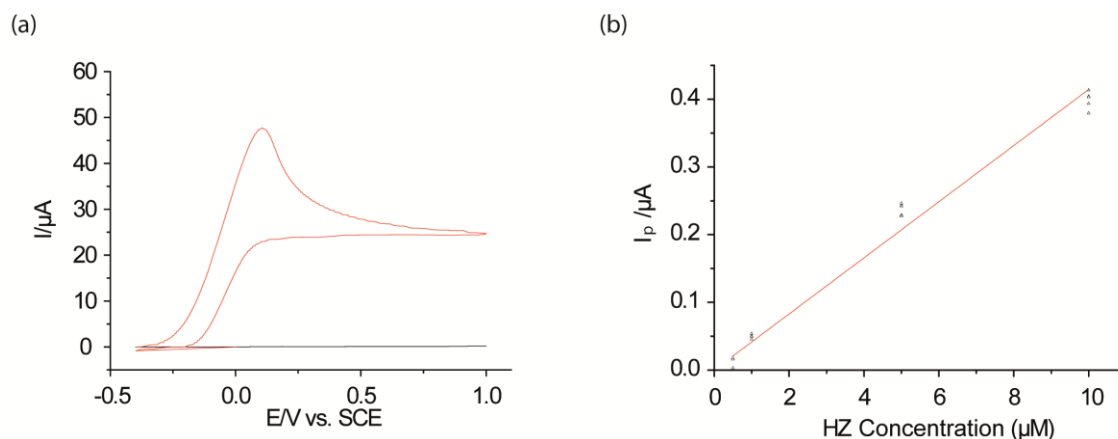


Figure 0.9: (a) CV response for (red) 1 mM HZ in MeCN with 0.1 M TBAHFP and (black) 0.1 M TBAHFP in MeCN, scan rate of 0.1 V s^{-1} ; (b) plot of i_p vs. HZ concentration for a concentration range of $0.5 - 10 \mu\text{M}$ HZ ($n = 5$).

The HZ oxidation mechanism in MeCN has been reported as follows:^{49, 50}



0.3

Here HZ undergoes a 2-electron oxidation. This incomplete oxidation (compared with in aqueous where just N_2 and H_2O are produced; see equation 0.1) is a result of the stability of $HN=NH$ in non-aqueous solutions. Furthermore, only one third of the available HZ is oxidised in this way at the electrode surface. The oxidation mechanism requires a proton acceptor species (in this case N_2H_4) to form two equivalence of $N_2H_5^+$ ions (which cannot be oxidised) for every molecule of HZ oxidised. As a result, the number of electrons in the overall process per HZ molecule is just a third of two.⁴⁹

3.3.4.2 Detection of hydrazine in DMSO

An oxidative peak corresponding to that of HZ was observed ca. +0.31 V at an AuNP-p-BDD electrode with DMSO as the solvent (see *Figure 0.10a*). The detection limits of HZ on an AuNP-p-BDD electrode in DMSO were calculated using the i_{lim} vs. HZ concentration plot shown in *Figure 0.10b*. LOD = $2 \pm 0.06 \mu M$ ($R^2 = 0.999$) was determined.

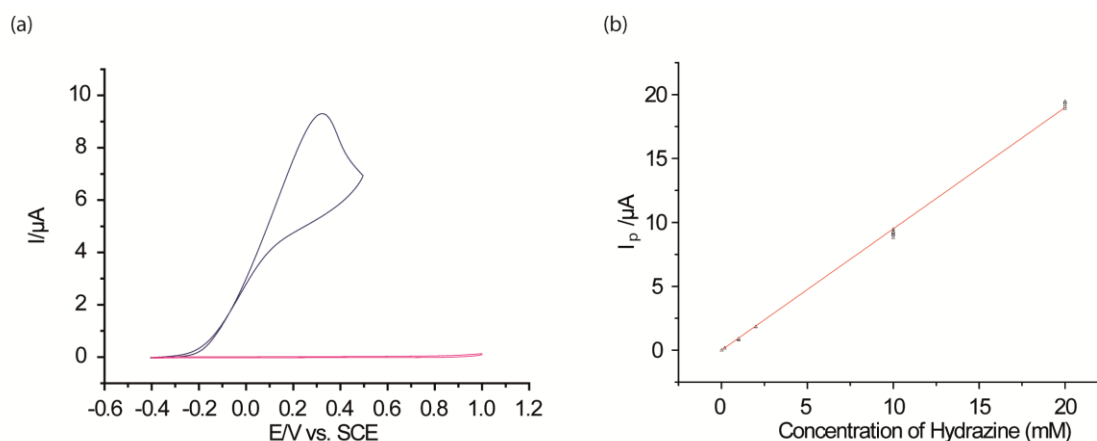
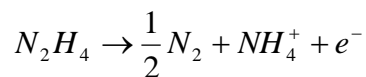


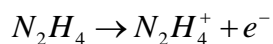
Figure 0.10: (a) CV response for (black) 10 mM HZ in DMSO with 0.1 M TBAHFP and (pink) a solution of just 0.1 M TBAHFP, scan rate of $0.1 V s^{-1}$; (b) plot of i_p vs. HZ concentration for solutions of concentrations ranging from 0.01 – 20 mM HZ ($n = 5$).

Work investigating the oxidation mechanism of HZ in aprotic solvents such as DMSO, suggest that HZ undergoes a one-electron oxidation process:⁵¹

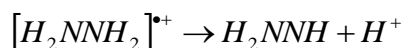


0.4

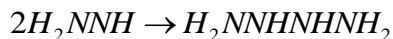
This same mechanism has also been suggested for the oxidation of HZ in aqueous solutions.⁵² Michlmayr et al⁵¹ described a break-down of this proposed mechanism (equations 0.6-0.9) based on the rate determining step being a one-electron transfer process producing a HZ radical ion (equation 0.6). Formation of a HZ radical ion during HZ oxidation is supported by the study of the reaction with electron paramagnetic resonance spectroscopy.⁵³



0.5



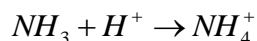
0.6



0.7



0.8



0.9

3.3.5 Detection of hydrazine derivatives in acetonitrile with an AuNP-p-BDD macroelectrode

Using an AuNP-pBDD electrode, the possibility of electrochemically detecting derivatives of HZ was also explored. 1 mM solutions of three HZ derivatives: 4-(trifluoromethyl)-phenylhydrazine, 2-hydroxyethylhydrazine and phenylhydrazine, were prepared in MeCN solvent and 0.1 M TBAHFP as electrolyte; molecular structures of the three derivatives are shown in *Figure 0.11*.

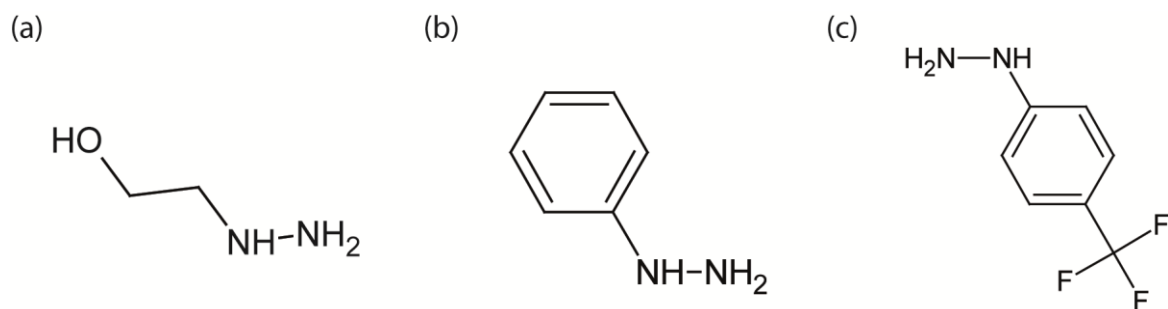


Figure 0.11: Molecular structures of (a) 2-hydroxyethylhydrazine, (b) phenylhydrazine, (c) 4-(trifluoromethyl)-phenylhydrazine.

The oxidation response for each derivative is shown in Figure 0.12a, with oxidation potentials of ca. 0.1 V, 0.3 V and 0.55 V vs. SCE observed for 2-hydroxyethylhydrazine (black line), phenylhydrazine (blue line) and 4-(trifluoromethyl)-phenylhydrazine (red dotted) respectively.

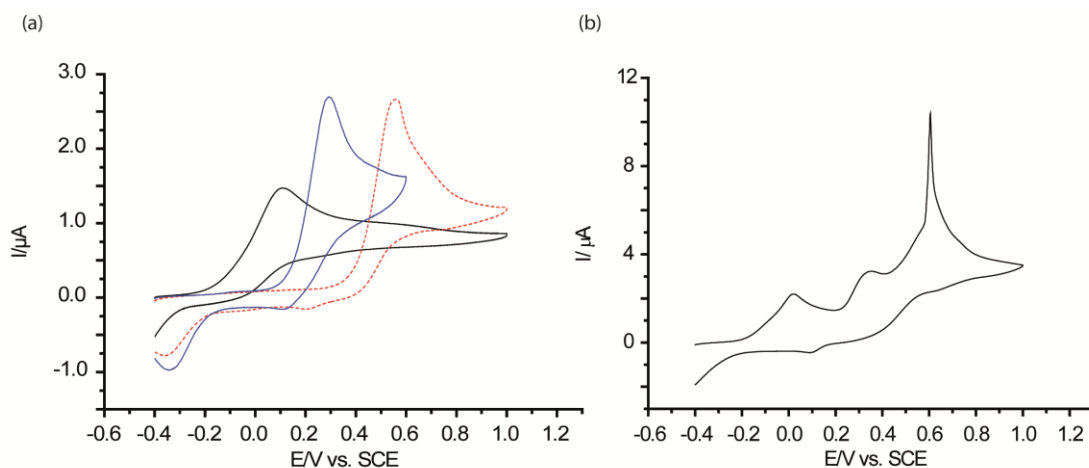
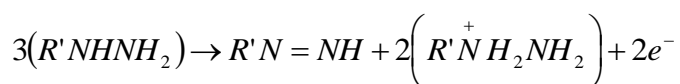


Figure 0.12: (a) CVs of acetonitrile solutions containing 1 mM: 2-hydroxyethylhydrazine (black), phenylhydrazine (blue) and 4-(trifluoromethyl)-phenylhydrazine (red dotted), all with TBAHFP as supporting electrolyte; (b) CV of acetonitrile solutions containing all three HZ derivatives at 1 mM concentrations of each.

The mechanism for the oxidation of HZ derivatives in acetonitrile is analogous to that described in equation 0.3, as follows:⁵⁴



0.10

where R' represents the derivative group e.g. hydroxyethyl ($-\text{CH}_2\text{CH}_2\text{OH}$).

The difference in oxidation potential observed between the different HZ derivatives represents a difference in energy required to drive the oxidation. From the CVs in *Figure 0.12a*, the order of oxidation potential, lowest to highest is 2-hydroxyethylhydrazine, phenylhydrazine and 4-(trifluoromethyl)-phenylhydrazine. This difference in oxidation energy may be a product of the ability of the HZ derivatives to act as proton acceptors i.e. their basicity. The electron withdrawing groups found in phenylhydrazine and 4-(trifluoromethyl)-phenylhydrazine make these compounds less basic⁵⁵ than 2-hydroxyethylhydrazine and so do not undergo protonation as readily. This would increase the energy barrier for oxidation as the protonation of two molarities of derivative are required in the electro-oxidation mechanism; see equation 0.10.

A single solution containing all three HZ derivatives at 1 mM concentration with 0.1 M TBAHFP was prepared. The response of this solution is shown in *Figure 0.12b*, again showing distinct oxidation peaks for each of the three derivatives. The current responses for the 2-hydroxyethylhydrazine and phenylhydrazine derivatives are comparable with that seen for the same concentration in solution not including the other two derivatives. At potentials more positive of 0.4 V, where oxidation peak for 4-(trifluoromethyl)-phenylhydrazine is expected, the current response wave begins in a diffusion controlled manner but is distorted by the appearance of a sharp secondary peak at ca. 0.6 V. This second, sharp peak is of a current magnitude far higher than that expected for a 1 mM concentration of 4-(trifluoromethyl)-phenylhydrazine (as observed in *Figure 0.12a*), and could indicate a more complex reaction with possible interactions between the generated species and reactant species/the electrode. Further work is required to establish whether this is the case.

3.3.6 Detection of hydrazine in polymer degradation

Methacryloyl hydrazide (MH) is a hydrazide functional monomer (see *Figure 0.13a*) that can be incorporated into copolymers as a method of controlling the solubility of microgel dispersions in water.⁵⁶ It is known that hydrazides undergo hydrolysis in aqueous solution, releasing HZ.⁵⁷ The polymerised MH (*Figure 0.13b*) was suspected to undergo hydrolysis in much the same way, as shown by the schematic in *Figure 0.13c*.

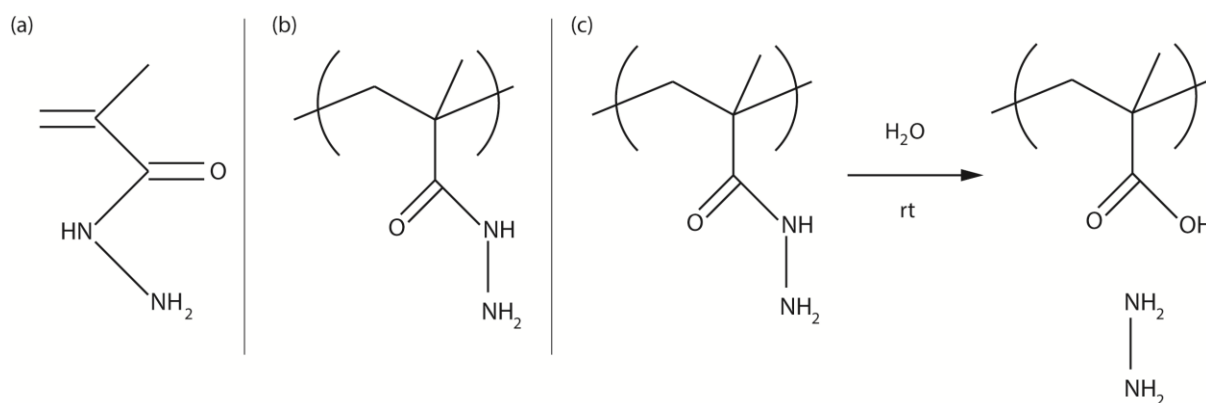


Figure 0.13: Molecular structures of (a) Methacryloyl Hydrazide monomer and (b) poly(methacryloyl hydrazide); (c) schematic of the hydrolysis of poly(methacryloyl hydrazide, producing HZ.

MH monomer synthesis and polymerisation were conducted by Y.Chen et al.⁵⁶

In order to track the release of HZ in a solution of dissolved poly-(MH) in 0.1 M PBS over time, a PtNP-pBDD electrode was employed to electrochemically detect HZ. The electroactivity of the MH monomer and polymer were assessed using CVs shown in *Figure 0.14a*. Here CV responses are shown for solutions of 0.015 % (w/w) MH polymer with 1 mM MH monomer and 0.3 mM HZ (black); 1 mM MH monomer (red); 0.015 % (w/w) MH polymer with 0.85 mM HZ (blue); 0.015 % (w/w) MH polymer (pink), all solutions in 0.1 M PBS. It is clear from electroanalysis that the polymer is not electroactive. However, the MH monomer is, showing an oxidation peak at ca. 0.5 V vs. SCE. The oxidation peak for the monomer is sufficiently higher in potential than that of HZ, making it possible to simultaneously detect both MH and HZ in the presence of the polymer. A solution of 0.15 % (w/w) MH polymer was filtered using dialysis to remove the MH monomer from solution. The resulting solution was diluted by a factor of 10 in 0.1 M PBS and kept away from exposure to light. A

series of CVs were run using a PtNP-pBDD electrode over a time period of 408 hrs (*Figure 0.14b*), with recordings being made at 24 hrs (black line), 168 hrs (red line), 336 hrs (blue line) and 408 hrs (pink line). A plot of i_p vs. time is presented in *Figure 0.14c* with a linear fit found ($R^2 = 0.999$) indicating the release of HZ with time.

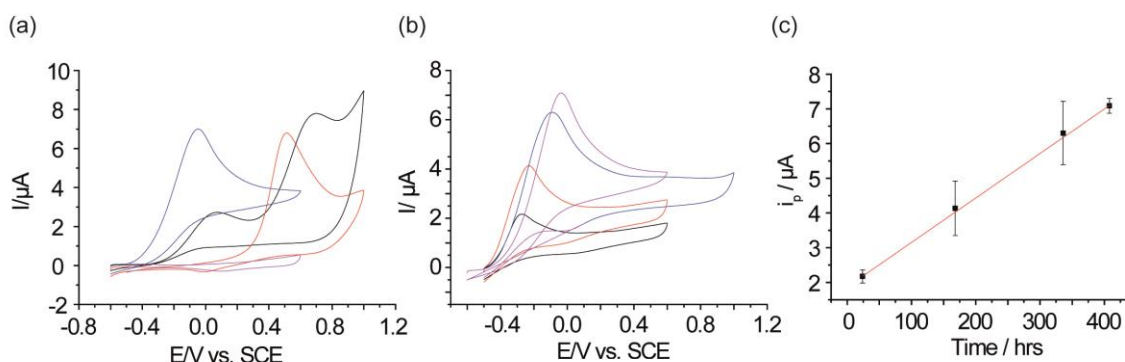


Figure 0.14: (a) CV responses for solutions of 0.015 % (w/w) MH polymer with 1 mM MH monomer and 0.3 mM HZ (black); 1 mM MH monomer (red); 0.015 % (w/w) MH polymer with 0.85 mM HZ (blue); back ground response of 0.015 % (w/w) MH polymer (pink), all solutions in 0.1 M PBS, scan rate of 0.1 V s^{-1} . (b) CVs for PtNP=pBDD electrode in solution of 0.015 % (w/w) MH polymer with 24 hrs (black), 168 hrs (red), 336 hrs (blue) and 408 hrs (pink scan rate of 0.1 V s^{-1}). (c) plot of i_p vs. time for HZ detection in polymer solution with time ($n = 5$).

Using a calibration plot of i_p as a function of HZ concentration, the concentration of HZ released by the gradual hydrolysis of the MH polymer was calculated to be $0.8 \pm 0.096 \text{ mM}$ with the release rate of HZ being determined as $0.0012 \text{ mM per hour}$.

3.4 Conclusions

This work has demonstrated electrochemical detection of the GI, HZ, in the presence of two electrochemically active APIs. For the case of HZ detection in the presence of excess ACM (1 mM), Au NP-pBDD macrodisk electrodes were found to be suitable enabling a LOD for HZ of $11.10 \pm 0.02 \mu\text{M}$ using DPV in stationary solution. However, in the presence of PZ the Au NP-pBDD electrode was not able to sufficiently resolve the DPV peaks for both the GI and the API. As HZ oxidation is

surface sensitive, this problem was solved by changing the chemical identity of the metal catalyst from Au to Pt, the latter which oxidises HZ at more negative potentials. Under these conditions, a LOD of $3.27 \pm 0.04 \mu\text{M}$ for HZ in the presence of excess PZ (1 mM) was obtained.

HZ detection in non-aqueous solvents, relevant to pharmaceutical synthesis has also been demonstrated with LOD = $2 \pm 0.02 \mu\text{M}$ and $2 \pm 0.06 \mu\text{M}$ determined for acetonitrile and DMSO, respectively, comparable to those found for aqueous systems.

The electrochemical detection of HZ derivatives 4-(trifluoromethyl)-phenylhydrazine, 2-hydroxyethylhydrazine and phenylhydrazine at an AuNP-pBDD electrode in acetonitrile solution are also presented. This data demonstrates the potential for electrochemical analyses as a means of distinguishing similar electroactive species, by virtue of their characteristic oxidation potentials. However, potential interaction problems were highlighted with all three species in the same solution.

Lastly, the release of HZ by the natural hydrolysis of hydrazide-based microgels in aqueous solutions has been monitored using a PtNP-pBDD electrode and a simple CV technique. From analysis of this data, the amount of HZ released by the polymer solution could be determined. This simple electrochemical technique is highly advantageous compared with conventional methods such as HPLC which would require pre-treatment of the analyte solution, for example, derivatisation of HZ with benzaldehyde is necessary as HZ does not have a useful UV-visible absorption spectrum for conventional UV-Visible detection.⁵⁸ This derivatisation step may require the removal of the polymer in solution as this could also undergo derivatisation.

Compared to conventional techniques for HZ detection in both pharmaceutical and polymer synthesis analysis, this electrochemical approach is inexpensive, fast and also requires no synthetic derivatization of the GI. By combining this measurement with hydrodynamic flow systems it will be possible to significantly improve detection limits.

3.5 References

1. D. I. Robinson, *Org. Process Res. Dev.*, 2010, **14**, 946-959.

2. R. Alzaga, R. W. Ryan, K. Taylor-Worth, A. M. Lipczynski, R. Szucs and P. Sandra, *J. Pharm. Biomed. Anal.*, 2007, **45**, 472-479.
3. L. Müller, R. J. Mauthe, C. M. Riley, M. M. Andino, D. D. Antonis, C. Beels, J. DeGeorge, A. G. M. De Knaep, D. Ellison, J. A. Fagerland, R. Frank, B. Fritschel, S. Galloway, E. Harpur, C. D. N. Humfrey, A. S. Jacks, N. Jagota, J. Mackinnon, G. Mohan, D. K. Ness, M. R. O'Donovan, M. D. Smith, G. Vudathala and L. Yotti, *Regul. Toxicol. Pharmacol.*, 2006, **44**, 198-211.
4. A. Poso, A. Vonwright and J. Gynther, *Mutat. Res., Fundam. Mol. Mech. Mutagen.*, 1995, **332**, 63-71.
5. X. Yu and J. Zhang, *Chem. Eur. J.*, 2012, **18**, 12945 – 12949.
6. J. Sanabria-Chinchilla, K. Asazawa, T. Sakamoto, K. Yamada, H. Tanaka and P. Strasser, *J. Am. Chem. Soc.*, 2011, **133**, 5425-5431.
7. H. Chen, J. M. Wang, X. C. Hong, H. B. Zhou and C. N. Dong, *Can. J. Chem.*, 2012, **90**, 758-761.
8. T. Kean, J. H. M. Miller, G. C. Skellern and D. Snodin, *Pharmeuropa scientific notes*, 2006, **2**, 23-33.
9. D. P. Elder, D. Snodin and A. Teasdale, *J. Pharm. Biomed. Anal.*, 2011, **54**, 900-910.
10. M. J. Sun, L. Bai and D. Q. Liu, *J. Pharm. Biomed. Anal.*, 2009, **49**, 529-533.
11. N. K. Jagota, A. J. Chetram and J. B. Nair, *J. Pharm. Biomed. Anal.*, 1998, **16**, 1083-1087.
12. H. Bhutani, S. Singh, S. Vir, K. K. Bhutani, R. Kumar, A. K. Chakraborti and K. C. Jindal, *J. Pharm. Biomed. Anal.*, 2007, **43**, 1213-1220.
13. A. Carlin, N. Gregory and J. Simmons, *J. Pharm. Biomed. Anal.*, 1998, **17**, 885-890.
14. M. Khan, S. Kumar, K. Jayasree, K. V. S. R. Krishna Reddy and P. K. Dubey, *Chromatographia*, 2013, **76**, 801-809.
15. G. Kokkinidis and P. D. Jannakoudakis, *J. Electroanal. Chem. Interfacial Electrochem.*, 1981, **130**, 153-162.
16. M. D. G. Azorero, M. L. Marcos and J. G. Velasco, *Electrochim. Acta*, 1994, **39**, 1909-1914.
17. M. Michlmayr and D. T. Sawyer, *J. Electroanal. Chem.*, 1969, **23**, 375-385.
18. X. Q. Cao, B. C. Wang and Q. Su, *J. Electroanal. Chem.*, 1993, **361**, 211-214.
19. S. Antoniadou, A. D. Jannakoudakis and E. Theodoridou, *Synth. Met.*, 1989, **30**, 295-304.
20. B. Hammer and J. K. Norskov, *Nature*, 1995, **376**, 238-240.
21. B. Álvarez-Ruiz, R. Gómez, J. M. Orts and J. M. Feliu, *J. Electrochem. Soc.*, 2002, **149**, D35-D45.
22. V. Kondratiev, T. Babkova and E. Tolstopjatova, *J. Solid State Electrochem.*, 2013, **17**, 1621-1630.
23. D. Oukil, L. Benhaddad, L. Makhloufi, R. Aitout and B. Saidani, *Sens. Lett.*, 2013, **11**, 395-404.
24. P. V. Dudin, M. E. Snowden, J. V. Macpherson and P. R. Unwin, *ACS Nano*, 2011, **5**, 10017-10025.
25. L. Hutton, M. E. Newton, P. R. Unwin and J. V. Macpherson, *Anal. Chem.*, 2009, **81**, 1023-1032.
26. H. Sun, L. Dong, H. Yu and M. Huo, *Russ. J. Electrochem.*, 2013, 1-5.
27. J. S. Xu, M. C. Granger, J. Wang, Q. Y. Chen, M. A. Witek, M. L. Hupert, A. Hanks, G. M. Swain, I. Sakaguchi, M. Nishitani-Gamo and T. Ando, *Structure-reactivity studies at boron-doped single and polycrystalline diamond thin-film electrodes: Relationship to applications in electroanalysis*, Electrochemical Society Inc, Pennington, 2000.
28. D. Wakerley, A. G. Guell, L. A. Hutton, T. S. Miller, A. J. Bard and J. V. Macpherson, *Chem. Commun.*, 2013, **49**, 5657-5659.
29. C. Batchelor-McAuley, C. E. Banks, A. O. Simm, T. G. J. Jones and R. G. Compton, *Analyst*, 2006, **131**, 106-110.
30. Y. Li and S. M. Chen, *Int. J. Electrochem. Sci.*, 2012, **7**, 2175-2187.
31. A. R. Khaskheli, J. Fischer, J. Barek, V. Vyskocil, Sirajuddin and M. I. Bhangar, *Electrochim. Acta*, 2013, **101**, 238-242.
32. A. P. P. Eisele, D. N. Clausen, C. R. T. Tarley, L. H. Dall'Antonia and E. R. Sartori, *Electroanalysis*, 2013, DOI: 10.1002/elan.201300137.

33. Y. W. Chen, C. C. Chu, Y. C. Chen, C. D. Kan and J. J. Wang, *Neurosci. Lett.*, 2012, **521**, 115-118.
34. C. Petit, K. Murakami, A. Erdem, E. Kilinc, G. O. Borondo, J. F. Liegeois and J. M. Kauffmann, *Electroanalysis*, 1998, **10**, 1241-1248.
35. M. M. Ayad, A. Shalaby, H. E. Abdellatef and H. M. Elsaid, *Microchim. Acta*, 2002, **140**, 93-96.
36. F. Belal, S. M. El-Ashry, I. M. Shehata, M. A. El-Sherbeny and D. T. El-Sherbeny, *Microchim. Acta*, 2000, **135**, 147-154.
37. S. Karp and L. Meites, *Journal of the American Chemical Society*, 1962, **84**, 906-912.
38. A. J. Bard, *Analytical Chemistry*, 1963, **35**, 1602-1607.
39. L. A. Hutton, J. G. Iacobini, E. Bitziou, R. B. Channon, M. E. Newton and J. V. Macpherson, *Anal. Chem.*, 2013, **85**, 7230-7240.
40. M. D. Garcia, M. L. Marcos and J. G. Velasco, *Electroanalysis*, 1996, **8**, 267-273.
41. J. Li, H. Q. Xie and L. F. Chen, *Sens. Actuators, B*, 2011, **153**, 239-245.
42. J. N. Miller and J. C. Miller, *Statistics and Chemometrics for Analytical Chemistry*, 5th edn., Pearson Education Limited, London, 2005.
43. E. Laborda, A. Molina, F. Martinez-Ortiz and R. G. Compton, *Electrochim. Acta*, 2012, **73**, 3-9.
44. A. C. F. Ribeiro, M. C. F. Barros, L. M. P. Veríssimo, C. I. A. V. Santos, A. M. T. D. P. V. Cabral, G. D. Gaspar and M. A. Esteso, *J. Chem. Thermodyn.*, 2012, **54**, 97-99.
45. J. Wiśniewska, P. Kita and G. Wrzeszcz, *Transition Met. Chem.*, 2007, **32**, 857-863.
46. J. Wiśniewska, P. Rzeźnicki and A. Topolski, *Transition Met. Chem.*, 2011, **36**, 767-774.
47. E. K. Kazakova, V. V. Syakaev, J. E. Morozova, N. A. Makarova, L. A. Muslinkina, G. A. Evtugyn and A. I. Kononov, *J. Inclusion Phenom. Macrocyclic Chem.*, 2007, **59**, 143-154.
48. S. Sansuk, E. Bitziou, M. B. Joseph, J. A. Covington, M. G. Boutelle, P. R. Unwin and J. V. Macpherson, *Anal. Chem.*, 2012, **85**, 163-169.
49. X. Cao, B. Wang and Q. Su, *Journal of Electroanalytical Chemistry*, 1993, **361**, 211-214.
50. A. D. Jannakoudakis, E. Theodoridou and D. Jannakoudakis, *Synthetic Metals*, 1984, **10**, 131-140.
51. M. Michlmayr and D. T. Sawyer, *Journal of Electroanalytical Chemistry and Interfacial Electrochemistry*, 1969, **23**, 375-385.
52. W. C. E. Higginson, D. Sutton and P. Wright, *Journal of the Chemical Society (Resumed)*, 1953, 1380-1386.
53. J. Q. Adams and J. R. Thomas, *The Journal of Chemical Physics*, 1963, **39**, 1904-1906.
54. A. D. Jannakoudakis and G. Kokkinidis, *Journal of Electroanalytical Chemistry and Interfacial Electrochemistry*, 1982, **134**, 311-324.
55. J. Clayden, N. Greeves, S. Warren and P. Wothers, *Organic Chemistry*, Oxford University Press, 2006.
56. Y. Chen, N. Ballard, O. D. Coleman, I. J. Hands-Portman and S. A. F. Bon, *Journal of Polymer Science Part A: Polymer Chemistry*, 2014, **52**, 1745-1754.
57. L. B. Colvin, *Journal of Pharmaceutical Sciences*, 1969, **58**, 1433-1443.
58. G. Elias and W. F. Bauer, *Journal of Separation Science*, 2006, **29**, 460-464.

Chapter 4: An electrochemical technique for probing the partition of electro-active bromine between aqueous and non-aqueous phases

Double potential step chronoamperometry (DPSC) is demonstrated as a technique for investigating partitioning between a solute in aqueous solution and non-polar oil droplet(s) immobilised at an electrode. Here a species in aqueous solution which does not partition into the oil phase is converted at the electrode surface into another species which either does not or does partition into the oil drop. The first case is investigated experimentally by considering generation of the ionic redox species, FcTMA^{2+} from FcTMA^+ , while the second case is exemplified by studies of Br_2 generation from Br^- . The case of molecular partitioning at the three phase interface has received little attention hitherto. To maintain oil droplet stability a boron-doped diamond electrode is employed functionalised with Pt nanoparticles to impart electrocatalytic activity on the electrode towards Br_2 production. An arrangement is utilised where the droplet(s) sit(s) on (but does not cover) the electrode surface. It is shown both experimentally and through finite element simulation how the charge-time profile for the generation and collection of electroactive species can be used to obtain information the extent of partitioning and how this is affected by factors such as the number and size of droplets. Finally, the suitability of this approach for investigating partitioning species induced reactions which take place within the droplet is highlighted.

4.1 Introduction

The interface between two immiscible (liquid/liquid) interfaces is of fundamental interest to a range of chemical processes^{1, 2}. Such an interface also serves as a simple model for biological membranes, allowing pharmacokinetic properties of drug/organic molecules, such as lipophilicity, to be determined.³⁻⁵ Liquid/liquid interfaces play a critical role in many classes of chemical reactions, for example, phase transfer catalysis,⁶⁻⁸ polymerization,⁹ and substitution reactions, involving interfacial ion transfer (IT), electron transfer (ET) and/or molecular transfer.^{10,11} As such, the electrochemical

and phase transfer properties of liquid/liquid interfaces have been the subject of extensive study.¹² Significant research has focused on ion transfer between aqueous and organic phases,¹³⁻¹⁷ with kinetics and mechanisms of two phase reactions determined via voltammetry¹⁸ or microscale techniques such as scanning electrochemical microscopy (SECM)¹⁹ and microelectrochemical measurements at expanding droplets (MEMED).^{20, 21} The study of ET between two species at the interface of an oil droplet and an aqueous solution using laser trapping techniques has also been reported.²²

Oil droplet modified electrodes represent an attractive format for the study of liquid/liquid interfaces, and also enable the study of ion transfer and photo-electrochemistry at three-phase junctions (solid-oil-water).²³⁻²⁵ To date the vast majority of electrochemical studies with oil droplets have employed polar oils or oils that are redox active.²⁶ Non-polar oils have received less attention, partly due to the difficulty of incorporating a suitable electrolyte within them. Among a fairly limited body of work, uniformly-sized non-polar oil droplets decorating an electrode surface,²⁷ have been sized using single step potential-step chronoamperometry; an approach which can also be used to size other blocking materials²⁸.

In this work, we demonstrate how double potential step chronoamperometry (DPSC) can be employed to probe the partitioning of an electrogenerated molecular species across the non-polar oil (o) droplet/aqueous solution (w) interface. Previous work has seen the use of SECM to directly measure molecular transport across this interface,²⁹ by using an ultramicroelectrode (UME), positioned in the aqueous phase (for example) to generate a molecular species, which is able to partition into the non-polar organic phase, during an initial potential step. Collection of the molecular species in a second step provides information on physicochemical parameters such as transfer kinetics and diffusion coefficient.³⁰

Herein, we adapt this DPSC method for an arrangement where a droplet (or multiple droplets) sit(s) on, but does not completely cover, an electrode surface, immersed in electrolyte solution. We show how the current-time profile for the collection of the partitioning species - electrogenerated Br₂ (from

Br^-) - depends not only on the size and number of droplet(s) on the electrode surface, but also on the time period of the generation step. The DPSC responses are also compared to those for a system where no partitioning occurs at the o/w interface, i.e. for an ionic redox couple. The potential advantage of this approach compared to SECM is a greatly simplified experimental arrangement, negating, for example, the need for tip positioning.

4.2 Experimental

4.2.1 Chemicals

Potassium bromide, 99.5% (Fisons Scientific Equipment, UK), 0.5 M sulfuric acid solutions diluted from 18 M sulfuric acid (VWR international Ltd. UK), ferrocene tetramethylammonium (FcTMA^+) hexafluorophosphate (produced in house via the metathesis of the corresponding iodide salt (99%, Strem) with ammonium hexafluorophosphate (99.5%, Strem)³¹) and dodecane (Sigma Aldrich, UK) were used herein. All aqueous solutions were made using 18.2 M Ω cm (25 °C) Milli-Q filtered water (Millipore Corporation).

4.2.2 Instrumentation and protocols

Negligible sp^2 content, polycrystalline boron doped diamond (pBDD) 1 mm diameter, macrodisc electrodes³² were prepared in house using a reported procedure,³³ from DIAFILM EA grade pBDD (supplied in wafer form by Element Six, Harwell; average boron dopant density $\sim 3 \times 10^{20}$ B atoms cm^{-3} and lapped to produce a surface roughness $\sim \text{nm}^{34}$). pBDD was employed as the electrode material to circumvent possible problems due to the reported instability of organic droplets on some metal electrodes under potential control.³⁵ As the Br^-/Br_2 heterogeneous redox process is sluggish on bare pBDD (*vide infra*) functionalisation of the pBDD substrate with Pt nanoparticles (NPs) was necessary. Pt NPs, 20-40 nm in size, were formed at the pBDD surface by electrodeposition from a solution containing 1 mM K_2PtCl_6 and 0.1 M HCl. The pBDD electrode was held at a potential of -1.0 V vs. a saturated calomel electrode (SCE) for 5 s, using a reported procedure³³. Prior to oil droplet deposition,

any Pt oxide present on the surface of the NPs was electrochemically reduced by holding the electrode at -1 V in a solution of 0.5 M sulfuric acid, for 40 s. This optimized the Pt NP-pBDD electrode towards the Br^-/Br_2 couple

The Pt NP-pBDD electrode was mounted vertically, facing upwards, in a 4 cm diameter Teflon cell base and secured in place with paraffin wax. The cell was completed by placing a glass cell body, containing a 2 cm diameter quartz window (for microscopy visualization), over the cell base, held in place with a rubber O-ring. The cell was filled with the solution of interest and electrochemical analysis was carried out using a CH Instruments Electrochemical Analyzer, model CHI 1105A (CH instruments, Austin, Texas, USA), in a 3-electrode mode, with a Pt wire counter electrode. All potentials are quoted versus SCE, which was employed as the reference electrode (BAS Inc., Tokyo, Japan). Measurements were made at room temperature (22 ± 1 °C).

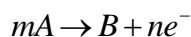
Dodecane oil droplets, typically in the size range 100 – 1450 μm diameter, were deposited on the surface of the Pt NP – pBDD electrode using 30-40 μm o.d. tapered borosilicate pipettes, pulled from 2 mm o.d, 1.16 mm i.d borosilicate tubes (Harvard Apparatus) using a pipette puller. The pipette was mounted on a manual micro-positioner (M433 series, Newport) which was capable of movement in the x , y and z directions, with micron resolution. Oil droplets were dispensed by applying pressure to the oil filled pipette using a 5 mL syringe (BD Plastipak) with the size controlled by the period of time for which the pressure was applied. The sizes of the oil droplets were determined optically, *in-situ*, using two PixelINK (Ottawa, Canada), 3-megapixel cameras, one positioned above the electrode (top view), and the other to the side facing the quartz window (side view). The top camera was fitted with a 4 \times telecentric lens (Edmund optics, model 62763) or 2 \times telecentric lens (Infinistix), while the side camera was fitted with a 2 \times telecentric lens (Infinistix). Illumination was provided by a Fiber-Lite DC-950 regulated illuminator (Dolan-Jenner Industries).

The partition coefficient (K) of Br_2 between dodecane and water, at room temperature, was determined by recording the UV-Visible absorption (Cary 50 Bio UV-Visible spectrophotometer) spectrum (peak maximum for Br_2 , A_{max} , at 393 nm) of aqueous 20 mM Br_2 (Fisher Scientific), before and after mixing thoroughly with an equal volume of dodecane, for 30 s. Longer mixing times were found to have no difference on the absorbance spectra recorded. We found $K = 10.6 \pm 0.7$ (1σ) at room temperature (22 ± 1 °C). For comparison, K was also determined using voltammetry on a 2 mm diameter Pt macrodisc electrode where the potential was swept from +1 V to +0.5 V (vs. SCE), scan rate 0.1 Vs^{-1} , in a solution of 20 mM Br_2 (aq) before and after shaking with an equal volume of dodecane. We obtained $K = 9.3 \pm 1.1$ (1σ) at room temperature, consistent with absorbance measurements.

4.2.3 Simulations

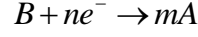
Simulations were performed on a Dell Optiplex 755, Intel Core 2 Quad 2.49 GHz computer equipped with 8 GB RAM running windows XP 64 bit edition. Comsol Multiphysics 4.2 (Comsol AB, Sweden) was used for finite element modeling. Simulations employed a minimum of 64,000 triangular mesh elements. The highest mesh resolution was focused around the electrode surface and o/w interfaces.

We consider a macroelectrode immersed in an aqueous electrolyte solution (phase w) supporting a droplet of dodecane (phase o) centered on the electrode surface, shown in *Figure 0.1* (a). During a typical DPSC experiment, in the forward step a potential is applied for a fixed amount of time, τ , sufficient to generate B via the electrooxidation of A in solution, at a diffusion-controlled rate, *i.e.*;



0.1

where n is the number of electrons transferred per mole of reactant, m is the stoichiometry of A. In the reverse step a potential is applied, for a further time, τ (total duration of experiment 2τ), sufficient to collect B via electroreduction to A in accordance with;



0.2

at a diffusion-controlled rate.

We consider two situations: (1) Where neither A nor B interacts with or partitions across the o/w interface, and (2) where A does not partition, but B does according to:³⁶

$$\frac{[B_{(org)}]}{[B_{(aq)}]} = K$$

0.3

The diffusion of species A and B is described by the following time-dependent diffusion equation and solved for the simulated axisymmetric cylindrical geometry formed from a 2D domain, shown in *Figure 0.1a*.

$$\frac{\partial c_j}{\partial t} = D_j \left(\frac{\partial^2 c_j}{\partial r^2} + \frac{1}{r} \frac{\partial c_j}{\partial r} + \frac{\partial^2 c_j}{\partial z^2} \right)$$

0.4

where c_j is the concentration of species A or B (mol cm^{-3}), D_j is the diffusion coefficient of a species A or B ($\text{cm}^2 \text{s}^{-1}$), z is the coordinate normal to the electrode surface (cm), r is the radial coordinate (cm) and t is time (s).

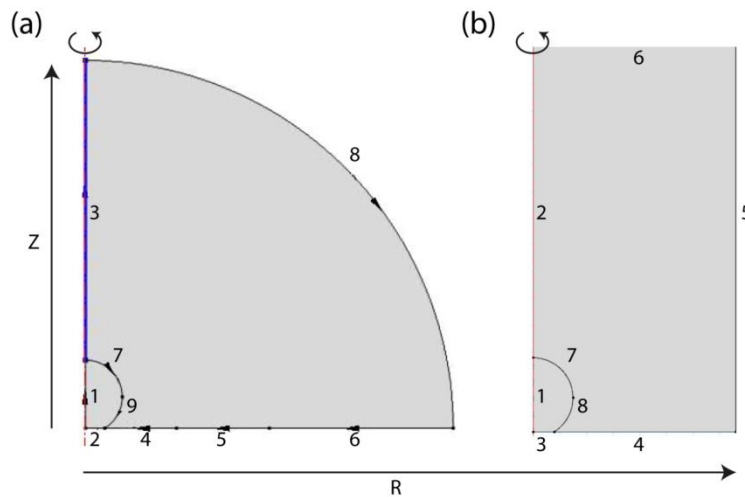


Figure 0.1: Simulation geometry for (a) single oil droplets on the electrode surface and (b) oil droplet arrays: boundary conditions defined in tables 4.1 and 4.2 respectively

The boundary conditions listed in *Table 0.1* were applied to create a model of the DPSC system. During the forward step (electrogeneration of redox species B from A), the concentration of A at the electrode boundary was set to $c = 0$. The outward flux of B at the electrode boundary was dependent on the inward flux of A and was set with $mA \rightarrow B$, where m is 1 for $\text{FcTMA}^+/\text{FcTMA}^{2+}$ and 2 for Br^-/Br_2 .

Edge Number	Physical representation	Boundary Conditions
1	Axial symmetry	$-\mathbf{n} \cdot \mathbf{N}_{B_o} = 0$
2	Blocked electrode	$-\mathbf{n} \cdot \mathbf{N}_{A_w} = 0$ $-\mathbf{n} \cdot \mathbf{N}_{B_o} = 0$
3	Axial symmetry	$-\mathbf{n} \cdot \mathbf{N}_{A_w} = 0$ $-\mathbf{n} \cdot \mathbf{N}_{B_w} = 0$
4	Electrode surface	$0 \leq t \leq \tau, c_{A_w} = 0$ $0 \leq t \leq \tau, -\mathbf{n} \cdot \mathbf{N}_{B_w} = \frac{1}{n} (D_{A_w} \nabla C_{A_w})$ $t > \tau, -\mathbf{n} \cdot \mathbf{N}_{A_w} = n (D_{B_w} \nabla C_{B_w})$ $t > \tau, c_{B_w} = 0$ $n = 1 \text{ (FcTMA}^{+/2+})$ $n = 2 \text{ (Br}^-/\text{Br}_2)$
5	Glass insulation	$-\mathbf{n} \cdot \mathbf{N}_{A_w} = 0$ $-\mathbf{n} \cdot \mathbf{N}_{B_w} = 0$
6/8	Bulk solution	$c = c^*$
7/9	Oil/water interface	$-\mathbf{n} \cdot \mathbf{N}_{A_w} = 0$ $-\mathbf{n} \cdot \mathbf{N}_{B_w} = 0 \text{ (FcTMA}^{+/2+})$ $-\mathbf{n} \cdot \mathbf{N}_{B_w} = -k_1 c_{B_w}$ $-\mathbf{n} \cdot \mathbf{N}_{B_w} = (k_{-1}) c_{B_o}$ $-\mathbf{n} \cdot \mathbf{N}_{B_o} = -(k_{-1}) c_{B_o}$ $-\mathbf{n} \cdot \mathbf{N}_{B_o} = k_1 c_{B_w}$

Table 0.1: Boundary conditions for the finite element model where \mathbf{n} is the inward-pointing unit normal vector; N is the normal flux of species; species A_w is A in the aqueous phase, species B_w is B in the aqueous phase and B_w is B in the oil phase (Br⁻/Br₂ system only), with the subscript denoting the phase occupied by the species; k_1 and k_{-1} are the mass transfer coefficients equal to 0.5 cm s⁻¹ and 0.05 cm⁻¹ respectively, D_j is the diffusion coefficient of a given species j where $j = A$ or B . When considering the Br⁻/Br₂ system, for species A_w , $D = 1.85 \times 10^{-5} \text{ cm}^2 \text{ s}^{-1}$; species B_w and B_o , $D = 9.4 \times 10^{-6} \text{ cm}^2 \text{ s}^{-1}$. For the FcTMA⁺²⁺ system, for both species A_w and B_w , $D = 7.6 \times 10^{-6} \text{ cm}^2 \text{ s}^{-1}$.

The model considered oil droplets of various sizes supported on the electrode surface. The droplet shape was approximated from contact angle measurements and using optical images of droplets on the electrode surface.

The diffusion coefficients for Br_2 and the Br^- ion in aqueous solution used in the model were taken from previous studies;²⁵ $D_{\text{Br}^- (\text{aq})} = 1.85 \times 10^{-5} \text{ cm}^2 \text{ s}^{-1}$ and $D_{\text{Br}_2 (\text{aq})} = 9.4 \times 10^{-6} \text{ cm}^2 \text{ s}^{-1}$. For Br_2 transport across the w/o interface, a fast mass transfer coefficient, k_l of 0.5 cm s^{-1} is assumed, which corresponds to a diffusion-controlled situation under the experimental conditions. A mass transfer coefficient, k_{-1} of 0.05 cm s^{-1} is implied for the reverse movement of Br_2 across the o/w interface, given $K = 10$. For the concentration of Br^- employed (and Br_2 produced) we can reasonably ignore the formation of Br_3^- .³⁷ The diffusion coefficient for both FcTMA^+ and FcTMA^{2+} was $7.6 \times 10^{-6} \text{ cm}^2 \text{ s}^{-1}$.³⁸ To investigate how the DPSC response for the Br^-/Br_2 system varied when employing arrays of oil microdroplets, simulations of homogeneously sized arrays, of spacing $d = 100 \text{ }\mu\text{m}$, were performed with a time pulse, τ , of 2 s. Array simulations utilized a diffusion domain approach, with an axial symmetric domain representing the electrode surface and bulk solution²³, (see *Figure 0.1b*) using the boundary conditions described in *Table 0.2*. The macroelectrode current is calculated from the flux of A_1 at the electrode surface.

Edge Number	Physical representation	Boundary Conditions
1	Axial symmetry	$-\mathbf{n} \cdot \mathbf{N}_{B_o} = 0$
2	Axial symmetry	$-\mathbf{n} \cdot \mathbf{N}_{A_w} = 0$ $-\mathbf{n} \cdot \mathbf{N}_{B_w} = 0$
3	Blocked electrode	$-\mathbf{n} \cdot \mathbf{N}_{A_w} = 0$ $-\mathbf{n} \cdot \mathbf{N}_{B_o} = 0$
4	Electrode surface	$0 \leq t \leq \tau, c_{A_w} = 0$ $0 \leq t \leq \tau, -\mathbf{n} \cdot \mathbf{N}_{B_w} = \frac{1}{2}(D_{A_w} \nabla c_{A_w})$ $t > \tau, -\mathbf{n} \cdot \mathbf{N}_{A_w} = 2(D_{B_w} \nabla c_{B_w})$ $t > \tau, c_{B_w} = 0$
5	Reflective boundary	$-\mathbf{n} \cdot \mathbf{N}_{A_w} = 0$ $-\mathbf{n} \cdot \mathbf{N}_{B_w} = 0$
6	Bulk solution	$c = c^*$
7/8	Oil/water interface	$-\mathbf{n} \cdot \mathbf{N}_{A_w} = 0$ $-\mathbf{n} \cdot \mathbf{N}_{B_w} = -k_1 c_{B_w}$ $-\mathbf{n} \cdot \mathbf{N}_{B_w} = (k_{-1}) c_{B_o}$ $-\mathbf{n} \cdot \mathbf{N}_{B_o} = -(k_{-1}) c_{B_o}$ $-\mathbf{n} \cdot \mathbf{N}_{B_o} = k_1 c_{B_w}$

Table 0.2: Boundary conditions for droplet array finite element model where \mathbf{n} is the inward-pointing unit normal vector; N is the normal flux of species; species A_w is A in the aqueous phase, species B_w is B in the aqueous phase and B_o , B in the oil phase (Br^-/Br_2 system only), with the subscript denoting the phase occupied by the species; k_1 and k_{-1} are the mass transfer coefficients equal to 0.5 cm s^{-1} and 0.05 cm s^{-1} respectively, D_j is the diffusion coefficient of a given species (A or B). When considering the Br^-/Br_2 system, for species A_w , $D = 1.85 \times 10^{-5} \text{ cm}^2 \text{ s}^{-1}$; species B_w and B_o , $D = 9.4 \times 10^{-6} \text{ cm}^2 \text{ s}^{-1}$.

4.2.4 DPSC Experiments

Two systems are considered herein: the fast ET, outer sphere redox species, $FcTMA^{+/2+}$ where $A = FcTMA^+$, $B = FcTMA^{2+}$, $n = 1$, and Br^-/Br_2 where $A = Br^-$, $B = Br_2$, $n = 2$. For DPSC with $FcTMA^{+/2+}$ in the forward step a potential of +0.6 V was applied of pulse width τ , whilst a potential of +0.15 V was applied, during the reverse step, for equal τ .

For the Br^-/Br_2 redox couple, DPSC experiments were performed by applying an open circuit potential to the electrode for 120 s (allowing the system to stabilize between experiments) before

holding at +1.2 V versus SCE (the forward step) for time, τ . The potential was then switched to +0.7 V (reverse step).

4.3 Results and Discussion

As shown in *Figure 0.2a*, the use of Pt NPs makes Br^-/Br_2 electrolysis more kinetically facile³⁹ (red dotted line), compared to pBDD alone (black line), while retaining the inherent low background currents of pBDD electrodes.⁴⁰ The density of Pt NPs is also sufficient that on the timescale of the cyclic voltammogram (CV) there is complete diffusional overlap and the response is comparable to that of a Pt macroelectrode (black dotted line). Importantly, the presence of Pt NPs on the electrode surface (see *Figure 0.2b*) does not lead to any destabilization of oil droplets on the electrode surface over the potential range applied in DPSC.

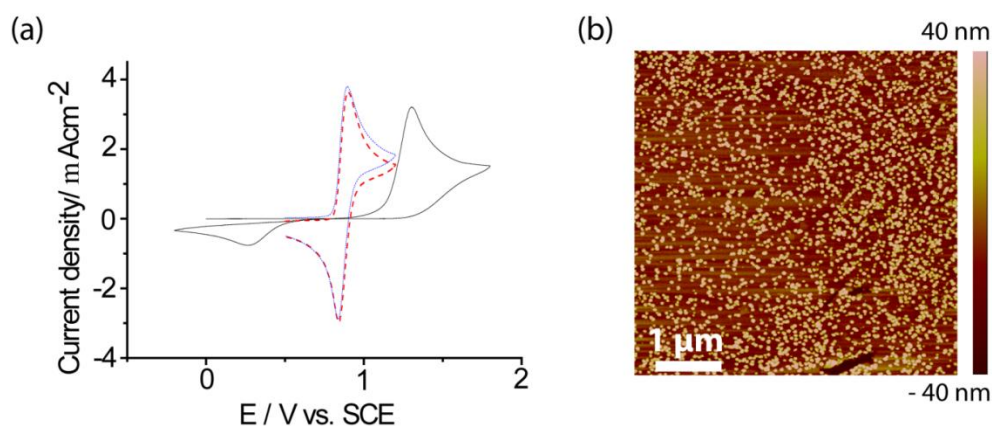


Figure 0.2: (a) CVs of 10 mM KBr in 0.5 M H_2SO_4 , scan rate 100 mV s^{-1} at a bare 1 mm diameter disc pBDD electrode (black line), 2 mm diameter disc Pt macroelectrode (red dashed line) and a Pt NP-pBDD electrode (blue line). The currents have been normalized with respect to electrode area. (b) Tapping mode AFM image of electrodeposited Pt NPs on the pBDD electrode surface.

4.3.1 Effect of droplet size

Charge-time (Q - t) responses of the $\text{FcTMA}^{+/2+}$ system were investigated experimentally for the Pt NP-pBDD electrode in the absence (black line) and presence of a single dodecane oil droplet, in the size range $d = 100 \text{ } \mu\text{m}$ (■), $200 \text{ } \mu\text{m}$ (▲) and $400 \text{ } \mu\text{m}$ (▼), as shown in *Figure 0.3a*. When comparing the DPSC responses, the presence of an oil droplet can be seen to diminish the current, and hence charge

(Q) response, for the generation step. In general the larger the droplet, the lower the Q passed (*Figure 0.3a*). This is clearly because the droplet blocks part of the electrode and hinders diffusion to part of the electrode near the droplet. By normalizing Q with respect to the maximum Q i.e. Q/Q_{max} (at $\tau = 2$ s), the amount of species collected back can be compared to the total amount generated during the forward step (*Figure 0.3b*).

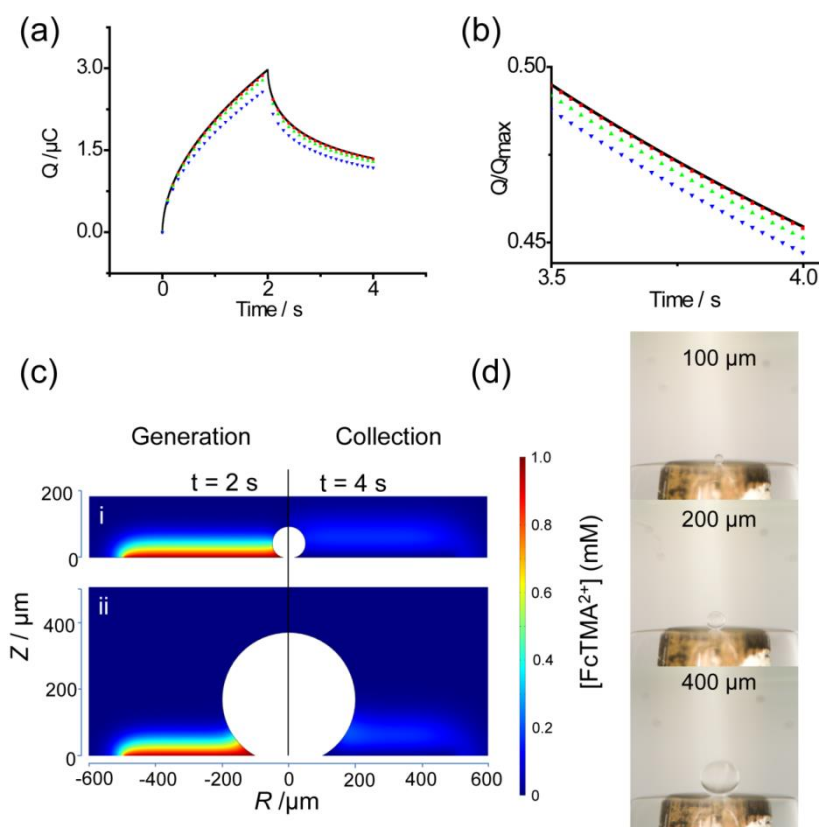


Figure 0.3: (a) Q - t plots generated from integrating the DPSC i - t response for 1 mM FcTMA^+ generation-collection at a bare Pt NP-pBDD electrode (-) and one containing a single dodecane droplet of diameter 100 μm (■), 200 μm (▲) and 400 μm (▼). (b) Plot of normalized charge (Q/Q_{max}) vs. t for the last 0.5 s of the collection step. (c) FEM-simulated diffusion profiles of $\text{FcTMA}^{+/2+}$ generation/collection in the presence of dodecane droplets of diameter (i) 100 μm and (ii) 400 μm diameter at times $t = 2$ s and $t = 4$ s. (d) Optical images of dodecane droplets (of diameter 100-400 μm) on a Pt NP-pBDD electrode.

Close inspection of the plot of Q/Q_{max} vs. t at long times reveals that in the presence of the oil drop the amount of charge collected back, relative to the amount of charge generated in the forward step is always greater than that at a bare electrode surface (i.e. lower Q/Q_{max} ; the current passed during generation is in the opposite direction to that passed during collection). Second, this effect is exacerbated the larger the oil drop as diffusion of the electrogenerated species, FcTMA^{2+} , away from

the electrode is hindered compared to the bare electrode case, due to the presence of the oil drop. This is shown clearly by the FEM-generated concentration profiles for $\text{FcTMA}^{+/2+}$ generation/collection for droplets of 100 μm diameter (*Figure 0.3ci*) and 400 μm diameter (*Figure 0.3cii*) at $\tau = 2\text{ s}$ and 2τ . As the droplet size increases a greater proportion of FcTMA^{2+} is "trapped" by the inert droplet, so that more is available locally for collection during the reverse potential step.

Figure 0.4a shows Q - t transients ($\tau = 2\text{ s}$), for the Br^-/Br_2 system, for a bare electrode surface (black line) and a surface covered with a single dodecane oil droplet, with d in the range 100 μm (■), 200 μm (▲), 400 μm (▼) 1000 μm (◀) and 1450 μm (◆). Optical images of the dodecane droplets are shown in *Figure 0.3d* and *Figure 0.4b*. As for FcTMA^{2+} generation, during the forward step as the size of the droplet increases, blocking the electrode, the amount of Br_2 generated (i.e. Q) decreases. In contrast to *Figure 0.3b*, however, the amount of Br_2 collected back, relative to the amount initially generated, is less than for a bare electrode surface (i.e. higher Q/Q_{max} values are seen at all times) and decreases with increasing droplet size (*Figure 0.4c*). This effect can be attributed to partitioning of the electrogenerated Br_2 from the aqueous phase into the non-polar oil droplet, thereby removing Br_2 from the electrochemically accessible region of the electrode during the collection step. For the largest droplet studied ($d = 1450\text{ }\mu\text{m}$) the Q/Q_{max} response tends towards 1, where 1 denotes no Br_2 collected back.

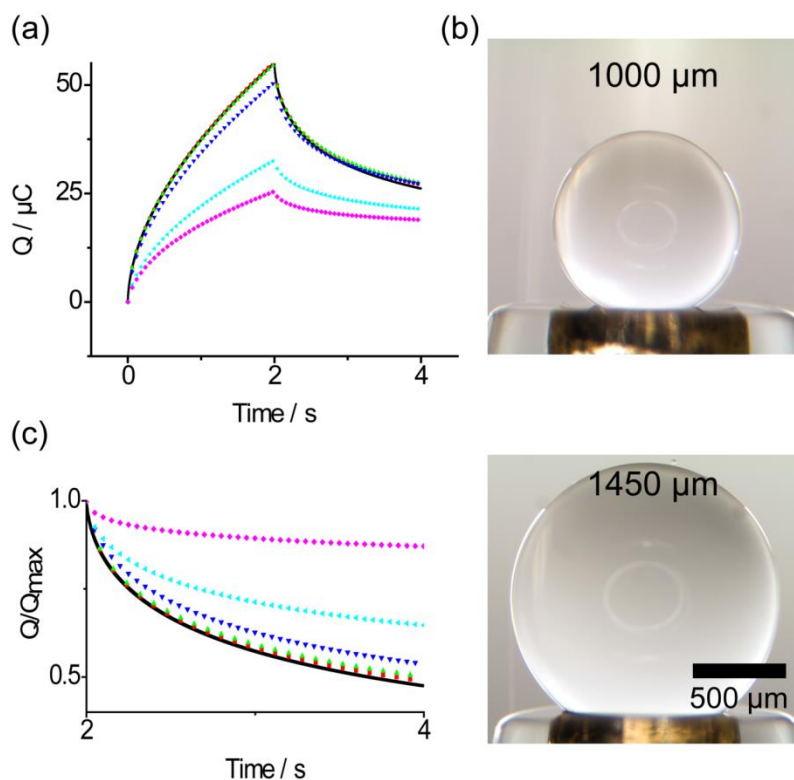


Figure 0.4: (a) Q - t plots for 1 mM Br^-/Br_2 generation-collection at a bare PtNP-pBDD electrode (-) and one containing a single dodecane droplet of diameter 100 μm (■), 200 μm (▲), 400 μm (▼), 1000 μm (◄) and 1450 μm (◆). (b) Optical images of dodecane droplets (of diameter 1000 and 1450 μm) on the PtNP-pBDD electrode. (c) Plot of normalized charge (Q/Q_{max}) vs. t for the collection step.

To explain the trend seen experimentally, Figure 0.5 shows simulated Br_2 concentration profiles at τ ($t = 2$ s) and 2τ for single (a) 100 μm and (b) 400 μm diameter droplets on an electrode. At the end of the forward potential step, the diffusion of electrogenerated Br_2 away from the electrode surface and into the oil phase can clearly be seen. For the case of the 100 μm diameter droplet and $\tau = 2$ s, the relatively higher interfacial area to volume ratio results in the oil droplet containing a significantly higher concentration of Br_2 than the 400 μm diameter droplet.

During the collection step, Br_2 is depleted at the electrode surface in the aqueous solution, resulting in oil-phase partitioned Br_2 being released into the aqueous solution for subsequent collection. For the small drop, the efficient trapping of Br_2 results in a high Br_2 collection efficiency. For larger droplets, the droplet actually provides an escape route away from the electrode with some Br_2 diffusing out of the drop into solution regions where collection cannot occur resulting in less Br_2 collected back and thus higher Q/Q_{max} values, at $t > \tau$.

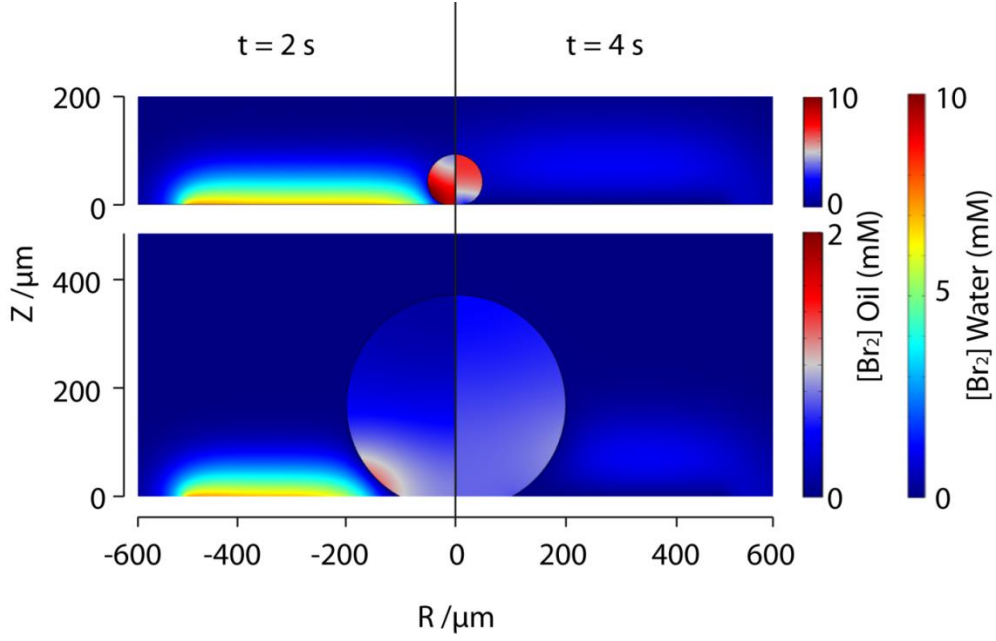


Figure 0.5: Diffusion profiles generated from FEM simulation of Br/Br_2 generation/collection in the presence of dodecane droplets (a) 100 μm and (b) 400 μm diameter at times $t = 2\text{ s}$ and $t = 4\text{ s}$. Note the different scale bars for Br_2 concentration inside the oil droplet for both (a) and (b).

Figure 0.6 presents the simulated DPSC response (Figure 0.6a), plotted as Q/Q_{max} vs. t for the collection step, alongside that observed experimentally (Figure 0.6b) for droplets of 100 μm , 200 μm and 400 μm diameter. Qualitatively, the simulated and experimental data show the same trend of decreasing Br_2 collection with increasing droplet size. There is a discrepancy between experiment and simulation, which could be due to subtle differences in the droplet shape in the model and experiments and/or natural convection effects, particularly in the larger droplets, which is not taken into account in the simple diffusion simulations.

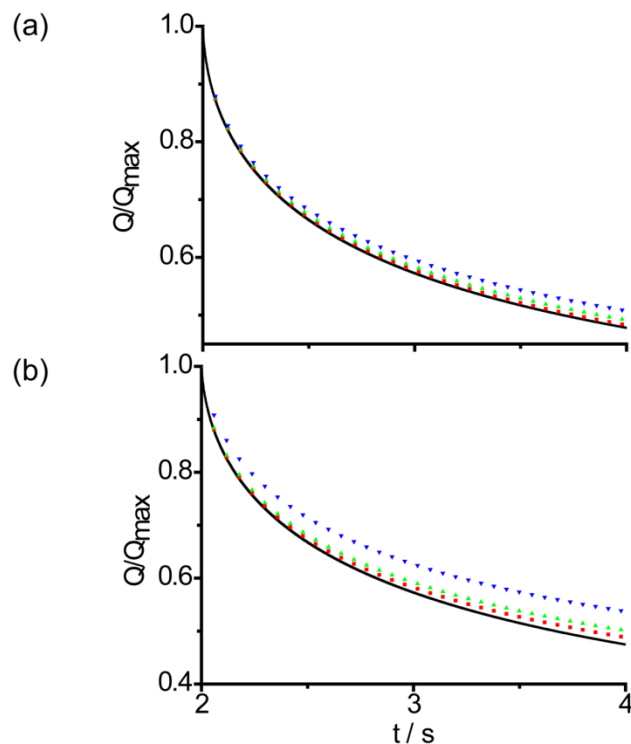


Figure 0.6: Plot of normalized charge (Q/Q_{max}) vs. t for the collection step i.e. collection of electrogenerated Br_2 at a bare electrode (—) and one containing a single dodecane droplet of diameter $100\ \mu m$ (■), $200\ \mu m$ (▲), $400\ \mu m$ (▼): (a) simulated data and (b) experimental data.

4.3.2 Effect of τ

The effect of τ on the Q/Q_{max} - t response for Br^-/Br_2 was investigated experimentally over the τ range 200 ms - 20 s. We focused on analysis of the reverse step as this informs on the partitioning process, i.e. we analyse data at $t \geq \tau$. Relatively small droplets were employed. Figure 0.7 shows Q/Q_{max} - t responses for both the bare electrode and one containing a single oil drop of $d = 100\ \mu m$ (●) and $200\ \mu m$ (▲). In general, as τ increases, more of the o/w interface becomes accessible to the expanding diffusion field of electrogenerated Br_2 , resulting in a decrease in the amount of Br_2 collected back (higher Q/Q_{max} value) for the reasons outlined above. Interestingly, for the shortest pulse times investigated ($\tau = 200$ ms and 1 s) (Figure 0.7a,b), very little difference was seen in the normalised Br_2 collection responses for droplets that were 100 and 200 μm in diameter. However, as τ increased, the

impact of Br_2 partitioning could be more easily differentiated (e.g. *Figure 0.7c* for $\tau = 10$ s). As τ increased further, this differentiation increased (*Figure 0.7d*).

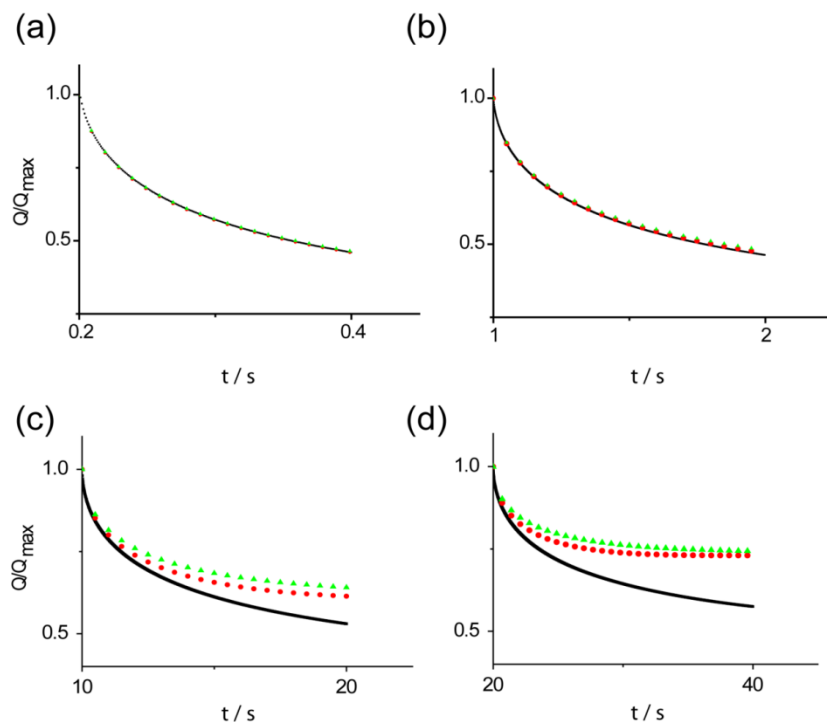


Figure 0.7: Normalized experimental Q - t plots for the DPSC Br_2 collection step with bare Pt NP-pBDD (-) and $100\ \mu\text{m}$ (●) and $200\ \mu\text{m}$ (▲) oil droplets present on the electrode for $\tau =$ (a) $200\ \text{ms}$, (b) $1\ \text{s}$, (c) $10\ \text{s}$ and (d) $20\ \text{s}$.

4.3.3 Effect of electrode size

To complement the studies above, we carried out further simulations keeping the droplet size constant at $100\ \mu\text{m}$ (red symbols) and $200\ \mu\text{m}$ (blue symbols) diameters but with different support electrode diameters of $100\ \mu\text{m}$ (●), $200\ \mu\text{m}$ (▲), $300\ \mu\text{m}$ (▼) and $500\ \mu\text{m}$ (■). These data are shown in *Figure 0.8*, (Q/Q_{max} versus t) for $\tau = 200\ \text{ms}$ along with the bare electrode response (black line). It can be seen that as the electrode size approaches that of the oil droplet the difference between the collection responses for $100\ \mu\text{m}$ and $200\ \mu\text{m}$ diameter droplets increases enabling differentiation and sizing. These data further illustrate that one can tune the relative sizes of electrode and droplet, as well as the

pulse time in DPSC to maximise the sensitivity with which the droplet can be sized and/or partitioning probed.

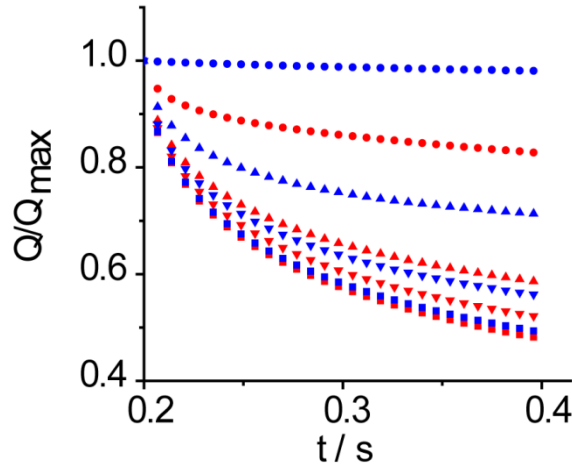


Figure 0.8: Plot of normalized charge (Q/Q_{max}) vs. t for the simulated collection step i.e. Br_2 collection for a PtNP - pBDD electrode of diameter 500 μm (■), 300 μm (▼), 200 μm (▲) and 100 μm (●) containing a single oil droplet of diameter 100 μm (red) and 200 μm (blue).

4.3.4 Non-spherical droplets

The contact area of an oil droplet with the surface of an electrode can have a pronounced effect on the collection response. In Figure 0.9a, two oil droplets, $d \sim 1000 \mu m$ (i ■) and $1700 \mu m$ (ii ●), where d is measured across the center of the droplet, have similar contact areas with the electrode surface but different droplet geometries. This is emphasized by optical images (Figure 0.9a) taken from above the electrode surface with a side light to define areas where contact between the dodecane oil and modified-diamond surface occurs (right hand side images). These larger droplets were deposited by addition of dodecane oil to the top of droplets pre-deposited on the electrode surface.

The generation and collection responses for $\tau = 2$ s for these two droplets (Figure 0.9b) are very similar, making it difficult to distinguish between them, even though the geometries are very different. In contrast, for two larger droplets of $d \sim 2500 \mu m$ (iii ▲) and $3000 \mu m$ (iv ▼), which again have similar contact areas with the electrode, there is now a clear difference in the current collection response. For the bigger droplet more Br_2 is collected back compared to the smaller droplet, in contrast to the trend observed for spherical droplets in Figure 0.4c. This is due to the significantly

distorted shape of the $d \sim 3000 \mu\text{m}$ droplet a product of the buoyancy of the dodecane oil resulting in a “balloon” like construct, effectively pulling the oil droplet away from the electrode surface. As the o/w interface is pulled away from the electrode surface, Br_2 partitioning into the oil droplet is less efficient and as a result, more Br_2 is collected back in the reverse potential step. This brief analysis highlights the care that needs to be taken in analyzing the charge (current) response if DPSC is to be used for accurate oil droplet sizing.

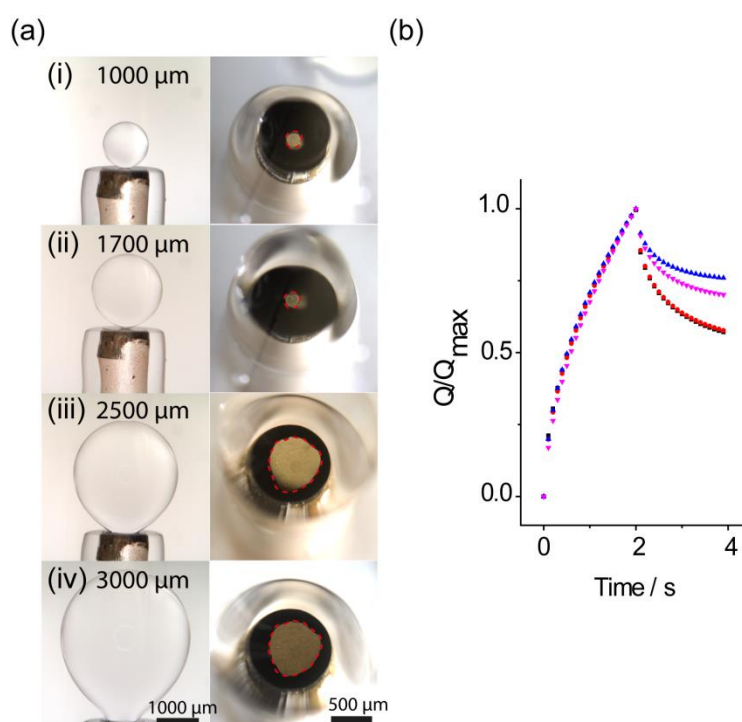


Figure 0.9: (a) Optical images of droplets of effective diameter (i) 1000 μm , (ii) 1700 μm , (iii) 2500 μm and (iv) 3000 μm taken side on (left hand side) and top down (right hand side). The dashed circles show the contact area of the droplet with the electrode. (b) Normalized Q - t plots for droplets of effective diameter 1000 μm (■), 1700 μm (●), 2500 μm (▲) and 3000 μm (▼).

4.3.5 Droplet arrays

Finally, the impact of multiple droplets on an electrode surface is considered. An array of twenty-one dodecane oil microdroplets ($d \sim 100 \mu\text{m}$) were created on the surface of a Pt NP-pBDD electrode and submerged in a solution of 10 mM KBr, 0.5 M H_2SO_4 ; Figure 0.10a. DPSC was performed on the droplet array ($\tau = 2 \text{ s}$). Normalized Q/Q_{max} - t plots are shown in Figure 0.10b for the bare electrode surface (black line), a single droplet ($d = 100 \mu\text{m}$: ■) and the array of droplets ($d = 100 \mu\text{m}$: ▲) with

an approximate spacing of $\sim 170\ \mu\text{m}$ (centre to centre). Crucially, compared to the bare electrode and the electrode functionalized with one oil droplet, significantly less Br_2 is collected back, because of the enhanced trapping of Br_2 by multiple droplets. *Figure 0.10c* shows the FEM-simulated Br_2 concentration profile for a small section of the droplet array, at $\tau = 2\ \text{s}$ (Br_2 generation step) created by stitching together multiple concentration profiles generated from the diffusion domain in *Figure 0.1b*. It can be seen that the majority of the o/w interface of each droplet sits well within the electrogenerated Br_2 diffusion field.

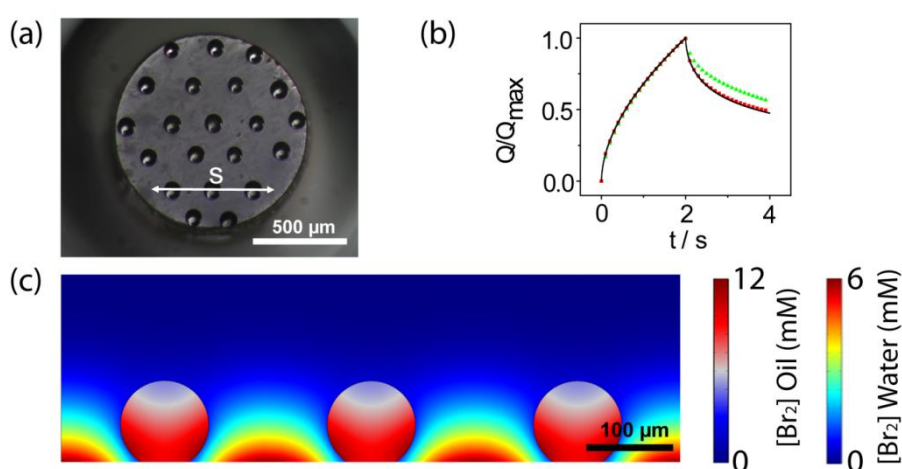


Figure 0.10: (a) Optical image of the oil microdroplet array on the Pt NP-pBDD electrode surface from above. (b) Normalized Q - t plots comparing the DPSC response of a single $\sim 100\ \mu\text{m}$ diameter droplet with a $\sim 100\ \mu\text{m}$ diameter microdroplet array (21 droplets in total). — Bare electrode, \blacktriangle $\sim 100\ \mu\text{m}$ droplet array, \blacksquare $\sim 100\ \mu\text{m}$ droplet. (c) Diffusion profile along vector “s” generated by an array simulation at $t = 2\ \text{s}$, multiple repeats of modelled diffusion domain stitched together.

4.4 Conclusions

DPSC has demonstrated sensitivity towards the sizing of non-polar oil droplets on an electrode surface, in aqueous solution. The importance of the interaction between the electrogenerated species and the oil droplet has been highlighted by DPSC responses on different sized dodecane droplets with both a partitioning electrogenerated species, i.e. Br_2 , and a non-partitioning electrogenerated species, i.e. FcTMA^{2+} . The amount of charge collected back, relative to the amount of charge generated in the forward step, is always greater than that at a bare electrode surface for the non-partitioning species

and less than that at a bare electrode for the partitioning species. DPSC can thus provide a facile approach to examining the extent of partitioning of an electrogenerated species.

Focusing on the partitioning species, key factors which influence the Q - t response and cause it to vary from that at a bare electrode have been identified. First, the oil droplet size and o/w interface/volume ratio is important. DPSC analysis of dodecane oil microdroplets combined with simulation data has emphasized how the size of the diffusion field (normal to the electrode) during the generation step in relation to the size of the oil droplet impacts the Q - t response. Droplets sitting within the generated diffusion field trap Br_2 which can be collected back at the electrode surface. In contrast, droplets which have significant portions lying outside the field provide a route by which Br_2 can escape detection in the collection step. For most efficient collection, the diffusion field should be of similar size or smaller than that of the oil droplet. The diffusion field size is controlled by τ . Second, the size of the electrode relative to that of the oil droplet is significant. As the size of the electrode approaches that of droplet, the amount of Br_2 collected back becomes significantly lower than that for a bare electrode alone. Finally, microdroplet arrays enhance the sensitivity of the overall approach. For future work, we envisage the use of DPSC to monitor reactions taking place within a droplet and also for probing partitioning at modified o/w interfaces.

4.5 References

1. D. W. D. Alexander G. Volkov, Darrell L. Tanelian, Vladislav S. Markin, *Liquid Interfaces in Chemistry and Biology*, John Wiley & Sons, INC, 1998.
2. D. W. D. Alexander G. Volkov, *Liquid-Liquid Interfaces Theory and Methods*, 1 edn., CRC Press, 1996.
3. F. Reymond, H. H. Girault, G. Steyaert, P.-A. Carrupt and B. Testa, *Helv. Chim. Acta*, 1996, **79**, 101-117.
4. R. Gulaboski, A. Galland, G. Bouchard, K. Caban, A. Kretschmer, P.-A. Carrupt, Z. Stojek, H. H. Girault and F. Scholz, *J. Phys. Chem. B*, 2004, **108**, 4565-4572.
5. G. Bouchard, A. Galland, P.-A. Carrupt, R. Gulaboski, V. Mirceski, F. Scholz and H. H. Girault, *Phys. Chem. Chem. Phys.*, 2003, **5**, 3748-3751.
6. H.-S. Wu and M.-C. Lu, *J. Mol. Catal. A: Chem.*, 1995, **104**, 139-146.
7. G. D. Yadav, Y. B. Jadhav and S. Sengupta, *J. Mol. Catal. A: Chem.*, 2003, **200**, 117-129.
8. S. K. Maity, S. Sen and N. C. Pradhan, *Chem. Eng. Sci.*, 2009, **64**, 4365-4374.
9. T. Kakiuchi and H. Sasao, *Russian Journal of Electrochemistry*, 2008, **44**, 73-77.
10. Y.-T. Kong, S.-i. Imabayashi and T. Kakiuchi, *J. Am. Chem. Soc.*, 2000, **122**, 8215-8219.
11. C. Forssten, K. Kontturi, L. Murtomäki, H. C. Hailes and D. E. Williams, *Electrochem. Commun.*, 2001, **3**, 379-383.
12. F. Reymond, D. Fermin, H. J. Lee and H. H. Girault, *Electrochim. Acta*, 2000, **45**, 2647-2662.
13. F. Scholz, *Annual Reports Section "C" (Physical Chemistry)*, 2006, **102**, 43-70.

14. R. Gulaboski, V. Mirčeski and F. Scholz, *Electrochem. Commun.*, 2002, **4**, 277-283.
15. R. Gulaboski, K. Riedl and F. Scholz, *Phys. Chem. Chem. Phys.*, 2003, **5**, 1284-1289.
16. F. Scholz, R. Gulaboski and K. Caban, *Electrochem. Commun.*, 2003, **5**, 929-934.
17. F. Quentel, V. Mirčeski and M. L'Her, *J. Phys. Chem. B*, 2005, **109**, 1262-1267.
18. C. Forssten, J. Strutwolf and D. E. Williams, *Electrochem. Commun.*, 2001, **3**, 619-623.
19. X. Q. Lu, D. F. Dong, X. H. Liu, D. N. Yao, W. T. Wang and Y. M. Xu, *Chin. Chem. Lett.*, 2010, **21**, 225-228.
20. C. J. Slevin and P. R. Unwin, *Langmuir*, 1997, **13**, 4799-4803.
21. C. J. Slevin, J. Zhang and P. R. Unwin, *J. Phys. Chem. B*, 2002, **106**, 3019-3025.
22. K. Nakatani, K. Chikama, H.-B. Kim and N. Kitamura, *Chem. Phys. Lett.*, 1995, **237**, 133-136.
23. F. Marken, J. D. Watkins and A. M. Collins, *Phys. Chem. Chem. Phys.*, 2011, **13**, 10036-10047.
24. J. D. Wadhawan, A. J. Wain and R. G. Compton, *ChemPhysChem*, 2003, **4**, 1211-1215.
25. J. Wadhawan, R. Compton, F. Marken, S. Bull and S. Davies, *J. Solid State Electrochem.*, 2001, **5**, 301-305.
26. C. E. Banks, T. J. Davies, R. G. Evans, G. Hignett, A. J. Wain, N. S. Lawrence, J. D. Wadhawan, F. Marken and R. G. Compton, *Phys. Chem. Chem. Phys.*, 2003, **5**, 4053-4069.
27. A. S. Barnes, N. Fietkau, F. G. Chevallier, J. d. Campo, R. Mas, F. X. Muñoz, T. G. J. Jones and R. G. Compton, *J. Electroanal. Chem.*, 2007, **602**, 1-7.
28. N. Fietkau, F. G. Chevallier, L. Jiang, T. G. J. Jones and R. G. Compton, *ChemPhysChem*, 2006, **7**, 2162-2167.
29. C. J. Slevin, J. V. Macpherson and P. R. Unwin, *The Journal of Physical Chemistry B*, 1997, **101**, 10851-10859.
30. J. V. Macpherson and P. R. Unwin, *Analytical Chemistry*, 1997, **69**, 2063-2069.
31. I. Dumitrescu, P. R. Unwin and J. V. Macpherson, *Electrochem. Commun.*, 2009, **11**, 2081-2084.
32. H. V. Patten, K. E. Meadows, L. A. Hutton, J. G. Iacobini, D. Battistel, K. McKelvey, A. W. Colburn, M. E. Newton, J. V. Macpherson and P. R. Unwin, *Angewandte Chemie International Edition*, 2012, **51**, 7002-7006.
33. L. Hutton, M. E. Newton, P. R. Unwin and J. V. Macpherson, *Anal. Chem.*, 2008, **81**, 1023-1032.
34. L. A. Hutton, J. G. Iacobini, E. Bitziou, R. B. Channon, M. E. Newton and J. V. Macpherson, *Anal. Chem.*, 2013, **85**, 7230-7240.
35. E. Bak, M. Donten and Z. Stojek, *Electrochem. Commun.*, 2005, **7**, 483-489.
36. W. J. Albery, A. M. Couper, J. Hadgraft and C. Ryan, *J. Chem. Soc., Faraday Trans. 1*, 1974, **70**, 1124-1131.
37. R. Compton, G. Stearn, P. Unwin and A. Barwise, *J Appl Electrochem*, 1988, **18**, 657-665.
38. J. L. Conyers and H. S. White, *Anal. Chem.*, 2000, **72**, 4441-4446.
39. W. D. Cooper and R. Parsons, *Transactions of the Faraday Society*, 1970, **66**, 1698-1712.
40. J. C. Angus, Y. V. Pleskov and S. C. Eaton, in *Semiconductors and Semimetals*, eds. E. N. Christoph and R. Jürgen, Elsevier, 2004, vol. Volume 77, pp. 97-119.

5 Electrochemical detection of phase changes in microfluidic systems

Chapter 5 describes the fabrication of microfluidic devices using traditional soft lithography techniques for producing oil/water two-phase flows in the form of droplets inhabiting a continuous phase. A simple device geometry is described for producing both “plug”-like droplets where the droplet phase occupies the entire width of the channel, and bubble-like droplets which occupy the centre of the flow profile without coming into contact with the channel walls. The direction of flow through the device geometry at different orientations dictates whether the two-phase flow profile is of the plug or bubble type. Thin-film metallic electrodes were integrated into the flow devices to detect electroactive mediators present in the aqueous droplet phase under plug flow conditions. The effect of volume flow rate and droplet size on current-time signals generated during chronoamperometric experiments at these electrodes was investigated. These measurements highlight the ability of an electrochemical sensor to determine both the phase and the velocity of a plug flow profile. Applications of such a sensor to processes requiring the assessment of multiphase flow such as those in the pharmaceutical and oil industries are highlighted.

5.1 Introduction

Microfluidic systems offer a number of attractive properties as described in chapter 1, however, they also come with limitations which are of critical importance to some applications, especially those involving two different solutions. Firstly, at such small length scales, pressure driven microfluidic systems are often characterised by parabolic velocity profiles.¹ In a flow injection analysis (FIA) type experiment, where the analyte of interest is injected into the mobile phase flow stream, the parabolic velocity profile results in axial dispersion of the analyte “plug” traversing along the channel^{2, 3} (as shown in *figure 1.23d*). This feature is of critical importance to sensory applications where dispersion of analytes results in reduced signal intensity and reduces the frequency with which samples can be analysed.⁴ However, dispersion within microfluidic channels can be reduced through careful optimisation of channel geometry^{3, 4} or the use of electrokinetic flows³. A second limitation is found

as a result of the low Reynolds numbers that characterise laminar microfluidic flows. Under laminar conditions, mixing of components within a continuous (single phase) flow, or between two parallel flows proceeds by diffusion only (see *Figure 1.23a*), which is comparatively slow to that of microfluidic timescales.⁵ This presents a problem for applications such as microfluidic reactors where efficient mixing of fluids in channels is required to reduce reaction times. In some applications laminar flow is advantageous such as in the patterning of microfluidic channels with metal films, microstructures,⁶ cell cultures⁷ or the alignment of nanotubes.⁸

Limited mixing in microfluidic channels has been addressed by the clever design of channel geometries to induce convective mixing under continuous flow conditions.⁵ However, both issues of analyte dispersion and poor mixing in microfluidic channels can be addressed by the implementation of a two-phase, segmented flow^{9, 10} either in the form of gas bubbles that segment the flow or droplets of an immiscible fluid flowing in a continuous fluid.¹¹ Dispersion of an analyte in flow can be hindered via the inclusion of gas bubble “breakers” that act to segment the continuous flow.¹² The encapsulation of an analyte within a droplet (assuming the analyte is insoluble in the continuous phase) is an effective strategy for reducing the dispersion within microfluidic flows.⁹ Droplets have proven effective for the encapsulation and analysis of biologically relevant molecules,^{13, 14} cells,^{15, 16} biological assays on bacteria¹⁷ and for microdialysis^{18, 19}. By comparison to continuous flow of two parallel streams, rapid mixing of the two components within the droplet phase; see figure *Figure 5.1a*, is observed in segmented flow due to convective flow induced inside droplets.^{9, 11, 20, 21} The same convective profile is seen in the surrounding flow between droplets;¹¹ see *Figure 5.1b*.

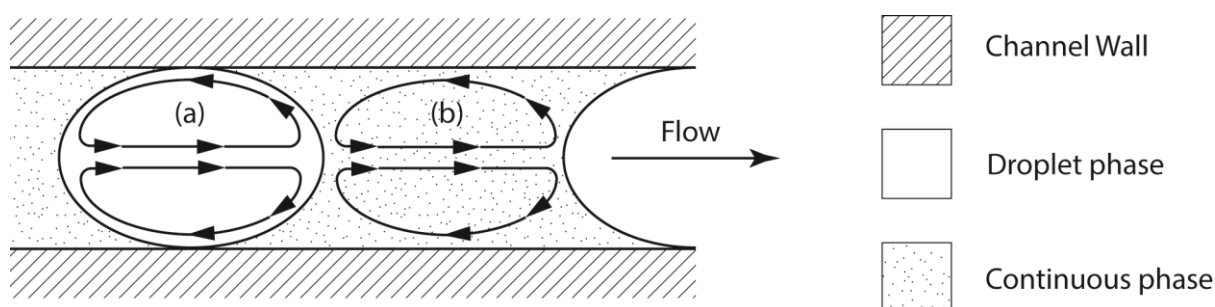


Figure 5.1: Schematic of the convective flow profile induced in (a) droplets and (b) in a continuous flow between droplets.

Droplets generated under microfluidic flows can be precisely controlled²⁰ to provide a simple method for encapsulating materials without dispersion or cross contamination between droplets.¹⁰ Such properties make droplets highly attractive for applications in biology,^{15, 22} pharmaceuticals,²³ chemical synthesis^{24, 25} and materials science.^{11, 26, 27}

Reproducibility of microdroplets generated via microfluidic devices greatly surpasses that of microdroplets produced in bulk media^{9, 28} using a homogeniser in an oil-surfactant mixture, which can see a high level of size polydispersity with size distributions of >100% reported.²⁸ Such polydispersity can be reduced using higher stirring frequencies, however, size distributions are still difficult to control²⁹ and for applications where enzymes are to be encapsulated, shear-forces generated by high frequency stirring can result in reduced enzyme activity.³⁰

Microdroplets can be formed in microfluidic channels passively i.e. without the application of an external force, using a range of geometries that rely on the induced flow field to deform the interface between two immiscible phases, a continuous phase (CP) and a droplet phase (DP), so that one phase i.e. the DP, breaks up into droplets. A number of channel geometries can be utilised, examples of which are shown in *Figure 5.2*: (a) Co-flow geometry³¹: parallel flow of the two phases causes them to meet so the DP forms into a “jet” which extends until interfacial instabilities cause the break-down of the jet into droplets. (b) A simple T-junction geometry³²: the DP flows perpendicular to the CP flow and is introduced to the CP flow via a “T”-shaped junction. The DP moves out into the CP stream, expanding out until it blocks the channel, causing an increase in pressure, up-stream from the droplet which in turn causes the droplet to be squeezed until it is “pinched” off to form a droplet. In microfluidic systems, at flow rates between 0.01 – 1 $\mu\text{L/s}$ and channel dimensions of the order of 100 μm , the size of droplets formed in T-junction devices is dependent entirely upon the ratio of volume flow rates, V_f , of DP and CP, as described by the following:³³

$$D_L / d_c = 1 + \alpha_g \frac{V_{f(DP)}}{V_{f(CP)}}$$

5.1

where D_L is the droplet length, d_c is the channel width and α_g is a geometry dependent constant. (c) The flow focus geometry³⁴ uses the coaxial flow of the two immiscible phases where the CP flows either side of the DP to deform the DP via elongation towards a constriction in the channel geometry. This forces the DP to form a thin neck which then breaks down into monodisperse droplets.

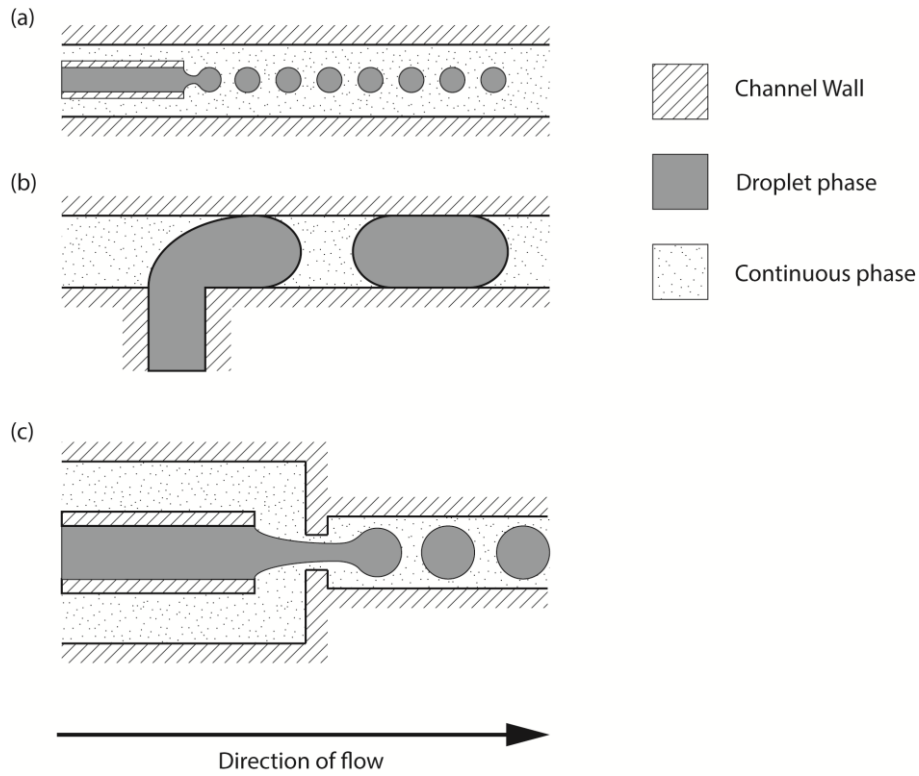


Figure 5.2: Schematics of common microfluidic droplet generating geometries: (a) Co-flow; (b) Restricted T-junction; and (c) Flow-focussing.

The dynamics of droplet break up in microfluidic channels greatly depend on the geometry of the channel as well as both viscous and interfacial forces. The formation of a droplet is governed by the viscous stresses and the dynamic pressure field surrounding an emerging droplet.³⁵ A measure of the interplay between viscous and interfacial forces is known as the Capillary number, Ca defined as³³

$$Ca = \mu U \gamma_i$$

5.2

where μ is the viscosity, and U is the mean velocity of the CP, and γ_i is the interfacial tension. For typical microfluidic systems, Ca is small (i.e. < 0.01)³³ which means the shear forces acting on the forming droplet are too weak to deform the droplet sufficiently to cause “pinch off”. Instead, the droplet is allowed to extend out into the channel, blocking the channel and forcing the CP flow through thin films on the channel wall inducing a pressure increase ahead of the forming droplet. The increasing pressure acts to squeeze the droplet so that the stream running between droplet and the channel introducing the DP into the main channel begins to thin. Eventually, this stream is broken and a droplet is formed. The time taken for the droplet to break off is dependent on V_f of the CP. The rate of growth during this time is dependent on V_f of the DP.³³ This is described in equation 5.1.

It is often common to add a surfactant to the CP in order to allow the formation and stabilisation of interfaces during droplet generation by lowering the interfacial energy.¹⁰ This prevents droplets from coalescing inside the channel. Surfactants were not used in this work as it was expected to interfere with electrochemistry at the droplet/electrode interface.

5.2 Results and Discussion

In this work, the design and fabrication of microfluidic devices for generating droplets of immiscible fluid in a continuous flow are described. A number of geometries are presented for producing both “plug”-like droplets that occupy the entire channel diameter as well as “bubble”-like droplets that have diameters smaller than that of the channel and do not touch the channel walls. Work then describes the integration of thin-film metal electrodes in the microfluidics channel in order to analyse droplet generation in terms of droplet size and velocity.

5.2.1 Fabrication of PDMS microfluidic devices

5.2.1.1 Mould fabrication from SU-8 photoresist

SU8-2100 photoresist (1 mL per 25 mm²) was spin-coated onto a 4" silicon wafer at a rotation speed of 3000 rpm for 30 s. This procedure produced a resist film approximately 100 µm thick. The wafer was then placed onto a leveled plate, lightly sprayed with EC solvent and left for 24 hrs heated to 25 °C, until the majority of solvent had evaporated. The wafer was then subjected to a soft bake program of 10 min at 65 °C followed by 30 mins at 95 °C on a levelled hotplate with temperature steps of 10°C every 10 mins. After cooling to room temperature, photolithography was applied to transfer a microfluidic channel design onto the SU8 photoresist using a UV-mask aligner (SUSS MicroTec). Microfluidic channel designs were incorporated into photofilm-emulsion acetate masks (JD Photo-tools, UK), aligned over the SU8 coated wafer and exposed to an Hg, 365 nm UV lamp for a 20 s. The wafer was then placed on a hot plate at 65 °C for 10 mins followed by 95 °C for 30 mins. After cooling to room temperature, the wafer was developed in EC solvent for 17 mins with mild agitation, removing all but the exposed SU-8 resist. The wafer was then washed with EC solvent followed by isopropyl alcohol, rinsed with deionised water and then dried with N₂.

Initial work fabricating SU-8 moulds presented a series of issues originating from the spin-coating of the SU-8 photoresist and photolithography. The SU-8 is first deposited onto a clean Si wafer; however this process results in a circular "puddle" in the center of the wafer. During the spin-coating process, centrifugal forces cause the SU-8 to spread out across from the center to the edge of the wafer. The SU-8 at the very edge of the wafer and on the leading edge of the spreading material experiences a higher degree of solvent evaporation resulting in a drop in the mobility of the SU-8 material making up the leading edge. Material behind the leading edge is then forced up and over this slower moving material resulting in the formation of an edge-bead: see *Figure 5.3*.

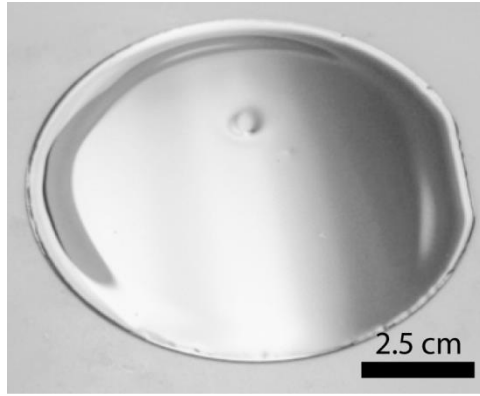


Figure 5.3: Photo of a 4" silicon wafer after spincoating with SU-8 photoresist. Edge-bead and air bubbles are present in photoresist.

The formation of the edge bead and air bubbles results in a heterogeneous resist thickness. This is particularly problematic during the photolithography process as the mask will not be in contact with the surface of the resist in the center of the wafer where the channel designs are patterned, during the UV exposure. The further away from the surface the mask is, the greater diffraction will occur during UV exposure causing the channel dimensions to become wider than intended.

Spraying the resist coated wafer post-spincoating with Microposit EC solvent and leaving on a leveled plate at 25 °C for 24 hours was found to remove both edge bead and air bubbles from the resist; see *Figure 5.4*. The literature also states that edge beads formed during spin coating can be removed by wiping the wafer edge with a solvent such as acetone.³⁶ Upon spraying the resist with EC solvent, the viscosity of the SU-8 is reduced allowing greater mobility of the resist. Areas such as edge bead and air bubbles are then eliminated.

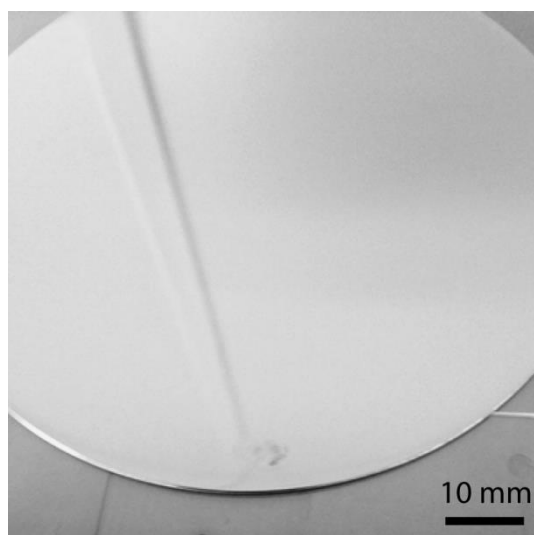


Figure 5.4: Photo of a 4" silicon wafer spincoated with SU-8, sprayed with EC solvent and left 24 hrs on a levelled hotplate at 25° C.

Although the dimensions of the patterned channels were improved with the EC solvent spray procedure, the SU-8 patterned wafers were not robust with some wafers not even surviving a single moulding with PDMS. Much of the SU-8 patterned features on the surface of the Si wafer would "pull-off" with the separation of the PDMS from the wafer; see *Figure 5.5*.

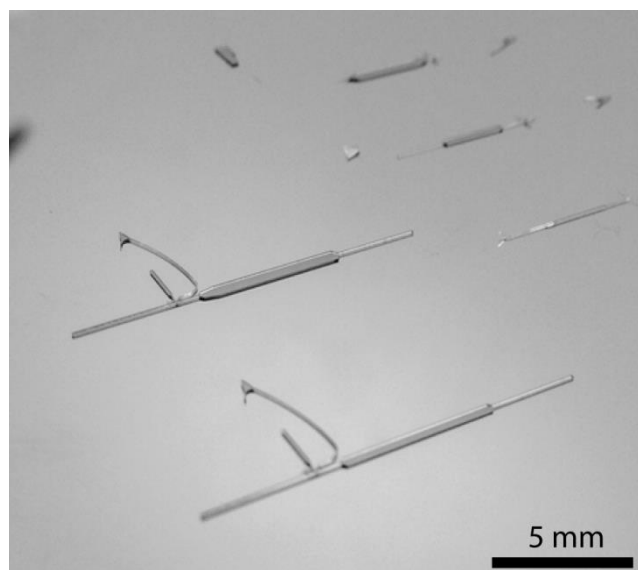


Figure 5.5: Photo of SU-8 patterned features on a 4" silicon wafer, broken after PDMS moulding.

SU-8 moulds of greater durability were achieved by ensuring the silicon substrate was clean of any grease or other contaminants. Submersion of the silicon wafer in a dilute solution of 4-5 % HF (VWR, France) for 10 s followed by rinsing in deionised water and drying under N₂ ensured the wafer was clean before spin coating. Slowly raising the temperature of the freshly spun wafer by 5 °C every 10 mins during the soft baking step resulted in fewer bubbles and distortions in the SU-8 layer. During heating of the SU-8 coated wafer, the mobilising solvent in the SU-8 layer (cyclopentanone)³⁷ must move through the resist from the surface of the wafer to the top surface of the SU-8 layer. If the resin layer is heated too quickly, the evaporating solvent creates bubbles in the resist as it becomes trapped at the SU-8/air interface. The mobilising solvent passes through the resin at a slower rate under shallower heating ramps which results in fewer bubbles forming under the resist and aids a smooth surface finish.

Development of SU-8 features in EC solvent post hard bake was performed so that exposure to the EC solvent was kept to a minimum. Greater agitation of the developer over the SU-8 features was performed in order to reduce the solvent exposure time. Although UV exposed photoresist exhibits greater resistance to the EC solvent, it was found that SU-8 features exposed to the EC solvent for the minimum amount of time showed greatest durability after development and during PDMS moulding.

5.2.1.2 Mould fabrication from RIE-ICP Si etching

Figure 5.6 shows a schematic for the fabrication of PDMS moulds using reactive ion etching inductively coupled plasma, (RIE-ICP): (a) clean silicon wafer is treated with primer, (b) PMGISF6 photoresist (Microchem, Newton, MA) is spin-coated (3000 rpm for 30 s) onto the wafer, baked at 170 °C for 10 mins, then flood exposed for 1 min under a 230-290 nm UV lamp. S1818 photoresist (Rohm and Haas, Denmark) is then spin-coated (3000 rpm for 4 s) onto the wafer, baked at 115 °C for 1 min. (c) The wafer is exposed to UV for 5 s using a mask aligner, then developed in MF-319 microposit developer (Rohm and Haas) for 1 min. (d) 250 nm of aluminum or nickel was sputtered onto the developed wafer using an automated sputtering system (Equipment Support Co. Ltd, England). (e) The wafer is then submerged in acetone to remove the S1818 photoresist and lift off any Al/Ni not forming the channel pattern. The PMGISF6 is then removed using MF-319. (f) After

inspection under a microscope, the patterned Si wafer is inserted into the Corial 200 IL RIE-ICP system (Corial, France). RIE-ICP system is run using 50 sccm SF_6 and 3 sccm O_2 at 10 mTorr, 5 °C producing an etch rate of around 500 nm/min. Si wafers were etched for 2 hrs producing a channel height of approximately 60 μm . Moulds such as both this and SU-8 are capable of containing multiple chip designs reducing the amount of fabrication necessary for an investigation of channel design.

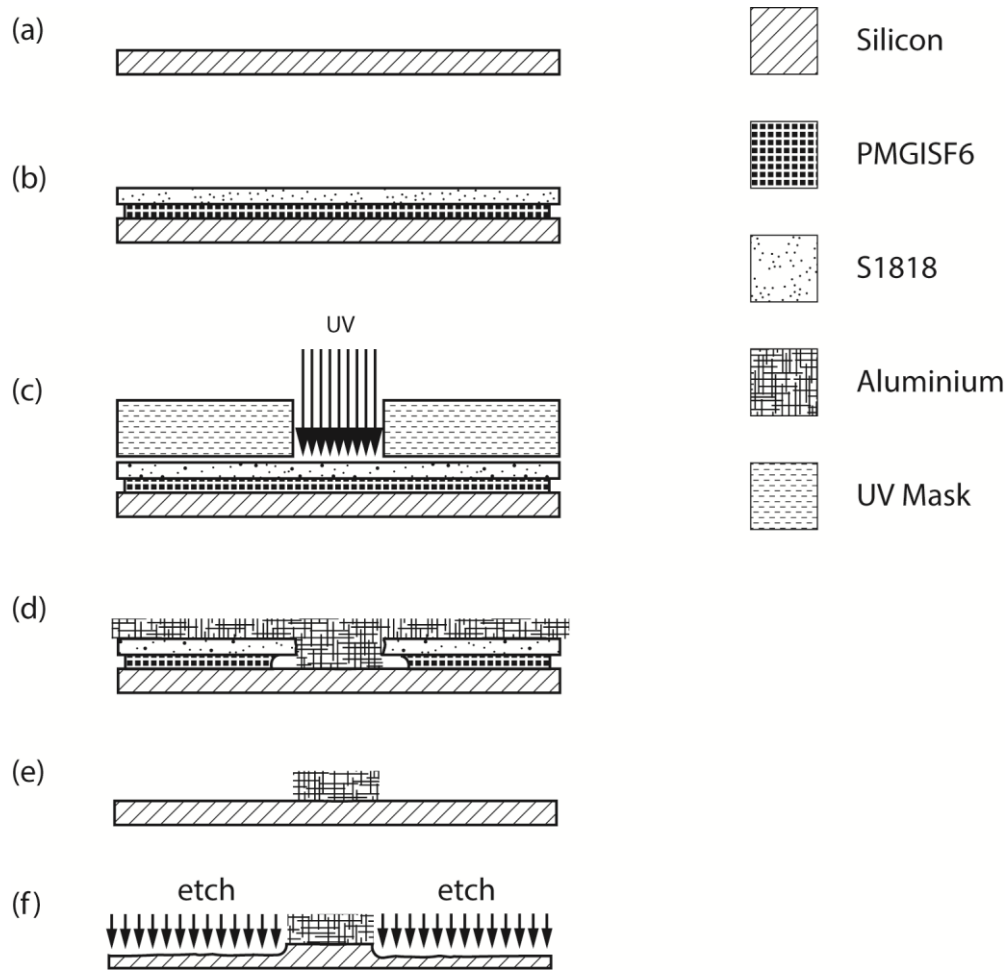


Figure 5.6: Schematic of silicon mould fabrication using RIE-ICP: (a) Silicon substrate is cleaned; (b) PMGISF6 deep UV resist and S1818 photoresists are spincoated onto the Si wafer; (c) Resists are exposed to UV through a patterned UV mask, and developed in MF-319 developer; (d) a thin film of metal e.g. aluminium is sputter deposited onto the patterned wafer; (e) metal “lift-off” is performed in acetone, dissolving the underlying photoresist; (f) silicon not protected by the metal film is etched by the RIE plasma to produce microfeatures in the silicon wafer.

The development of the Si etching process using RIE-ICP offered an alternative to the SU-8 patterning method for producing microfluidic chip moulds (see *Figure 5.7*) with a much higher success rate and increased robustness. The depth of the RIE-ICP etch process was found to be limited

by the metal mask used for the patterning. Al metal masks were initially tried but the etch depth was limited to approximately 30 μm due to the etch rate of the Al being too high for the metal mask to survive beyond 2 hours. With the etch rate being approximately 30 μm per hour, a new mask was necessary to achieve greater etching depths. Ni has been reported in the literature to etch at a rate around 3 times slower than Al.³⁸ Etches using Ni as a mask were used to achieve etch depths between 50 – 60 μm .

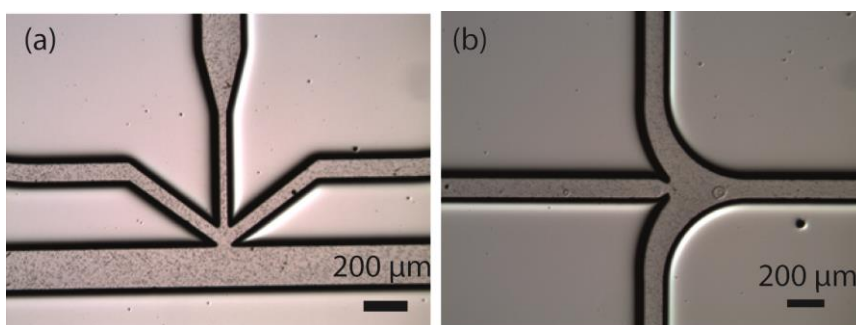


Figure 5.7: Silicon microfeatures created by RIE-ICP etching: (a) 3-armed T-junction device; (b) focus flow device

5.2.1.3 PDMS moulding

Scotch tape was first wrapped around a patterned Si wafer mould (both SU-8 and RIE etched moulds were used throughout this work) creating a wall around the wafer. PDMS Sylgard 184 silicon elastomer (Dow Corning, US) was added to the setting agent in a 10:1 ratio (elastomer: setting agent) then mixed thoroughly and degassed using a vacuum desiccator. The mixture was poured onto the mould wafer and degassed as before. Once bubble free the PDMS and mould were placed in an oven at 70 °C for 3 hours to set. Once set, the PDMS was cut into individual chips, the inlets punched through using a 1 mm and 2 mm diameter Harris Uni-core (Sigma Aldrich, UK). A glass microscope slide was placed in the oxygen (O_2)-plasma asher along with a corresponding PDMS chip, ensuring the patterned side of the PDMS chip faced towards the plasma. Both components were exposed to an O_2 plasma for 40 s at 100 W. This process oxygen-functionalises both the glass and PDMS surface with Si-O groups³⁹. Lightly pressing these two surfaces together allows an irreversible bond³⁹ to form between the PDMS and glass through the Si-O-Si functionalities. After combining the two faces, the

PDMS/glass chip was left for 5 min. In order to preserve the O₂ functionalisation, i.e. hydrophilic surfaces inside the microfluidic channels, the channels were filled with water and capped with 5 min epoxy (RS components, UK) to prevent evaporation. If hydrophobic surfaces are desired, the PDMS/Glass chips were left in air for > 24 hrs. Leaving the PDMS channels in air after O₂ plasma treatment allows low-molecular-weight polymer chains to migrate to the channel surface, creating a hydrophobic surface.⁴⁰

5.2.2 Droplet generation geometries

Three microfluidic droplet generators have been investigated, as shown in *Figure 5.8*, (a) 3-armed T-junction device, (b) simple T-junction and (c) flow focus device.

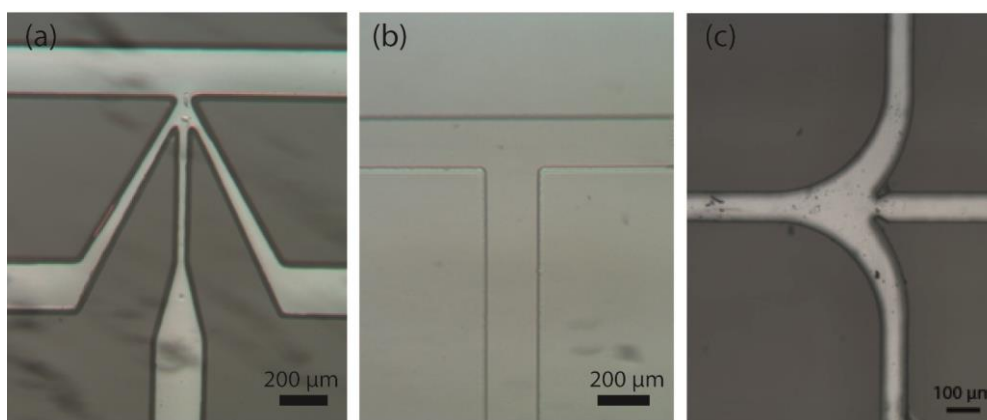


Figure 5.8: Microscope images of (a) 3-armed T-junction device; (b) a simple T-junction device; and (c) a focus flow device, all created from SU-8 moulds, with no flow.

Initial work with these devices used dodecane (oil). However, it was found that PDMS devices swelled after period of around 15 minutes upon exposure to dodecane causing the channels to distort producing uncontrollable flow and droplet formation; see *Figure 5.9*. The same effect was observed to a far greater extent when using hexane with PDMS. Swelling occurred immediately upon exposure to the solvent; see *Figure 5.10*. In light of this, octanol and mineral oil were adopted as the oil phase as they caused little or no swelling of the PDMS chips. The use of PDMS as a material for microfluidic chips is unfortunately limited to aqueous and certain organic polar solvents⁴¹ due to this inherent swelling problem and dissolution of the PDMS polymer. Alternative materials to PDMS include

polymethyl methacrylate (PMMA)⁴² and glass⁴³. Glass is a particularly attractive alternative as it remains unaffected by polar or non-polar solvents. Synthetic diamond can also be considered for the same reasons as glass, see Chapter 6, but with the added benefits of chemical resistance and ability to incorporate co-planar boron doped diamond electrodes into an all diamond device⁴⁴.

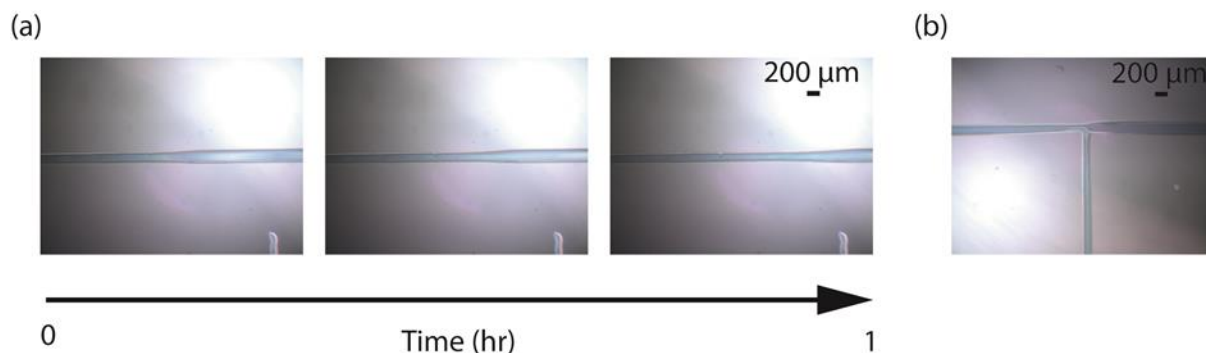


Figure 5.9: (a) Microscope images of a PDMS device under a flow of dodecane and aqueous solution containing blue dye. Images show the extent of PDMS swelling due to dodecane over the space of an hour; (b) T-junction geometry after an hour of flow with dodecane

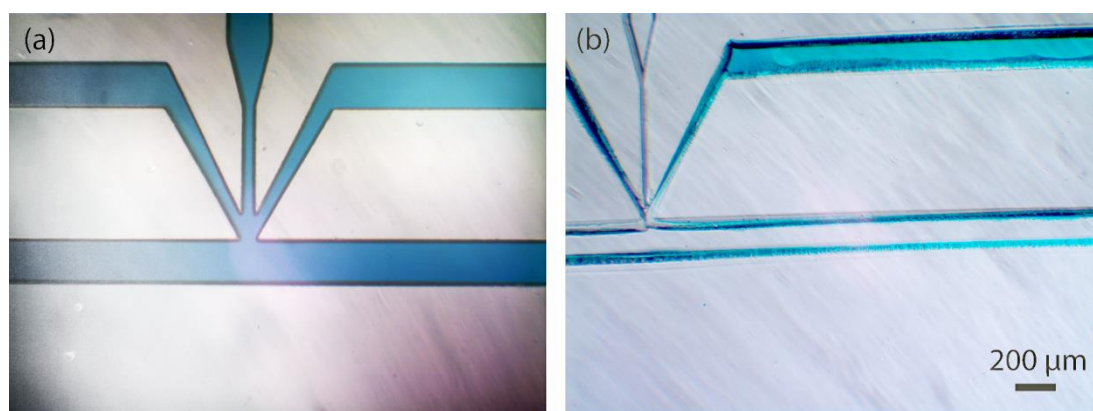


Figure 5.10: (a) 3-armed T-junction device under a flow of aqueous solution containing blue dye; (b) device after introduction of hexane.

All three devices in *Figure 5.8* were fabricated using a SU-8 patterned wafer mould. *Figure 5.11* and *Figure 5.12* show both the 3-armed T-junction devices and simple T-junction respectively, generating droplets of octanol (non-polar oil) into (in both cases) a 200 μm wide, 150 μm high channel with a continuous water phase containing a blue food colouring dye (Dr. Oetker, Germany). Droplets

produced by the 3-armed T-junction (*Figure 5.11*) appear smaller by comparison to the droplets produced by the simple T-junction device shown in *Figure 5.12* which is unexpected given that the ratio of V_f for CP vs. DP is the same in both devices. One would expect that the produced droplets would be of a similar size. This observation may be a product of the flow focussing action seen at the 3-armed T-junction device as the DP is surrounded by CP at the point before entering the T-junction geometry, the amount of DP reaching the T-junction geometry for droplet “pinch-off” is smaller than that for the simple T-junction where only the DP is in the channel perpendicular to the CP flow. Also, the entrance channel for the DP into the main CP channel is smaller in the 3-armed T-junction device compared with the simple T-junction i.e. 100 μm wide compared to 200 μm wide. This undoubtedly plays a role in determining the droplet size.

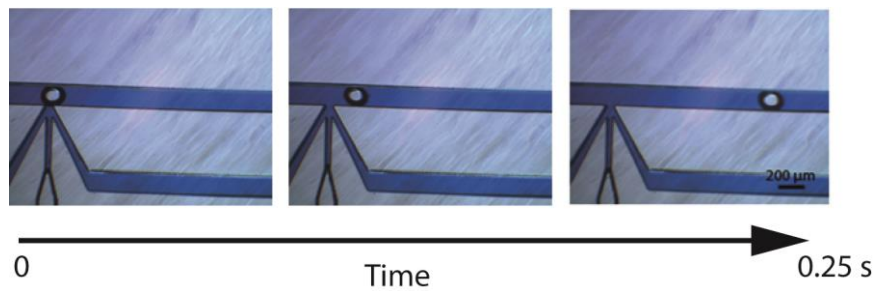


Figure 5.11: Microscope images of a 3-armed T-junction generating droplets of octanol (DP) in a 200 μm wide, 150 μm high channel with a continuous aqueous phase containing a blue dye (CP). $V_f = 0.1$ and 1 $\mu\text{L}/\text{min}$ for DP and CP respectively.

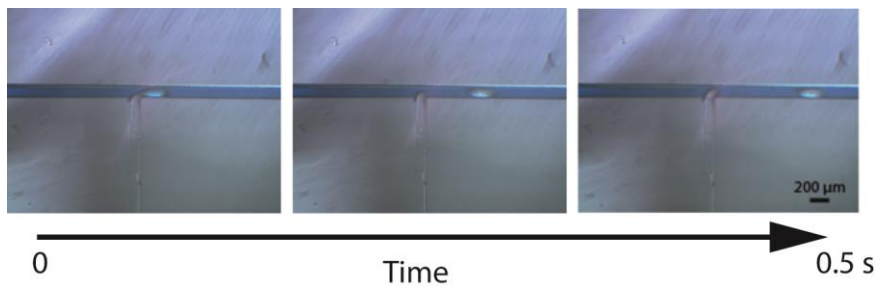


Figure 5.12: Microscope images of a simple T-junction generating droplets of octanol (DP) in a 200 μm wide, 150 μm high channel with a continuous aqueous phase containing a blue dye (CP). $V_f = 0.1$ and 1 $\mu\text{L}/\text{min}$ for DP and CP respectively.

A fourth microfluidic geometry was fabricated consisting of an asymmetric rectangular cross-junction focus-flow arrangement with a narrowed channel adjacent to two unequal-width channels; as shown

in *Figure 5.13*. The orientation of the device was reversed so that the DP flowed in different directions: towards the channel restriction after meeting the CP (*Figure 5.14a*) or passing through the channel restriction before meeting the CP (*Figure 5.14b*). The orientation of this focus-flow device had a drastic effect on the resulting droplet flow; see *Figure 5.15*.

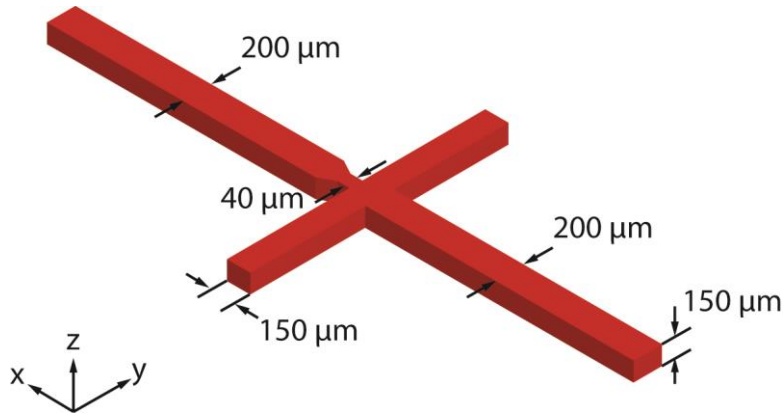


Figure 5.13: A three-dimensional schematic of a focus-flow geometry with a 40 μm restriction at the intersection point between a 150 μm wide channel and a 200 μm wide channel. The height of the channels is 150 μm .

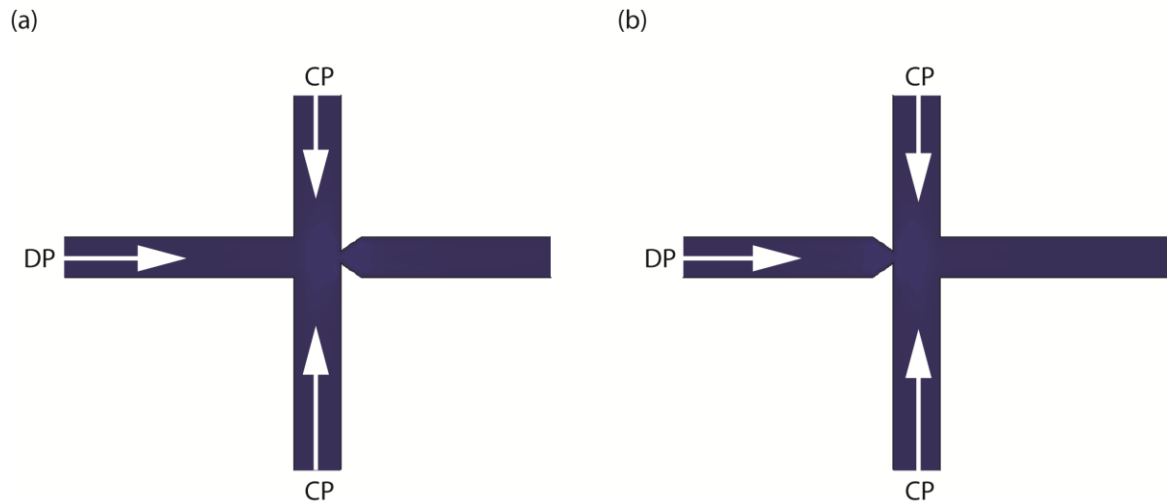


Figure 5.14: Droplet geometry orientations for producing: (a) “bubble”-like droplets; (b) “plug”-like droplets.

In the orientation where the DP reaches the channel restriction after meeting the CP, “pinch-off” of the droplet occurs soon after the DP contacts the edges of the restricted channel upon expansion of the DP into the focus-flow geometry. This leads to the formation of highly reproducible “bubble”-like droplets with diameters smaller than the channel width, where the droplets do not touch the channel

walls. The size and frequency of droplets generated were found to be dependent on V_f ratio of DP to CP as shown in *Figure 5.16* where DP is water and CP is mineral oil. The plot in *Figure 5.16e* shows the relationship between the “bubble”-like droplet diameter (measured via optical microscopy $\pm 2 \mu\text{m}$) as a function of $V_f(\text{DP}) / V_f(\text{CP})$. It suggests a non-linear increase in droplet diameter with increasing $V_f(\text{DP}) / V_f(\text{CP})$. It is expected that maintaining the ratio of $V_f(\text{DP}) : V_f(\text{CP})$ while increasing the total V_f in the channel will result in a constant droplet size but an increasing frequency of droplet generation. This has been found in work on droplet analysis.⁴⁵ As shown in equation 5.1, for “plug”-like droplets formed by T-junction devices, the size of droplets is also determined by the ratio of $V_f(\text{DP}) / V_f(\text{CP})$.³³ The frequency of droplets generated also appears to increase with increasing $V_f(\text{DP}) / V_f(\text{CP})$. However, limitations in the capture rate of the digital camera used to record droplet generation, made it difficult to obtain information on droplet frequency at V_f faster than $2 \mu\text{L}/\text{min}$.

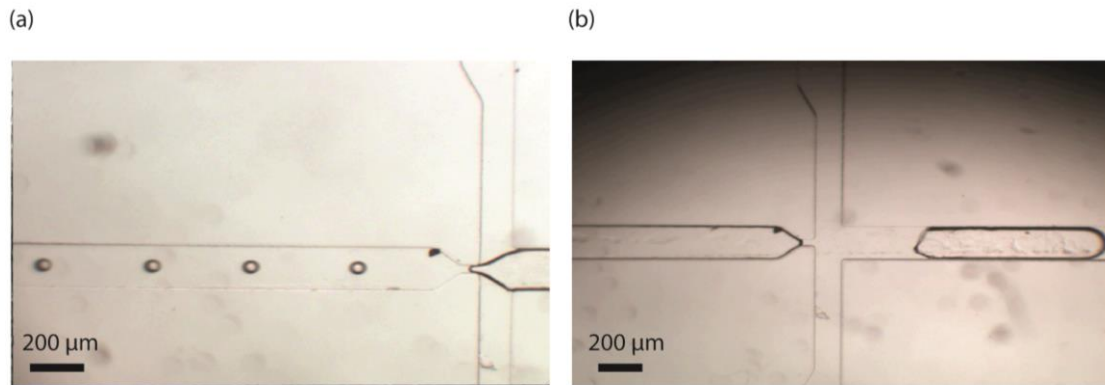


Figure 5.15: Microscope images of focus flow geometry producing (a) “bubble”-like droplets, $V_f(\text{DP}:\text{CP}) = 0.02 \mu\text{L}/\text{min}: 1.3 \mu\text{L}/\text{min}$ and (b) “plug”-like droplets, $V_f(\text{DP}:\text{CP}) = 1 \mu\text{L}/\text{min}: 2 \mu\text{L}/\text{min}$

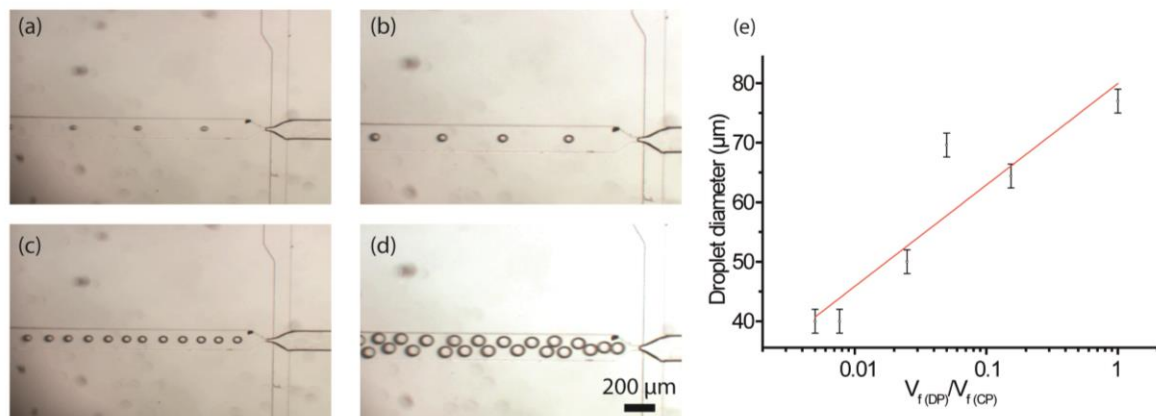


Figure 5.16: “bubble”-like water droplet generation, in mineral oil CP, within a focus flow geometry under different relative $V_f(DP:CP)$: (a) 0.05 $\mu\text{L}/\text{min}$: 2 $\mu\text{L}/\text{min}$, (b) 0.2 $\mu\text{L}/\text{min}$: 1.3 $\mu\text{L}/\text{min}$, (c) 0.05 $\mu\text{L}/\text{min}$: 1 $\mu\text{L}/\text{min}$, (d) 1 $\mu\text{L}/\text{min}$: 1 $\mu\text{L}/\text{min}$; (e) Plot of droplet diameter as measured via microscopy ($N = 15$) as a function of $V_f(DP)/V_f(CP)$.

Under the alternative orientation (Figure 5.14b), the DP expands out from the restricted channel into the focus-flow geometry with droplet “pinch-off” occurring after the DP has fully expanded into the adjacent channel. This results in “plug”-like droplets that have a diameter equal to that of the channel width; see Figure 5.17. The dependence of plug droplet size with $V_f(DP)/V_f(CP)$ is explored later with an electrochemical sensor.

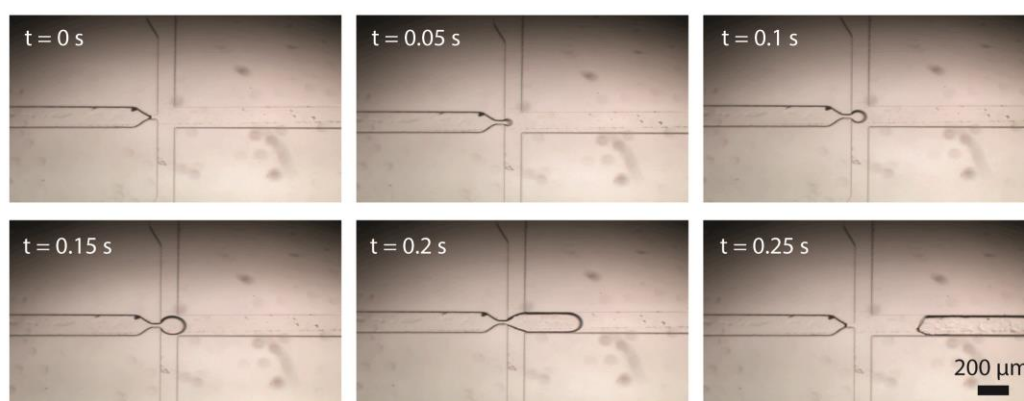


Figure 5.17: “plug”-like water droplet generation in mineral oil CP, within a focus flow geometry $V_f(DP):V_f(CP) = 1\text{ }\mu\text{L}/\text{min}:2\text{ }\mu\text{L}/\text{min}$.

5.2.3 Integration of thin-film metal electrodes in microfluidic devices

Electrochemistry as an analysis method provides a great deal of information on chemical processes such as mass transfer and kinetics of reactions but also presents a simple, low cost alternative to techniques already employed in microfluidic platforms such as mass spectrometry,⁴⁶ Raman spectroscopy⁴⁷ and fluorescence spectroscopy.⁴⁸ Electrochemical systems have found applications on microfluidic chips⁴⁹ as a means to drive microfluidic flow,⁵⁰ as a sensor⁴⁹ and in microdroplet detection using electrolysis,⁵¹ capacitive sensors⁵² and electrical impedance.⁵³

5.2.3.1 Fabrication

Glass microscope slides were spin-coated with S1818 and masked using photolithography. Each slide contained three sets of four electrodes. An adhesion layer of 10 nm titanium followed by a 200 nm layer of platinum or gold was sputtered onto the slides before lift-off with acetone. Each glass slide was O₂ bonded to a PDMS chip as described previously, each chip consisting of three sets of 4 electrodes positioned at equal distance (18 mm) along a 200 μ m wide, 100 μ m high channel. Of the four thin-film electrodes fabricated as a set, only three were used and were configured as reference electrode (80 μ m width), working electrode (40 μ m width) and counter electrode (400 μ m width) where the separations between electrodes was 80 μ m (reference to working) and 40 μ m (working to counter); as shown in *Figure 5.18*.

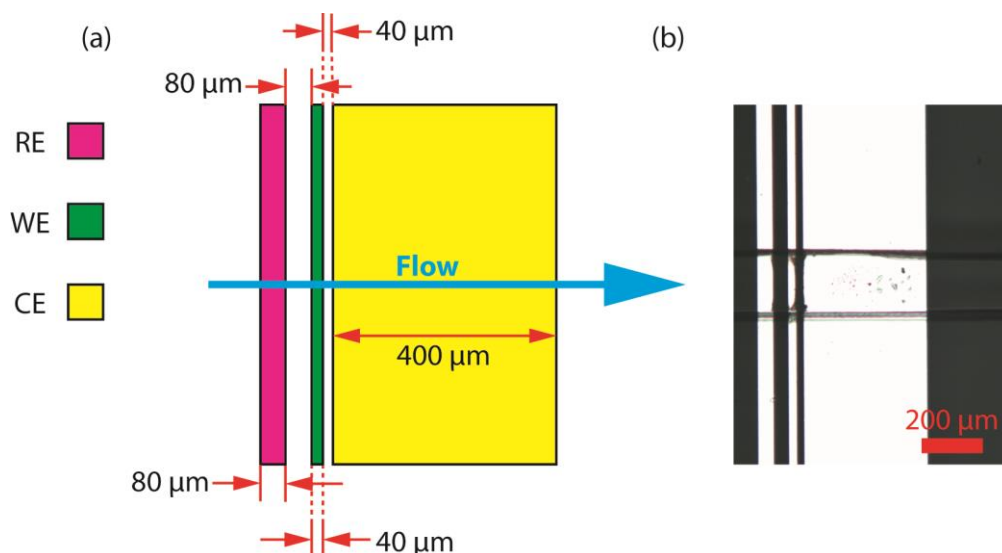


Figure 5.18: (a) Schematic of channel electrodes consisting of reference electrode (RE: 80 μm width), working electrode (WE: 40 μm width) and counter electrode (CE: 400 μm width); (b) optical image of Pt channel electrodes integrated into a PDMS microfluidic channel (200 × 100 μm, w × h)

The ordering of the electrodes relative to the flow direction as well as the inter-electrode distance is of critical importance. Firstly, the proximity of the electrodes must be sufficient to avoid effects from uncompensated resistance, namely the inter-electrode distance between the working and reference electrode should be minimised.⁵⁴ Uncompensated resistance can also occur as a result of inadequate conductance of the cell solution or inherent resistance in the electrode material, and so these should also be addressed. Under flow, any species generated at an upstream electrode is carried downstream to neighbouring electrodes. The order of electrodes relative to the flow direction is of particular importance for electrodes that are sensitive to solution changes which may impact on how they function; as is the case for the reference electrode. Hence this electrode is the first electrode placed upstream. Equally, placement of the working electrode should be chosen to avoid reactions at the counter electrode. This latter electrode is thus placed the furthest downstream.

5.2.3.2 Electrochemical characterisation

A single channel (200 μm width, 100 μm height) device with integrated electrodes was set up on an inverted microscope with inlets for DP, CP and outlets, connected using Teflon tubing (Cole Parmer Ltd., UK) push fitted into 1-10 μl Finn pipette tips (Cole Parmer Ltd., UK) which were then pressed

into the inlet holes punched into the PDMS chip as described previously. Electrode contacts were made via a pin attached to a set of micropositioners (Newport, UK), and connected to a potentiostat (CH Instruments, USA). A schematic of the set-up is shown in *Figure 5.19*.

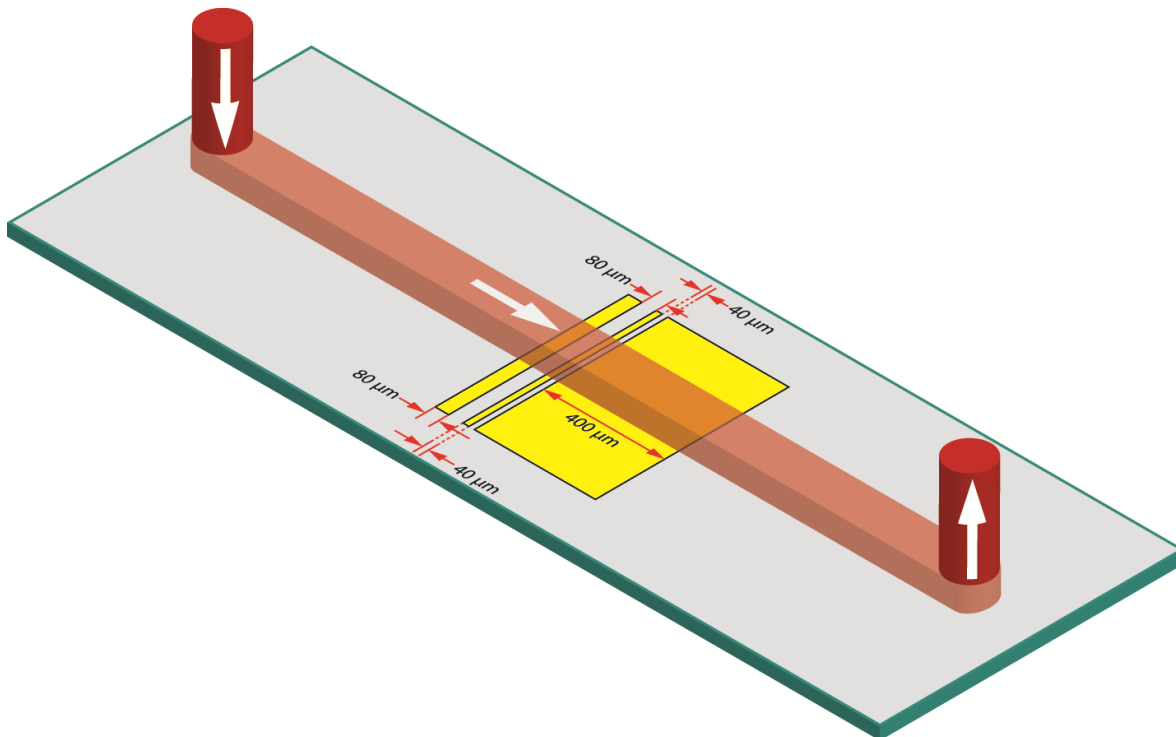


Figure 5.19: A schematic of a single channel microfluidic device (200 μm width, 150 μm height, 50 mm long) shown in red with integrated electrodes shown in yellow supported on a glass slide. PDMS has been omitted for clarity.

In order to verify mass transport to the working electrode within the single 200 μm wide, 150 μm high microfluidic channel (see *Figure 5.19*) electrochemical measurements on Au band electrodes (*Figure 5.18*) were carried out using a simple one electron, outer-sphere mediator couple, FcTMA⁺²⁺ ($E_o = 0.37$ V vs. SCE). LSV responses (*Figure 5.20a*) for V_f (where $V_f = V_f(\text{CP}) + V_f(\text{DP})$) in the range 0 – 100 μl/min were recorded using 1 mM FcTMA⁺ in 0.1 M KNO₃. Under laminar flow conditions and with the application of the L  v  que approximation⁵⁵, the limiting current on a band electrode in a channel can be described by the Levich equation:⁵⁶

$$i_{\text{lim}} = 1.165nF[O]D_o^{2/3}U^{1/3}h^{-1/3}wx_e^{2/3}$$

where $[O]$ is the bulk concentration of the mediator (mol/cm^3), D_O is the diffusion coefficient ($D_{\text{FcTMA}^+} = 8 \times 10^{-6} \text{ cm}^2/\text{s}$), h is the height of the microfluidic channel, d_c is the width of the microfluidic channel (cm), w and x_e are the width (cm) and length (cm) of the band electrode respectively. U is the mean fluid velocity (cm/s), which is related to V_f (cm^3/s) via⁵⁷:

$$U = \frac{V_f}{2hd_c}$$

5.4

Under stationary conditions i.e. no flow, the LSV response shows a current peak for FcTMA^+ oxidation around 0.4 V vs. the Au quasi-reference electrode. This is a similar potential position to that expected for a system using a traditional reference electrode such as AgCl .⁴⁴ As V_f is increased from 0 to 100 $\mu\text{L}/\text{min}$, the LSV attains a steady-state (i_{lim}) current *Figure 5.20a*, and increases in magnitude. The i_{lim} data is linear with respect to $V_f^{1/3}$ ($R^2 = 0.9998$) as shown in *Figure 5.20b* (Δ experimental). In this plot a comparison with Levich (equation 5.3) behaviour was also made (\blacksquare Levich).

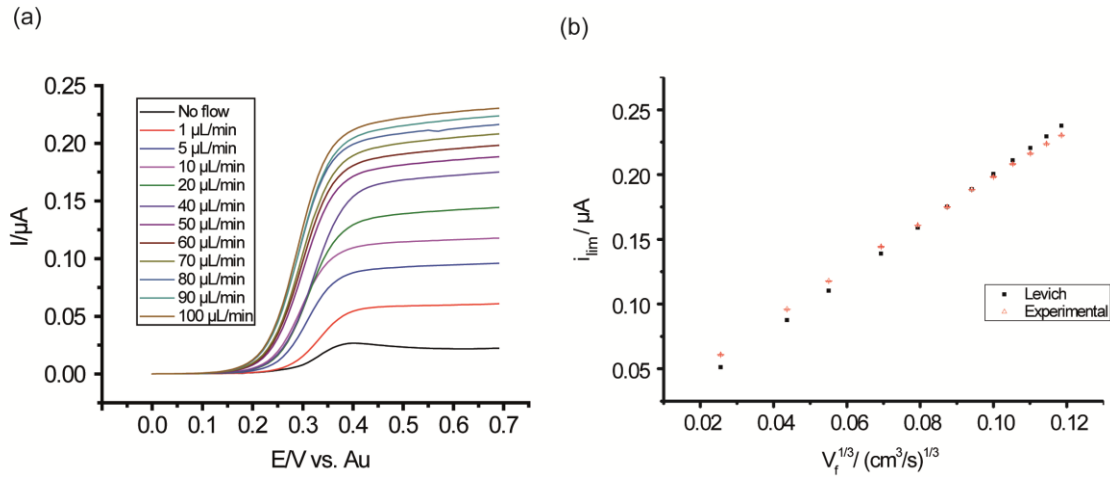


Figure 5.20: (a) LSV responses of microfluidic channel electrodes for 1 mM FcTMA^+ with 0.1 M KNO_3 under various flow rates; (b) Plot of I_{lim} vs. $V_f^{1/3}$ for LSV responses at various flow rates: comparing experimental (red triangle) to Levich fitted to experimental (black square) with $h = 75 \mu\text{m}$ and both d and $w = 290 \mu\text{m}$.

Here the height and width of the microfluidic channel were adjusted from the values measured in air using a stylus-profiler in order to obtain good agreement with the experimental data. The Levich

theory plot used values of $h = 75 \mu\text{m}$ with both d_c and $w = 290 \mu\text{m}$ to fit experimental data. This fit suggests the microfluidic channel was distorted during fabrication, reducing the channel height while broadening the channel width. This is quite possible as the PDMS is pressed against the glass slide immediately after O_2 plasma treatment. If the channel was squashed during this fabrication step, the channel dimensions can be expected to have changed since measuring the SU-8 mould with the stylus-profiler. The entrance length of the flow is around 25 mm, as such, laminar flow most certainly would have been established in the channel, suggesting the device should fit Levich. Confirmation of the actual channel geometry could be made using interferometry through the glass slide supporting the PDMS channel, however, this would be challenging due to the refractive interference of the glass on the measurement.⁵⁸

At a V_f of 30 $\mu\text{L}/\text{min}$ the half wave potential, $E_{1/2}$, shifts slightly more positive by 40 mV, which is most likely due to the use of a non-conventional reference electrode (Au), the potential of which will depend on the solution composition and surface charge. This shift in wave potential can be seen in *Table 5.1* which shows $E_{1/2}$ as a function of V_f . This shift may have been caused by surface fouling, which was then removed during the subsequent increase in V_f .

V_f ($\mu\text{L}/\text{min}$)	1	5	10	20	30	40	50	60	70	80	90	100
$E_{1/2}$ (V) $\pm 1 \text{ mV}$	0.32	0.31	0.30	0.31	0.35	0.32	0.30	0.30	0.30	0.29	0.29	0.29

Table 5.1: $E_{1/2}$ of LSV waves recorded on channel electrodes in a single channel (200 μm width, 100 μm height) microfluidic device as a function of V_f .

Reference electrode instability can be combated using a stable classical reference such as $\text{Ag}|\text{AgCl}$, placed in the outlet of the microfluidic device. However, this can result in increased electrical resistance as the distance between the working and reference is increased.⁵⁴ The discontinuous nature of segmented, droplet flow also makes the adoption of a reference electrode in the outlet impractical for droplet flow experiments as the solution connection between the reference and working electrodes

would be blocked by the insulating oil phase. Another strategy to provide a more stable reference electrode in-chip is to electrodeposit a film of Ag onto the reference band electrode, the Ag coated band acting as a quasi-reference electrode^{45, 59} or chloridising the Ag to turn into AgCl.^{59, 60} Other reports of an AgCl reference electrode with a liquid junction, integrated in a microfluidic chip have been made.⁶¹

5.2.4 Electrochemical detection of water droplets containing an electroactive mediator

Before introducing electroactive mediator, flow experiments were carried out with just electrolyte (0.1 M KNO₃) present in the DP. A focus flow device described in *Figure 5.13* was orientated to generate “plug”-like droplets and fabricated with integrated gold band electrodes described in *Figure 5.18*. A schematic of this device is shown in *Figure 5.21*.

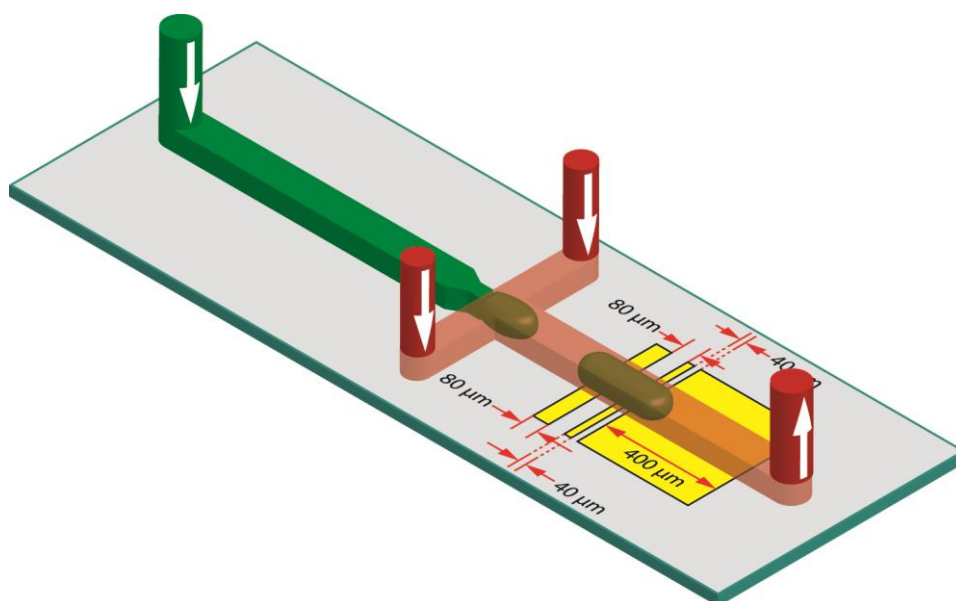


Figure 5.21: Schematic of focus-flow device for generating “plug”-like droplets of electrolyte solution (green) in a continuous flow of mineral oil (red) with integrated electrodes shown in yellow.

In order to generate an electrochemical signal from the channel electrodes, all three electrodes must be in contact with electrolyte solution in order to create an electrochemical cell (*Figure 5.22a*). This places limitations on the types of droplets detectable by this electrode system as droplets need to be large enough to bridge all three electrodes i.e. have a length of $> 160\ \mu\text{m}$ (*Figure 5.22b*). However,

this is only the case for “plug”-like droplets since “bubble”-like droplets, by comparison, do not make contact with the channel walls and so do not contact the electrodes at all (*Figure 5.22c*) Strategies for addressing “bubble”-like droplets are discussed later.

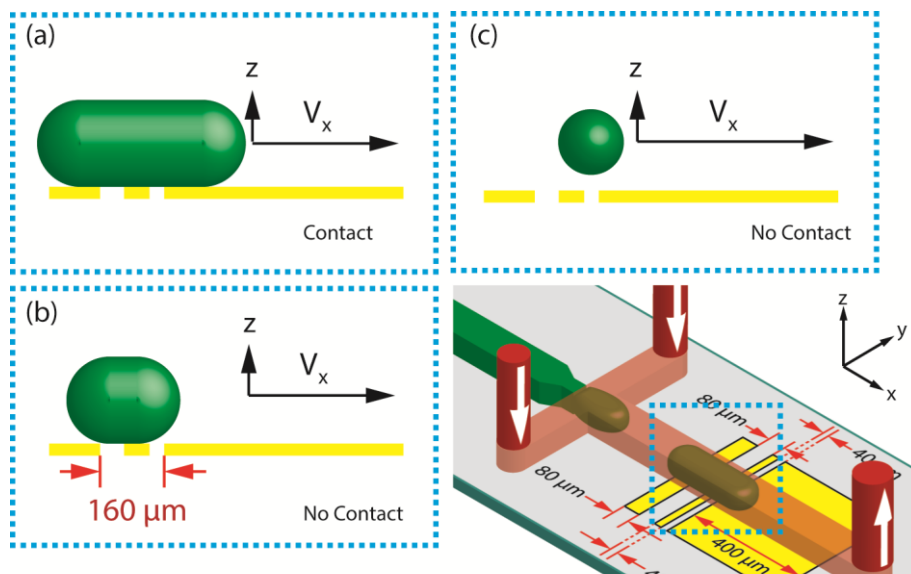


Figure 5.22: Schematic of aqueous droplet (green) interaction with channel electrodes as flowing through a channel with velocity V_f : (a) “plug”-like droplet bridging all three channel electrodes creating an electrical contact; (b) “plug”-like droplet smaller than the bridging distance to contact all three electrodes resulting in no electrical contact; (c) “bubble”-like droplet does not contact electrodes at all.

While under flow, the gold working band electrode was held at +0.5 V versus the gold reference band to access the capacitive region of the CV shown in *Figure 5.23*. Here the background current as a result of capacitive charging of the electrode/solution interface can be seen followed by the onset of gold oxidation at more positive potentials i.e. $E > +0.5$ V. On the reverse scan, the reduction of the gold oxide is seen at +0.25 V. Electrochemical signals for electrolyte droplets in the device described in *Figure 5.21* are displayed in *Figure 5.24*. Electroanalysis was carried out over 300 s with a data acquisition rate of 5 ms^{-1} . The resulting i - t plot for a period of 4 s, typical of that recorded over a 300 s period is shown in *Figure 5.24a*.

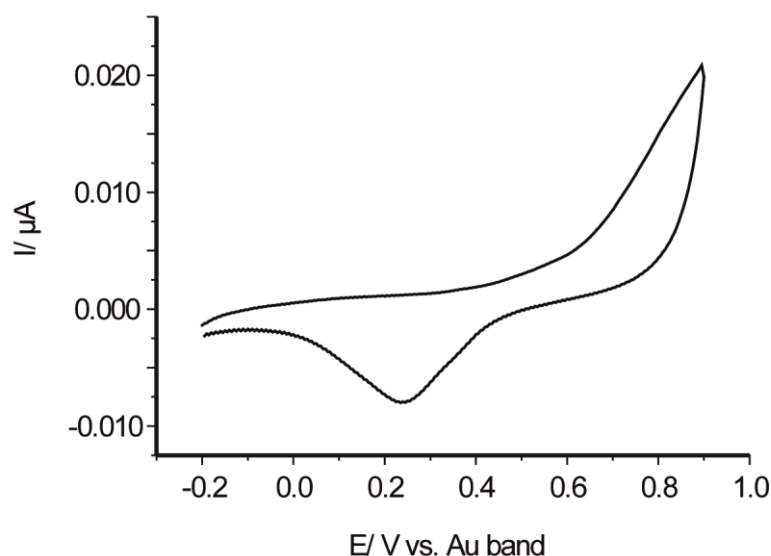


Figure 5.23: CV response for 0.1 M KNO_3 solution on Au channel electrodes (scan rate = 100 mV/s) showing the capacitance region between 0 – 0.5 V.

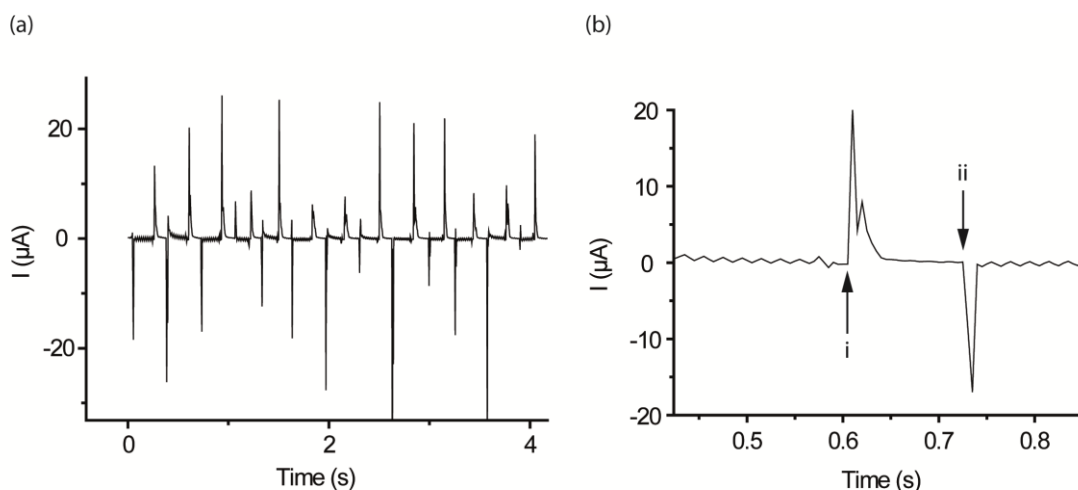


Figure 5.24: (a) Current-time response of electrolyte (0.1 M KNO_3) containing water droplets flowing in a mineral oil continuous phase ($\text{DP} = 8 \mu\text{L/min}$, $\text{CP} = 10 \mu\text{L/min}$) on microfluidic channel electrodes held at 0.5 V versus Au quasi-reference electrode; (b) a single electrolyte droplet event on the channel electrodes where (i) dictates the onset of a droplet event and (ii) signifies the end of a droplet event.

During flow, when the non-polar oil CP passes over the electrode, no current is observed, however, when electrolyte solution, which forms the droplet arrives at the electrode surface, a charging current is observed (Figure 5.24b), followed by a discharging event upon the droplet's departure. The

currents observed for charging and discharging are of opposite polarity, analogous with a DPSC experiment as described in Chapter 1.

The i - t plot in *Figure 5.24a* shows reproducible droplet events with the time separation between charging and discharging events and frequency of events remaining fairly consistent; as shown in *Figure 5.25*.

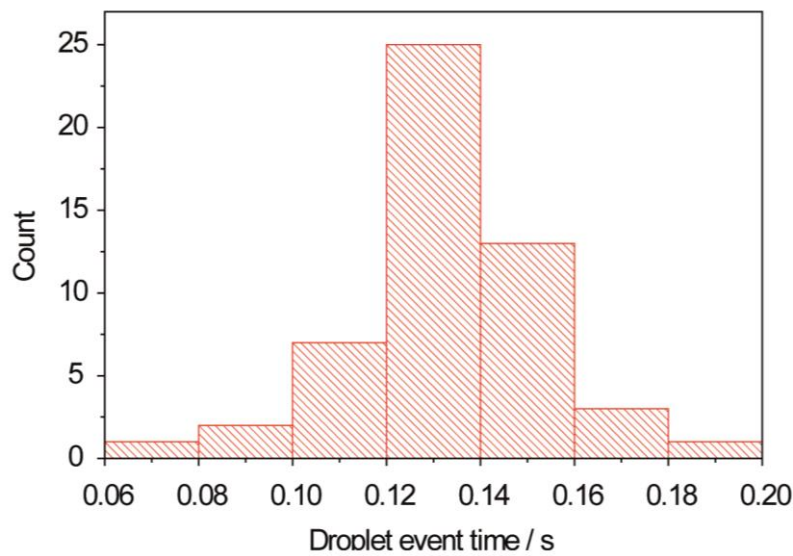


Figure 5.25: Histogram of the time separation between 54 droplet charging/discharging events over a period of 30 s.

Inconsistencies in charging current magnitude are likely to be an artefact of the low sampling rate used by the potentiostat. As a simple technique, the charging and discharging of electrolyte/electrode interfaces as a method for detecting plug droplets of aqueous electrolyte is of potential interest.

Knowing V_f inside the measurement channel, which is the combined V_f of the DP and CP, enables the size (length) of the droplet to be calculated from the residence time of the droplet over the electrodes i.e. the time between charging and discharging. To determine the length of a droplet passing over the electrodes, U is calculated using equation 5.4 and the residence time of the droplet on the electrodes, t_{res} , where $t_{res} = t_{ii} - t_i$, determined from the i - t plot in *Figure 5.24b*, so that:

$$D_L = S_e + (U \cdot t_{res})$$

5.5

where S_e is the separation between the reference and counter band electrodes i.e. $S_e = 160 \mu\text{m}$. Figure 5.26 shows a schematic of a droplet event (a) and the corresponding position of the droplet over the electrodes (b). Upon contact of the droplet with all three electrodes (bi) a charging current is observed in the i - t plot (aii). As the droplet continues to pass over the electrodes (bii) the charging current decays to zero. Once contact between the droplet and the first electrode is broken (biii), a discharging current peak is seen in the i - t plot (aiii).

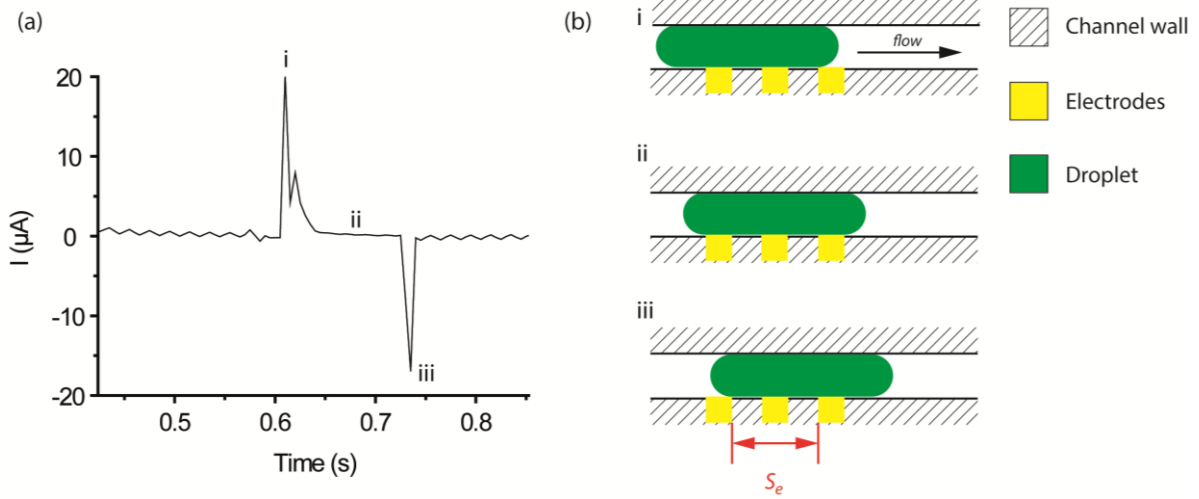


Figure 5.26: (a) i - t plot of an electrolyte droplet event on Au band electrodes under flow with labels corresponding to subsections in (b): Schematics of droplets of water moving through a microfluidic channel containing Au band electrodes with a separation of S_e between the first and final electrodes: (i) droplet makes contact with all three electrodes; (ii) droplet moves over electrodes following the direction of flow, maintaining contact with all three electrodes; (iii) droplet breaks contact with first electrode.

Using equation 5.5, the average length of droplets seen in Figure 5.24 were calculated to be $380 \mu\text{m} \pm 15 \mu\text{m}$. Unfortunately, at the time of running these experiments, optical measurements were not possible due to the limited frame-rate performance of the cameras used and the speed of the droplets moving through the channel. Limitations to the minimum size (length) of droplets detectable with such a system will be placed on the minimum electrode dimensions i.e. a resolution of $5 \mu\text{m}$ for lithographic techniques used in the fabrication of electrodes yielding a minimum droplet length of >15

μm . In order for the generated droplet to be “plug”-like, it must extend the full width of the microfluidic channel it occupies with the smallest producible droplet being greatly dependent on the focus-flow geometry which in turn determines the minimum volume of DP able to form a droplet before “pinch-off” occurs.

The device described is a capacitive sensor, detecting the charging current as a result of the capacitive charging of the electrolyte/electrode interface at contact points between droplet and electrode. As shown here, such a sensor can be used to detect water droplets in an oil CP and, knowing the total V_f in the measurement channel, the length/size of the droplet can be determined. Equally, if the droplet size could be determined independently e.g. optically, the sensor could be used to determine the mean velocity of the droplet. In order to measure both the mean velocity and size of the droplet, a sensor could incorporate two sets of electrodes i.e. 2×3 electrodes, each set positioned with a well-defined separation. The time take for a droplet to pass between the two sets of electrode could be used to determine the droplet velocity. This information could then be used to determine the droplet size using the time separation between charging and discharging currents seen in the droplet events on either set of electrodes. A similar arrangement has been implemented in an electrochemical droplet detector using an electroactive mediator in an organic CP to determine the presence of water droplets in flow.⁵¹ Here, the electrochemical signal generated in the CP is disrupted by droplets moving through the channel. Both “plug”-like droplets and “bubble”-like droplets were detected in this way via the disruption of mass transport at the electrode. Successful as this sensor is at detecting droplets, it does so indirectly and as a result is not selective for the droplet phase rather it detects a restriction in the transport of electroactive material at the electrode. For example, a bubble of air travelling through the channel could generate a similar signal as a water droplet passing over the electrode.

Under well controlled hydrodynamic conditions, the introduction of an electroactive mediator into the DP allows the possibility of measuring both the size of a “plug”-like droplet i.e. from the time resolution of the droplet signal event, as well as U , while at the same time, droplet detection would be phase selective. In order to test such a system, a microfluidic device such as the one described previously for the analysis of electrolyte droplets was constructed and the experimental parameters

repeated but with the inclusion of 1 mM FcTMA⁺ in the DP. The V_f of the DP was kept constant at 1 $\mu\text{L}/\text{min}$ while V_f of the CP (mineral oil) was varied between 1 – 4 $\mu\text{L}/\text{min}$. The working electrode was held at 0.6 V vs. the reference electrode, sufficient to oxidise FcTMA⁺ at a diffusion-controlled rate. The i - t plots for droplet flows over 60 s are displayed in *Figure 5.27* for CP flow rates of (a) 1 $\mu\text{L}/\text{min}$, (b) 2 $\mu\text{L}/\text{min}$ and (c) 4 $\mu\text{L}/\text{min}$.

Since V_f of a channel flow can be correlated to a limiting current observed at a channel electrode, as per equations 5.3 and 5.4, it is interesting to compare the limiting currents observed for the droplet flow with that of the expected Levich current given the deformed channel geometry determined earlier. This comparison is made in *Table 5.2* with a plot displaying the signals corresponding to a single droplet event seen at the channel electrodes in *Figure 5.28*.

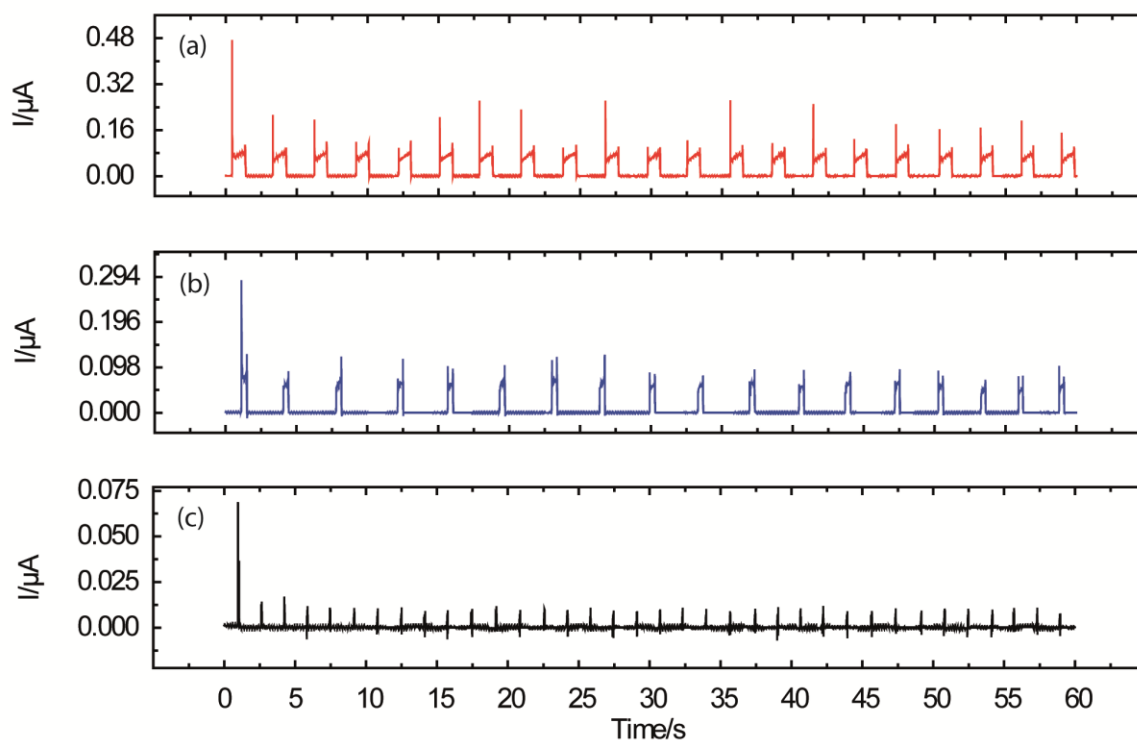


Figure 5.27: Current-time responses for two-phase flows of DP = 1 $\mu\text{L}/\text{min}$ with (a) CP = 1 $\mu\text{L}/\text{min}$; (b) CP = 2 $\mu\text{L}/\text{min}$; and (c) CP = 4 $\mu\text{L}/\text{min}$. Electrodes held at 0.6 V vs. reference with the DP containing 1 mM FcTMA⁺ in 0.1 M KNO₃.

The observed currents for droplets under flow are not comparable with those expected via Levich for a mediator in continuous flow with the limiting current observed for a droplet passing over the

electrode being, to some degree, inversely proportional to V_f . It may be that the wetting of the electrodes is less effective at higher flow rates with the droplet residence time being shorter, the area over which oxidation of the mediator can occur is reduced and so the corresponding current is also reduced.

The charging current observed at the start of a droplet event (*Figure 5.27*) should scale with the area of the working electrode as is the case with faradaic current (see section 1.1.2.3). Considering the band electrodes in the microfluidic channel remain the same size, the reduction in current with increasing V_f of CP suggests the area of the electrodes exposed to the droplets is decreasing possibly as a result of electrode fouling by the CP. At slower flow rates, the water droplets may be able to clear more of the electrode area of oil as a result of extended residence times. With increasing flow rate, the water droplets spend less time over the electrodes and so may be less effective at clearing the fouling oil.

Flow rate ($\mu\text{L}/\text{min}$)	Calibrated (Levich) current (μA)	Average droplet current (μA)	Approximate droplet length (μm)
2	0.075	0.083 (N = 21)	4000
3	0.084	0.074 (N = 18)	1783
5	0.096	0.0189 (N = 36)	1083

Table 5.2: Comparison of current signals from aqueous droplets and calibrated Levich currents for flow under various flow rates. Approximate droplet lengths are determined optically.

The convective regime inside droplets in microfluidic flows (*Figure 5.1*) may not be completely compatible with the assumptions of the Levich equation as towards the ends of the droplet, the transport will be enhanced compared with a continuous laminar flow.

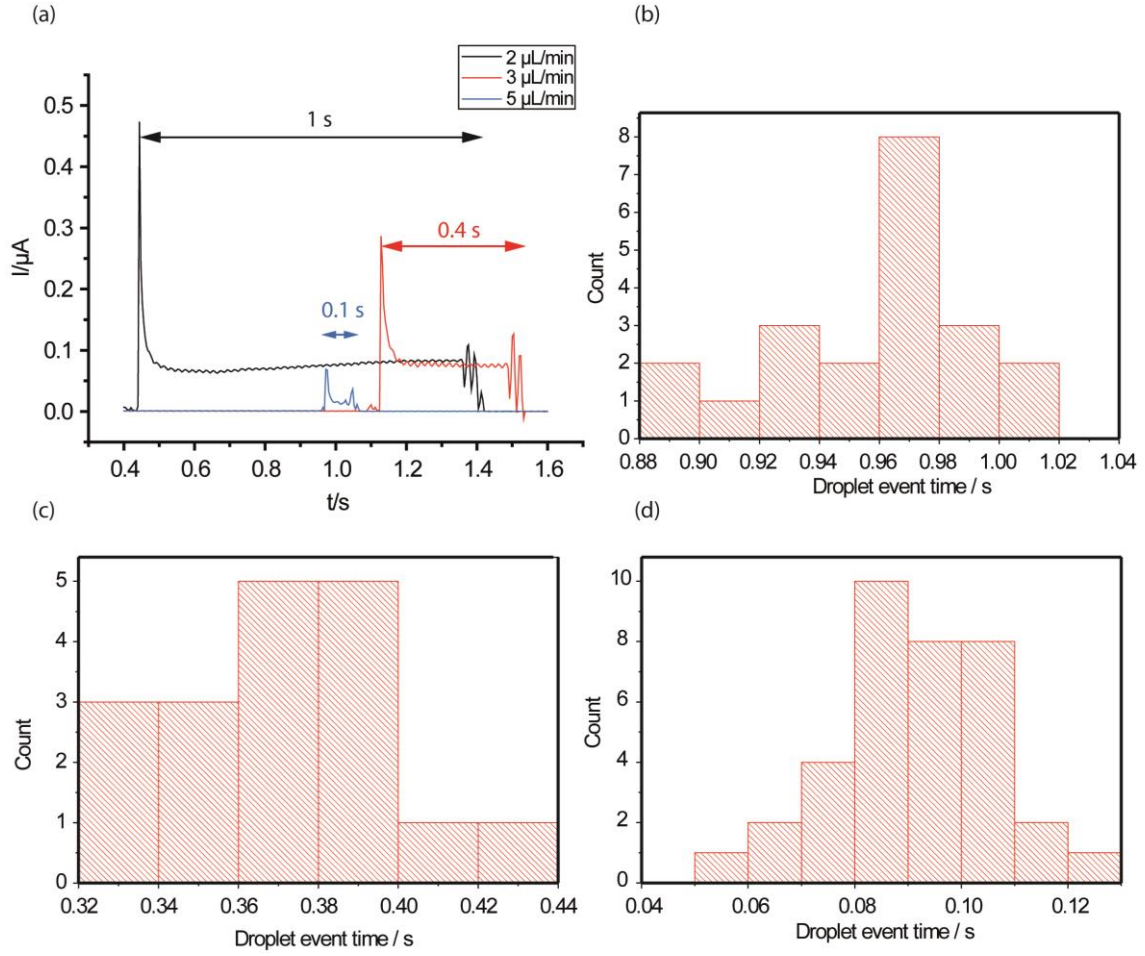


Figure 5.28: (a) Comparison of single droplet events for current-time responses of droplets described in Table 5.2 with droplet event times indicated by the coloured arrows corresponding to the relevant volume flow rate; Histograms of droplets events for two-phase flows of $DP = 1 \mu\text{L}/\text{min}$ with (b) $CP = 1 \mu\text{L}/\text{min}$; (c) $CP = 2 \mu\text{L}/\text{min}$; and (d) $CP = 4 \mu\text{L}/\text{min}$.

Crooks et al⁴⁵ used a narrow channel geometry to squash microdroplets of water containing an electroactive mediator while the droplets passed over a set of band electrodes. In these experiments, the authors were able to fit the resulting current signals to Levich theory. There are two key differences in this work compared with that presented in this thesis. (i) Silanisation of the microfluidic channels with *1H,1H,2H,2H-perfluorooctyl-trichlorosilane*: This ensures the wetting properties of the microfluidic channels are consistent, which was not the case here where the glass substrate supporting the electrodes and PDMS channels were not treated. In these untreated devices, the glass slide base was hydrophilic while the PDMS channel walls were hydrophobic and (ii) the V_f adopted in the devices. Crooks et al used V_f of the order of nanolitres per min rather than microliters per min, corresponding to a U of 0.24 cm/s compared with 0.19 cm/s for this work. These mean velocities are

not that dissimilar and yet the device described by Crooks conforms to Levich. Therefore the V_f adopted in this thesis cannot be the reason for the deviation from Levich for plug flow. The effect of a uniformly wetting channel on the characteristics of channel electrodes in microfluidic channels requires further investigation. It may be that deviation from Levich can be avoided with a uniformly wetting channel.

5.3 Conclusions

Electrochemistry has been demonstrated as an effective tool for detecting phase changes in microfluidic flows of two immiscible solvents, under a droplet/segmented flow regime where one phase contains electrolyte. As a simple analytical tool, band electrodes configured to directly detect and characterise the movement of droplets in flow may present applications in multiphase flow metering or in pharmaceutical reactors, where the ability to detect phase changes in-situ, cheaply, consistently and with low maintenance is desired.⁶²

Electrochemical signals generated from flows of aqueous droplets containing electroactive mediators can be used to characterise the frequency and size of droplets passing over band electrodes incorporated into a microfluidic channel. Work by other authors has shown the application of such systems⁴⁵ as a means of detecting droplets/contents of droplets. It is clear then that electrochemical devices can be used in multiphase flow situations to detect both phase changes in flow and the presence of mediator species but also monitor the frequency of phase changes and infer the velocity of flow.

Further work, would be focussed on assessing the application of electroactive redox mediators as a means to monitor flow velocity without the need for invasive flow manipulation seen in other work.⁴⁵

The unexplained results observed for electrochemical oxidation of FcTMA^+ in aqueous droplets in a continuous oil flow need to be further examined with investigations into the effects of channel wetting and electrowetting effects on the observed electrochemistry made clear. The major deviation from Levich for droplet flows described in this work is in stark contrast to that achieved by others using similar volume flow rates. It would be of great interest to determine the cause of such deviations

particularly if the direct electrochemical detection of droplets, at common flow rates (i.e. microliters per min), is to find applications as a sensor in microfluidic flows. With better understanding of electrochemistry in such systems, the adoption of generation/collection regimes like that described in chapter 4 for droplet detection under flow conditions could be investigated. The application of a generation/collection regime (see *Figure 5.29*) could provide a method for detecting the “bubble”-like droplets which, as shown in *Figure 5.22c*, would otherwise not interact with any channel electrode. For this work, the continuous phase would need to contain an electroactive, reversible mediator capable of operating under a generation/collection regime. Reports of electrochemical sensors incorporated into microfluidic channels for detecting “bubble”-like droplets via the distortion of a diffusion field generated at a channel electrode exist.⁵¹ These systems would not be able to distinguish between different droplet phase compositions i.e. whether the droplet was an air bubble, oil or a solid material. Any droplet/particle moving over the electrode would distort/interfere with the electrode diffusion field in the same way; see *Figure 5.29ai-iv*. However, applying the partitioning probe system described in chapter 4, a generation/collection regime operating under flow could allow one to distinguish between droplets of air or oil from solid particles in flow by differences in the up-take of the generated species through partitioning. Collection of the generated species in a droplet under flow would potentially reduce the subsequent collection current at the down-stream electrode. The size of the droplet could be inferred by the magnitude of current drop seen at the generation electrode while consideration of the respective collection current could be used to infer the extent of partitioning and so the phase composition of the droplet. In order to maximise the interaction between the diffusion field generated at the up-stream electrode and the DP/CP interface, a configuration whereby the electrodes surround the channel, as with a cylindrical channel containing ring electrode, could be implemented; see *Figure 5.29bi-ii*. This would ensure the droplet is surrounded by electro-generated species, maximising partitioning. Devices that generate “bubble”-like droplets in cylindrical, capillary channels using a co-flow configuration (see *Figure 5.2a*) have been described.^{63, 64} However, the fabrication of individually addressable electrodes in cylindrical, capillary channels would present a potential challenge, although, a similar device has been realised in synthetic diamond.⁴⁴

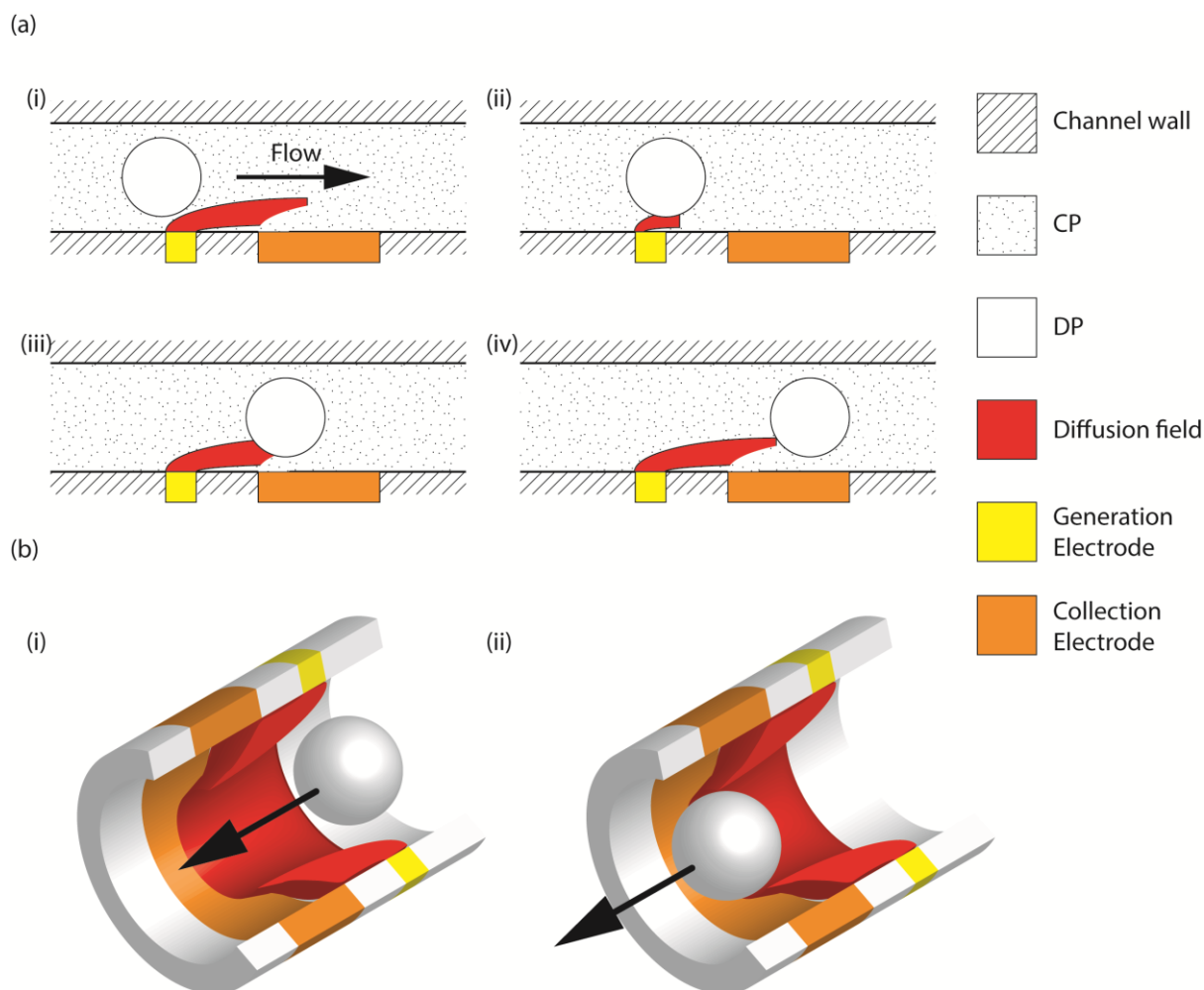


Figure 5.29: Schematic of (a) microfluidic channel electrodes configured for a generation/collection regime where an (i) electroactive species is generated at the first electrode in flow and subsequently collected at an electrode further down-stream; (ii) introduction of a droplet/particle flowing over the electrode distorts the diffusion field at the generation electrode reducing the observed current at both electrodes; (iii) the droplet/particle moves off the first electrode and onto the second, restoring the diffusion field profile and increasing the generation current while reducing the collection current due to the presence of the droplet; (iv) droplet/particle moves off collection electrode restoring the diffusion field generated and subsequently increasing the current. (b) 3D schematics of generation/collection regime with droplet/particles under flow through a cylindrical channel with ring electrodes (arrow indicates direction of flow) (i) droplet/particle before passing over generation electrode; (ii) droplet/particle after passing over collection electrode.

5.4 References

1. N. T. Nguyen and S. T. Wereley, *Fundamentals and Applications of Microfluidics*, Artech House, 2002.
2. G. Taylor, *Proceedings of the Royal Society of London. Series A, Mathematical and Physical Sciences*, 1953, **219**, 186-203.
3. D. Dutta and D. T. Leighton, *Analytical Chemistry*, 2000, **73**, 504-513.
4. D. Dutta, A. Ramachandran and D. Leighton, Jr., *Microfluid Nanofluid*, 2006, **2**, 275-290.
5. N.-T. Nguyen, *Micromixers: Fundamentals, Design and Fabrication*, William Andrew Inc., 2008.

6. P. J. A. Kenis, R. F. Ismagilov and G. M. Whitesides, *Science*, 1999, **285**, 83-85.
7. S. Takayama, J. C. McDonald, E. Ostuni, M. N. Liang, P. J. A. Kenis, R. F. Ismagilov and G. M. Whitesides, *Proceedings of the National Academy of Sciences of the United States of America*, 1999, **96**, 5545-5548.
8. J.-U. Park, M. A. Meitl, S.-H. Hur, M. L. Usrey, M. S. Strano, P. J. A. Kenis and J. A. Rogers, *Angewandte Chemie*, 2006, **118**, 595-599.
9. A. Huebner, S. Sharma, M. Srisa-Art, F. Hollfelder, J. B. Edel and A. J. deMello, *Lab on a Chip*, 2008, **8**, 1244-1254.
10. R. Seemann, M. Brinkmann, T. Pfohl and S. Herminghaus, *Reports on Progress in Physics*, 2012, **75**, 016601.
11. H. Song, D. L. Chen and R. F. Ismagilov, *Angewandte Chemie International Edition*, 2006, **45**, 7336-7356.
12. F. Trachsel, A. Günther, S. Khan and K. F. Jensen, *Chemical Engineering Science*, 2005, **60**, 5729-5737.
13. V. Srinivasan, V. K. Pamula and R. B. Fair, *Analytica Chimica Acta*, 2004, **507**, 145-150.
14. R. Arayanarakool, L. Shui, S. W. M. Kengen, A. van den Berg and J. C. T. Eijkel, *Lab on a Chip*, 2013, **13**, 1955-1962.
15. H. N. Joensson and H. Andersson Svahn, *Angewandte Chemie International Edition*, 2012, **51**, 12176-12192.
16. E. W. M. Kemna, L. I. Segerink, F. Wolbers, I. Vermes and A. van den Berg, *Analyst*, 2013, **138**, 4585-4592.
17. J. Q. Boedicker, L. Li, T. R. Kline and R. F. Ismagilov, *Lab on a Chip*, 2008, **8**, 1265-1272.
18. M. Wang, G. T. Roman, K. Schultz, C. Jennings and R. T. Kennedy, *Analytical Chemistry*, 2008, **80**, 5607-5615.
19. M. Wang, G. T. Roman, M. L. Perry and R. T. Kennedy, *Analytical Chemistry*, 2009, **81**, 9072-9078.
20. S.-Y. Teh, R. Lin, L.-H. Hung and A. P. Lee, *Lab on a Chip*, 2008, **8**, 198-220.
21. J. D. Tice, H. Song, A. D. Lyon and R. F. Ismagilov, *Langmuir*, 2003, **19**, 9127-9133.
22. H. Song and R. F. Ismagilov, *Journal of the American Chemical Society*, 2003, **125**, 14613-14619.
23. L. Malet-Sanz and F. Susanne, *Journal of Medicinal Chemistry*, 2012, **55**, 4062-4098.
24. N. de Mas, A. Günther, M. A. Schmidt and K. F. Jensen, *Industrial & Engineering Chemistry Research*, 2003, **42**, 698-710.
25. Z. T. Cygan, J. T. Cabral, K. L. Beers and E. J. Amis, *Langmuir*, 2005, **21**, 3629-3634.
26. I. Shestopalov, J. D. Tice and R. F. Ismagilov, *Lab on a Chip*, 2004, **4**, 316-321.
27. B. K. H. Yen, A. Günther, M. A. Schmidt, K. F. Jensen and M. G. Bawendi, *Angewandte Chemie International Edition*, 2005, **44**, 5447-5451.
28. D. S. Tawfik and A. D. Griffiths, *Nat Biotech*, 1998, **16**, 652-656.
29. J. J. Agresti, B. T. Kelly, A. Jäschke and A. D. Griffiths, *Proceedings of the National Academy of Sciences of the United States of America*, 2005, **102**, 16170-16175.
30. O. J. Miller, K. Bernath, J. J. Agresti, G. Amitai, B. T. Kelly, E. Mastrobattista, V. Taly, S. Magdassi, D. S. Tawfik and A. D. Griffiths, *Nat Meth*, 2006, **3**, 561-570.
31. A. S. Utada, L.-Y. Chu, A. Fernandez-Nieves, D. R. Link, C. Holtze and D. A. Weitz, *MRS Bulletin*, 2007, **32**, 702-708.
32. T. Thorsen, R. W. Roberts, F. H. Arnold and S. R. Quake, *Physical Review Letters*, 2001, **86**, 4163-4166.
33. P. Garstecki, M. J. Fuerstman, H. A. Stone and G. M. Whitesides, *Lab on a Chip*, 2006, **6**, 437-446.
34. S. L. Anna, N. Bontoux and H. A. Stone, *Applied Physics Letters*, 2003, **82**, 364-366.
35. G. F. Christopher and S. L. Anna, *Journal of Physics D: Applied Physics*, 2007, **40**, R319.
36. M. Shaw, D. Nawrocki, R. Hurditch and D. Johnson, *Microsystem Technologies*, 2003, **10**, 1-6.
37. A. d. Campo and C. Greiner, *Journal of Micromechanics and Microengineering*, 2007, **17**, R81.

38. M. Lazar, H. Vang, P. Brosselard, C. Raynaud, P. Cremillieu, J. L. Leclercq, A. Descamps, S. Scharnholtz and D. Planson, *Superlattices Microstruct.*, 2006, **40**, 388-392.
39. S. Bhattacharya, A. Datta, J. M. Berg and S. Gangopadhyay, *Microelectromechanical Systems, Journal of*, 2005, **14**, 590-597.
40. T. Murakami, S.-i. Kuroda and Z. Osawa, *Journal of Colloid and Interface Science*, 1998, **202**, 37-44.
41. J. N. Lee, C. Park and G. M. Whitesides, *Anal. Chem.*, 2003, **75**, 6544-6554.
42. H. Qi, X. Wang, T. Chen, X. Ma and T. Zuo, *Microsystem Technologies*, 2009, **15**, 1027-1030.
43. X. Li, T. Abe, Y. Liu and M. Esashi, *Microelectromechanical Systems, Journal of*, 2002, **11**, 625-630.
44. L. A. Hutton, M. Vidotti, J. G. Iacobini, C. Kelly, M. E. Newton, P. R. Unwin and J. V. Macpherson, *Analytical Chemistry*, 2011, **83**, 5804-5808.
45. H. Liu and R. M. Crooks, *Lab on a Chip*, 2013, **13**, 1364-1370.
46. L. M. Fidalgo, G. Whyte, B. T. Ruotolo, J. L. P. Benesch, F. Stengel, C. Abell, C. V. Robinson and W. T. S. Huck, *Angewandte Chemie International Edition*, 2009, **48**, 3665-3668.
47. H. B. Lin, J. D. Eversole and A. J. Campillo, *Optics Communications*, 1990, **77**, 407-410.
48. J.-C. Baret, O. J. Miller, V. Taly, M. Ryckelynck, A. El-Harrak, L. Frenz, C. Rick, M. L. Samuels, J. B. Hutchison, J. J. Agresti, D. R. Link, D. A. Weitz and A. D. Griffiths, *Lab on a Chip*, 2009, **9**, 1850-1858.
49. W. B. Zimmerman, *Chemical Engineering Science*, 2011, **66**, 1412-1425.
50. H.-C. Chang and L. Y. Yeo, *Electrokinetically-Driven Microfluidics and Nanofluidics*, Cambridge University Press, 2010.
51. S. Liu, Y. Gu, R. B. Le Roux, S. M. Matthews, D. Bratton, K. Yunus, A. C. Fisher and W. T. S. Huck, *Lab on a Chip*, 2008, **8**, 1937-1942.
52. C. Elbuken, T. Glawdel, D. Chan and C. L. Ren, *Sensors and Actuators A: Physical*, 2011, **171**, 55-62.
53. S. Sadeghi, H. Ding, G. J. Shah, S. Chen, P. Y. Keng, C.-J. C. Kim and R. M. van Dam, *Analytical Chemistry*, 2012, **84**, 1915-1923.
54. J. C. Myland and K. B. Oldham, *Analytical Chemistry*, 2000, **72**, 3972-3980.
55. J. A. Cooper and R. G. Compton, *Electroanalysis*, 1998, **10**, 141-155.
56. R. G. Compton and P. R. Unwin, *Journal of Electroanalytical Chemistry and Interfacial Electrochemistry*, 1986, **205**, 1-20.
57. M. E. Snowden, P. R. Unwin and J. V. Macpherson, *Electrochemistry Communications*, 2011, **13**, 186-189.
58. S. T. Koev and R. Ghodssi, *Review of Scientific Instruments*, 2008, **79**, -.
59. B. J. Polk, A. Stelzenmuller, G. Mijares, W. MacCrehan and M. Gaitan, *Sensors and Actuators B: Chemical*, 2006, **114**, 239-247.
60. T. Matsumoto, A. Ohashi and N. Ito, *Analytica Chimica Acta*, 2002, **462**, 253-259.
61. J. Zhou, K. Ren, Y. Zheng, J. Su, Y. Zhao, D. Ryan and H. Wu, *ELECTROPHORESIS*, 2010, **31**, 3083-3089.
62. G. Falcone, G. Hewitt and C. Alimonti, *Multiphase Flow Metering: Principles and Applications*, 2009.
63. A. S. Utada, E. Lorenceau, D. R. Link, P. D. Kaplan, H. A. Stone and D. A. Weitz, *Science*, 2005, **308**, 537-541.
64. L.-Y. Chu, A. S. Utada, R. K. Shah, J.-W. Kim and D. A. Weitz, *Angewandte Chemie International Edition*, 2007, **46**, 8970-8974.

6 All-Diamond Microfluidic Devices for Solution Analysis

Synthetic diamond is unique as a microfluidic material in that it is highly resistant to chemical attack, fouling and harsh environments and enables the incorporation of equally resilient co-planar pBDD electrodes, which can withstand aggressive cleaning procedures. In this chapter a microfluidic device fabricated from polycrystalline intrinsic diamond with laser machined microchannels and integrated polycrystalline pBDD band electrodes for electrochemical analysis of single and multiple phase fluid flows is described.

6.1 Introduction

6.1.1 Micro-scale devices fabricated from synthetic diamond

Microfluidics provide a versatile platform for chemical analysis, and as such have received much attention in recent years¹ with applications in biology², pharmaceuticals³ and materials science⁴. Traditionally, microfluidic devices are fabricated from polydimethylsiloxane (PDMS) which although it is advantageous for rapid fabrication, is limited to use with aqueous media due to incompatibility with non-polar, volatile solvents. This limitation is often overcome by fabricating microfluidic devices from glass or solvent resistant polymers.⁵

Synthetic diamond exhibits a range of properties: optically transparent in the wavelength range 2.5 μm to 225 nm,⁶ high thermal conductivity (25 W/cm.K)⁶ with low thermal expansion coefficient, high mechanical hardness and chemical inertness,⁷ as well as biological compatibility, making it an ideal material for electronic and microfluidic applications.

Integration of electrochemical sensors into microfluidic devices is of growing interest for chemical detection and microreactors⁸. Gold-band thin film electrodes are typically used due to the ease of fabrication; however, they are prone to disintegration with time due to corrosion of the adhesion layer (typically chromium) between the gold and the substrate.^{9, 10} Thin film metal electrodes are also prone

to dissolving with repeated application of anodic potentials.⁹ This problem could be eradicated through the use of conducting diamond electrodes.

The electrical properties of diamond range from insulating (intrinsic) through to semi-metallic conductors (boron doped), the latter being particularly advantageous in electrochemistry. Boron doped diamond (BDD) electrodes exhibit wide potential windows of around 4 V in aqueous solutions (defined as the region between the potentials at which solvent electrolysis takes place where a current of $\pm 0.4 \text{ mA cm}^{-2}$ is not exceeded)¹¹ with low capacitance ($\sim 6 \text{ } \mu\text{F cm}^{-2}$)¹¹ making them ideal for high-performance trace level analysis sensors of a wide range of electroactive analytes. Examples of BDD sensors are described in section 6.2.2.

Diamond can be machined using Reactive-Ion etching (RIE)¹²⁻¹⁴ or laser micromachining.^{15, 16} Examples of devices fabricated from diamond materials can be found in the literature where authors use overgrowth/ sacrificial layer technology^{17, 18} to create microfluidic channels. The use of femtosecond lasers has also been reported for producing shallow ($< 1 \text{ } \mu\text{m}$) trenches in single-crystal diamond substrates.¹⁹

For microfluidic applications, it is often important to control the wettability of a channel surface to better suit the composition of flow. Typically this is achieved by chemical modification of the channel surface using oxygen plasma,²⁰ corona discharge,²¹ UV/ozone modification²² and UV-initiated graft polymerisation.²³ An advantage of diamond is the versatility of surface functionalization. A relatively short treatment in either a hydrogen plasma or an acid cleaning procedure can yield a diamond substrate with hydrophobic or hydrophilic surfaces respectively.²⁴

6.1.2 Laser machining of diamond

The mechanical machining of diamond presents a challenge due to diamond's extreme hardness.²⁵ As such laser machining is typically used for cutting diamond²⁶ while mechanical methods are widely used for polishing.²⁷ Laser machining of diamond has applications in jewellery as a method for removing trapped inclusions, thus enhancing the clarity grade of a diamond.²⁸

Upon application of a laser pulse on a diamond film surface, atomic bonds of the diamond are disintegrated as a result of high energy fluence (energy delivered per unit area) transferred from the laser pulse. This interaction typically takes place over a period of nanoseconds²⁹ but results in the formation of a plasma composed of the disintegrated material released from the surface. The surface around the laser beam is then heated by the formation of the high-temperature plasma inducing thermal reactions and oxidation of the surface.³⁰

The output wavelength of the laser beam used for diamond machining is of critical importance to the effectiveness of the laser-diamond interaction and thus the thermal load on the diamond surface. The laser power requirements for laser machining are greatly influenced by the optical properties and thus the absorptivity of a material but also the thermal properties of the material.³¹ Hard materials that display low thermal conductivity are the most suited to laser machining.³¹ Diamond is more transparent to lasers with wavelengths in the IR range, as is typical for Nd:YAG (1064 nm). As a result, there is less efficient coupling of the laser photons (1.2 eV) with the diamond and so a higher energy dose is required to induce material removal via a thermally driven mechanism instead of physical ablation of C-C bonds³². This thermally driven process causes graphitisation of the diamond surface³³ through the thermal decomposition of C-C bonds. Coupling of the lasers 1.2 eV photons is more efficient between the generated non-diamond carbon resulting in further sublimation of the surface.³² The increased kinetic energy of these interactions causes a greater deal of structural damage to the surface in areas around the laser beam.

Lasers with an output frequency in the UV-range such as ArF (193 nm, 6.4 eV) couple more effectively with the diamond surface (Band gap 5.45 eV) compared with IR lasers. As a result laser machining proceeds via an ablation mechanism.³² The Nd:YAG system used in this work has a wavelength of 355 nm. This is energetically lower (3.5 eV) than needed for effective coupling to the diamond. However, the energy dose required to induce thermal decomposition of the diamond material is lower than that for a 1064 nm system and so is more efficient at machining diamond.

The etching rate induced by laser ablation is dependent on the pulse duration and beam spot size for nanosecond lasers but independent of spot size for lasers with pulse durations of femtoseconds or less.³⁰ In the case of nanosecond lasers, the plasma plume produced by material ablation around the laser beam is well established during the laser pulse. This is a result of the velocity of disintegrated material ejected from the surface, typically 1-10 $\mu\text{m}/\text{ns}$ ³⁰ and serves to attenuate the laser radiation reducing the rate of ablation. Lasers of sufficiently shorter pulse durations allow the ablation of material before a plasma plume is able to expand over the beam spot area. This serves to maximise the ablation rate and also reduces the amount of thermal damage incurred at a surface by the formation of high-energy plasma.³⁰ This has important implications for laser machining thermally sensitive materials such as polymers and glass where femtosecond lasers are often employed to reduce the heat-affected zone (HAZ) and avoid thermally induced damage.^{29, 34, 35}

6.2 Results and Discussion

6.2.1 The fabrication of microfluidic channels in synthetic, intrinsic diamond using laser micromachining.

In order to fabricate channel structures in diamond, a triple-Nd:YAG (355 nm) laser equipped with a computerised numerical control (CNC) stage capable of traversing motion in the X, Y and Z axis with 0.1 μm resolution was utilised. According to the manufacturers, the theoretical laser spot size upon focussing the beam for this system is $\sim 6 \mu\text{m}$ however, in practice, it was found that the minimum resolution of lasered features is between 20-30 μm depending on the power output and other laser parameters, which affect the power density distribution across the focussed beam. Photographs of polycrystalline intrinsic diamond with laser machined features are shown in *Figure 6.1*.

The output power of the laser beam was controlled using a motorised attenuator consisting of a polariser and a half-wave plate. The attenuator sets the energy of the beam by controlling the ratio of transmitted and reflected light as the beam passes through the attenuator module.³⁶ Typical power output from the Nd:YAG system was around 6.5 W at a laser pulse frequency of 10 kHz. The

attenuator power is reported as a percentage of the maximum power output at a given laser pulse frequency.

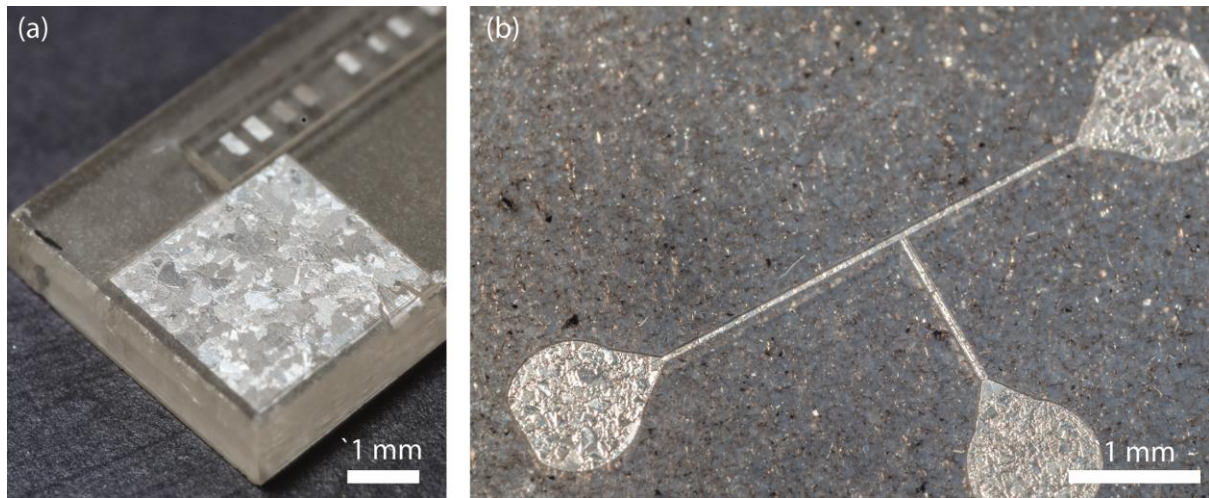


Figure 6.1: Photographs of (a) 4×4 mm square and (b) microfluidic channels with inlets/outlets, laser micromachined into polycrystalline intrinsic wafers.

In order to calibrate the machining depth achieved per laser pass, a series of tests were conducted whereby 100-500 μm squares were machined into thermal grade (TG1 see *table 2.1*, chapter 2) polycrystalline, intrinsic diamond wafers. These square structures were created by moving the CNC stage supporting the diamond substrate according to the hatch pattern shown in *Figure 6.2*. The speed of the stage movement along with the pulse frequency and attenuated power of the laser were controlled and varied in order to investigate not only the depth of feature achievable but also the surface roughness after laser machining. Control of the pulse frequency allows the inter-pulse distance during stage traversing to be maintained. An inter-pulse distance of half the focussed laser beam width (3 μm) was chosen to ensure sufficient overlap between pulses to irradiate the entire diamond surface to be machined; see *Figure 6.3ai*. For a CNC stage speed of 0.3 mm/s, a pulse frequency of 100 Hz is required to maintain an inter-pulse distance of 3 μm .

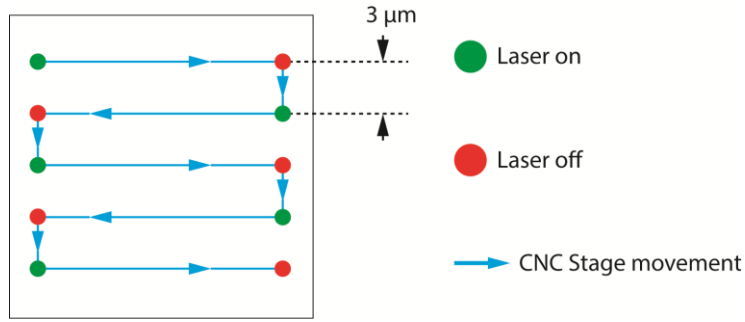


Figure 6.2: schematic of the “hatch” pattern used for laser machining of features

A series of thirty $100\text{ }\mu\text{m}$ squares were machined using the hatch pattern described in Figure 6.2. Of these thirty squares, half were machined with two passes of the laser whilst the other were machined with a single pass. Five $100\text{ }\mu\text{m}$ squares (with 3 repeats of each) were machined with an attenuator power ranging from 30-70 %. Depth profiles and surfaces roughness (RMS and Ra) achieved under these conditions were measured using analysis of topography recorded by white light interferometry (WLI) and are shown in Figure 6.3.

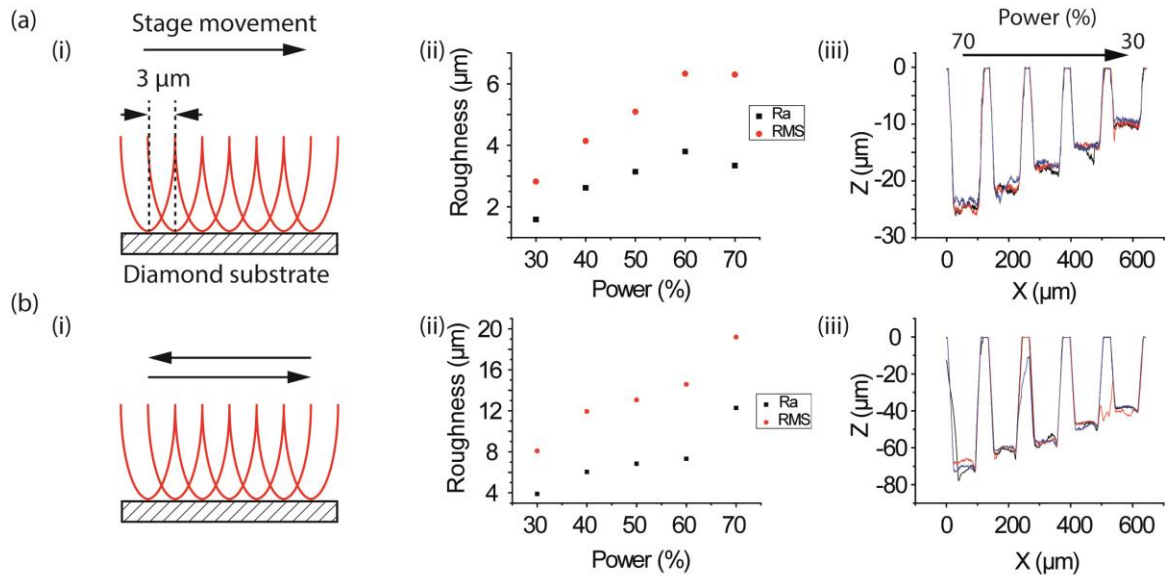


Figure 6.3: Machining of a $100\text{ }\mu\text{m}$ square with (a) one pass and (b) two passes of the laser beam set to a laser pulse frequency of 100 Hz and stage traversing speed of 0.3 mm/s: (i) a schematic of the beam path and separation between laser pulses (red) achieved; (ii) machined surface roughness measured via WLI for $100\text{ }\mu\text{m}$ squares machined at attenuator power ranging from 30-70 %; (iii) depth profiles measured by WLI for $100\text{ }\mu\text{m}$ squares machined with attenuator powers of 30-70 %.

Surface roughness of the machined diamond is seen to rise with increasing attenuator power for both single and double passes; see *Figure 6.3aii* and *bii*. The depth of the machined feature is also seen to increase with higher attenuator powers (*Figure 6.3aiii* and *biii*). This trend is expected as the increase in energy provided by higher attenuator powers results in a higher etch rate of the diamond material under the laser beam and so a greater penetration depth. This also results in an increased surface roughness. Increased laser power generates a plasma of higher energy during the ablation process, causing greater damage to the material surrounding the laser beam, and so a greater surface roughness. There will also be some contribution to the surface roughness from the different laser ablation efficiencies of different grains composing the polycrystalline diamond material.

These tests were repeated but with faster machining speeds i.e. increasing the CNC stage movement speed and increasing the laser pulse frequency so that a pulse separation of 3 μm was maintained during machining. The WLI data of these tests are displayed in *Figure 6.4*. The surface roughness achieved at these higher machining speeds is greater than for the slower speed, particularly at higher attenuator powers (*Figure 6.4ai* and *bi*) where there is a significant difference i.e. an RMS of 14.58 μm at 70 % for a machining speed of 0.9 mm/s compared to an RMS of just 6.3 μm for a machining speed of 0.3 mm/s. The depths achieved at these higher machining speeds are noticeably greater than seen at 0.3 mm/s. This increased etch rate of diamond material at the higher machining speeds is a result of the higher laser pulse frequencies used.

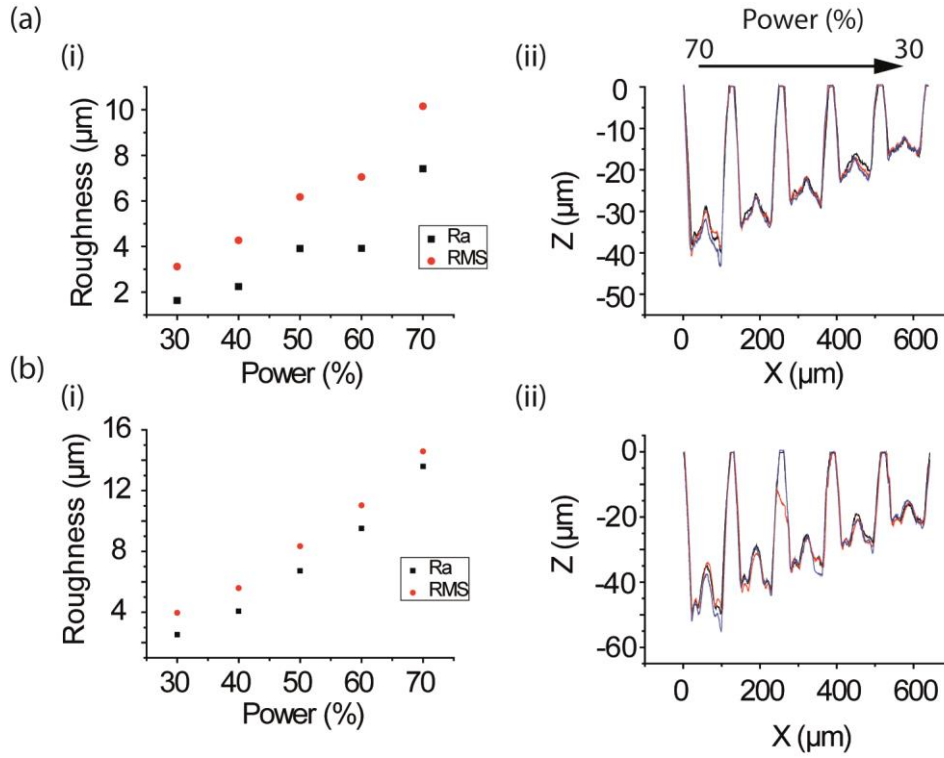


Figure 6.4: Machining of a 100 μm square with one pass of the laser beam set to a laser pulse frequency and stage traversing speed of (a) 200 Hz, 0.6 mm/s and (b) 300 Hz, 0.9 mm/s: (i) machined surface roughness measured via WLI for 100 μm squares machined at attenuator power ranging from 30-70 %; (ii) depth profiles measured by WLI for 100 μm squares machined with attenuator powers of 30-70 %.

The output power of the laser depends on the pulse frequency with the power per pulse increasing with higher pulse frequency, until reaching a maximum power per pulse at a pulse frequency of 9-10 kHz; see Figure 6.5. By raising the laser pulse frequency with increasing machining speed, the power output of the laser beam is higher and so a greater penetration through the diamond material is possible.

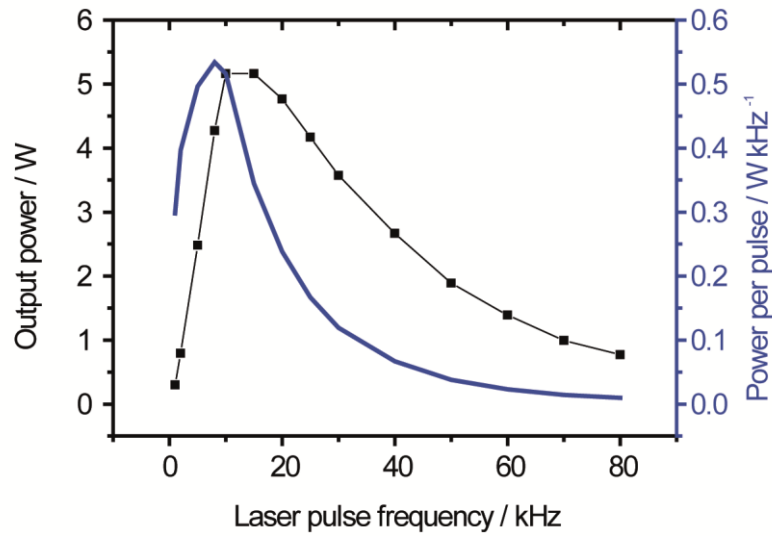


Figure 6.5: Plot of laser output power as a function of laser pulse frequency and corresponding power per pulse for the 355 nm Nd:YAG laser system used.

A heterogeneous machining depth is achieved at these higher machining speeds as evident in *Figure 6.4a* and *b*. The machined square trench appears to be shallower at the centre of the trench while deeper at the edges. This appears most pronounced at the fastest machining speed and also at the higher attenuator powers at both machining speeds. This feature is a result of an acceleration effect caused by the CNC stage. At higher traversing speeds, the software controlling the stage is unable to regulate the speed of the stage correctly. At the start of a traversing motion, the stage begins to move at a slower speed than stipulated by the programmed instructions. The CNC controllers respond to this by accelerating the stage to compensate. This acceleration results in the stage moving faster than the stipulated traversing speed which the CNC controllers once again compensate for by decelerating the stage. This results in a traversing motion whereby the stage is moving fastest in the middle of the motion and slowest at the start and end. Since the etch rate of the laser is dependent on the dwell time the beam spends over an area of material, the laser machining is more effective at the edges of the machined trench and least effective in the centre. This acceleration issue with the CNC stage is commonly rectified using more advanced software; however, this was not available. Therefore, diamond machining was carried out at a speed not exceeding 0.3 mm/s to avoid any acceleration issues with the CNC stage which might result in uneven laser machining. To further reduce possible

acceleration effects laser machining was conducted in the direction of the longest geometric dimension i.e. for channels or electrode band structures laser machining was performed along the length rather than the width of the feature. In the case of microfluidic channels the ends of the channels were removed during the machining of inlet holes in order to remove any laser machining artefacts.

6.2.2 Boron-doped diamond electrodes

As an electrode material for electrochemical sensing, pBDD has a number of attractive properties such as a wide potential window (see *Figure 6.8*), low background currents, a high resistance to fouling, robustness and as discussed in chapter 1, high quality pBDD material can be grown using the CVD process consistently and cheaply. It is unsurprising then that there is interest in pBDD as a material for constructing electrode devices on the micro-scale. For example, microelectrode arrays comprised of a series of 10 – 50 μm diameter pBDD UMEs, equally spaced in a hexagonal pattern have been fabricated; as shown in *Figure 6.6*.³⁷

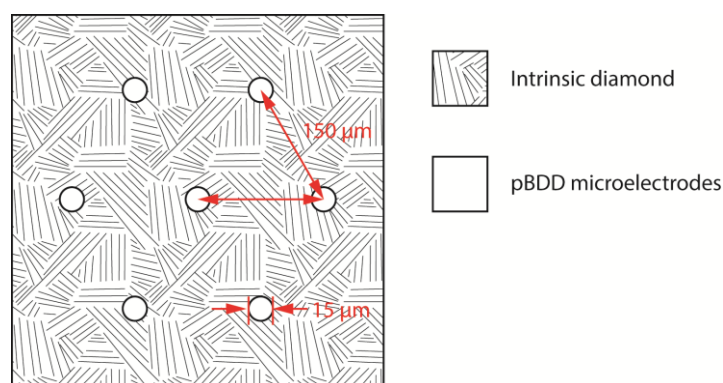


Figure 6.6: Schematic of a hexagonal 15 μm diameter pBDD microelectrode array fabricated in intrinsic diamond as reported by Compton et al³⁷

Laser ablation was employed on a CVD grown pBDD wafer surface, leaving a series of 10-25 μm diameter, 25 μm high, tapered columns of pBDD in a hexagonal configuration. Overgrowth with a layer of intrinsic diamond via CVD, and polishing back, revealed the final device structure. However, the UMEs in the produced array were not individually addressable. For many applications, the ability to address electrodes individually is of critical importance, especially if such devices are to incorporate classical two or three-electrode configurations.

Another method for fabricating diamond electrodes has been reported using boron-doped nanocrystalline diamond (BNCD) deposited on silicon wafers; see *Figure 6.7*.³⁸ The authors present a series of individually addressable band electrodes formed from a 500 nm thick layer of BNCD deposited onto a silicon oxide coated wafer.

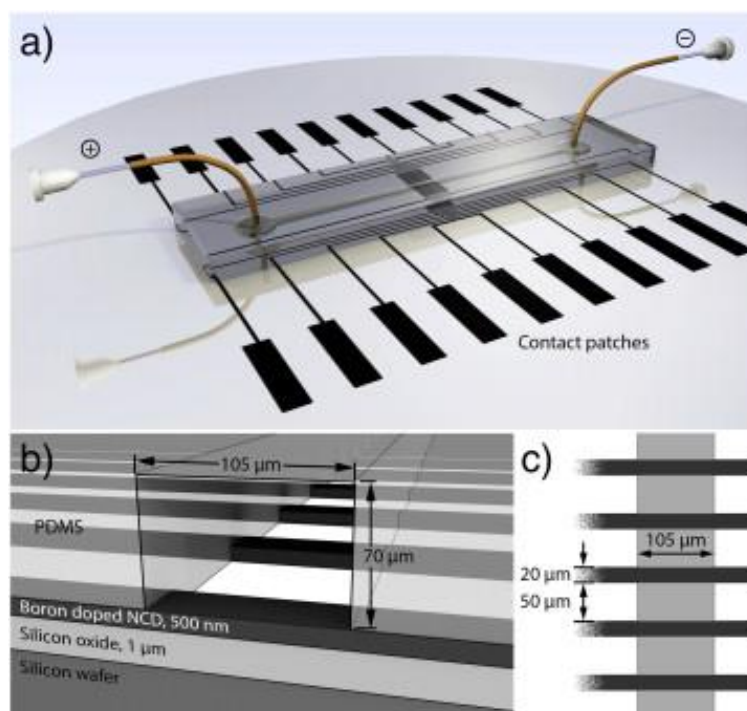


Figure 6.7: Schematics of BNCD electrode containing microfluidic described by Forsberg et al.³⁸ (a) Overview, + and – indicate contacts for applying a voltage yielding an external electric field in the channel. (b) Cross section view showing the device layers and dimensions (not to scale). (c) Top view of the channel and electrodes.

The wafer was patterned using photolithography techniques and the BNCD RIE etched to leave a series of 20 μm wide BNCD bands spaced 50 μm apart. Compression of the solvent window in the electrochemical characterisation presented for these electrodes suggest a sp^2 presence in the BNCD material. This is not surprising given the use of BNCD which has a high percentage of grain boundaries where sp^2 carbon can accumulate during the growth process. When integrated into a microfluidic channel fabricated from PDMS, the electrodes showed good steady-state behaviour under flow using one of the BNCD bands as a quasi-reference electrode. Importantly, the electrodes

were shown to be highly stable with prolonged use (up to 5 hrs) at high potentials i.e. 1.5 V contrary to that of gold band electrodes.⁹ The diamond bands were also capable of surviving very aggressive cleaning procedures consisting of (1) a 10 min treatment in a solution of ammonium hydroxide and hydrogen peroxide at 75-80 °C; (2) a further 10 min treatment in a solution of hydrochloric acid and hydrogen peroxide. Electrochemical characterisation of the bands post-cleaning was consistent with pre-cleaning performance.

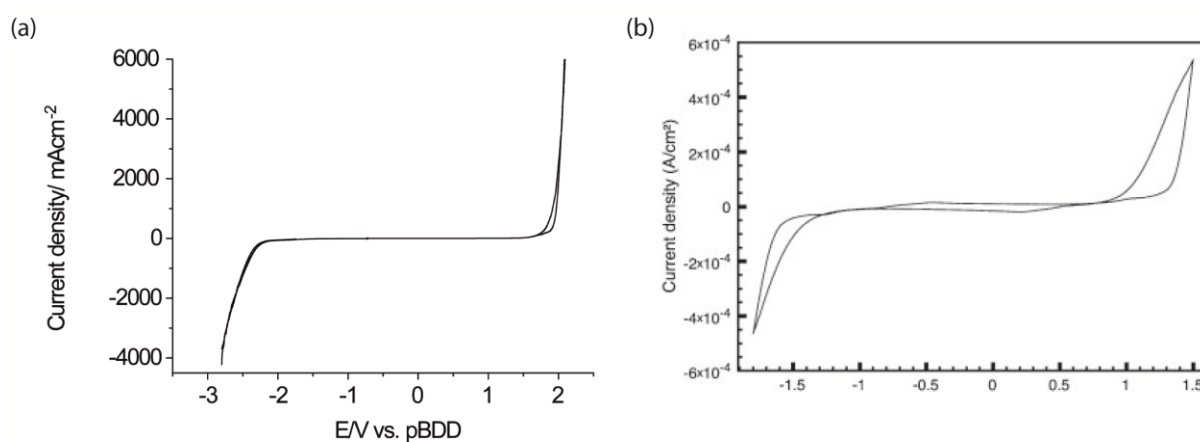


Figure 6.8: (a) A typical solvent window generated by CV on a CVD grown, polished microcrystalline, 40 μm wide pBDD band electrode in a solution of 0.1 M KNO_3 . (b) A solvent window of BNCD electrodes in 0.5 M KNO_3 presented by Forsberg *et al.*³⁸

6.2.2.1 Fabrication of boron-doped diamond electrodes with insulation diamond surrounds

Individually addressable pBDD electrodes were fabricated in a similar manner to that described by Joseph *et al.*³⁹ with the electrode geometries patterned into an insulating diamond wafer and pBDD grown into the patterned trenches. These trenches were fabricated using laser machining with the electrode geometry incorporated into a hatching program using laser parameters given in Table 6.1.

Laser pulse frequency / Hz	Stage speed / mm s^{-1}	Attenuator power / %	Number of passes
100	0.3	40	7

Table 6.1: Laser parameters used for electrode structure fabrication in intrinsic diamond

The depth of the trenches was determined by the number of laser passes made which was first calibrated using WLI. The machined electrode structures were characterised using WLI; see *Figure 6.9*.

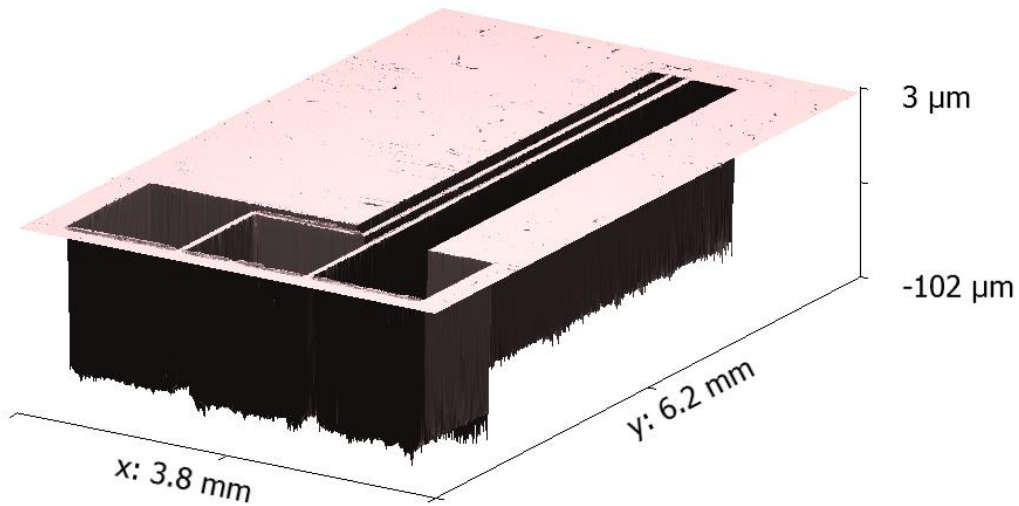


Figure 6.9: A 3D depth profile generated using interferometry of a laser machined trench structure in an intrinsic wafer. Such structures are used for pBDD electrode fabrication via an overgrowth process.

The geometries of pBDD electrode structures are consistent with that described for metal film electrodes in chapter 5. A schematic of a typical pBDD overgrowth structure is shown in *Figure 6.10* with a three electrode configuration of reference electrode ($120\ \mu\text{m}$ width), working electrode ($80\ \mu\text{m}$ width) and counter electrode ($400\ \mu\text{m}$ width). All electrodes are separated by $80\ \mu\text{m}$ of intrinsic diamond.

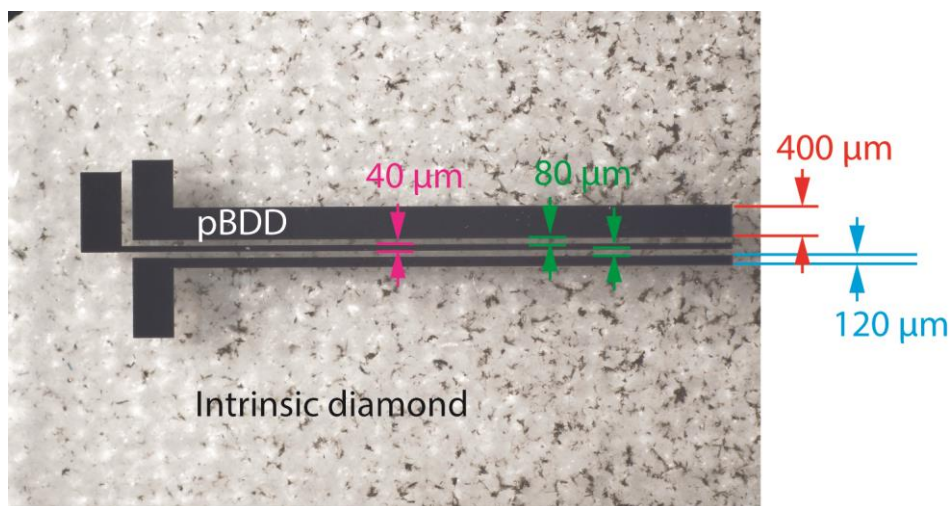


Figure 6.10: Schematic of overgrown pBDD electrode designs with: reference electrode (blue), width 120 μm; working electrode (pink), width 80 μm; counter electrode (red) width 400 μm; with a separation (green) of 80 μm.

Figure 6.11 shows a schematic for the fabrication of pBDD electrode structures overgrown in intrinsic diamond wafers. All CVD growth and wafer polishing was performed using facilities and expertise of Element Six Ltd. (a) First, an intrinsic wafer is grown via CVD and polished to a surface roughness of 3-5 nm (a). (b) The polished wafer is laser machined to create an electrode geometry in the form of a trench. During the CVD overgrowth of pBDD, the transport of growth species to the bottom of the trenches is crucial if the trench is to be filled before lateral growth closes off the top of the trench structure.³⁹ This places a limit on the aspect ratio of trench structures if successful pBDD overgrowth is to be achieved. The aspect ratio of width/ depth was ≥ 1 for all trench structures. Freshly machined wafers were acid cleaned using a solution of concentrated sulphuric acid saturated in KNO_3 and heated to $>300^\circ\text{C}$, removing sp^2 carbon generated during laser ablation of diamond (c) The wafer is overgrown with pBDD via CVD before being polished back (d) to reveal the pBDD electrode structure, co-planar with the surrounding intrinsic diamond.

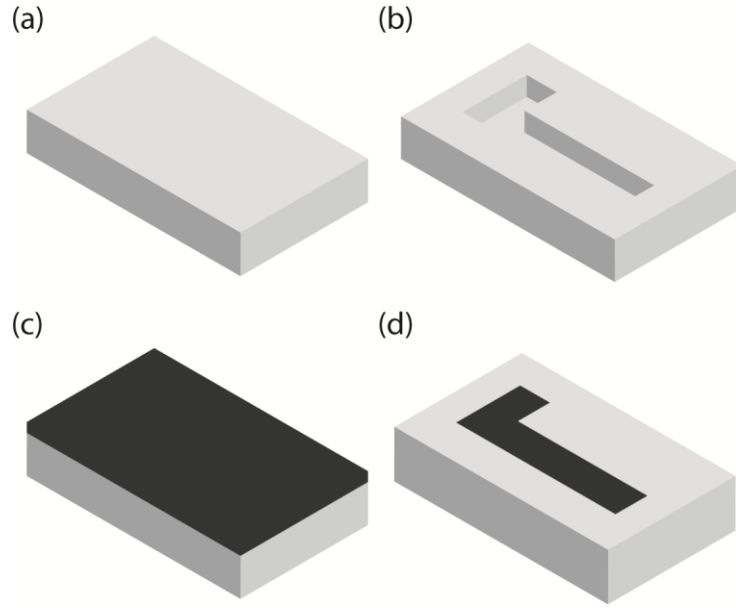


Figure 6.11: Schematic of the overgrowth procedure used to fabricate diamond electrode structures: (a) An intrinsic diamond wafer is polished to a roughness of approx. 3 nm; (b) laser micromachining is used to create a trench structure in the diamond wafer as per the electrode design; (c) a layer of pBDD is overgrown on the machined wafer via MWCVD; (d) the resulting pBDD layer is polished back until the electrode design is revealed.

Figure 6.12 shows field-emission scanning electron microscopy (FE-SEM) images of an overgrown pBDD electrode structure.

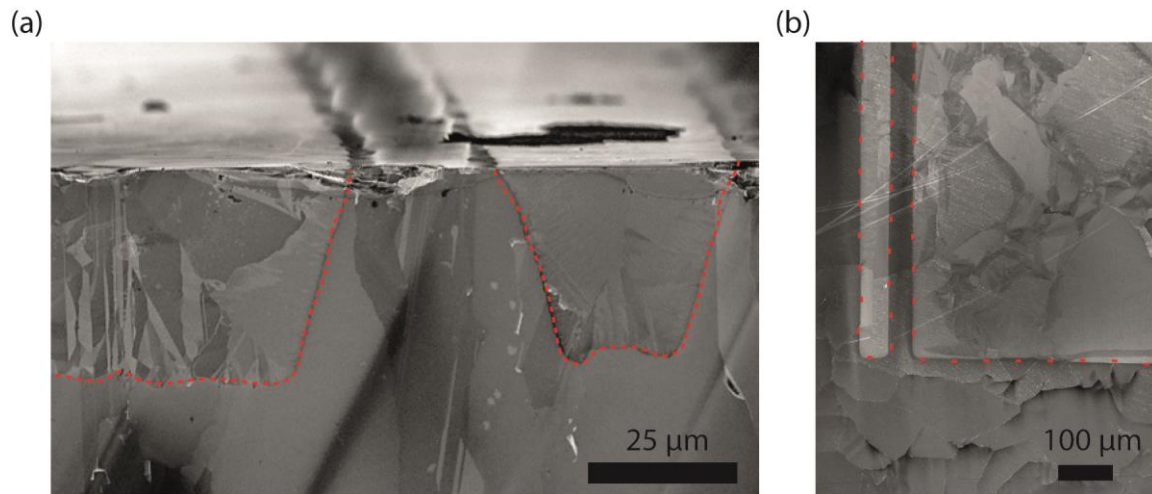


Figure 6.12: Field-emission scanning electron microscopy of pBDD band electrodes overgrown in intrinsic diamond via CVD: (a) cross-section view of pBDD bands (outlined in red); (b) top view of pBDD bands (outlined in red).

Since each electrode is completely isolated from one another in the insulating diamond wafer, the electrodes are individually addressable. However, as a result, the electrodes must each be contacted in order to create an electrochemical device. This can be done via a top contact (*Figure 6.13*) placed directly onto the exposed pBDD electrode surface, consisting of a Ti/Au film (10 nm and 200 nm respectively) deposited (via sputtering) onto a laser-roughened section of the electrode and annealed at 500 °C for 4 hrs.

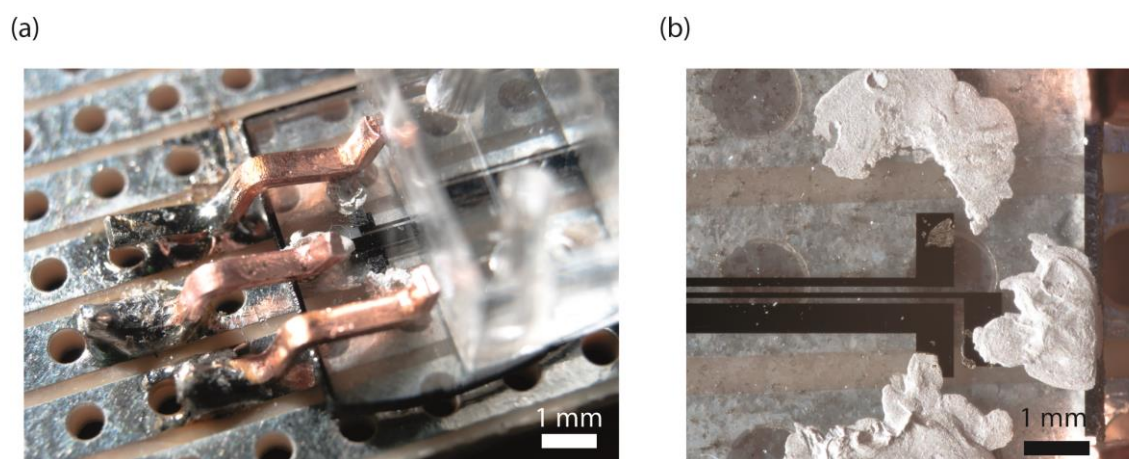


Figure 6.13: (a) A photograph of a diamond electrode device set up with copper contact pins and a PDMS microfluidic channel; (b) top-contact pads of deposited Ti/Au film on a laser roughened section of pBDD with silver paint added to protect the Ti/Au films.

The top contacts were found to be easily damaged with repeated connection/disconnection. This can be seen in *Figure 6.13b* where the gold contact pad has worn away from the pBDD surface. The incorporation of overgrown pBDD electrodes into microfluidic channels requires that any electrical contact does not interfere with the formation of the flow cell. For this reason and to increase the robustness of electrode contacts, laser machined back-contacting holes (750 μm diameter) were fabricated that pass through the electrode structure from the side opposite the exposed electrodes through to the back of the encapsulated pBDD electrodes. Typical WLI recorded during the fabrication of a back-contact hole is shown in *Figure 6.14a* with the depth achieved per laser pass shown.

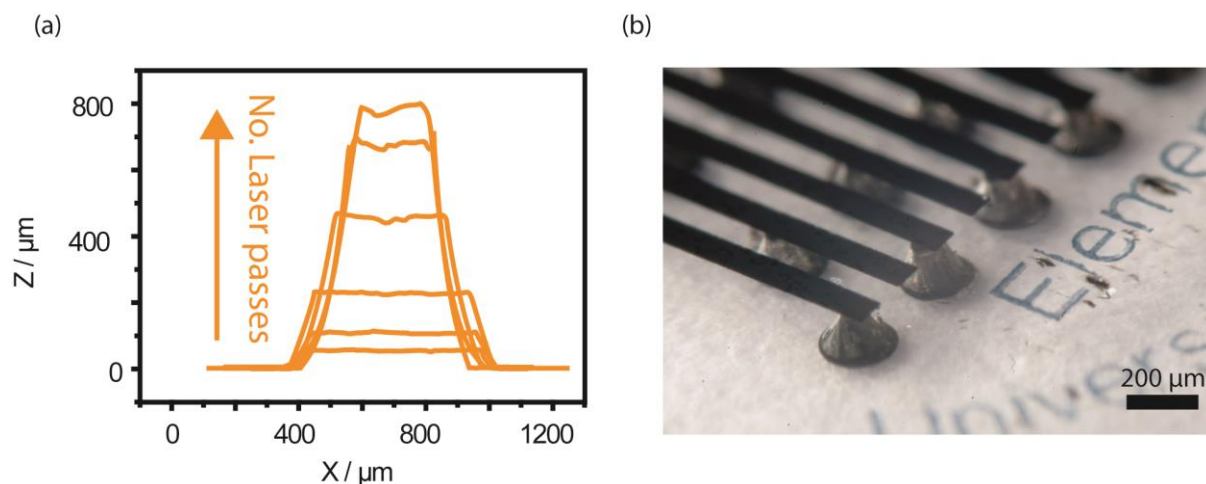


Figure 6.14: (a) interferometry data for a laser machined back-contact hole made in a diamond wafer containing an electrode structure; (b) a photograph of back-contact holes contacting a set of 100 μm wide pBDD electrodes in an intrinsic wafer.

Back-contact holes fabricated using laser machining techniques generated a “cone” structure (see Figure 6.14b) where the hole is wider at the top and narrower with increased machining depth. During the fabrication of a back-contact hole, graphitic carbon is formed inside the hole which provides an electrical contact with the underlying pBDD band. To ensure contact with the pBDD band was Ohmic, the graphitic carbon was removed from the back-contact holes via acid cleaning and a Ti/Au film (10 nm and 200 nm respectively) was deposited into the holes (see Figure 6.15) and annealed for 4 hours at 500 $^{\circ}\text{C}$, forming an Ohmic contact.⁴⁰

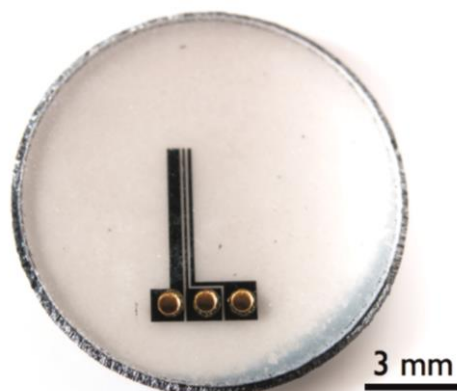


Figure 6.15: Photograph of a diamond electrode structure with laser machined back-contact holes coated with a Ti/Au metal film, deposited via sputtering, providing an Ohmic contact with the pBDD bands on the reverse of the structure.

6.2.2.2 Characterisation of boron-doped diamond electrode structures

The insulating and conducting regions of the all diamond electrode device were characterised using Raman spectroscopy to assess the quality of the diamond and qualitatively provide information on boron content. Raman spectra for a typical electrode structure can be seen in *Figure 6.16*. Raman reveals a characteristic diamond sp^3 peak present at 1332 cm^{-1} . This is seen in both (ai) the intrinsic and (aii) BDD. A clear attenuation of the 1332 cm^{-1} peak (Fano resonance) is seen in the spectrum corresponding to the BDD region spectrum. This feature in addition to the presence of a peak at 500 cm^{-1} is associated with the presence of high boron-doping level ($\geq 3 \times 10^{20}\text{ B atoms cm}^{-3}$). There is no sign of sp^2 impurities i.e. at 1560 cm^{-1} in both spectra reflecting the high quality of the CVD diamond material.

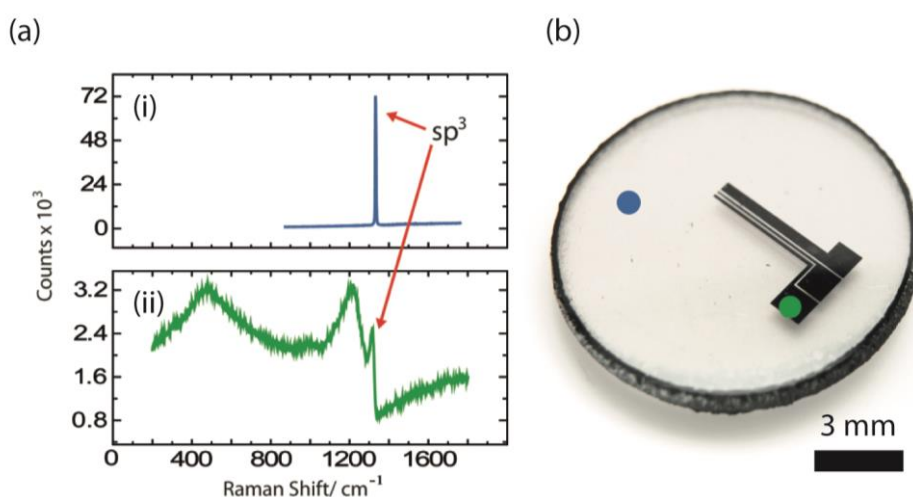


Figure 6.16: (a) Raman spectroscopy of (i) intrinsic diamond (blue) and (ii) pBDD regions (green) of the electrode structure shown in (b). The characteristic peak corresponding to sp^3 carbon at 1332 cm^{-1} is indicated with arrows.

6.2.3 Fabrication of diamond microfluidic device with integrated diamond electrodes

6.2.3.1 Construction of microfluidic device

Microfluidic channels were laser machined into optical quality, polycrystalline intrinsic wafers (DR-3 – see *table 2.1*, chapter 2) using the laser parameters described in *Table 6.1*. Inlets were created by laser machining in circular passes, 1 mm diameter and stepping the z-focus of the laser by $100\text{ }\mu\text{m}$ with each pass at a pulse frequency of 10 kHz, stage speed of 0.9 mm/s and attenuator power of 100%. Seven passes were required to machine through a 1 mm thick intrinsic diamond wafer using

these parameters. A typical diamond, single-channel microfluidic device is shown in *Figure 6.17a* with the corresponding depth profile of the channel recorded by WLI; see *Figure 6.17b*. The machined channel appears tapered, a feature of the laser machining process⁴¹ where ablation is less effective at the walls of the fabricated trench creating a “kerf” at the edge. Channel dimensions of 200 μm width by 150 μm depth were intended to replicate device geometries previously described in chapter 5 for PDMS channels. It was hoped this would make data collected with diamond devices comparable to those fabricated previously in PDMS. Using laser machining a channel 6 mm long, 200 μm wide (at wafer surface) tapered to 110 μm at channel base, with a depth of 135 μm was achieved.

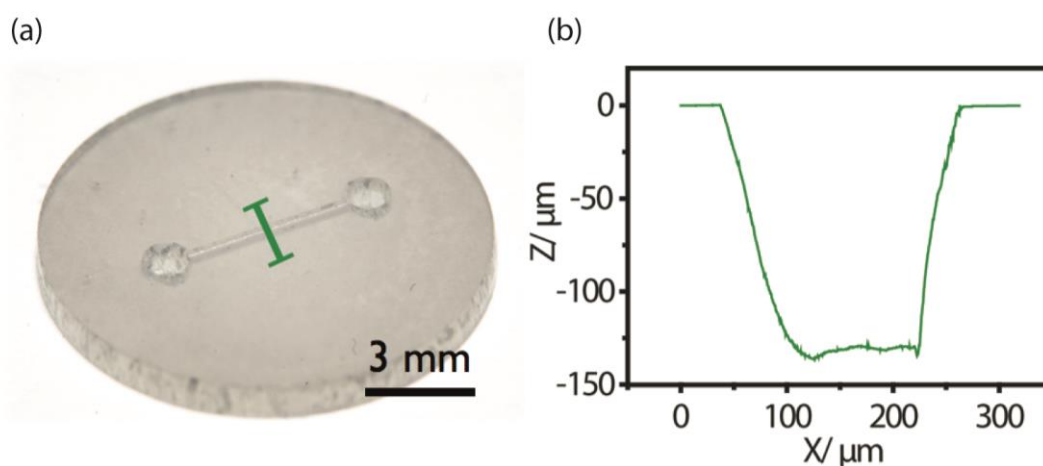


Figure 6.17: (a) photograph of a 200 μm tapered to 110 μm wide, 135 μm deep microfluidic channel laser machined into a polycrystalline intrinsic diamond wafer; (b) depth profile of laser machined microfluidic channel recorded by WLI.

Diamond microfluidic devices were constructed by clamping together the two 12 mm diameter, 1 mm thick diamond wafers: one containing the electrode structures, the other the microfluidic channels. The steel clamp set up used is described in *Figure 6.18*.

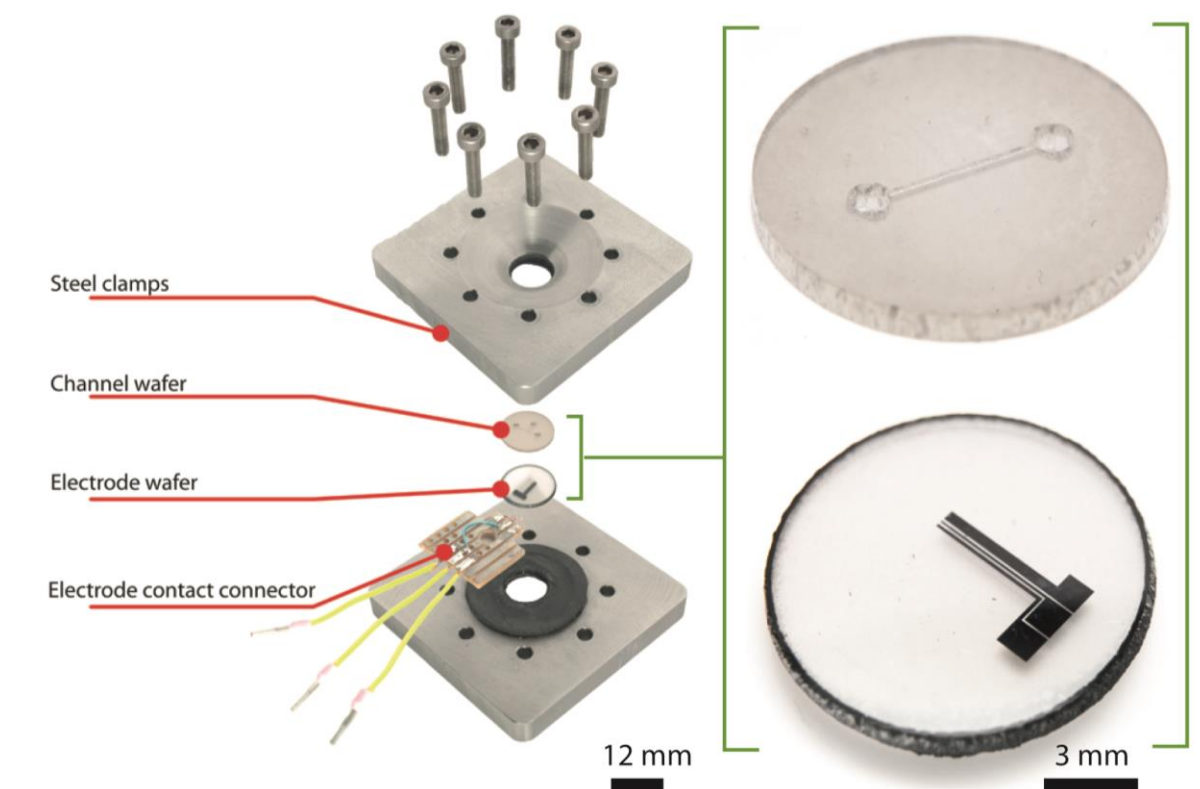


Figure 6.18: An exploded view of an all-diamond microfluidic device with components indicated.

Electrical contact was made to the electrodes via a set of copper pins inserted into the back-contact holes on the under-side of the electrode containing diamond wafer. Pressing the two diamond wafers together in this manner did not create a good enough seal to prevent solution leaking between the two wafers when solution was flowed through the device.

Although the wafers were polished within a nanometre roughness, any bow created in the wafers as a result of polishing conditions needed to be assessed, and the low deformation of diamond makes creating a seal challenging. Using a Tally-Surf profiler, the upward bow in the channel containing wafer was measured to be $2.097\text{ }\mu\text{m}$ (peak to valley) over a 9 mm area. The same measurement of the electrode containing wafer is still to be performed however, a similar bow is expected given the wafers are polished using the same technique. Had this bow not been present, the clamping of two co-planar wafers of nanometre roughness would more likely result in a seal. Removal of this bow is

possible however; polishing a wafer to be flat and have a nanometre roughness is time consuming and could not be achieved at the time of writing this thesis.

In order to create a seal a 1-3 μm thick gasket of PDMS was spin-coated (3000 rpm, 30 s) onto the channel containing wafer (*Figure 6.19*), cured and then clamped against the electrode containing wafer.



Figure 6.19: Photograph of a diamond electrode structure with a spin-coated, 3 μm thick PDMS gasket present over the electrodes.

The deformation of the PDMS gasket created a good seal between the two diamond wafers, restricting solution flow to the channel when aqueous solution was used in the device. This is particularly important for ensuring only electrode surfaces occupying the microfluidic channel are exposed to solution.

6.2.3.2 Electrochemical characterisation of diamond electrodes

Electrochemical characterisation of the pBDD microfluidic channel electrodes was carried out using 1 mM FcTMA⁺ with 0.1 M KNO₃ electrolyte solution flowed through the microfluidic channel at various volume flow rates ranging from 10-100 $\mu\text{L}/\text{min}$. CV responses for the all-diamond device are shown in *Figure 6.20a*. The i_{lim} as a function of $V_f^{1/3}$ for CV responses under flow was plotted (*Figure 6.20b*) and compares well with that expected from Levich; see equation 5.3.

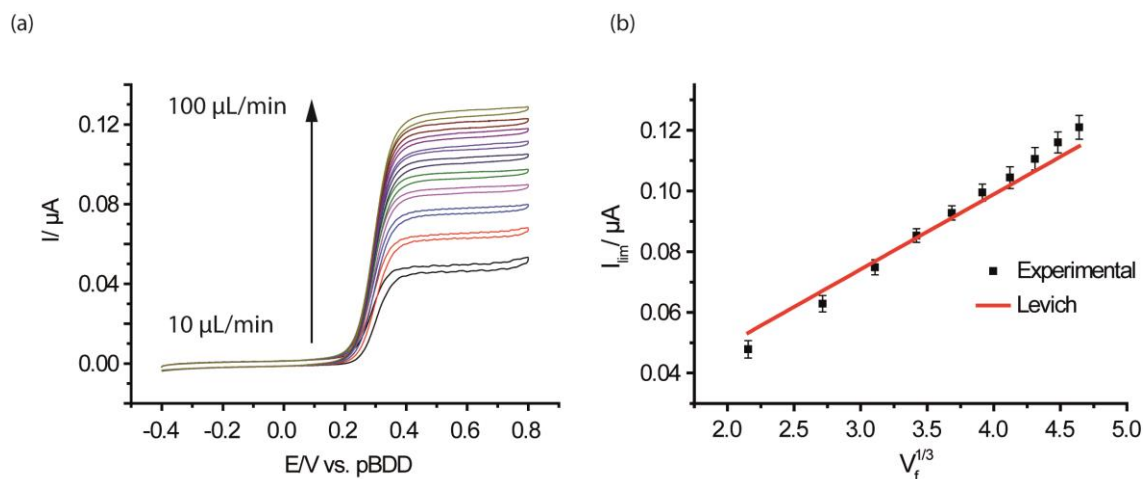


Figure 6.20: (a) CVs for 1 mM FcTMA⁺ oxidation on pBDD channel electrodes with 0.1 M KNO₃ electrolyte at a range of volume flow rates: 10-100 µL/min; (b) Plot of I_{lim} vs. $V_f^{1/3}$ for CV responses at various flow rates: comparing experimental (Black square) to Levich (red line).

The Levich fit was made by approximating the channel cross-section (see Figure 6.21a) to a rectangular channel of width 155 µm and height 135 µm in order to calculate U (see equation 5.4). A value of 200 µm was used for the electrode width, w corresponding to the measured width of the channel geometry adjacent to the pBDD electrodes; see Figure 6.21b.

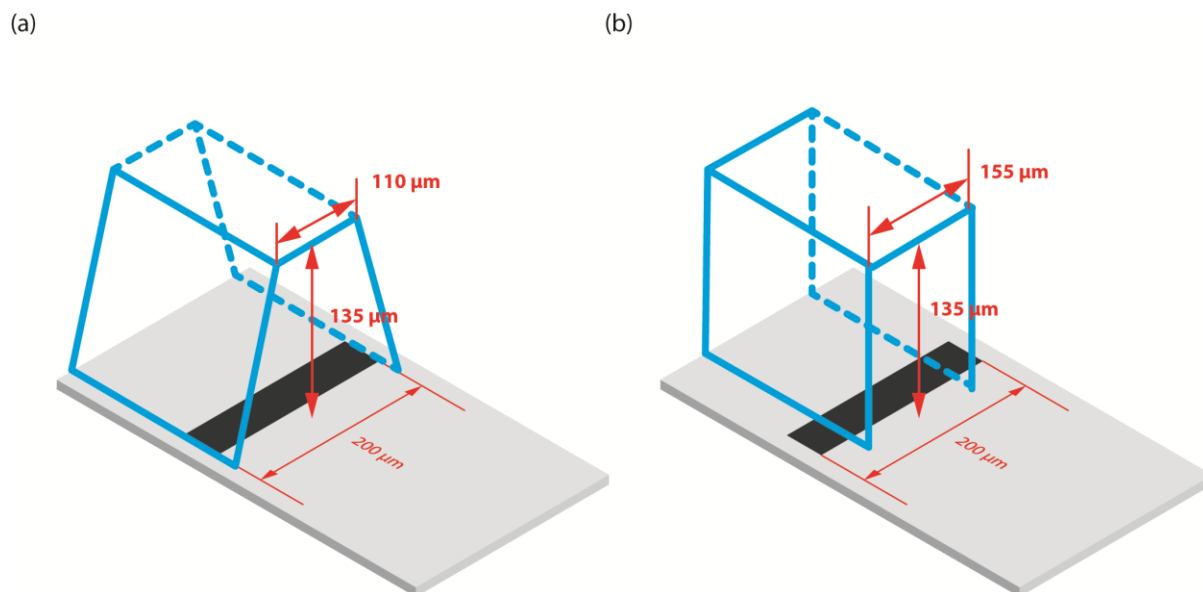


Figure 6.21: Schematics of the channel and electrode geometry as (a) measured and (b) channel geometry approximated for calculation of corresponding Levich current.

The fit to Levich with experimental data achieved using this approximation (based on the measured geometry) suggests that the measured geometry is maintained after device fabrication, unlike the PDMS microfluidic device described in chapter 5 that showed evidence of channel deformation. Here, the experimental data would only fit Levich with a modification to the measured dimensions of the flow device, to account for channel deformation during device fabrication.

To take full advantage of the chemical resistance of the all-diamond microfluidic device, a flow experiment using electroactive ferrocene (Fc) in acetonitrile with tetrabutylammonium hexafluorophosphate (TBAHFP) as supporting electrolyte was devised. It was hoped that the PDMS gasket would survive under these conditions given the very small area exposed to the incompatible acetonitrile in the channel. However, the acetonitrile was almost immediately absorbed into the PDMS upon introduction into the device, wetting the entire pBDD electrode geometry with electrolyte solution.

To address the incompatibility of PDMS gasket with volatile solvents such as acetonitrile, attempts were made to fabricate a gasket using a spin-coated film of Teflon AF-1600 which has previously been reported for fabricating chemically resistant valves in glass microfluidic devices.⁴² Teflon gaskets were fabricated from a solution of 6% (by mass) AF-1600 in Fluorinert® FC40 solvent (3M Company, USA) spin-coated (3000 rpm, 30 s) onto a 12 mm diameter diamond wafer containing microfluidic channels. The coated wafers were then placed on a hot plate at 165 °C to evaporate the FC40 solvent. At the time of writing this thesis, a good seal using the spin-coated Teflon gaskets was not achieved. It is thought that the deformation in the gasket is not sufficient to seal between the diamond wafers. Tests using a temperature induced deformation of the Teflon gaskets combined with the application of light pressure have been designed and will form the basis for future work.

6.2.4 Microdroplet generation in a diamond microfluidic device

As discussed in chapter 5, microfluidic platforms for generating micro-droplets are of great interest to a host of biological and chemical application. The ability to generate droplets under flow in an all-diamond microfluidic device presents a number of advantages in that diamond is biologically

compatible, chemically inert and has a tuneable surface functionality. Applications to electrochemical multiphase flow analysis under harsh conditions, where ordinary metallic electrodes would be unsuited can be imagined.

A simple T-junction channel geometry was laser machined into an intrinsic wafer using parameters described previously for a single-channel device (*Figure 6.22a*). The device was designed to create plug-droplets of mineral oil containing a Sudan blue II dye in a continuous aqueous flow. The channel containing wafer was clamped against another wafer containing pBDD electrodes (not used in this study); see *Figure 6.22b*. No PDMS gasket was used as this would have lined the otherwise hydrophilic diamond channel walls making wetting interactions with generated oil droplets possible.

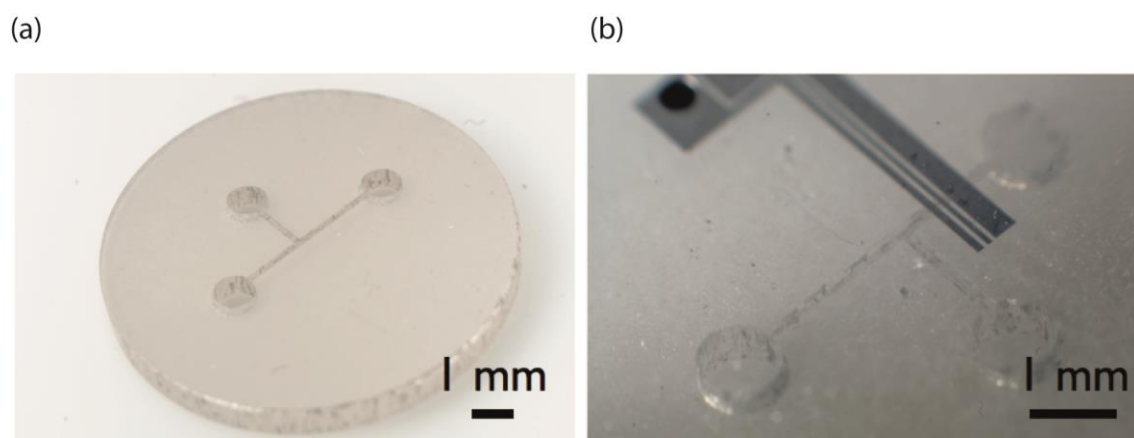


Figure 6.22: Photographs of (a) a microfluidic T-junction geometry laser machined in a polycrystalline intrinsic diamond wafer; (b) pBDD electrodes incorporated into a T-junction device for electrochemical droplet analysis.

Figure 6.23 shows the generation of mineral oil “plug”-like droplets in an aqueous continuous flow within an all-diamond microfluidic device with volume flow rates of 1 $\mu\text{l}/\text{min}$ and 3 $\mu\text{l}/\text{min}$ for the DP and CP respectively.

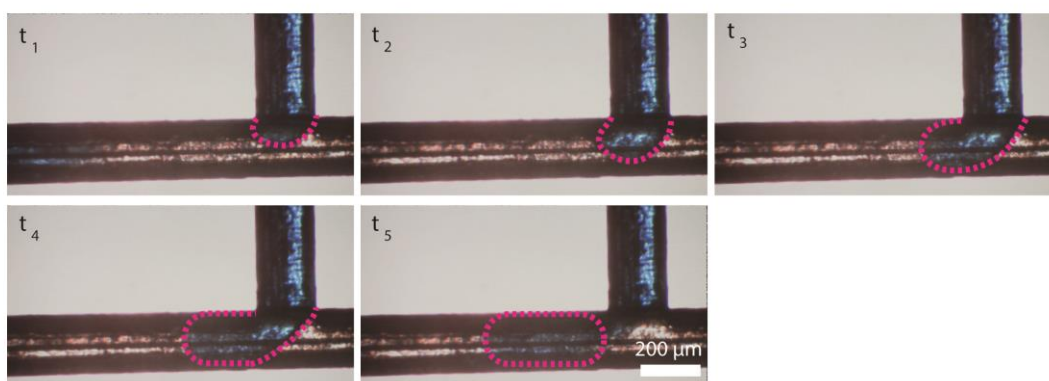


Figure 6.23: Microscope images of a T-junction device ($200 \times 100 \mu\text{m}$, $w \times h$) fabricated from diamond without a PDMS gasket generating “plug”-like droplets of mineral oil (coloured with Sudan blue II dye and outlined in pink for clarity) in an aqueous continuous phase.

The lack of a gasket allowed the aqueous CP to leak from the microfluidic channels into the gap between the diamond wafers (*Figure 6.24a*) which was observable optically. However, none of the oil DP was seen to leak between the two diamond wafers, instead droplets were restricted to the channel; as shown schematically in *Figure 6.24b*. It may be that the V_f applied to the device, did not generate sufficient pressure to overcome the unfavourable interactions between the oil phase and the hydrophilic diamond. Therefore, these surface interactions prevented the DP from entering the gap between the diamond wafers, which instead was filled by the hydrophilic CP only.

Although this device was successful in creating oil droplets under aqueous flow, such a system would not be suitable for electrochemical analysis where the fluid phases would need to be confined to the channel and not allowed to expose the entire electrode geometry. Leakage in devices is not ideal as it makes it difficult to control flow conditions in the channel and limits the ability to precisely define the system.

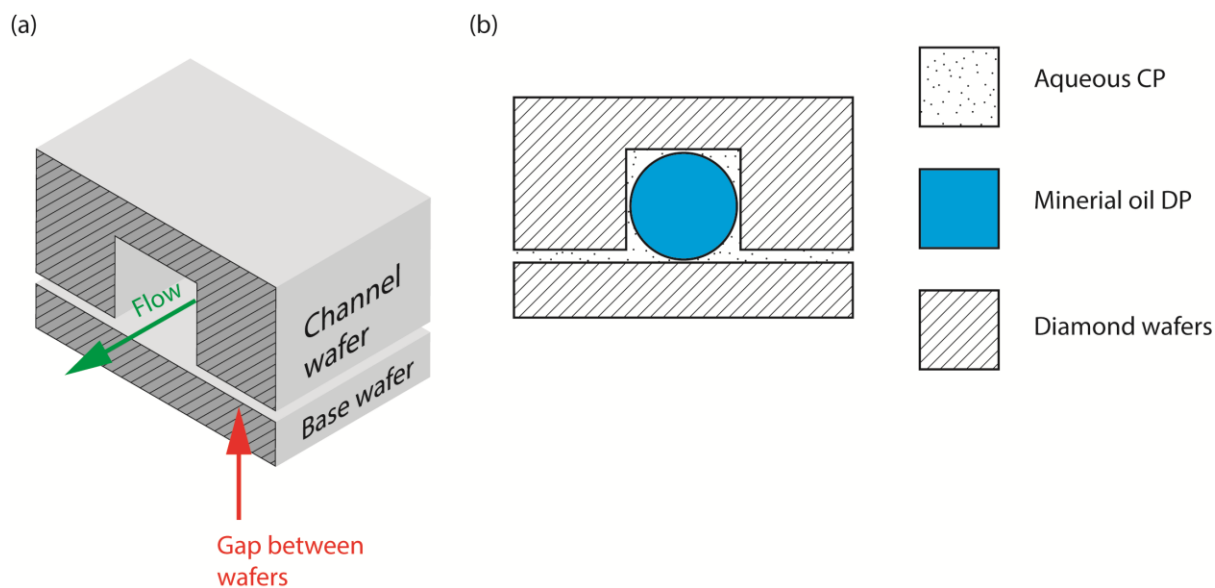


Figure 6.24: Schematic of (a) a diamond microfluidic channel with no gasket present between the diamond wafers; (b) An oil droplet occupying a microfluidic channel without interacting with the channel walls.

6.3 Conclusions

In this work a simple method for fabricating microfluidic devices from synthetic polycrystalline diamond grown via CVD has been presented. The application of a triple Nd:YAG laser for micromachining micro-scale channels in intrinsic diamond material is demonstrated with careful control of laser machined geometries achieved by manipulation of laser parameters such as: laser pulse frequency stage traversing speed, attenuator power and the number of laser passes over a substrate.

High-quality pBDD electrode structures were successfully fabricated using an overgrowth technique and integrated into a diamond microfluidic channel, characterised by electrochemistry with good agreement to Levich theory.

The sealing of a diamond device constructed by pressing two wafers together has proven problematic unless a gasket of a compressible material i.e. PDMS is incorporated between the wafers. Although this strategy has been demonstrated for aqueous systems, the use of volatile solvents, in this case acetonitrile was found to be incompatible with the PDMS material. Limitations on the use of the

device by materials such as PDMS defeat the reasoning for utilising diamond in the first place and so new strategies for creating a leak-free, all-diamond device need investigation.

Attempts were made to fabricate a solvent resistant gasket from spin-coated Teflon however; these were not successful using the procedure employed. The potential for spin coated Teflon gaskets to solve the leakage issue could be realised with improved gasket fabrication procedures. Such improvements include the use of a heat-assisted deformation of a Teflon gasket in order to better seal the gap between diamond wafers. The initial procedure for inserting a Teflon gasket simply pressed a pre-formed Teflon film, approximately 3 μm thick and spin-coated onto the channel containing diamond wafer against the pBDD electrode containing wafer. The deformation of the Teflon gasket with light force applied by clamping may not be sufficient to create a seal, particularly where the recessed pBDD electrodes reside. The Teflon would need to deform into these recessions to prevent areas of the electrodes not in the microfluidic channel from being exposed to solution. Initial tests have found Teflon deformation/melting to occur at temperatures close to 320 $^{\circ}\text{C}$ by application of a soldering iron as a heat source. This is consistent with values found in the literature.⁴³

As mentioned previously, the technique of polishing diamond wafers is vital in creating a wafer that is both flat and has a low, nanometre surface roughness. It may be possible to create a good seal between two diamond wafers if both wafers are sufficiently flat as well as smooth. At the time of writing this thesis, improvements in the polishing (conducted by Element Six) to fabricate wafers that are both flat and smooth were in the process of testing. In addition to flatter wafers, thinner wafers more tolerant of flexing were under investigation. In this case a set of 60 μm thick, 12 mm diameter intrinsic wafers were polished to a nanometre finish. It is thought that pressing thin, flexible diamond wafers against flatter, channel containing wafers could create better sealing between diamond wafers. This work is ongoing.

Monolithic diamond microfluidic devices have been reported in the literature.^{18, 44} Both of these utilise the growth of CVD diamond around a sacrificial mould material that acts to define the microfluidic channel and is then subsequently removed via chemical etching to leave an all-diamond channel.

Figure 6.25 shows a schematic of the fabrication process used to create monolithic diamond microchannels with a sacrificial silicon mould. First, the silicon mould for the microchannels is fabricated using RIE (a). CVD diamond is grown over the mould (b) and the supporting silicon wafer is etched away until reaching a silicon dioxide layer. This oxide layer acts as a marker and prevents the silicon etch from removing the silicon in the microfluidic channel. This silicon oxide layer is then etched away using a different chemistry to the silicon etch, leaving the CVD diamond and sacrificial silicon in the channel. CVD diamond is then overgrown on the resulting etched surface (c), after which the sacrificial silicon mould in the channel is etched away leaving a hollow microchannel in the CVD diamond (d).

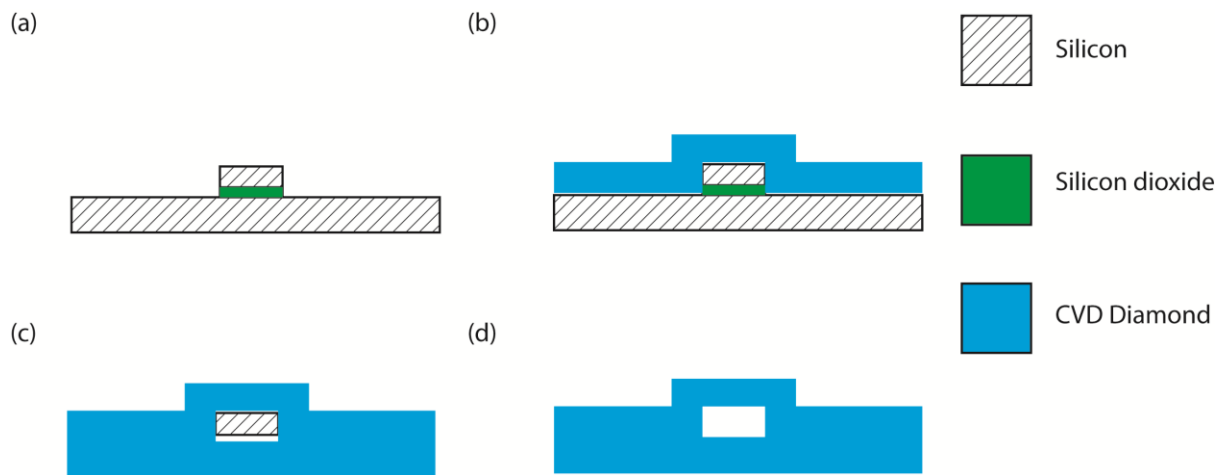


Figure 6.25: Schematic of the fabrication of a diamond microfluidic channel using a sacrificial mould: (a) a silicon wafer mould is fabricated; (b) CVD diamond is grown onto the silicon mould; (c) the silicon is etched off stopping just after the silicon dioxide layer is removed and CVD diamond is grown over the resulting surface; (d) silicon encapsulated by the diamond is etched out leaving behind a hollow channel.

These devices have not incorporated pBDD electrodes which could potentially be achieved using the electrode structure overgrowth procedure described in this thesis.³⁹ Future work would seek to realise an electrode containing monolithic device fabricated using a sacrificial mould material.

Another strategy for fabricating micro channels in diamond is to use a three-dimensional laser writing technique to graphitise subsurface diamond material in the wafer.^{16, 45, 46} This graphitic carbon could

then be selectively etched via an oxidative acid clean, creating sub-surface channels. However, the incorporation of pBDD band electrodes into such structures would be challenging if not impossible.

Owing to its high refractive index, diamond has found use as an attenuated total reflection (ATR) element in fourier-transform infrared detection (FT-IR). The high mechanical hardness and chemical inertness of diamond make it particularly suited to ATR-FTIR when applied to challenging or harsh chemical environments and has been demonstrated in high-performance liquid chromatography (HPLC) coupled FTIR systems.⁴⁷ Recently, examples of microfluidic channels combined with ATR crystals for ATR-FTIR analysis of fluidic flows in microchannels have been reported.^{48, 49} These devices have employed channels made from PDMS and combine the advantages of microfluidic systems i.e. small sample volumes and high throughput with the highly sensitive material characterisation abilities of FTIR.^{49, 50} Electrochemical integration with ATR-FTIR and AFM has also been reported where pBDD electrodes were deposited onto an ATR crystal.⁵¹ The ability to grow pBDD electrodes, or diamond channels, directly onto diamond ATR crystals would be attractive for combined electrochemical - FTIR analysis, especially when employing aggressive media.

6.4 References

1. D. Mark, S. Haeberle, G. Roth, F. von Stetten and R. Zengerle, *Chemical Society Reviews*, 2010, **39**, 1153-1182.
2. T. Schneider, J. Kreutz and D. T. Chiu, *Analytical Chemistry*, 2013, **85**, 3476-3482.
3. S. Goyal, M. R. Thorson, G. G. Z. Zhang, Y. Gong and P. J. A. Kenis, *Crystal Growth & Design*, 2012, **12**, 6023-6034.
4. P. He, G. Greenway and S. J. Haswell, *Chemical Engineering Journal*, 2011, **167**, 694-699.
5. Z. T. Cygan, J. T. Cabral, K. L. Beers and E. J. Amis, *Langmuir*, 2005, **21**, 3629-3634.
6. R. S. Balmer, J. R. Brandon, S. L. Clewes, H. K. Dhillon, J. M. Dodson, I. Friel, P. N. Inglis, T. D. Madgwick, M. L. Markham, T. P. Mollart, N. Perkins, G. A. Scarsbrook, D. J. Twitchen, A. J. Whitehead, J. J. Wilman and S. M. Woollard, *Journal of Physics: Condensed Matter*, 2009, **21**, 364221.
7. G. Davies, *Properties and growth of diamond*, INSPEC, the Institution of Electrical Engineers, 1994.
8. W. B. Zimmerman, *Chemical Engineering Science*, 2011, **66**, 1412-1425.
9. O. Ordeig, N. Godino, J. del Campo, F. X. Muñoz, F. Nikolajeff and L. Nyholm, *Analytical Chemistry*, 2008, **80**, 3622-3632.
10. S. Nilsson, O. Klett, M. Svedberg, A. Amirkhani and L. Nyholm, *Rapid Communications in Mass Spectrometry*, 2003, **17**, 1535-1540.
11. L. A. Hutton, J. G. Iacobini, E. Bitziou, R. B. Channon, M. E. Newton and J. V. Macpherson, *Analytical Chemistry*, 2013, **85**, 7230-7240.

12. O. Dorsch, M. Werner and E. Obermeier, *Diamond and Related Materials*, 1995, **4**, 456-459.
13. Y. Ando, Y. Nishibayashi, K. Kobashi, T. Hirao and K. Oura, *Diamond and Related Materials*, 2002, **11**, 824-827.
14. C. L. Lee, E. Gu and M. D. Dawson, *Diamond and Related Materials*, 2007, **16**, 944-948.
15. M. P. Ray, J. W. Baldwin, T. I. Feygelson, J. E. Butler and B. B. Pate, *Review of Scientific Instruments*, 2011, **82**, -.
16. T. V. Kononenko, V. I. Konov, S. M. Pimenov, N. M. Rossukanyi, A. I. Rukovichnikov and V. Romano, *Diamond and Related Materials*, 2011, **20**, 264-268.
17. R. Müller, R. Gronmaier, K. Janischowsky, J. Kusterer and E. Kohn, *Diamond and Related Materials*, 2005, **14**, 504-508.
18. R. Müller, P. Schmid, A. Munding, R. Gronmaier and E. Kohn, *Diamond and Related Materials*, 2004, **13**, 780-784.
19. S. Su, J. Li, G. C. B. Lee, K. Sugden, D. Webb and H. Ye, *Applied Physics Letters*, 2013, **102**, 231913-231913-231915.
20. S. Bhattacharya, A. Datta, J. M. Berg and S. Gangopadhyay, *Microelectromechanical Systems, Journal of*, 2005, **14**, 590-597.
21. H. Hillborg and U. W. Gedde, *Polymer*, 1998, **39**, 1991-1998.
22. Y. Berdichevsky, J. Khandurina, A. Guttman and Y. H. Lo, *Sensors and Actuators B: Chemical*, 2004, **97**, 402-408.
23. S. Hu, X. Ren, M. Bachman, C. E. Sims, G. P. Li and N. Allbritton, *Analytical Chemistry*, 2002, **74**, 4117-4123.
24. O. A. Williams and R. B. Jackman, *Semiconductor Science and Technology*, 2003, **18**, S34-S40.
25. T. Nakamoto and S. Shabouk, *J. Micro-Nano Mech.*, 2008, **4**, 121-129.
26. M. Weikert and F. Dausinger, in *Femtosecond Technology for Technical and Medical Applications*, eds. F. Dausinger, H. Lubatschowski and F. Lichtner, Springer Berlin Heidelberg, 2004, vol. 96, pp. 155-165.
27. C. J. Evans, E. Paul, D. Dornfeld, D. A. Lucca, G. Byrne, M. Tricard, F. Klocke, O. Dambon and B. A. Mullany, *CIRP Annals - Manufacturing Technology*, 2003, **52**, 611-633.
28. N. B. Dahotre and S. P. Harimkar, *Laser Fabrication and Machining of Materials*, Springer, 2008.
29. R. R. Gattass and E. Mazur, *Nat Photon*, 2008, **2**, 219-225.
30. D. Bäuerle, *Laser Processing and Chemistry*, 2 edn., Springer, 1996.
31. G. Chryssoulouris, *Laser Machining: Theory and Practice*, Springer-Verlag, 1991.
32. P. M. Fabis, *Surface and Coatings Technology*, 1996, **82**, 320-325.
33. M. Rothschild, C. Arnone and D. J. Ehrlich, *Journal of Vacuum Science & Technology B*, 1986, **4**, 310-314.
34. S. Baudach, J. Bonse and W. Kautek, *Appl Phys A*, 1999, **69**, S395-S398.
35. F. Beinhorn, J. Ihlemann, K. Luther and J. Troe, *Appl Phys A*, 2004, **79**, 869-873.
36. Y. Zhao, Y. Jia, J. Yang and X. Zhu, *OPTICE*, 2007, **46**, 044301-044301-044306.
37. M. Pagels, C. E. Hall, N. S. Lawrence, A. Meredith, T. G. J. Jones, H. P. Godfried, C. S. J. Pickles, J. Wilman, C. E. Banks, R. G. Compton and L. Jiang, *Analytical Chemistry*, 2005, **77**, 3705-3708.
38. P. Forsberg, E. O. Jorge, L. Nyholm, F. Nikolajeff and M. Karlsson, *Diamond and Related Materials*, 2011, **20**, 1121-1124.
39. M. B. Joseph, E. Bitziou, T. L. Read, L. Meng, N. L. Palmer, T. P. Mollart, M. E. Newton and J. V. Macpherson, *Analytical Chemistry*, 2014, **86**, 5238-5244.
40. K. Das, V. Venkatesan, K. Miyata, D. L. Dreifus and J. T. Glass, *Thin Solid Films*, 1992, **212**, 19-24.
41. A. K. Dubey and V. Yadava, *Journal of Materials Processing Technology*, 2008, **204**, 412-418.
42. P. A. Willis, B. D. Hunt, V. E. White, M. C. Lee, M. Ikeda, S. Bae, M. J. Pelletier and F. J. Grunthaner, *Lab on a Chip*, 2007, **7**, 1469-1474.
43. H. W. Starkweather, *Macromolecules*, 1986, **19**, 1131-1134.
44. H. Björkman, P. Rangsten and K. Hjort, *Sensors and Actuators A: Physical*, 1999, **78**, 41-47.

45. R. D. Simmonds, P. S. Salter, A. Jesacher and M. J. Booth, *Opt. Express*, 2011, **19**, 24122-24128.
46. P. Olivero, G. Amato, F. Bellotti, O. Budnyk, E. Colombo, M. Jakšić, C. Manfredotti, Ž. Pastuović, F. Picollo, N. Skukan, M. Vannoni and E. Vittone, *Diamond and Related Materials*, 2009, **18**, 870-876.
47. A. Edelman, J. Diewok, J. Baena and B. Lendl, *Anal Bioanal Chem*, 2003, **376**, 92-97.
48. S. Kazarian, *Anal Bioanal Chem*, 2007, **388**, 529-532.
49. K. L. A. Chan, S. Gulati, J. B. Edel, A. J. de Mello and S. G. Kazarian, *Lab on a Chip*, 2009, **9**, 2909-2913.
50. E. N. Lewis, P. J. Treado, R. C. Reeder, G. M. Story, A. E. Dowrey, C. Marcott and I. W. Levin, *Analytical Chemistry*, 1995, **67**, 3377-3381.
51. D. Neubauer, J. Scharpf, A. Pasquarelli, B. Mizaikoff and C. Kranz, *Analyst*, 2013, **138**, 6746-6752.

7 Conclusions and Further Work

Work in this thesis has demonstrated the use of pBDD as an electrode material for a variety of different sensing applications in both aqueous and oil-water environments. Diamond offers reduced fouling of surfaces, chemical inertness, mechanical hardness, biological compatibility and a broad spectral transparency.¹ As an electrode material pBDD exhibits very low background currents and a broad solvent window making it highly attractive for sensor applications. Importantly, the performance of diamond devices will not deteriorate upon exposure to aggressive media, harsh environments or strong cleaning procedures, making pBDD highly applicable to studies under extreme conditions. Fabrication methods for producing pBDD electrodes in a range of geometries: from simple 1 mm diameter macros through to multi-band electrodes encased in insulating diamond are described. These devices are then employed to study systems that present challenging environments for electrochemical analysis.

In Chapter 3, pBDD macroelectrodes, encased in glass, are used as an electrochemically inert support for catalytic metal NPs allowing the detection of GIs in pharmaceutically relevant matrixes in both aqueous and non-aqueous solutions. Through the appropriate selection of metal catalyst, the metal NP functionalised pBDD electrode was optimised to detect micromolar concentrations of hydrazine in quiescent solutions. In particular, detection limits of 11.1 μM and 3.3 μM hydrazine in the presence of excess electroactive pharmaceutical species acetaminophen and promazine, were determined respectively. The inherently low background currents of pBDD make this material a suitable support for catalytic metal NPs. Compared to using a pure metal electrode, electrodeposition of metal NPs on the BDD surfaces, reduces the overall amount of metal on the electrode surface which serves to both reduce the cost of sensor fabrication as well as reducing the overall surface area dependent capacitive currents associated with the metal electrodes. At sufficiently high densities, mass transport to the electrodeposited NPs, results in diffusional overlap, resulting in a diffusion profile equivalent to that for a planar electrode, on the timescale of measurements made. As such, the

currents observed on the NP-pBDD electrode are as expected for a metal electrode of the same geometric area but with a significant reduction in the background currents.

The electrochemical detection of hydrazine and a number of hydrazine derivatives in non-aqueous solvents was also demonstrated. This initial proof-of-concept demonstrates the potential use of electrochemical detection techniques for fast, direct analysis of electroactive GIs present in pharmaceutical systems. The same sensor was also demonstrated for monitoring the accumulation of hydrazine in a solution containing a dissolved, unstable polymer material that breaks-down to release hydrazine over time. Further work, moving to flow regimes in order to enhance detection limits, and the use of GI or API extraction systems for enhancing the performance of an electrochemical sensor applied in pharmaceutical analysis is discussed.

In Chapter 4, metal NP functionalised pBDD electrodes are used to detect the presence of non-polar oil droplets on the electrode surface, using electrogenerated bromine (from bromide) as a probe. The extent of bromine partitioning into single non-polar oil droplets of various sizes ranging from 100 – 3000 μm diameter and arrays of 100 μm diameter droplets was monitored electrochemically via DPSC demonstrating sensitivity towards the size and number of oil droplets present on the electrode surface. It was determined that arrays of microdroplets enhance the sensitivity of the DPSC approach by maximising the electrode surface coverage and by increasing the oil/water interface-to-volume ratio, compared to that of a single oil droplet. Carrying this approach forward, DPSC could be employed as a method for monitoring reactions taking place within droplets both in stationary, or even under flow conditions. The use of DPSC to detect non-polar oil phases, particularly under flow, lends itself to applications in multiphase flow profiling.

Work in Chapter 5 describes the fabrication of PDMS microfluidic devices with channel geometries designed to generate microdroplets under flow. Metal thin-film electrodes in a three-electrode configuration were integrated into these microfluidic devices to study the effect of droplet flow on the electrochemical responses in systems where the droplets contain (i) electrolyte only (capacitive detection) and (ii) an electroactive mediator, e.g.. FcTMA^+ . These devices demonstrated

the ability to both detect droplets electrochemically and monitor the frequency of droplets moving over the electrodes. The observed electrochemical responses for droplet events allow the calculation of the speed and size of droplets moving through a microfluidic channel. However, the use of PDMS microfluidic devices proved problematic when using volatile, non-polar solvents where the elastomer material would swell compromising the microfluidic channel geometry and making the devices unusable. Further studies on these systems require a microfluidic device fabricated from a chemically inert material, which supports integration of the sensor electrodes.

I_{lim} vs. V_f electrochemical data recorded in a single PDMS channel device for the oxidation of FcTMA^+ fitted to Levich theory, however, the dimensions of the channel inputted suggested the PDMS channel has been deformed during fabrication. Channel dimensions of 75 μm (height) and 290 μm (width) were determined via electrochemical characterisation rather than the expected dimensions of 100 μm (height) and 200 μm (width) measured in components before fabrication. This highlights the importance of careful fabrication and robustness of PDMS devices.

The different PDMS channel geometries were employed to generate both bubble-like and plug-like droplets. For plug-like droplets, the minimum detectable size of droplet was limited by the size of the three electrode configuration adopted.

In Chapter 6, a method for fabricating microfluidic channels in synthetic, polycrystalline intrinsic diamond is described utilising laser micromachining to ablate diamond material, creating trenches in a polished 12 mm diameter diamond wafer. This is an alternative to the less robust PDMS approach described in Chapter 5. It was shown that laser micromachining combined with CVD overgrowth procedures is a successful procedure for the creation of high-quality pBDD electrodes encapsulated in insulating diamond, which is then polished to result in a coplanar conducting-insulating diamond structure. Construction methods for forming a microfluidic device with integrated pBDD electrodes are described using a steel clamp that presses two diamond wafers together: one containing a microfluidic channel, the other containing the pBDD electrodes. The adoption of a PDMS gasket between the diamond wafers was necessary to prevent solution leakage. Although

electrochemical characterisation of this device yielded a good fit to that expected by Levich theory for a channel electrode (matching the dimensions measured), the progression of the device to systems using volatile, non-aqueous solvents was not realised due to the instability of the PDMS gasket under such conditions. Work focused on replacing the PDMS gasket with spin-coated Teflon AF-1600. However, ultimately a method for fabricating a true “all-diamond” device is of greatest interest. Examples of all-diamond microchannel devices have been reported in the literature using a series of lithographic techniques combined with MEMs etching procedures and CVD overgrowth steps to fabricate free-standing, hollow diamond channel structures.² These devices do not yet incorporate pBDD electrodes.

In summary, the fabrication and application of diamond sensors has been demonstrated in challenging environments such as non-aqueous solvents, in the presence of non-polar oil phases and an excess of electroactive matrix. These sensors have been shown to enhance detection abilities in pharmaceutical mediums using electroanalysis and provide a method to detect local solution phase changes. The development of electrochemical methods capable of directly detecting phase changes under flow conditions have been presented which would be of interests as a proof of concept for electrochemical sensors in multiphase flow analysis. Finally, a route for fabricating all-diamond microfluidic devices with integrated pBDD electrodes is discussed with further work in developing strategies for creating monolithic diamond devices raised. Such devices would present a high performance platform for the study of microfluidics in extreme conditions with a robustness that allows repeated use without degradation of the device.

References

1. R. S. Balmer, J. R. Brandon, S. L. Clewes, H. K. Dhillon, J. M. Dodson, I. Friel, P. N. Inglis, T. D. Madgwick, M. L. Markham, T. P. Mollart, N. Perkins, G. A. Scarsbrook, D. J. Twitchen, A. J. Whitehead, J. J. Wilman and S. M. Woollard, *Journal of Physics: Condensed Matter*, 2009, **21**, 364221.
2. H. Björkman, P. Rangsten and K. Hjort, *Sensors and Actuators A: Physical*, 1999, **78**, 41-47.